Development of a stacked detector system and its application as an X-ray polarimeter

Dissertation
der Mathematisch-Naturwissenschaftlichen Fakultät
der Eberhard Karls Universität Tübingen
zur Erlangung des Grades eines
Doktors der Naturwissenschaften
(Dr. rer. nat.)

vorgelegt von

Daniel Maier

aus Ulm

Tübingen
2015

Gedruckt mit Genehmigung der Mathematisch-Naturwissenschaftlichen Fakultät der Eberhard Karls Universität Tübingen.

Tag der mündlichen Qualifikation:	23.02.2015
Dekan:	Prof. Dr. Wolfgang Rosenstiel
1. Berichterstatter	Prof. Dott. Andrea Santangelo
2. Berichterstatter	Prof. Dr. Klaus Werner
3. Berichterstatter	Dr. Philippe Laurent

Abstract

Astronomical observations in the X-ray range must be performed outside of earth's atmosphere and are nowadays mainly done by the use of X-ray satellites. The optics which defines the field of view of the satellite and the sensor which detects the X-ray radiation are two essential parts of an X-ray satellite. The use of a focusing optics which concentrates the radiation to a small sensor achieves a high spatial resolution and a low detector background and results therefore in a high sensitivity to detect weak X-ray sources.

The recent development of multi-layer-coated X-ray optics allows to focus radiation up to the hard X-ray range and requires new detector concepts. A stacked detector setup consisting of a low energy detector (LED) and a high energy detector (HED) that is placed behind the LED to cover such a wide energy range has been developed in this work. The main advantage of a stacked detector system is its effective detection of broad band X-ray radiation (0.1 keV to 80 keV) that is focused by the optics.

The main goal of this work is the construction of a stacked detector system and the investigation of its properties with analysis software that was especially developed for this purpose. In this context, the mutual influence between both detector systems is of special interest and shall be studied experimentally. The LED is realized by a silicon based active pixel matrix with a maximal readout speed of 410 frames per second. The HED consists of cadmium telluride Schottky diodes with a self-triggered integrated readout electronics.

The performance of both detectors was first studied individually to become acquainted with their individual characteristics. The construction of the LED subsystem is especially worth mentioning because it is to a large fraction an in-house development of the IAAT (Institute for Astronomy and Astrophysics Tübingen). Besides the detector control electronics, the signal digitization, the signal preprocessing, and the data transfer were newly developed and tested during the construction of the LED setup. To a large fraction, this was done in the framework of this work.

The combined operation of the LED and the HED in the stacked configuration results in a minor mutual heating between both detectors, the appearance of fluorescence lines (emitted by the HED and detected by the LED), and the flux reduction of the HED for energies below $\sim$25 keV. A signal crosstalk between both systems was not observed.

The presented work shows that these negative mutual influences of both detector systems can not only be compensated with an appropriate data analysis but that also typical detector artifacts, e.g. escape peaks, can be suppressed. Furthermore,

the combined operation of the stacked system allows for additional quantities to be measured which is presented in the example of a Compton camera and a Compton polarimeter. In this context, the expected efficiency of the setup to operate as a Compton camera and its sensitivity as a Compton polarimeter are analyzed. This includes a statistical analysis which shows a novel way to construct point and interval estimations for the degree and the angle of polarization.

Zusammenfassung

Astronomische Beobachtungen im Röntgenbereich können nur außerhalb der absorbierenden Erdatmosphäre stattfinden und werden heutzutage nahezu ausschließlich mit Hilfe von Röntgensatelliten durchgeführt. Wesentliche Bestandteile eines Röntgensatelliten sind seine Optik, welche das Gesichtsfeld des Satelliten festlegt und seine Sensorik, welche die Röntgenstrahlung detektiert und in elektrische Signale umwandelt. Die Verwendung einer fokussierenden Optik, welche das Röntgenlicht bündelt und auf einen kleinen Sensor abbildet, ermöglicht eine hohe räumliche Auflösung und einen geringen Detektorhintergrund und somit eine verbesserte Sensitivität für die Detektion von schwachen Röntgenquellen.

Aufgrund der ständigen Weiterentwicklung von fokussierenden Röntgenoptiken, welche nun bis weit in den harten Röntgenbereich effizient arbeiten können, werden neue Detektorkonzepte möglich. Ein gestapeltes Detektorsystem, bestehend aus einem Niederenergiedetektor (LED) und einem sich dahinter befindenden Hochenergiedetektor (HED) ist solch ein neues Detektorkonzept, das in dieser Arbeit untersucht wurde. Der Hauptvorteil eines gestapelten Detektorsystems besteht darin, die durch die Optik fokussierte Strahlung in einem breiten Energiespektrum (ca. 0.1 keV bis 80 keV) effizient zu erfassen.

Das Hauptziel dieser Arbeit ist der Aufbau eines gestapelten Detektorsystems und dessen systematische Untersuchung mittels speziell dafür erstellter Analysesoftware. Dabei soll insbesondere die gegenseitige Wechselwirkung zwischen beiden Detektorsystemen experimentell analysiert werden. Der LED ist durch eine siliziumbasierte aktive Pixelmatrix realisiert, welche bis zu 410 mal pro Sekunde ausgelesen werden kann. Der HED besteht aus Cadmiumtellurid-Schottky-Dioden mit einer selbstauslösenden integrierten Ausleseelektronik.

Die beiden Detektoren wurden zuerst einzeln untersucht, um deren individuelle Charakteristika kennenzulernen. Dabei ist insbesondere der Aufbau des LED-Systems zu erwähnen, welches zum größten Teil eine Eigenentwicklung des IAAT (Institut für Astronomie und Astrophysik Tübingen) ist. Neben der Detektoransteuerungselektronik wurden die Signaldigitalisierung, die Signalvorverarbeitung und die Datenübertragung des LED-Systems neu entwickelt und getestet, was zum großen Teil im Rahmen dieser Arbeit geschah.

Der gemeinsame Betrieb von LED und HED in der gestapelten Konfiguration zeigt eine geringfügige gegenseitige Erwärmung beider Detektoren, das Auftreten von Fluoreszenzlinien (emittiert vom HED, detektiert vom LED) und eine Flussverringerung des HED unterhalb von $\sim$25 keV. Ein Signalübersprechen zwischen beiden Systemen konnte nicht beobachtet werden.

Die vorliegende Arbeit zeigt, dass durch eine entsprechende Datenanalyse diese negativen Beeinflussungen beider Detektorsysteme nicht nur kompensiert werden können, sondern dass auch typische Detektorartefakte wie z.B. „escape peaks“ unterdrückt werden können. Zudem ermöglicht der gemeinsame Betrieb des gestapelten Systems neue Analysemöglichkeiten, welche anhand einer Compton-Kamera und eines Compton-Polarimeters vorgestellt werden. Die erwartete Effizienz im Betrieb als Compton-Kamera und die Sensitivität im Betrieb als Compton-Polarimeter werden in diesem Zusammenhang analysiert. Dies beinhaltet eine statistische Analyse, welche neue Möglichkeiten aufzeigt Punkt- und Intervallabschätzungen für den Grad und die Richtung der Polarisation zu bestimmen.

Contents

Overview **13**

I. CANDELA: a setup to test a stacked detector system 15

1. Introduction to CANDELA **17**
1.1. Scientific motivation . . . 17
1.1.1. Active galactic nuclei . . . 21
1.1.2. NGC 4051 . . . 25
1.2. A brief introduction to semiconductor detectors . . . 28
1.2.1. Generation of signal charges . . . 28
1.2.2. Charge separation and transportation . . . 33
1.3. Signal generation . . . 34
1.3.1. Split events . . . 39
1.3.2. Pile-up . . . 41
1.3.3. Noise . . . 46
1.4. CANDELA setup . . . 49
1.4.1. The mechanical setup . . . 49
1.4.2. The electrical setup . . . 53
1.4.3. SpaceWire communication . . . 54

2. The LED: a Si DEPFET detector **55**
2.1. Properties of Si-based detectors . . . 56
2.2. The DEPFET pixel structure . . . 56
2.3. The DEPFET matrix . . . 59
2.3.1. SWITCHER chips . . . 60
2.3.2. CAMEX readout chip . . . 61
2.4. Analog-to-digital conversion . . . 63
2.5. D3C: a detector readout- and control electronics . . . 64
2.5.1. Sequencer SEQ . . . 65
2.5.2. Event preprocessor EPP . . . 66
2.5.3. Interface controller IFC . . . 69
2.6. LED operation . . . 71
2.7. Offline data analysis . . . 72
2.7.1. Analyzing dark-frame measurements . . . 72
2.7.2. Analyzing flat-field measurements . . . 75

2.7.3. Analyzing scientific observations . . . 77
2.8. Results . . . 81
2.8.1. Bad pixel analysis . . . 81
2.8.2. Split events . . . 82
2.8.3. Energy offset . . . 86
2.8.4. Spectral properties of the LED . . . 87
2.8.5. Comparison with a Geant4 simulation . . . 91
2.8.6. Temporal behavior of the LED . . . 93
2.8.7. Study of the charge cloud shape . . . 93
2.9. Summary . . . 95

3. The HED: a CdTe-detector 97
3.1. The CdTe band structure . . . 98
3.1.1. The HED, a CdTe-Al Schottky device . . . 98
3.2. The phenomenon of crystal polarization . . . 100
3.3. The polarization effect: a quantitative view . . . 102
3.4. Timing evolution of crystal polarization . . . 106
3.5. Hardware configuration of Caliste-64 . . . 108
3.5.1. Readout process . . . 108
3.5.2. HED cooling environment . . . 111
3.5.3. HED high voltage connection . . . 112
3.5.4. HED timing accuracy . . . 112
3.6. HED operation . . . 114
3.7. Offline data analysis . . . 115
3.7.1. Energy calibration . . . 116
3.8. Results . . . 121
3.8.1. Comparing different methods for the energy calibration . . . 122
3.8.2. Spectral properties of the HED pixels . . . 124
3.8.3. Temporal stability of the HED . . . 125
3.9. Summary . . . 128

4. LED and HED in a stacked setup 129
4.1. The stacked setup . . . 129
4.2. Mutual influence . . . 130
4.3. Data analysis . . . 132
4.3.1. The common coordinate system . . . 133
4.3.2. Timing . . . 134
4.4. New possibilities to analyze stacked detectors . . . 137
4.5. Summary . . . 139

II. X-ray polarimetry 141

5. Applications for CANDELA 143
5.1. Overview . . . 143
5.2. History of X-ray polarimetry . . . 144
5.3. Scientific motivation . . . 144
5.4. The generation of polarized radiation . . . 146
5.5. The interactions of photons with matter . . . 147
5.5.1. Photoelectric effect . . . 148
5.5.2. Compton Scattering . . . 150
5.5.3. Pair production . . . 153
5.6. The sensitivity of CANDELA for Compton forward scattering . . . 155
5.7. CANDELA as a Compton camera . . . 159
5.8. CANDELA as a polarimeter . . . 160
5.8.1. The modulation factor . . . 161
5.8.2. Optimizing the sensitivity of the polarimeter . . . 162
5.9. Summary . . . 164

6. Statistics in polarimetric measurements 165
6.1. Basic parameters and terminology . . . 165
6.1.1. The $\frac{\Delta C(\phi)}{\Delta \phi}$-distribution . . . 166
6.1.2. The Stokes parameters . . . 167
6.1.3. The bivariate probability density function $\rho_{\mathrm{p},\,\Psi}$ . . . 168
6.2. Frequentist analysis . . . 171
6.2.1. The univariate probability distribution ρ_p . . . 171
6.2.2. Point estimations of the degree of polarization p . . . 173
6.2.3. Interval estimations on p_0 . . . 175
6.2.4. The univariate probability distribution ρ_Ψ . . . 179
6.2.5. Point estimations on Ψ_0 . . . 179
6.2.6. Interval estimations on Ψ . . . 180
6.3. Bayesian analysis . . . 180
6.3.1. The univariate probability distribution ρ_{p_0} . . . 181
6.3.2. Point estimations on p_0 . . . 183
6.3.3. Interval estimations on p_0 . . . 184
6.3.4. Point estimations on Ψ_0 . . . 185
6.3.5. Interval estimations on Ψ_0 . . . 185
6.4. Monte Carlo simulation . . . 187
6.4.1. Simulating credibility intervals $\Delta p_0(p)$ . . . 187
6.4.2. Simulating credibility intervals $\Delta \Psi_0(p)$ . . . 188
6.5. Analysis in the limit of high polarizations . . . 189
6.6. Binning the ϕ-distribution . . . 190
6.6.1. Data binning . . . 190
6.6.2. Monte Carlo Simulation . . . 191
6.7. Summary . . . 199

7. Summary and outlook **201**

A. Klein-Nishina formula in polar coordinates **207**

B. LED start routine **209**

C. Least square fits **211**
C.1. Estimated polarization $\hat{p}_0(p)$ . . . 211
C.2. Regions of best estimator performance as fct. of p_0 . . . 211
C.3. Optimal $\lambda(p_0)$ . . . 211
C.4. Confidence intervals $\Delta p_0(p)$ . . . 212
C.5. Optimal $\lambda(p)$ . . . 212
C.6. Credibility intervals $\Delta p_0(p)$ . . . 213
C.7. Confidence intervals $\Delta\Psi_0(p_0)$ . . . 213
C.8. Regions of best estimator performance as fct. of p . . . 214
C.9. Credibility intervals $\Delta\Psi_0(p)$ . . . 214

D. Calculations **215**
D.1. Correcting the binning reduced amplitude . . . 215
D.2. Trammell-Walter equation 1 . . . 216
D.3. Trammell-Walter equation 2 . . . 216
D.4. The input-output ratio λ for TRM . . . 217
D.5. Estimating the maximal split ratio for quadruple events . . . 218
D.6. Time variability . . . 219

"The magic is always in the detail."

(Theodor Fontane)

Overview

The thesis in hand summarizes parts of my work during the last five years at the *Institut für Astronomie und Astrophysik Tübingen* (IAAT). The presented work is in heritage of my diploma thesis [Maier, 2009] that initiated the construction of a stacked detector setup.

In the beginning, the setup was destined for a science verification model for the planned X-ray satellite mission *Simbol-X* [Ferrando et al., 2008]. After the cancellation of *Simbol-X* in 2009, the setup developed to a more general laboratory to test detector physics in a wide range. This includes the building and testing of control and readout electronics, detector calibration, data preprocessing, and data analysis.

The presented thesis is divided into two parts. The **first part** is directed to the operation of the stacked detector setup and contains all the experimental work, but also some elaborate theoretical considerations on detector physics, signal formation, and on the polarization phenomenon of cadmium telluride crystals.

Chapter 1 motivates the scientific use of a stacked detector setup, gives an overview of the basic detector physics, and describes the layout of the CANDELA setup.

Chapter 2 and 3 give a description of the low energy detector (LED) and of the high energy detector (HED). The operation mechanisms of both detectors and the detector performances are studied for the LED and the HED independently. In these two chapters, the description of the setup and of the used tools contains already many results. To put results into the descriptive sections is chosen purposely and describes the applied way of working which is based on a step-by-step development of new tools and ideas and the study of their implications. The correct way of detector operation and of data analysis developed during the work with the setup and a lot of insights came up by doing things wrong.

In **Chapter 4**, both detector subunits are combined into a stacked detector setup and the resulting mutual influences between both detectors are described; new ways of analyzing this stacked detector configuration are introduced and build the transition to the second part of this thesis.

In the **second part**, two possible applications of a stacked detector setup—a Compton camera and a Compton X-ray polarimeter—are investigated theoretically.

Chapter 5 introduces the basic properties of the photoelectric effect and of Compton scattering. The expected efficiency of the CANDELA setup to detect Compton scattered events is calculated as a function of the incident photon energy. Possible changes of the geometrical configuration of the setup are considered and their resulting effects on the detection efficiency and the sensitivity for polarimetric observations are investigated.

The polarization of radiation is not directly measured by the polarimeter. Instead, a sophisticated analysis is needed to work the polarimetric information out of the data. **Chapter 6** describes the theoretical basis of this analysis with its underlying statistics that governs polarimetric measurements. Besides the classical frequentist approach, point and interval estimations on the degree and the angle of polarization are presented with a Bayesian analysis.

In **Chapter 7**, both parts of the thesis are summarized. An outlook on what kind of investigations are possible with the CANDELA setup in the near future completes this work.

The intent of this thesis is that it shall not only be descriptive but also explanatory. In order to enable also a quick access to the work, the most important results are presented at the end of each chapter (with exception of Chapter 1) in a summary. Fundamental derivations are presented in the appendix.

This work summarizes and extends what is presented in the publications Schanz et al. [2009], Maier et al. [2010, 2012, 2014,a], Maier et al. [2014,b].

Part I.

CANDELA: a setup to test a stacked detector system

1. Introduction to CANDELA

The stacked detector setup CANDELA (**ca**dmium telluride and silico**n** **de**tector **la**boratory) is a heritage of the mission study *Simbol-X* [Ferrando et al., 2008]. The basic idea is to build a focusing X-ray telescope that is sensitive in soft X-rays ($100\,\mathrm{eV} < E < 15\,\mathrm{keV}$) as well as in hard X-rays ($15\,\mathrm{keV} < E < 100\,\mathrm{keV}$).* Instead of building two separate telescopes, one for each energy range, one telescope with a broad band detector system can achieve equal scientific performances and use the available resources in a more efficient way.

To build a broad band detector, a silicon-based low energy detector (LED) is placed in front of a cadmium telluride based high energy detector (HED). The stacked detector system combines the excellent spectro-imaging performance of the LED ($\Delta E = 168\,\mathrm{eV}$ FWHM @ 6 keV, 500 µm x 500 µm pixel) at soft X-rays with the very good spectro-imaging performance of the HED ($\Delta E = 1050\,\mathrm{eV}$ FWHM @ 60 keV, 1 mm x 1 mm pixel) at hard X-rays. In this stacked configuration, the LED detects mainly soft X-rays and becomes transparent for higher photon energies. These hard X-rays can then (after transiting the LED) be detected by the HED. The used definition of soft and hard X-rays matches to this behavior, as the probability for a 15 keV photon to be detected in the LED is about the same as to be detected in the HED. See also Fig. 4.1 to get an impression on how a 15 keV photon "sees" the combination of LED and HED.

Possible astronomical sources and scientific questions that are addressed by such a detector system are presented in Section 1.1. An overview of semiconductor detector physics concerning the LED and the HED is following in Section 1.2, while the CANDELA setup is described in Section 1.4. Each detector subsystem is studied in detail in the Chapters 2 and 3.

1.1. Scientific motivation

Observational strategies in X-ray astronomy are typically divided into two energy ranges. For photon energies $E < 15\,\mathrm{keV}$, focusing optics in combination with small detectors yield good results in terms of spatial resolution and sensitivity. The term *sensitivity* expresses the capability of an instrument to detect faint signals in a given exposure time. Beside the signal, the instrument also detects background radiation. To detect the signal within this background it is favorable to have a large signal collecting area A_{eff} and a small, also background observing, detector (with an area A_{det}).

* The energy ranges of *soft* and *hard* X-rays are not consistently defined in literature. The definition above is used in the following chapters, if not mentioned explicitly in another way.

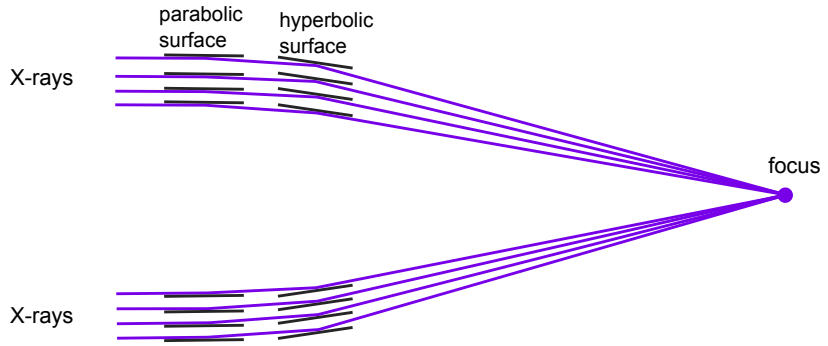

Figure 1.1. Wolter 1 telescope: the combination of a parabolic and a hyperbolic mirror allows to focus X-rays under grazing incidence.

The X-ray satellite XMM-Newton with an effective area of $A_{\mathrm{eff}} \approx 1000\,\mathrm{cm}^2$ and a detector area of $A_{\mathrm{det}} = 36\,\mathrm{cm}^2$ (pn-camera) gains this way a sensitivity of $A_{\mathrm{eff}}/A_{\mathrm{det}} \approx 28$.

Focusing optics use the fact that X-rays (with energy E) are reflected from a surface (with density ρ) if their incidence angle is smaller than a critical angle [Als-Nielsen and McMorrow, 2011, Eq. (3.2)]

$$\alpha_{\mathrm{c}} \sim \sqrt{\rho}/E. \tag{1.1}$$

This concept of external reflection under grazing incidence is implemented in the Wolter-1 geometry, a combination of paraboloid and hyperboloid mirror shells [Wolter, 1952], see Fig. 1.1. The effective area A_{eff} of such a geometry can be expressed as a function of the focal length f and the critical angle α_{c} [de Korte, 1988]

$$A_{\mathrm{eff}} \sim f^2\,\alpha_{\mathrm{c}}^2. \tag{1.2}$$

It is difficult to focus hard X-rays as the effective area A_{eff} of the telescope decreases with increasing energy. A long focal length or an increase in the density of the mirror material can result in large effective areas even at high energies, but both parameters are limited. The focal length is limited by the dimension of the spacecraft, which has to fit into the launching vehicle and the density of the mirror material cannot be increased much further, as the existing mirrors already use heavy elements like gold or iridium. Hard X-ray telescopes are therefore using collimators or coded masks and detectors with roughly the same area as the aperture. As $A_{\mathrm{eff}} \approx A_{\mathrm{det}}$, the sensitivity of such instruments is worse compared to focused instruments.

New telescope concepts try to focus hard X-rays by enlarging the focal length with extendable optical benches (see for example HEXIT-SAT [Fiore et al., 2004] or NuSTAR [Harrison and the NuSTAR collaboration, 2013]) or with formation flying configurations (like Simbol-X [Ferrando et al., 2008]). Additionally, Bragg reflection on multilayer coated mirrors increase the critical angle α_{c} over a broad energy range [Mao et al., 1997, Pareschi et al., 2009]. This results in the development of focusing optics for X-rays with energies up to 100 keV.

As the spectral range of the optics exceeds the spectral range in that one semiconductor detector is operating optimally, a stack of multiple, in our case two, different detectors yields a sensitive, broad band spectro-imager and allows an unprecedented investigation of the universe in soft and hard X-rays with respect to spatial resolution and sensitivity.

The study of active galactic nuclei (AGN) and the cosmic X-ray background radiation (CXB) will benefit of such sensitive broad band X-ray detections and the combined simultaneous measurements of two detectors. AGN, the CXB, and the related science that can be addressed with a stacked detector system are presented in detail in the next section. The following, by no means exhaustive, examples give an overview of the range of scientific applications:

- The study of **active galactic nuclei**, their accretion and feedback mechanism as well as their contribution to the cosmic matter cycle (see Sect. 1.1.1).

- The study of the **cosmic X-ray background radiation** and analysis of the history of galaxy evolution (see Sect. 1.1.2).

- Observations of the **accretion process** in galactic black hole binaries (GBHBs) and measurements of the **relativistic broadened iron $\mathbf{K_\alpha}$ line**. The variability time scale Δt of accreting GBHBs and AGN scales with the mass of the black hole m_{BH} and is in the order of msec for galactic black holes and tens of ksec for AGN [Wilms, 2008b]. While AGN observations allow to study the accretion process in a frozen snapshot, observations on GBHBs allow to study the evolution of the accretion flow.

  Broad band X-ray spectra are produced by both sources and consist of:

  - a soft thermal emission from the disc,
  - a hard Comptonization spectrum generated by soft disc photons scattered on hot electrons in the corona around the black hole,
  - a "Compton reflection hump" generated by hard X-rays which are reprocessed in the disc,
  - and fluorescence line emission produced by the illuminated disc.

  A broad band detection is required to disentangle these spectral components and to observe their interactions and dependencies.

  Besides a good energy resolution for the detection of the iron line, a broad band observation is necessary to determine the continuum spectrum which superimposes the iron line. Measuring this continuum emission up to hard X-rays will help to determine the continuum around the Fe-K_α line more precisely than using only soft X-rays. This will improve investigations on the relativistic broadened iron line as such studies are based on continuum subtracted iron lines [Wilms, 2008a]. See Laor [1991] for calculations on the shape of relativistic iron lines around rotating black holes.

- Investigation of **particle acceleration** in pulsar wind nebulae (PWN) by observation of their synchrotron emission up to 80 keV. Gaensler and Slane [2006] review PWN; Nynka et al. [2014] present NuSTAR observations of G21.5-09 ranging from 3-45 keV.

- Study of **particle acceleration** in young supernova remnant shock waves. In these shocks, thermal emission at energies $E < 10$ keV is accompanied with hard X-rays ranging up to 30 keV. The origin of this hard emission is not clarified up to now and can be investigated best by simultaneous observations of the soft- and the hard X-rays. See Yamazaki et al. [2014] for more information.

- Clarification of the nature of the **non-thermal emission of galaxy clusters** and study of the evolution of galaxy clusters. Galaxy clusters are the largest gravitationally bound objects in the universe, with a total mass of about 10^{15} solar masses and a volume of about 100 Mpc^3. They consist mainly of dark matter ($\sim 80\,\%$), luminous matter in the galaxies (3-5 %), and a diffuse, hot gas (15-17 %) [Feretti et al., 2012].

  The hot gas (10^7 K) results in thermal Bremsstrahlung detected in **soft X-rays**. Additionally, two non-thermal radiation components resulting from relativistic electrons are reported:

  - **diffuse radio emission** (reported in about 80 clusters [Feretti et al., 2012]): radio observations indicate through the analysis of synchrotron radiation that galaxy clusters are permeated by large-scale magnetic fields ($0.1 - 1\,\mu$G) and relativistic electrons with energies between 1 GeV and 100 GeV.
  - **hard X-rays** (confirmed in the Ophiuchus cluster [Murgia et al., 2010], controversially debated for several other clusters): a hard X-ray emission is assumed to be generated due to inverse Compton scattering of cosmic microwave background photons with the relativistic electrons that produce also the diffuse radio emission [Sarazin, 1999].

  A sensitive detection at hard X-ray energies can help to clarify the origin of the non-thermal emissions of galaxy clusters. The intensity of the synchrotron radiation depends on the magnetic field strength *and* on the density of the relativistic electrons; an analysis of the diffuse radio emission cannot disentangle both properties. Combining the analysis of inverse Compton scattering and synchrotron emission allows to conclude on the magnetic field strength and on the density of the relativistic electrons.

  Galaxy clusters are formed via collisions of small units (galaxies, small cluster of galaxies). The collisions build larger structures and generate shocks driving into the intracluster medium. It is believed that the relativistic electrons are accelerated during this process and are therefore direct relict of cluster formation and evolution. See Feretti et al. [2012] for a detailed review.

1.1.1. Active galactic nuclei

Active galactic nuclei (AGN) are point-like, luminous, broad band sources associated with galaxies. It is believed that supermassive black holes (SMBHs) with a mass between a million and ten billion solar masses constitute the center of the galaxies. AGN accrete matter from a surrounding accretion disc which results in very luminous broad band radiation*. Antonucci [1993] and Urry and Padovani [1995] suggested a unified model of AGN. According to this model, various astronomical sources like radio galaxies, Seyfert I and II galaxies, BL-Lac objects, quasars and blazars, are all AGN observed under different inclination angles. See Fig. 1.2 for an X-ray image of Centaurus A, the closest ($d \approx 3.4\,\mathrm{Mpc}$) AGN to our galaxy.

Figure 1.2. Centaurus A, observed by Chandra in 199 hours. Color code in keV: red (0.5-1.0); green (1.0-1.5); blue (1.5-2.0). Credit: NASA/CXC/CfA/R. Kraft et al.

Besides the SMBH and the accretion disc, a hot corona, close to the innermost stable circular orbit, a relativistic jet, perpendicular to the disc, and a thick dust torus around the disc play an essential role in emission and absorption of X-ray radiation. Furthermore, a narrow line region (NLR) and a broad line region (BLR) can be observed in the optical. The NLR emits narrow lines from slow rotating clouds which are located distant to the SMBH, while the BLR emits broad lines from fast rotating clouds close to the SMBH. Figure 1.3 shows a simplified model of an AGN.

Close to the SMBH, the accreting material in the disc is heated up to several 100 eV and emits thermal radiation as soft X-rays. The heating mechanism of the corona is not fully understood presently, even though magneto-hydrodynamical heating seems to be a prominent candidate [Jiang et al., 2014]. Low energetic disc photons can be scattered in the corona to energies of about 200 keV, or even beyond [Bisnovatyi-Kogan and Blinnikov, 1976], by inverse Compton effect. These high energetic X-rays can interact again with the disc or the torus and produce material specific fluorescence lines like the prominent Fe-K_α line.

* Normal galaxies are radiating dominantly in the optical, and additionally in the mid-infrared if the radiation is reprocessed in dusty environments, with a typical luminosity of $L_* \approx 10^{44}\,\mathrm{erg/s}$. AGN spectra have, on average, no dominating energy band but a relatively constant energetic flux from mid-infrared to X-rays. Their luminosity range is $(10^{42} \lesssim L_{\mathrm{AGN}} \lesssim 10^{48})\,\mathrm{erg/s}$. The X-ray luminosity of AGN is about a factor $10^3 - 10^4$ higher than in inactive galaxies [Krolik, 1999, § 1].

Seyfert II galaxies and the CXB

The optical spectra of Seyfert I galaxies show narrow and broad lines while Seyfert II galaxies only show narrow lines. This is explainable with a distant dust torus that can obscure the inner part (disc, SMBH, BLR) of an AGN if the galaxy is observed edge-on or nearly edge-on (Seyfert II). Observing the AGN more face-on exposes the BLR (and the NLR) so that the AGN is classified as Seyfert I. It is important to note that the term *obscured* refers to optical observations. An X-ray obscured source is called *Compton thick*. With this terminology obscured sources (in the optical) can be Compton thin (transparent in X-rays) or Compton thick (also opaque in X-rays).

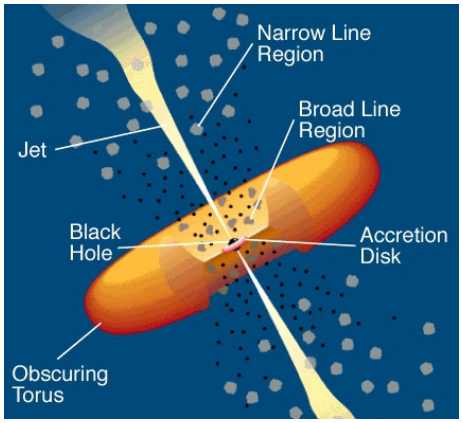

Figure 1.3. Urry and Padovani model for radio-loud AGN. Credit: Urry and Padovani [1995].

The hydrogen column density* N_{H} is used to quantify the X-ray opacity. An AGN is called Compton thick† if $N_{\mathrm{H}} > 1.5 \cdot 10^{24}\,\mathrm{cm}^{-2}$. It is expected that at least half of the Seyfert II galaxies in the local universe are Compton thick with $N_{\mathrm{H}} > 10^{25}\,\mathrm{cm}^{-2}$ [Maiolino et al., 1998, Risaliti et al., 1999]. Matt [2000] estimates that obscured, (mildly) Compton thick ($N_{\mathrm{H}} > 10^{23}\,\mathrm{cm}^{-2}$) AGN outnumber unobscured AGN by a factor of 10-20 in the local universe, and even more at larger distances.

As photoelectric absorption increases with decreasing photon energy, the low energetic part of the spectrum (optical, UV, and soft X-rays) is cut-off for Compton thick AGN so that a large fraction of all AGN cannot be observed in soft X-rays ($E < 10\,\mathrm{keV}$). Above 10 keV the nuclear emission is directly visible for mildly Compton thick ($N_{\mathrm{H}} < 10^{25}\,\mathrm{cm}^{-2}$) AGN [Comastri, 2004]. If the column density is even higher, the core emission is reprocessed in the torus to infrared radiation by Compton down scattering and photoelectric absorption and is no longer directly visible. For the same reasons, the column density is also no longer directly measurable. Instead, a source can be classified as Compton thick indirectly by the presence of a fluorescence iron line at 6.4-7 keV [Matt et al., 1996] and a flat Compton reflection component that peaks around 20-30 keV [George and Fabian, 1991].

---

* The hydrogen column density describes an absorbing column between the source and the observer expressed in hydrogen equivalent numbers. It is equal to the number density of hydrogen atoms integrated along the line of sight.

† If radiation with the intensity I_0 enters a medium, the radiation intensity $I(x)$ in a depth x decreases in an exponential way according to Beer's law: $I(x) = I_0 \cdot \exp(-x/\lambda)$, with the mean free path λ. This equation can be rewritten with the absorption cross section σ and the column density $N(x)$ as $I(x) = I_0 \cdot \exp(-\sigma\, N(x))$. Assuming hydrogen as absorber and Thomson scattering as interaction ($\sigma = \sigma_{\mathrm{Th}}$), results in the definition of *Compton thickness*: $N_{\mathrm{H}} = \sigma_{\mathrm{Th}}^{-1} = 1.5 \cdot 10^{24}\,\mathrm{cm}^{-2}$. This definition does not directly hold for photon absorption via photoelectric or Compton effect, but, assuming cosmic abundances, the relevant cross-sections are in the same order of magnitude at $E \approx 10\,\mathrm{keV}$. Following this definition, the probability that a photon can transit a Compton thick medium is less than $\mathrm{e}^{-1} \approx 37\,\%$ at photon energies around 10 keV.

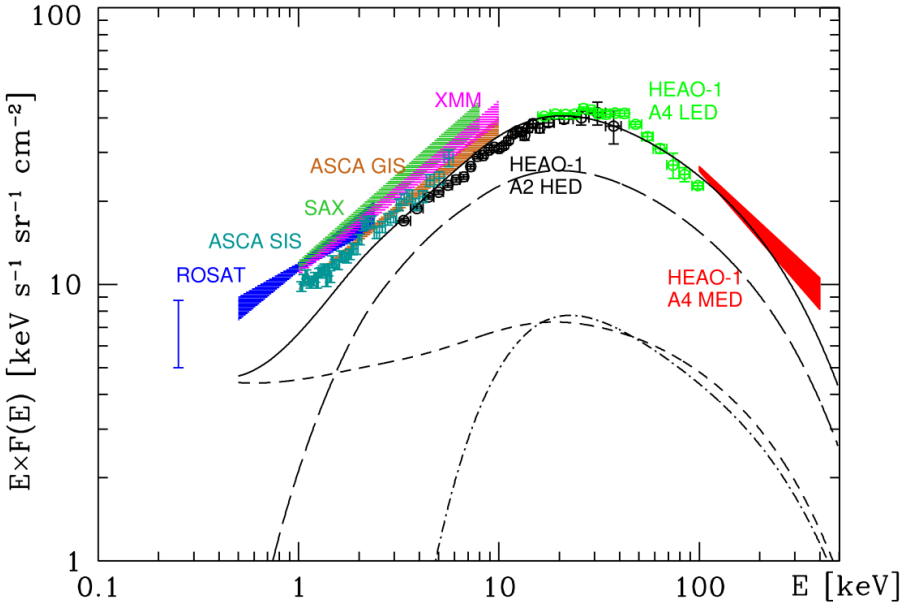

Figure 1.4. Spectral radiance multiplied with energy for the cosmic X-ray background radiation measured with different instruments (points and shaded areas as labeled). The synthesis model is the following: Compton thin AGN (long-dashed line), Compton thick AGN (dot-dashed line), unobscured AGN (dashed line), and the superposition of all (solid line). Credit: Comastri [2004].

Today it is believed, that the cosmic X-ray background radiation* can be explained with the integrated contribution of unresolved AGN over cosmic time scales [Gilli et al., 2007]. Figure 1.4 shows the energy multiplied spectral radiance for the cosmic X-ray background radiation measured with different instruments. A strong contribution of Compton thin AGN is needed to fit the measurements in the soft X-ray region ($E < 10\,\mathrm{keV}$). To explain the spectral peak around 30 keV, Setti and Woltjer [1989] suggested to include strongly absorbed, Compton thick sources. The mixing between Compton thin and Compton thick AGN is still a question of debate as their spectral shapes are similar.

The spectral distribution of the CXB could in principle also be matched with a pure Compton thin contribution, see Comastri [2004, Fig. 8.3]. On the other hand, Fabian et al. [1990] had the idea to fit the CXB with a dominant Compton thick contribution. Even though some discrepancies between AGN models and observations persist, it seems that "the contribution of Compton thick AGN cannot be neglected in building up a synthesis model† for the CXB" [Comastri, 2004].

Studying the true nature of the CXB is important as it helps to understand the accretion of matter onto SMBHs which gives a direct link to the evolution of black holes during cosmic history. The mass of a SMBH is proportional to the mass and

* Giacconi et al. [1962] discovered the CXB in 1962 as "diffuse background radiation".
† The CXB synthesis model describes how the AGN luminosity and obscuration evolve with redshift.

the bulge luminosity [Kormendy and Richstone, 1995], and to the velocity dispersion* [Gebhardt et al., 2000, Ferrarese and Merritt, 2000] of its host galaxy. This indicates a strong correlation between the evolution of the SMBH and the evolution of the host galaxy. Hence, the CXB contains the history of all active galaxies over cosmic time scales. Furthermore, the reprocessing (Compton down scattering and photoelectric absorption) of hard X-rays in the dust torus results in strong emission of infrared light and it is assumed that Compton thick sources that contribute to the CXB account for a substantial part of the cosmic infrared background radiation (CIB) [Comastri, 2004], see Fig. 1.5. Therefore, a deeper understanding of the CXB and especially its Compton thick sources will enhance our understanding of the CIB as well.

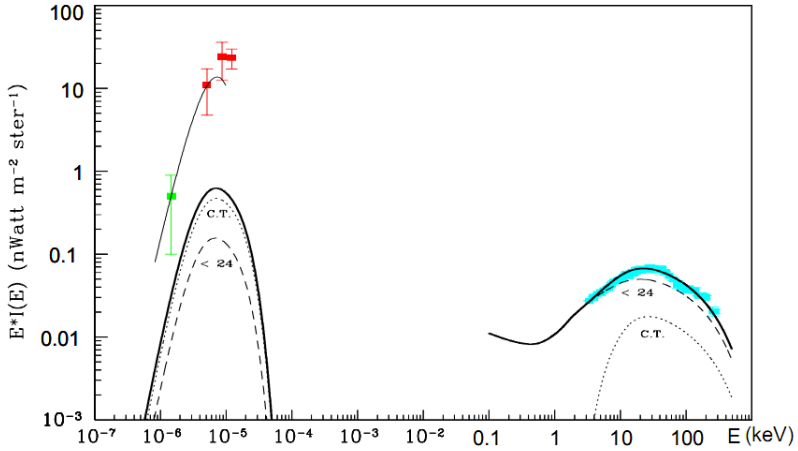

Figure 1.5. Spectral radiance multiplied with energy for the CIB (green and red data points) and the CXB (blue data points). The predicted AGN contribution is printed with a solid thick line which is divided in Compton thin (dashed line) and Compton thick (C.T. dotted line). The best fit to the CIB is printed as solid thin line. Compton thick AGN are the dominant AGN contribution to the CIB. Credit: Comastri [2004].

In conclusion, the CXB can be studied by observing its up to now unresolved sources. A deep census of AGN will help to build more accurate CXB synthesis models and allows a better understanding of the history of galaxy evolution. The identification of obscured, partially Compton thick AGN is based on the observation of a fluorescence iron K_α line at 6.4 keV and a Compton reflective hump around 30 keV. Because of this, a detector that operates in both energy ranges is an ideal instrument to resolve the cosmic X-ray background.

The high variability of AGN, which is especially pronounced in X-rays†, enforces a simultaneous detection of soft and hard X-rays which is most easily done with a single telescope. NGC 4051 as an extreme example of an X-ray variable AGN and the analytical capabilities of X-ray reverberation studies are introduced in the next section.

* The velocity dispersion σ describes the spread of velocities of stars about their mean velocity.

† "Significant changes (of the X-ray luminosity) in a few hours are not at all uncommon" [Krolik, 1999, § 8.1.4]

1.1.2. NGC 4051

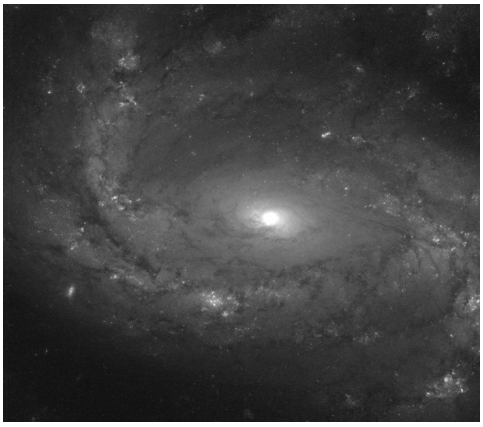

Figure 1.6. NGC 4051, observed with the Hubble space telescope (HST). Based on observations made with the NASA/ESA HST, and obtained from the Hubble Legacy Archive.

The AGN unification model explains the classification of different objects as a mainly inclination angle dependent effect. This reveals an important meaning for the geometrical structure of AGN. Unfortunately, AGN cannot be resolved directly by imaging as their large distances let them (almost) all appear point like. The nearest radio galaxy Centaurus A has a distance of 3.4 Mpc, which is equivalent to 16 pc/1".* The very long base line radio interferometer (VLBI), a world wide combination of radio observatories with the highest possible angular resolution achievable today, has a theoretical angular resolution of 0.00015" and could, at that distance, resolve structures with a size of about 2.4 mpc or 2.8 ld†. The radius of the accretion disc (seen at a wavelength of $\lambda = 250$ nm) can be approximated according to Morgan et al. [2010] to 1.2 ld, assuming $M_{\mathrm{SMBH}} = 2 \cdot 10^8\,\mathrm{M}_\odot$. This rough estimation shows that today, even the closest AGN cannot be resolved up to its innermost core‡, even with the best instruments.§

Instead, the geometrical structure of an AGN is usually inferred via spectroscopy. It is useful to distinguish between primary and secondary radiation. In AGN, primary radiation is produced, for example, in the accretion disc or in the disc corona. The structure of primary radiators can be modeled assuming different radiation processes, like thermal radiation, Bremsstrahlung, or synchrotron radiation. Comparing the observed spectrum with the modeled spectrum determines the quality of the model. Reprocessing primary radiation via scattering, absorption, fluorescence emission or comptonization yields secondary radiation. The structure of secondary radiators, like the dust torus, can be modeled by assuming a geometrical structure and predicting the energy spectrum depending on the primary radiation.

Primary radiation can be influenced by secondary radiators, for example due to absorption, but there is at least the chance to observe primary radiators directly. The uncertainty of the geometrical structure and of the spectral properties of primary radiators propagates into an even higher uncertainty for the models of secondary radiators. NGC 4051 is an exceptional example of an AGN that has revealed its structure in a more direct way than due to spectrum modeling. Moreover, it illustrates

* This means that a structure of 16 pc scale is observed at an angle of 1".

† One light-day is a 365th of a light-year: 1 ld = 1/365 ly.

‡ There are a few examples of spatially resolved, multiple parsec scale, structures, like the NLR [Evans et al., 1991] or the dusty torus [Jaffe et al., 2004].

§ *RadioAstron*—a ground-space VLBI with a maximal baseline of 350 000 km and a theoretical resolution of $\sim 10^{-5}$" at 20 GHz—can resolve structures with a size of ∼0.2 mpc for Centaurus A.

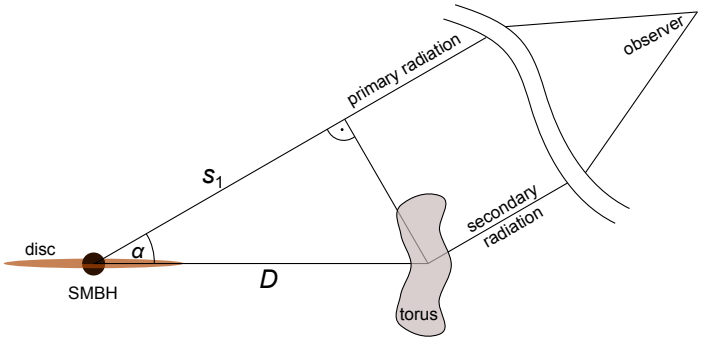

$$\Delta s = D - s_1 \tag{1.3}$$
$$= D\,(1 - \cos(\alpha)) \tag{1.4}$$
$$\Delta t = \Delta s/\mathrm{c} \tag{1.5}$$
$$= \frac{D}{c}\,(1 - \cos(\alpha)) \tag{1.6}$$

Figure 1.7. Scheme for the time delay between primary and secondary radiation.

the benefit of *simultaneous* measurements of the soft and hard X-ray spectrum.

The following discussion refers to an observation of the Seyfert I galaxy NGC 4051 (see Fig. 1.6 for an optical image of it) with the X-ray satellite *BeppoSAX* on 9-11 May, 1998 [Guainazzi et al., 1998]. During the three days, the source was in a constant ultra-dim X-ray state (the 2-10 keV flux was $1.26 \cdot 10^{-12}$erg cm^{-2} s^{-1}, which is about 20-times less than its historical average flux) which was associated with a shutdown of the primary nuclear source. Such a switch-off can be explained with a reduction of the accretion rate or with a "transition of the disc from a radiatively efficient Shakura-Sunayev disc to an inefficient advection-dominated flow", [Guainazzi et al., 1998].

The secondary radiation (radiation from the nucleus that is reprocessed in the dust torus) has a longer path length as the directly observed primary radiation, see Fig. 1.7. A rough estimation shows that the time delay Δt between both kinds of radiation depends on the inclination angle α at which the disc is observed and can be expressed with Eq. (1.6). A typical distance between the SMBH and the torus is at least on parsec scale [Antonucci, 1993], so that the time delay Δt between the flux reduction of the primary and the secondary radiation is expected to be in the order of weeks to years. Guainazzi et al. [1998] analyzed NGC 4050 with switched off primary radiation but still active secondary radiation; they showed that:

- The observed spectrum is best fitted with a Gaussian accounting for the iron fluorescence and a Compton reflection continuum model, see Fig. 1.8.
- "The spectral index of the illuminating (but now invisible) power-law (for the Compton reflection continuum model), $\Gamma = 1.92$, is perfectly consistent with the typically observed value for NGC 4051". So, the echo observed in the off-state is produced by the primary radiation in the on-state.
- "A column density of at least $1.4 \cdot 10^{26}\,\mathrm{cm}^{-2}$ is needed, if the fading is due to absorption rather than a switch-off of the primary source". Such a high column density is hard to explain and controversial.

All these arguments are indicative that Guainazzi et al. [1998] may have found in NGC 4051 the "first direct evidence for the presence of large amount of circumnuclear

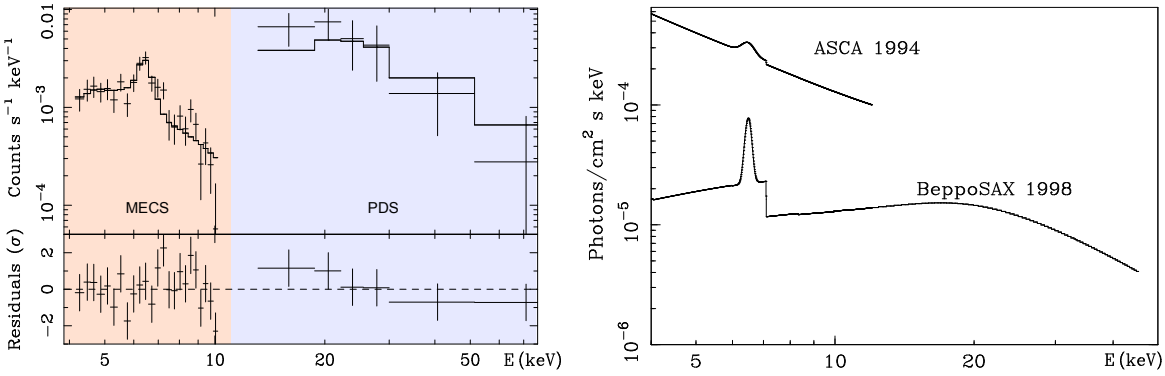

Figure 1.8. X-ray spectrum of NGC 4051. Credit: [Guainazzi et al., 1998].
Left: the observed spectrum (crosses) is compared to the used model (a Gaussian with a Compton reflection continuum; solid line) by their residuals (bottom). The different counting rates shown in red and blue, arise from the different effective areas of the *medium-energy concentrator spectrometer* (MECS) and the *phoswitch detector system* (PDS) of BeppoSAX. Be aware of the units of the ordinate.
Right: best fit model for the 1994 ASCA [Guainazzi et al., 1996] and 1998 BeppoSAX observation [Guainazzi et al., 1998]. The BeppoSAX observation shows the absence of the primary power law component.

cold, thick matter" in a Seyfert I galaxy. As the time delay between the termination of the primary and the secondary radiation was not observed, the distance of the torus could not be estimated in this case. But it shall be mentioned explicitly that such an analysis for variable X-ray sources would be feasible with a sensitive, broad band X-ray detector, even for cases in which the primary radiation is not completely switched off.

With a reverberation analysis, the structure of a component, echoing a primary radiation, can be studied in a new way. It is similar to walking around and observing an object under different lines of sight. If the primary radiation is not completely switched off but only gets dimmer, the analysis becomes more difficult as the primary radiation can be still more prominent as the reprocessed one. Furthermore, the spectral composition of the primary radiation is likely to change during the transition from an "on" to a "dim" state. For a proper data deconvolution, it is therefore necessary to observe both kinds of radiation in their full energy range. The power of an X-ray reverberation analysis and the requirements to the detector system is nicely summarized by Bianchi et al. [2012]:

> "In principle, the geometry and distance of the torus could be estimated by doing accurate X-ray reverberation analysis of the iron line and the Compton reflection component, in order to take into account in detail how the material reacts to the intrinsic variability of the central source. Unfortunately, such a study is extremely difficult and uncertain with current X-ray missions."

1.2. A brief introduction to semiconductor detectors

Before discussing the details of the low and the high energy detector, the basic concept of semiconductor detectors and the requirements needed for operation shall be presented briefly. A detailed overview on semiconductor physics can be found in Sze [1981] while the application of semiconductors for radiation detection is discussed in Lutz [1999], Knoll [2000], Spieler [2005], and Lowe and Sareen [2013].

1.2.1. Generation of signal charges

The detection principle of semiconductor detectors is based on the photoelectric absorption of radiation*. The semiconductor crystal works as a transducer that converts the incoming radiation to electron-hole pairs. This transformation is done in multiple steps:

1. **Photoelectric absorption:** conservation of momentum requires a momentum transfer from the photon to the atomic nucleus. Therefore, a photoelectric interaction with a tightly bound, innermost electron (K-shell) is most probable. The kinetic energy of the photoelectron E_e can be calculated knowing the energy of the absorbed photon E_γ and the binding energy of the photoelectron E_b (see Fig. 1.9) via

$$E_\mathrm{e} = E_\gamma - E_\mathrm{b}. \tag{1.7}$$

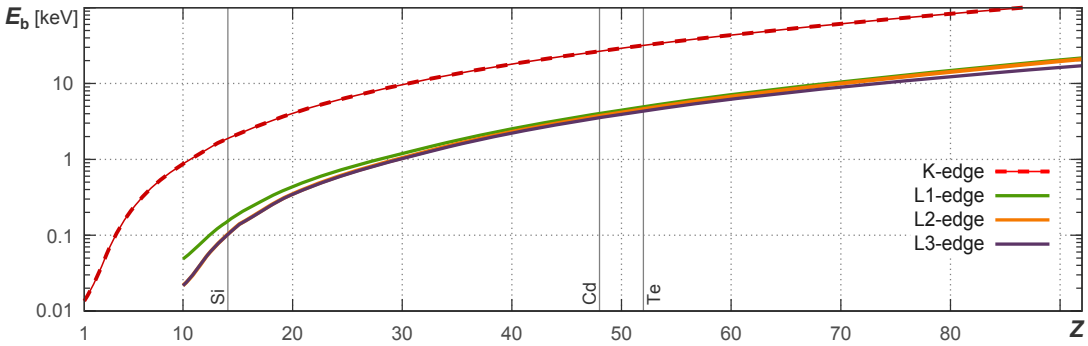

Figure 1.9. Binding energy E_b as function of the atomic number Z [Thompson, 2009].

2. The **photoelectron** travels a short distance (the mean free path for inelastic scattering for a 1 keV electron in e.g. silicon is 2.8 nm [Powell and Jablonski, 1999, Tab. 4]) and starts to create electron-hole pairs due to inelastic scattering. The electron is scattered approximately each mean free path along its track. This secondary ionization can be modeled with a modified† version of the Bethe-Bloch formula. An analytic formula for the electron range r_max is given by Tabata et al. [1996], see Fig. 1.10. For a 1 keV electron $r_\mathrm{max} = 11.8$ nm in silicon.

* In the following, the term *radiation* is used for electromagnetic radiation in the X-ray energy range.
† This modification takes the low mass of the electron and the indistinguishability of two interacting electrons into account.

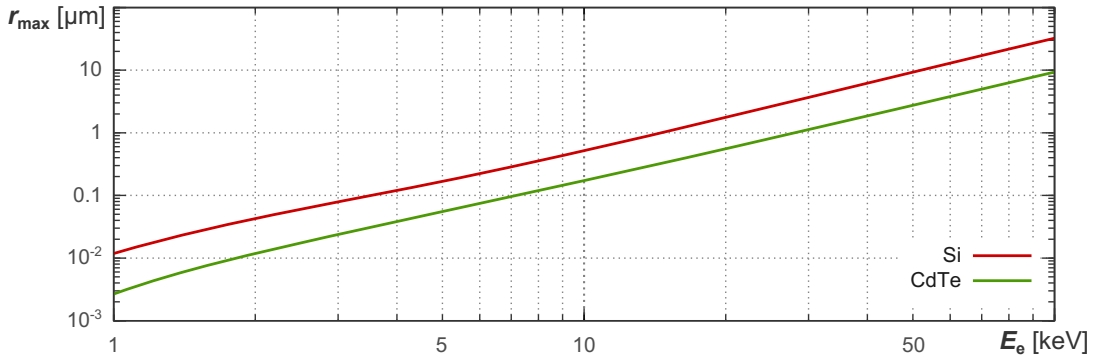

Figure 1.10. Electron range $r_{\max}$ according to Tabata et al. [1996]. The path of an electron with the initial kinetic energy E_e is on average $r_{\max}$. For cadmium telluride, $Z = 50$ is assumed.

3. The empty state in the primary ionized atom is filled with an electron of a higher (sub)shell* of the same atom or by an external electron. In this transition a **fluorescence photon** or an **Auger electron** can be emitted. In general, the Auger effect is dominant for light elements, while for heavy elements fluorescence becomes more and more prominent. Additionally, the Auger or fluorescence yield y depends on the quantum mechanical state of the filled vacancy, see Fig. 1.11. Both, the fluorescence photon and the Auger electron create further electron-hole pairs.

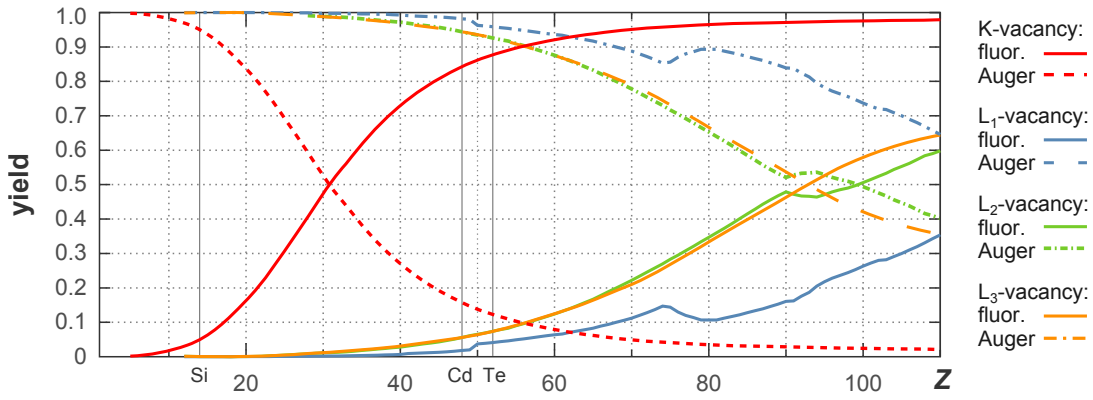

Figure 1.11. Fluorescence and Auger yield for K and L-vacancies. For silicon, Auger electron emission dominates fluorescence line emission, but for CdTe the interaction depends on the photon energy E_γ. If $E_\gamma > 26.7\,\text{keV}$ (Cd K-edge) a photoelectric interaction with a K-shell electron followed by fluorescence radiation is most probable. For lower photon energies, an L-shell photoelectric interaction and the emission of an Auger electron is most probable. All data are taken from Krause [1979]. Auger and Coster-Kronig yields are summed and labeled as Auger.

*If the vacancy is filled with an electron originating from a subshell of the same shell as the vacancy (e.g. an L_2-L_1-transition), the transition is radiationless and an Auger electron is emitted. This special Auger effect is known as *Coster-Kronig transition*. The following discussion does not distinguish between Auger and Coster-Kronig transitions.

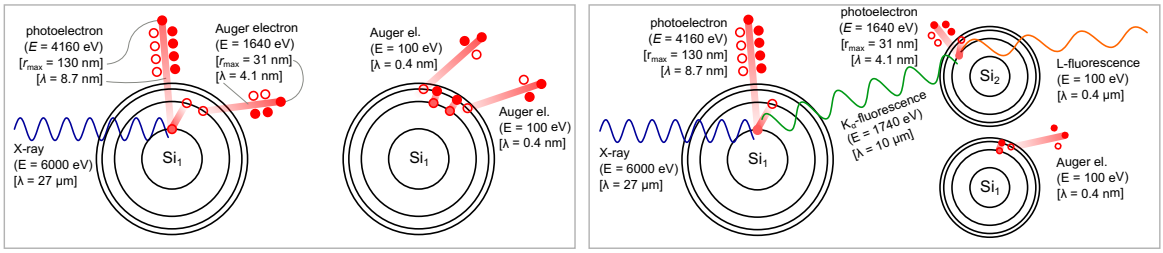

Figure 1.12. Absorption of a 6 keV X-ray photon in silicon. The mean free paths λ of the electrons and the photons and the electron range $r_{\max}$ are calculated according to [Powell and Jablonski, 1999, Eq. (24), Tab. 4], Eq. (5.6) and [Tabata et al., 1996]. The (simplified) absorption edges of Si are: K-edge = 1840 eV, L-edge = 100 eV, and M-edge = 0 eV (quasi continuum). The photon interacts with a K-shell electron:
Left: the vacant state in the K-shell is filled with an L-shell electron and the energy difference between K and L-shell is used to ionize an L-shell Auger electron. The two vacant states in the L-shell are filled with two M-shell electrons and another two Auger electrons are ejected.
Right: the vacant 1s state is filled with a 2p electron emitting a K_α-fluorescence line. Compared to the mean free paths of the electrons, this fluorescence photon can travel a large distance ($\lambda = 10\,\mu$m). It is absorbed by another Si-atom (Si_2) and makes a photoionization of an L-shell electron. The vacant state of Si_1 results in an Auger electron.

Figure 1.12 shows a possible absorption scenario of a 6 keV photon in silicon. Considering all possible photoelectric interactions with electrons of different (sub)shells, the possibility of emitting Auger electrons or fluorescence radiation, and the conversion of secondary electrons or radiation to electron-hole pairs shows that the ionization of a semiconductor can only be studied on a statistical level: the conversion factor w states how much photon energy E_γ it takes on average to create one electron-hole pair. The average amount N of electron-hole pairs created can be calculated via

$$N = E_\gamma / \omega. \tag{1.8}$$

The conversion factor ω is considerably larger than the band gap E_G of the semiconductor. It can be approximated as $\omega \approx 2.8 E_G + 0.6\,\text{eV}$ [Owens and Peacock, 2004]. The energy difference between E_γ and $N \cdot E_G$ transforms into heat. The variance Var of the detector signal due to the stochastic signal charge generation is

$$Var = F \cdot N. \tag{1.9}$$

It is difficult to calculate the Fano factor F [Fano, 1947] exactly, but it can be estimated by considering the relationship between ionization and phonon excitation [Spieler, 2005, § 2.2.3]. Using Eq. (1.9), the noise contribution of the transducer can be expressed as full energy width at half maximum (FWHM). The Fano limited energy resolution of silicon and cadmium telluride detectors is presented in Fig. 1.13.

$$\Delta E_{\text{FWHM}} = 2.35 \cdot \omega \cdot \sqrt{Var} \tag{1.10}$$

$$= 2.35 \sqrt{F\, E_\gamma\, \omega}. \tag{1.11}$$

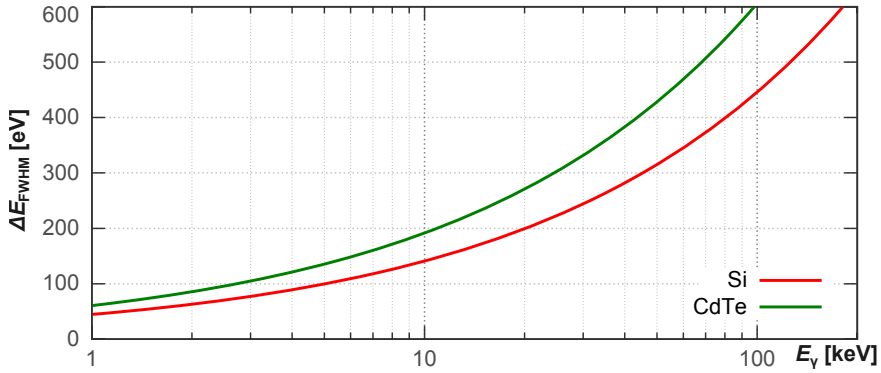

Figure 1.13. Fano limited energy resolution for silicon and cadmium telluride detectors according to Eq. (1.11) and Tab. 1.1.

Escape peaks

If, after a photoionization, the refilling of the vacant state results in fluorescence, the fluorescence photon can escape from the detector volume. In this case the escaping photon cannot contribute to the signal charge and the energy of the detected event is diminished by the energy of the escaping photon. As result, a "ghost peak" shifted by the energy of the fluorescence photon ΔE (mainly K_α) develops. Figure 1.14 shows schematically a Mn-K_α and Mn-K_β line detected with a silicon detector and the corresponding escape peaks. In principle, this scenario also applies to Auger electrons, but as their mean free path is considerably shorter than the one of photons, escaping electrons are unlikely, see Fig. 1.12.

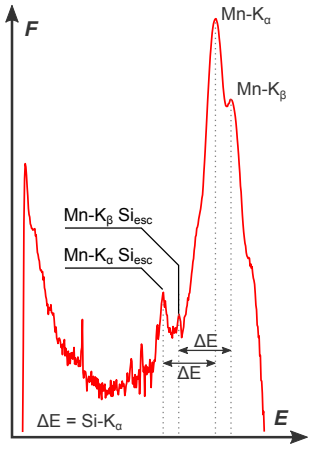

Figure 1.14. Scheme of two silicon escape peaks.

The intensity of an escape peak depends on the intensity of the peak the escape peak is originating from, on the type of the escape photon (K_α, K_β...), on the energy of the primary radiation, and on the absorbing material and its geometry, see again Fig. 1.11. More energetic primary radiation is more likely to be absorbed deep in the detector volume, which makes a fluorescence escape unlikely. But, close to absorption edges, this general rule does not apply. This is most easily demonstrated with an example: a photon with $E_1 = 26.5\,\text{keV}$ impinging on a CdTe detector (K-edge of Cd $\approx 26.7\,\text{keV}$) has a long mean free path ($\lambda_1 \approx 190\,\mu\text{m}$) in contrast to the (most likely) generated L-fluorescence photon ($E_2 \approx 3.1\,\text{keV}$, $\lambda_2 \approx 2.2\,\mu\text{m}$). Additionally, L-shell fluorescence is unlikely for CdTe (5.5 % yield averaged over L_1, L_2, L_3), see Fig 1.11. In contrast, for $E_1 = 27\,\text{keV}$, the photon has enough energy to interact with a K-shell electron which reduces the mean free path to $\lambda_1 \approx 61\,\mu\text{m}$. The generated K_α-fluorescence photon ($E_2 = 23.1\,\text{keV}$, 86 % fluorescence yield) has an even longer mean free path of $\lambda_2 \approx 114\,\mu\text{m}$.

To calculate the intensity of the escape peak, all possible escaping paths, at a given depth z, have to be considered according to their probability of escaping. This calculation has to be repeated for all absorption depths z weighted with the probability that a photon gets absorbed in this depth. For a photon with a trajectory perpendicular to an infinitely large and infinitely thick detector plane (see Fig. 1.15) the probability for escaping fluorescence emission P can be expressed as

$$P(E_1, E_2) = y(E_1, E_2) \cdot \frac{1}{\lambda_1(E_1)} \int_0^{\infty} \underbrace{\frac{0.5}{\pi/2} \int_0^{\pi/2} \exp\left(-\frac{z/\cos(\alpha)}{\lambda_2(E_2)}\right) \mathrm{d}\alpha}_{\text{calculate all escaping paths}} \cdot \exp\left(-\frac{z}{\lambda_1(E_1)}\right) \mathrm{d}z. \tag{1.12}$$

The outer integral (blue, $\int \mathrm{d}z$) is the integration of Beer's law expressed as probability density function. It represents the probability that a photon with energy E_1 and mean free path λ_1 is absorbed within $[z, z+\mathrm{d}z]$. The inner integral (red, $\int \mathrm{d}\alpha$) calculates an average of all possible escaping paths for a fluorescence photon with energy E_2 and mean free path λ_2 at an absorption depth z. The additional factor of 0.5 accounts for the fact that the escape direction is only considered towards the entrance window of the detector. This approach assumes that any emitting angle $0 \leq \alpha \leq 90°$ is equally probable. A numerical integration of Eq. (1.12) with $\lambda_1 = 61\,\mu\mathrm{m}$ and $\lambda_2 = 114\,\mu\mathrm{m}$ is shown in Fig. 1.15. In this case, only a layer with a thickness of about 150 µm contributes to the escape peak. So, the idea to consider only the photon entrance side of the detector as escaping direction is very reasonable. The assumption of an infinitely large detector plane underestimates the escape peak and, especially for small detectors (with respect to λ_2), a more sophisticated calculation is necessary.

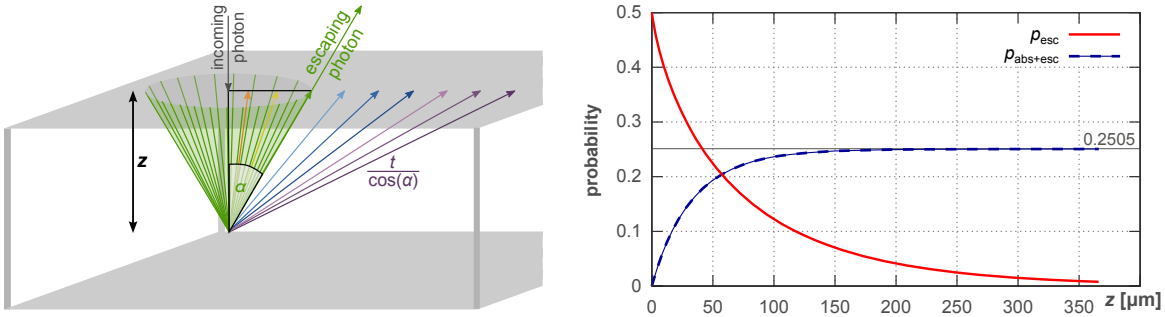

Figure 1.15. Calculation of the escape peak intensity. **Left:** a photon ionizes a medium in a depth z. A fluorescence photon can escape via multiple paths (colored). For the same fluorescence angle α, the escape probability is the same (green cone). **Right:** numerical solution of Eq. (1.12) for $E_1 = 27\,\mathrm{keV}$, $E_2 = 23.2\,\mathrm{keV}$, $\lambda_1 \approx 61\,\mu\mathrm{m}$, and $\lambda_2 \approx 114\,\mu\mathrm{m}$ (Cd-K-shell interaction in CdTe). The red curve p_{esc} (also red part of Eq. (1.12)) is the probability for escaping from a depth z. The blue curve $p_{\mathrm{abs+esc}}$ (blue part of Eq. (1.12)) weights this probability with the probability that a photon gets absorbed in a depth z. It is shown as a cumulative distribution, i.e. the integral in Eq. (1.12) is calculated up to z and not up to infinity. The total probability for an escaping Cd-K$_\alpha$ photon is ($y = 86\,\%$): $P \approx 0.86 \cdot 0.2505 = 21.5\%$.

1.2.2. Charge separation and transportation

The signal charges, electrons and holes, created in the semiconductor material represent a non-equilibrium state that tends to return to equilibrium and lose its signal information by recombination. Recombination is avoided by weakening the inherent crystal conditions for it and by working against it with an external electric field:

- **Crystal conditions:** direct recombination of an electron with a hole is forbidden for indirect semiconductors* and unlikely for direct semiconductors. But defect states with energy levels located in the center of the band gap are an effective center for recombination and must therefore be avoided as much as possible. Furthermore, defect states enhance the dark current of the detector for temperatures $T > 0\,\mathrm{K}$. Therefore, enormous efforts in purity are undertaken during crystal growth and crystal processing.
- **Electric field:** a reversed-biased semiconductor forms a space charge region with an intrinsic electric field. This has two main effects: the charge carrier concentration decreases dramatically and makes the detector volume sensitive to signal charges. Additionally, the field separates electrons and holes so that recombination is no longer possible. A fast separation requires high electric fields. Thus, the contacts to the semiconductor must supply high depletion voltages in combination with low leakage currents.

Both electrons and holes can move through the crystal along an applied (constant) electric field $\vec{E}$ with a constant drift speed $\vec{v}$

$$\vec{v} = \pm\,\mu \cdot \vec{E}. \tag{1.13}$$

The mobility μ is different for electrons and holes,† see Table 1.1.

Table 1.1. Properties of Si and CdTe at $T = 300\,\mathrm{K}$: atomic number Z, density ρ, band gap E_G, conversion factor ω, mobility μ, life time τ, and Fano factor F. The atomic number of CdTe is averaged ($Z_\mathrm{Cd} = 48$, $Z_\mathrm{Te} = 52$). The mobility μ and the lifetime τ are typical values that change for different crystal conditions and temperatures [Sellin et al., 2005]. Sources for the data: [Spieler, 2005, Tab. 2.3] and [Lutz, 1999, Tab. 4.1].

	Z	$\rho\,[\frac{\mathrm{g}}{\mathrm{cm}^3}]$	$E_\mathrm{G}\,[\mathrm{eV}]$	$\omega\,[\mathrm{eV}]$	$\mu_\mathrm{e}\,[\frac{\mathrm{cm/s}}{\mathrm{V/cm}}]$	$\mu_\mathrm{h}\,[\frac{\mathrm{cm/s}}{\mathrm{V/cm}}]$	$\tau_\mathrm{e}\,[\mu\mathrm{s}]$	$\tau_\mathrm{h}\,[\mu\mathrm{s}]$	F
Si	14	2.33	1.12	3.63	1450	450	>1000	2000	0.10
CdTe	50	5.85	1.44	4.43	1100	100	2.7	2	0.15

* In indirect semiconductors, the top of the valence band and the bottom of the conduction band have different momenta. Direct recombination is forbidden due to momentum conservation.

† As holes are not point-like but associated with a spatial distortion over many unit cells their effective mass is higher than the effective electron mass [Lowe and Sareen, 2013, § 1.4]. The higher effective mass decreases the mobility.

1.3. Signal generation

The drifting electrons and holes represent a short current pulse that can be used directly as detector output signal. The Shockley-Ramo theorem combined with charge trapping effects (Hecht equation) and its effect to the observed pulse height spectrum (Trammell-Walter equation) are phenomenologically discussed in the following sections. As it turns out, a deep investigation of signal development related to the electric field is necessary to understand the HED performance; a quantitative discussion for the HED is given in Sect. 3.3. In other detector geometries, like the LED, the electric field is only used for charge separation and transportation to a readout electronics. In such geometries, the electric field is not directly coupled to the signal generation.

Shockley-Ramo Theorem

Assume a detector with two planar electrodes, a cathode and an equally sized anode, with an applied depletion voltage U_0 along a distance d, see Fig. 1.16. The electric field $\vec{E}$ between both electrodes is constant

$$\vec{E} = -\left(U_0/d\right)\,\hat{\mathrm{e}}_\mathrm{z}. \tag{1.14}$$

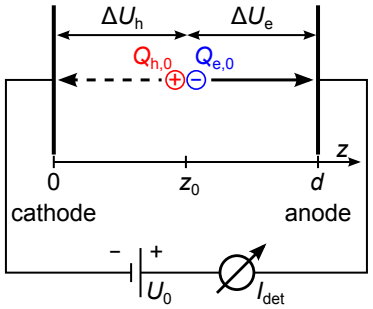

Figure 1.16. Simple detector geometry illustrating the Shockley-Ramo theorem.

The Shockley-Ramo theorem states that an electrical current I_det, which serves as detector signal, is continuously generated by signal charges drifting along an electric field $\vec{E}$ and not instantaneously by charges reaching the cathode or anode. In the context of semiconductors, the term *signal charges* refers to electrons (with the initial total charge $Q_{\mathrm{e},0}$) and holes ($Q_{\mathrm{h},0}$). The concept is based on the idea that moving charges exert an instantaneous long-distance effect on the electrodes via electric field changes. The original idea is presented by Shockley [1938] and Ramo [1939]; Lowe and Sareen [2013, § 1.7.2] show in a comprehensive review

$$Q_\mathrm{det} = Q_{\mathrm{e},0}\frac{\Delta U_\mathrm{e}}{U_0} + Q_{\mathrm{h},0}\frac{\Delta U_\mathrm{h}}{U_0}. \tag{1.15}$$

The detected charge Q_det is only equal to the initial electron charge $Q_{\mathrm{e},0}$ if all electrons and all holes are collected at the anode and cathode, respectively. Taking the voltage difference for the holes to $\Delta U_\mathrm{h} = -\left(U_0 - \Delta U_\mathrm{e}\right)$ and $Q_0 \coloneqq Q_{\mathrm{e},0} = -Q_{\mathrm{h},0}$, leads to

$$\begin{aligned} Q_\mathrm{det} &= Q_0\frac{\Delta U_\mathrm{e}}{U_0} - Q_0\frac{-U_0 + \Delta U_\mathrm{e}}{U_0} \\ &= Q_0. \end{aligned} \tag{1.16}$$

The same result can be obtained using the lengths of the charge drifts:

$$Q_\mathrm{det} = Q_0\frac{d - z_0}{d} + Q_0\frac{z_0}{d} = Q_0. \tag{1.17}$$

The assumption of a constant electric field does not hold if cathode and anode are of different size or structure. Many detector types have geometries different to the one presented in Fig. 1.16. In typical geometries, an unstructured back contact serves as a common electrode (mostly cathode) and the readout electrode (mostly anode) is realized through the use of guard rings, readout strips, pixelation, or drift rings of much smaller size. The concept of **weighting potentials** is used to take these geometries into account. He [2001] reviews the Shockley-Ramo theorem and its application in semiconductor detectors with a focus on the calculation of weighting potentials. Without going into details, large common cathodes and small readout anodes have the effect that the signal develops close to the end of the electron trajectory.

Hecht Equation

The Shockley-Ramo theorem gets its spice by introducing charge traps. Crystal defects can capture electrons or holes, or both types, on their way to the corresponding electrode. The trapped charge, if not released during the collection time, cannot contribute further to the signal formation. But, according to the Shockley-Ramo theorem, the trapped charge has contributed to the signal all the way from its generation (z_0) up to its capture, even without reaching an electrode. The Hecht equation takes this partial contribution into account by introducing a characteristic drift length L,

$$L = \mu\tau E \tag{1.18}$$

after which an initial charge Q_0 decays to Q_0/e. Hecht [1932] (see also Lowe and Sareen [2013, 1.7.4] for a compact calculation) shows that the detected charge Q_{det} can be expressed as

$$Q_{\mathrm{det}}(z_0) = Q_0 \cdot \left\{ \frac{L_{\mathrm{e}}}{d} \left(1 - \mathrm{e}^{-\frac{(d-z_0)}{L_{\mathrm{e}}}} \right) + \frac{L_{\mathrm{h}}}{d} \left(1 - \mathrm{e}^{-\frac{z_0}{L_{\mathrm{h}}}} \right) \right\}. \tag{1.19}$$

The drift lengths for electrons and holes, L_{e} and L_{h} are in general different. As the hole mobility is smaller than the electron mobility, holes become trapped easier.

The charge collection efficiency *CCE* is defined as the ratio between the detected charge and the initial signal charge

$$CCE(z_0) = \frac{Q_{\mathrm{det}}}{Q_0} = \left\{ \frac{L_{\mathrm{e}}}{d} \left(1 - \mathrm{e}^{-\frac{(d-z_0)}{L_{\mathrm{e}}}} \right) + \frac{L_{\mathrm{h}}}{d} \left(1 - \mathrm{e}^{-\frac{z_0}{L_{\mathrm{h}}}} \right) \right\}. \tag{1.20}$$

The charge collection efficiency is plotted in Fig. 1.17 as a function of absorption depth for a variety of different drift lengths L_{e} and L_{h}. If $L_{\mathrm{e}} = L_{\mathrm{h}}$ the *CCE* is maximal for absorptions in the center of the detector $z_0 = d/2$ and decreases to both electrodes in a symmetrical way. In the usual case of $L_{\mathrm{e}} > L_{\mathrm{h}}$, the *CCE* rises if the electrons drift longer distances as the holes, i.e. when the absorption takes place near the cathode, which is normally the entrance window for radiation.

The long drift lengths in silicon result in a *CCE* that is nearly independent of the absorption depth. The compound cadmium telluride semiconductor suffers much

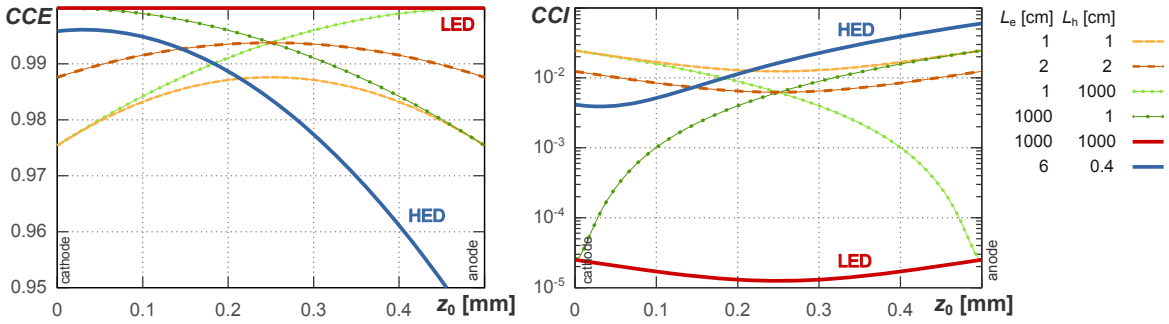

Figure 1.17. The charge collection efficiency CCE and inefficiency ($CCI = 1 - CCE$) as a function of the absorption depth z_0 according to Eq. (1.20). The detector depth is chosen as $d = 0.5\,\mathrm{mm}$. The CCE of the silicon LED (bold red) is nearly independent of the absorption depth (see the logarithmic CCI plot on the right for details). The CCE of the cadmium-telluride HED (bold blue) shows strong trapping effects.

more from trapping effects.* Note that the Hecht equation presented here assumes a constant electric field $\vec{E}$ and can therefore not be applied to the CdTe crystal of the HED, as polarization effects inside CdTe result in an inhomogeneous electric field. See Section 3.3 for a modified version of the Hecht equation that considers non-uniform electric fields.

Assuming no trapping ($L_{\mathrm{e,h}} \to \infty$), a Taylor approximation of the Hecht equation (Eq. (1.19)) yields the same result as the Shockley-Ramo theorem (Eq. (1.16)).

$$Q_{\mathrm{det}} = Q_0 \cdot \left\{ \frac{L_\mathrm{e}}{d} \left(1 - \left[1 - \frac{(d - z_0)}{L_\mathrm{e}} + ... \right] \right) + \frac{L_\mathrm{h}}{d} \left(1 - \left[1 - \frac{z_0}{L_\mathrm{h}} + ... \right] \right) \right\} \tag{1.21}$$

$$= Q_0 \cdot \left\{ \frac{L_\mathrm{e}}{d} \left(\frac{(d - z_0)}{L_\mathrm{e}} + ... \right) + \frac{L_\mathrm{h}}{d} \left(\frac{z_0}{L_\mathrm{h}} + ... \right) \right\} \approx Q_0 \tag{1.22}$$

Despite the fact that both, electrons *and* holes contribute to the signal current, some detectors are classified as *single carrier detectors*. In such detector systems, the detected signal depends on only one type of signal carrier, usually electrons. This can be the case for several reasons:

- When measuring soft X-rays, the charge generation occurs, on average, close to the entrance window, $z_0 \ll d$, see Eq. (1.17).
- The semiconductor material has a lot of traps ($L_\mathrm{h} \ll d$) and the hole contribution to the signal vanishes, see Eq. (1.19).
- The detector geometry and its associated weighting potential concentrates the signal development to a region near the readout electrode.
- The readout method is not performed on the basis of a charge induced current, but on the presence of charge itself, like the DePFET concept of the LED.

* In general, compound semiconductors entail more crystal defects. Some kind of defects, like antisite defects (atoms of different type exchange their position), can only occur in compound systems.

Trammell-Walter Equation

With the theory discussed above, we can now calculate, in a simplified way, the spectral shape of the detected signal of a monochromatic radiation source. The calculation connects how likely radiation is absorbed in a specific depth z with the efficiency of signal generation in that depth. Therefore, we have to introduce the relative pulse height* h which equals the relation of the measured pulse height (of one photon detection) to the maximal pulse height (of all photon detections). h is a dimensionless number between 0 and 1. The probability P to detect a photon with a relative pulse height within $[h, h+\mathrm{d}h]$ can be calculated via the probability density function $PDF(h)$

$$P = PDF(h) \cdot \mathrm{d}h. \tag{1.23}$$

Trammell and Walter [1969] present the idea to calculate the $PDF(h)$ by dividing the detector in slices of width $\mathrm{d}z$, calculate the probability that charge is deposited in a slice (Beer's law), multiply this probability with the $CCE(z)$ of this slice, and add a Gaussian noise distribution to account for Fano noise. The observed spectrum can then be obtained by summarizing (integrating) over all slices, see also Fig. 1.18:

$$PDF(h) = \int_0^d \rho_{\mathrm{abs}}(z) \cdot \frac{1}{\sqrt{2\,\pi}\,\sigma} \exp\left(\frac{(h - CCE(z))^2}{2\,\sigma^2}\right) \mathrm{d}z \tag{1.24}$$

Here, Beer's law $\rho_{\mathrm{abs}}(z)$ is expressed in terms of probability and not as usual in terms of flux. With the absorption coefficient μ_{abs} which depends on the energy of the radiation, Beer's law can be expressed as

$$\rho_{\mathrm{abs}}(z) = \mu_{\mathrm{abs}}\, \mathrm{e}^{-\mu_{\mathrm{abs}}\, z}. \tag{1.25}$$

Equation (1.24) is solved in general by numerical integration. An analytical solution can be obtained with the following approximations. The charge collection efficiency

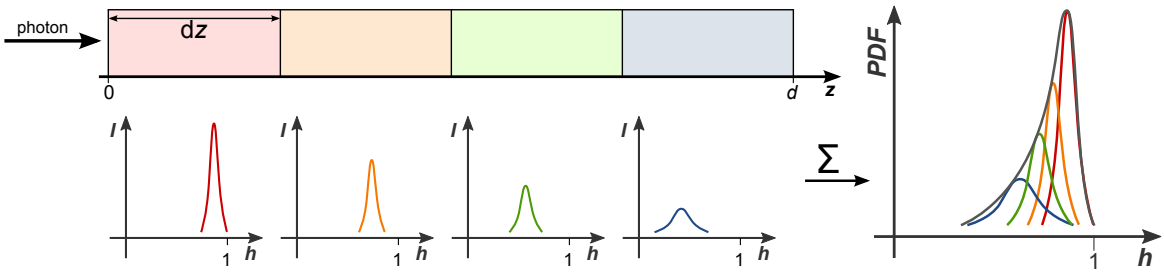

Figure 1.18. Visualization of the Trammell-Walter equation (Eq. (1.24)). The detector thickness d is divided in several slices of width $\mathrm{d}z$. The signal formation in each slice is shown in red, orange, green, and blue as intensity I vs. relative pulse height h. The summed spectrum (gray) on the right shows an asymmetrical low energy tail.

* Be aware, that the term *pulse height* refers to the energy of a signal and not to the height (intensity) of a measured spectral peak.

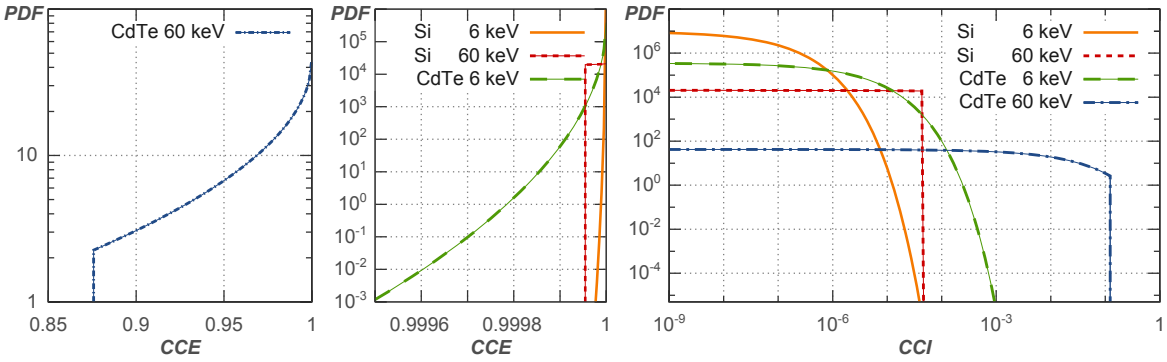

Figure 1.19. Signal formation in Si and CdTe for photon energies of 6 keV and 60 keV according to Eq. (1.27). The hole drift lengths are chosen as $L_{\mathrm{h,LED}} = 1000\,\mathrm{cm}$ and $L_{\mathrm{h,HED}} = 0.4\,\mathrm{cm}$. $L_{\mathrm{e}} = \infty$ in both cases. The charge collection efficiency CCE is equal to the relative pulse height h. The charge transfer inefficiency CCI equals $1 - h$. The edges result from the limited detector thickness ($d = 1\,\mathrm{mm}$). Example: in a 1 mm thick CdTe detector, a 60 keV photon has a minimal CCE of 87.5 % (absorption close to the anode). All PDFs are cut at a minimal possible h_{min} and normalized (see App. D.3).

$CCE(z)$ is combined with the z-dependent absorption probability ρ_{abs}, but the influence of the Fano noise is neglected. This approximation is rough, as the Fano noise has a large impact on the spectral shape, but allows to see the effect of charge trapping on signal formation in a more direct way. All edges in the resulting plots become smeared out with the introduction of noise. The PDF can be constructed with the composition $\rho_{\mathrm{abs}} \circ CCE^{-1}$.

$$PDF\colon\ h \xrightarrow[Eq.\,(1.26)]{CCE^{-1}} z \xrightarrow[Eq.\,(1.25)]{\rho_{\mathrm{abs}}} \text{probability density}$$

CCE^{-1} is the inverse function of the charge collection efficiency (Eq. (1.20)), which can be approximately obtained with a 2nd-order Taylor expansion of $CCE(z)$, see Eq. (1.26). To obtain an analytical solution for $PDF(h)$, we have to assume additionally that only holes get trapped ($L_{\mathrm{e}} \to \infty$). See Appendix D.2 and D.3 for calculation details.

$$z(h) = \sqrt{2\,d\,L_{\mathrm{h}}\,(1-h)} \tag{1.26}$$

$$PDF(h) = n^{-1} \cdot \mathrm{e}^{-\mu_{\mathrm{abs}}\sqrt{(1-h)\cdot 2\,d\,L_{\mathrm{h}}}} \qquad \text{with } n = \frac{\left(1 - \mathrm{e}^{-d\mu_{\mathrm{abs}}}\,(1 + d\mu_{\mathrm{abs}})\right)}{\mu_{\mathrm{abs}}^2\,d\,L_{\mathrm{h}}} \tag{1.27}$$

Figure 1.19 shows the signal generation for a 1 mm thick detector in case of Si and CdTe according to Eq. (1.27). Despite the approximations made during the calculation, two effects are clearly visible. First, charge trapping results in a low energy tail that makes the peak shape asymmetric. Second, the formation of a low energy tail depends on the drift lengths of the detector material (the longer the better), the energy of the radiation (the softer the better), and on the detector thickness (the thinner the better).

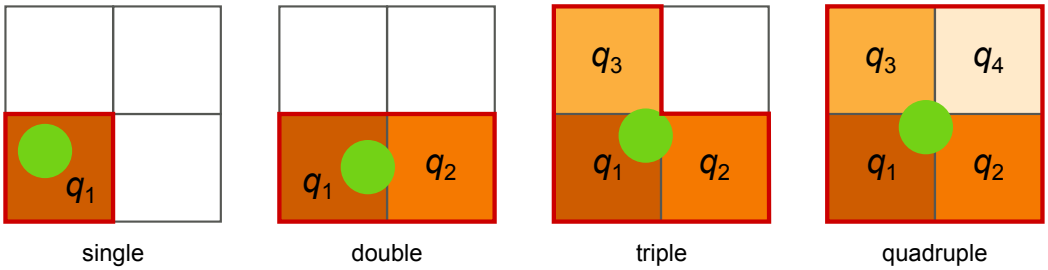

Figure 1.20. The signal charge cloud (green circle, not to scale) deposits charge to a maximum of four pixels. The color strength represents the relative amount of charge.

1.3.1. Split events

A photon absorption with pure Auger transitions yields a very compact* initial electron charge cloud. The collection time t_{coll} is defined as the time between charge generation and charge localization. In an ideal case, t_{coll} depends only on the absorption depth and the drift speed (Eq. (1.13)). In addition to this, charge traps, generated by crystal imperfections, prolong the collection time t_{coll}. During t_{coll}, the charge cloud widens due to two reasons:

- **Mutual electrical repulsion** of the negatively charged electrons.
- **Diffusion:** the number density of electrons n_{e} gets diluted with time. After the collection time t_{coll}, a point-like distribution at $(x_0/y_0/z_0)$ widens to a three dimensional Gaussian distribution with width σ

  $$\sigma = \sqrt{D \cdot t_{\mathrm{coll}}}. \tag{1.28}$$

  The diffusion constant D is related to the electron mobility μ_{e} through the Einstein relation

  $$D = \frac{\mathrm{k_B} T}{\mathrm{q_e}} \cdot \mu_{\mathrm{e}} \tag{1.29}$$

  with temperature T, Boltzmann constant $\mathrm{k_B}$, and elementary charge $\mathrm{q_e}$.

Doing the calculations shows that the dominant effect that determines the extension of the charge cloud is the diffusion of the charge carriers, see Mathieson et al. [2002, Tab. 1]. A typical width of a charge cloud produced by a 6 keV photon in a 450 µm thick fully depleted ($U_{\mathrm{bias}} = 250$ V) silicon detector is reported with $\sigma \approx 9$ µm [Kimmel et al., 2010].

The distribution of the signal charge q_0 over more than one pixel is classified as charge sharing or as split event. As the size of the charge cloud is typically much smaller than the pixel size, split events can only occur if the X-ray interacts near the pixel boundary. If the pixel pitch is less than the charge cloud extension (normal case) the signal charge can be distributed to a maximum of four pixels with fractional

* The extent of a charge cloud generated by a 6 keV photon in silicon is in the range of some 100 nm, if all secondary transitions are radiationless (Auger effect). See the discussion to Fig. 1.12.

charges q_1, q_2, q_3, and q_4. The complete charge deposition in one, two, three, or four pixels are termed as single, double, triple, or quadruple events, see Fig. 1.20. In the following, the split ratio η_n is defined as

$$\eta_n = \frac{q_n}{q_0}$$
$$q_0 = q_1(+q_2(+q_3(+q_4))). \tag{1.30}$$

The split ratio η_1 for doubles, triples, and quadruples is on average much larger than 1/2, 1/3, or 1/4, i.e. the signal charge is not shared equally, but leaks just a bit into the neighboring pixel(s). See Section 2.8.2 for LED measurements of η_n.

Uncorrected charge sharing has two effects: the original peak in the energy spectrum gets a prominent low energy tail due to the diminished signal charge $q_1 < q_0$ and the remaining charges contribute to the low energetic background. Fortunately, the spectroscopic effects of charge sharing can be corrected in two ways:

- Consider only single events and reject all events that have neighbors with non-vanishing detected charges. Dependent on the pixel size and the pixel geometry, this event rejection can diminish the quantum efficiency of the detector dramatically.

- Sum up all shared charges and take advantage of Eq. (1.30). Assuming that the average time between two photons hitting two neighboring pixels is much longer than the detector readout time, it is more likely that the charges of neighboring pixels result from a shared signal charge than from different photon events. If this is not the case *pattern pile-up* occurs, see next section.

Summing charges is an idea emerging from the underlying physical process of charge sharing but cannot be implemented in data analysis. Instead, a charge equivalent pulse height analysis *PHA* has to be considered. Furthermore, due to noise fluctuations (Section 1.3.3), all pixels show occasionally non-vanishing *PHA* values. To reject this noise contribution, a threshold PHA_{th} is introduced: all pixels with $PHA < PHA_{\mathrm{th}}$ are considered as being affected by noise and not by signal charge. The choice of PHA_{th} is critical, as it adds noise, if the threshold is too low but leads to the mentioned effects of uncorrected split events, if it is chosen too high.

Whether a charge cloud results in a split event depends on its extension σ, the position of its center (x_0/y_0), the detection threshold of the neighboring pixels PHA_{th}, and the pixel geometry. A computer simulation that takes all these parameters as input and that calculates the expected spatial distribution of the different split types was written in the framework of this thesis, see Fig. 1.21.

Besides its negative impacts on the spectrum, charge sharing makes it possible to achieve a sub-pixel spatial resolution by calculating the center of the signal charge r_0

$$r_0\, q_0 = \sum_{i=1}^{4} r_i \cdot q_i. \tag{1.31}$$

Assuming a charge cloud extension of $\sigma = 7.5\,\mu\mathrm{m}$, for a pixel size of $50\,\mu\mathrm{m}$ Strüder [2000, § 5.2.5] reports an improved spatial resolution of less than $15\,\mu\mathrm{m}$.

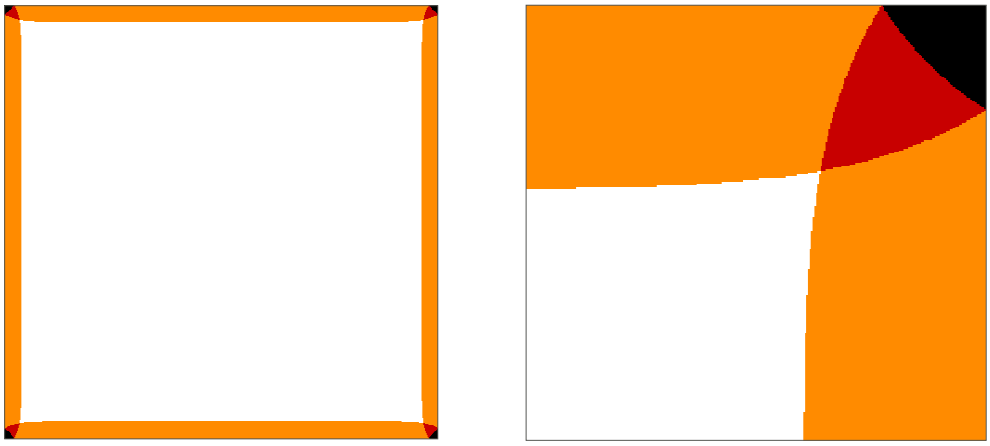

Figure 1.21. Simulated spatial distribution of single (white), double (orange), triple (red), and quadruple (black) events of a $500\,\mathrm{x}\,500\,\mu\mathrm{m}^2$ pixel (left). The threshold for event detection PHA_{th} is expressed as energy equivalent $E_{\mathrm{th}} = 765\,\mathrm{eV}$. The width of the 3D Gaussian charge distribution is $\sigma = 17\,\mu\mathrm{m}$. The pixel is grated in $3000\,\mathrm{x}\,3000$ sub-pixels that can be seen in the zoomed image of the right-top edge (right). The ratio between the number of subpixels with the same event type and all subpixels is the expected probability for this event type: singles 85.3 %, double 14.4 %, triples 0.23 %, quadruples 0.11 %.

1.3.2. Pile-up

Pile-up occurs if two or more X-ray photons are counted as one. In pixelated detectors, two kinds of pile-up can be distinguished:

- **Energy pile-up:** two photons with energies E_1 and E_2 hit the same pixel during one readout cycle and their energy equivalent charges add up. It is no longer possible to conclude on the individual energies E_1 and E_2 but only on their sum $E_1 + E_2$.

- **Pattern pile-up:** two photons hit two neighboring pixels during one readout cycle. Their individual energies may be detected correctly (in the case of two single events) but the correction for split events will add them and treat the result as one event.

Considering the incoming photons as uncorrelated in temporal and in spatial distribution allows a unified analysis for both kinds of pile-up. As (non-edge) pixels have eight neighboring pixels, the chance for pattern pile-up is eight times higher than for classical pile-up. Another difference between both kinds of pile-up is that only pattern pile-up can be excluded at the expense of detection efficiency by analyzing only single events. Both kinds of pile-up have similar effects on the energy spectrum. But before investigating the spectral implications of pile-up, a mathematical model to describe pile-up has to be introduced.

Quantitative analysis

In the following, energy pile-up is investigated in a statistical way. For a detailed study of pattern pile-up see Ballet [1999]. The averaged incoming photon rate R_{in} (in terms of counts per pixel per second [cps]) and the readout rate R_{out} define the input-output ratio

$$\lambda = \frac{R_{\text{in}}}{R_{\text{out}}} = \frac{T_{\text{out}}}{T_{\text{in}}} \tag{1.32}$$

with the readout time interval T_{out} and the average time interval between two incoming photons T_{in}. λ gives a first estimate how likely pile-up occurs: if $\lambda \ll 1$ pile-up is unlikely as the detector readout is more frequent as the incoming photon rate. For $\lambda \to 1$ pile-up gets more and more probable and for $\lambda > 1$ pile-up is the usual case.

Besides the input-output ratio, the readout mode of the detector is another parameter that defines the event counting statistics. In a **continuous readout mode** (CRM), the occurrence of a photon event is checked in a periodic time interval, the frame-time T_{f}.

$$T_{\text{out}} = T_{\text{f}} \quad \Leftrightarrow \quad R_{\text{out}} = T_{\text{f}}^{-1} \quad [\text{frames per second (fps)}] \tag{1.33}$$

In a **triggered readout mode** (TRM), a pixel is only read out, if an incoming photon triggers a readout process. The readout time T_{trig} depends on the trigger latency t_{th} and the shaping time t_{shape}. The trigger latency is the time between photon arrival and triggering which in turn depends on the trigger threshold. The shaping time describes the time it takes to measure the event properly (see also Sect. 1.3.3).

$$T_{\text{out}} = T_{\text{trig}} \quad \Leftrightarrow \quad R_{\text{out}} = T_{\text{trig}}^{-1} \quad [\text{s}^{-1}] \tag{1.34}$$

$$T_{\text{trig}} = t_{\text{th}} + t_{\text{shape}} \tag{1.35}$$

Usually, T_{trig} is much less* than T_{f}, which makes triggered detectors less susceptible to pile-up. Figure 1.22 shows the continuous and triggered readout modes and their effects on event pile-up for the (unusual) case $T_{\text{f}} = T_{\text{trig}}$. Here, the triggered readout can result in pile-up for cases in which the continuous readout is free of pile-up.

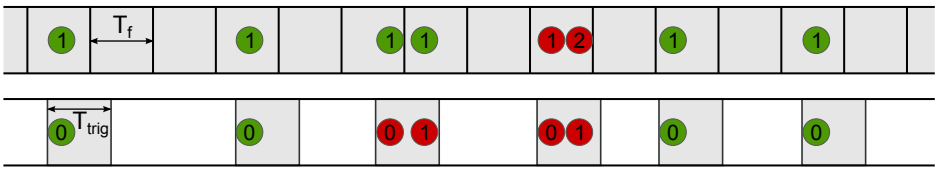

Figure 1.22. Event detection for a continuous readout mode (top) and a triggered readout mode (bottom) presented as temporal readout of one pixel. Green indicates a correct event detection while red indicates pile-up. The numbers (k) refer to the statistical treatment in the main text. $T_{\text{f}} = T_{\text{trig}}$.

* The LED (continuous readout) frame time is $T_{\text{f}} \approx 2.4\,\text{ms}$; the HED (triggered readout) shaping time, which is the largest part of T_{trig}, is $t_{\text{shape}} \approx 10\,\mu\text{s}$.

The difference between both readout modes has a direct consequence in the counting statistics. The Poisson distribution $P_k(\lambda)$

$$P_k(\lambda) = \frac{\lambda^k}{k!} \cdot \mathrm{e}^{-\lambda} \qquad \text{with } \lambda = \frac{T_{\mathrm{out}}}{T_{\mathrm{in}}} = \frac{R_{\mathrm{in}}}{R_{\mathrm{out}}} \tag{1.36}$$

describes the probability that k events (with the average rate R_{in}) are observed within the time interval T_{out}. This way, k represents the possible number of photons within a readout cycle for CRM. In contrast, for a triggered readout there are $k+1$ photons in one readout cycle, as k states how many additional photons can arrive during T_{out}. The term *x-fold* is used to describe an event consisting of x photons; pile-up occurs for $x \geq 2$. The relation between x and k is different for CRM and TRM and summarized in Table 1.2. Compare also Fig. 1.22 with its k-numbered events.

Table 1.2. Poisson distribution for continuous and triggered readout.

k	$P_k(\lambda)$	continuous readout mode	triggered readout mode
0	$\mathrm{e}^{-\lambda}$	no event	1-fold event
1	$\lambda \cdot \mathrm{e}^{-\lambda}$	1-fold event	2-fold piled-up event
2	$\lambda^2/2 \cdot \mathrm{e}^{-\lambda}$	2-fold piled-up event	3-fold piled-up event
3	$\lambda^3/6 \cdot \mathrm{e}^{-\lambda}$	3-fold piled-up event	4-fold piled-up event

Figure 1.23 depicts the pile-up probability $P_k(R_{\mathrm{in}}/R_{\mathrm{out}})$ as a function of R_{in} and R_{out}. With conditions that make pile-up unlikely ($\lambda \ll 1$) it is most probable to detect no event in the case of a continuous readout and 1-fold events for a triggered readout.

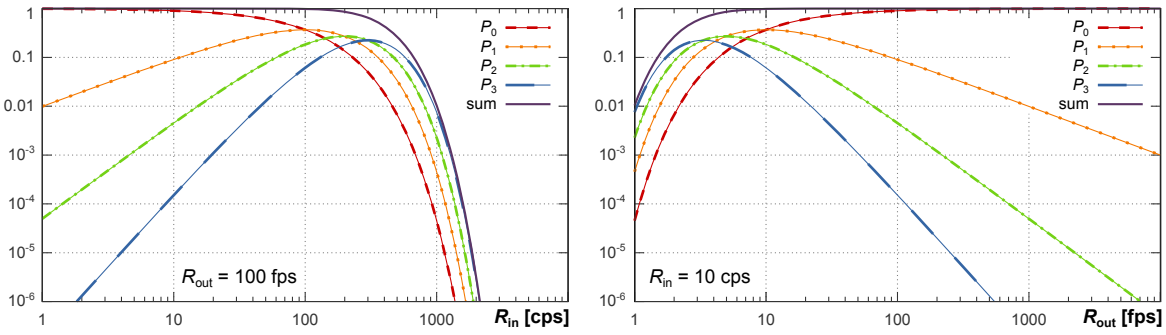

Figure 1.23. Pile-up probability $P_k(R_{\mathrm{in}}/R_{\mathrm{out}})$ as a function of the average incoming photon rate R_{in} with constant readout rate $R_{\mathrm{out}} = 100\,\mathrm{fps}$ (left) and as a function of R_{out} with constant $R_{\mathrm{in}} = 10\,\mathrm{cps}$ (right). Be aware of the different definitions of P_k according to Tab. 1.2. The summation of the probabilities for $k \leq 3$ ($sum = P_0 + P_1 + P_2 + P_3$) shows that for $\lambda < 1$ it is appropriate (sum ≈ 1) to consider only these 4 contributions. For $\lambda > 1$ the chance for events with $k \geq 4$ is no longer negligible ($sum < 1$). fps = frames per second; cps = counts per second.

Spectroscopic implications of pile-up

Pile-up changes the measured photon flux and the shape of the energy spectrum as two (or more) events are "missing" at their original energies and one event is inserted falsely at their summed energy. In line spectra, these effects can be observed directly: the original peaks become smaller than expected and additional *ghost peaks* develop at multiples of the line energies. In continuous spectra, the presence of pile-up is more subtle; in general, the spectrum gets harder. Additional to this spectral shifts, the total flux becomes smaller as several photons are joined together to form one event. See Mück [2014] for an XMM analysis of pile-up.

To investigate spectral effects in more detail, it is assumed that the detector is uniformly illuminated. Furthermore, the following calculations only consider energy pile-up. This is no severe restriction, as pattern pile-up is just a factor $\xi(\lambda)$ larger than energy pile-up: $2 \leq \xi(\lambda) \leq 8$. The factor $\xi(\lambda)$ depends on the detector geometry as edge pixels have less chances for pattern pile-up. It is a function of the input-output ratio λ as diagonal splits, which are rejected by the pattern correction, can become legal triple or quadruple events if λ increases and pile-up is more likely. As this effect is based on three- or more-fold pile-up, it can be neglected for $\lambda \ll 1$.

Let us consider a monoenergetic source with the true energy E_0 and the true (pile-up free) flux F_0. The detected spectrum consists of a peak at $E_1 = E_0$ with the diminished flux F_1 and additional ghost peaks at $E_n = n\,E_0$. It is

$$F_0 = \sum_{n=1}^{\infty} n \cdot F_n = F_1 + 2\,F_2 + 3\,F_3 + ... \qquad (1.37)$$

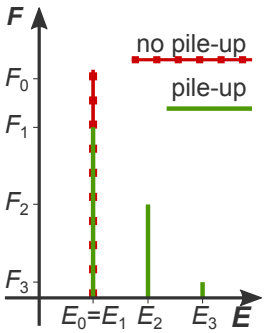

Figure 1.24. Spectrum of a monoenergetic source with pile-up.

as photons are redistributed but not lost. Therefore, the original flux F_0 can be calculated by measuring all the pile-up peaks and sum them according to Eq. 1.37. In the context of noise and especially with spectra that have broad band structures, it can be difficult to detect all relevant pile-up peaks and a correction method that is only based on the observed line (E_1, F_1) with its 2-fold pile-up (E_2, F_2) would be desirable.

A possible solution is to calculate the input-output ratio λ via the ratio between the 2-fold pile-up peak (with flux F_2) and the reduced original peak (with flux F_1)

$$\frac{F_2}{F_1} = \frac{\frac{\lambda^2}{2}\mathrm{e}^{-\lambda}}{\lambda \mathrm{e}^{-\lambda}} = \frac{\lambda}{2} \qquad \text{CRM} \qquad (1.38)$$

$$\frac{F_2}{F_1} = \frac{\lambda \mathrm{e}^{-\lambda}}{\mathrm{e}^{-\lambda}} = \lambda \qquad \text{TRM} \qquad (1.39)$$

and use the calculated λ to deduce F_0. In case of CRM, the fluxes F_n can be calculated

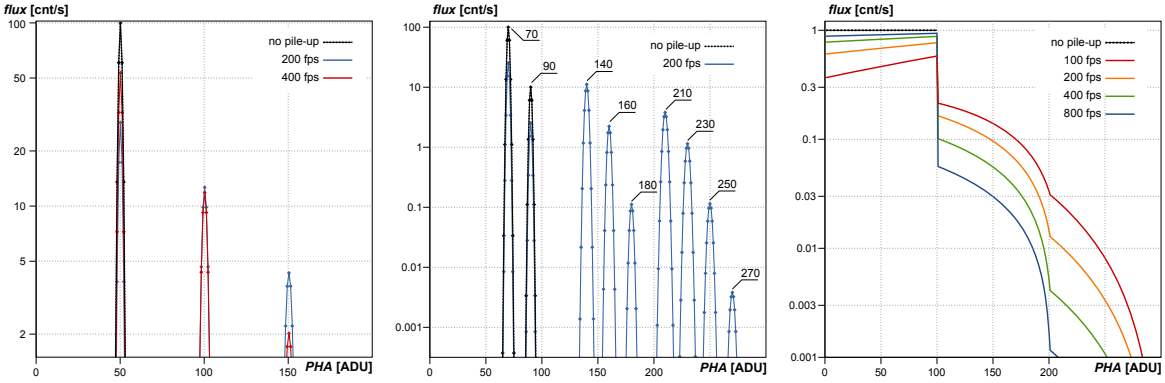

Figure 1.25. Spectral impact of pile-up calculated with *PileItUp* in CRM.
Left: photons of a monoenergetic source (peak at 50 ADU) can only interact with themselves and produce ghost peaks at multiple energies.
Center: photons of two monoenergetic sources (peaks at 70 ADU and 90 ADU) can pile-up to three 2-fold peaks and four 3-fold peaks.
Right: a continuous spectrum was modeled by 100 individual peaks between 1 ADU and 100 ADU. The hardening of the continuum is clearly visible.

by multiplying the probability $P_k(\lambda)$ with the frame rate R_{out}:

$$\begin{aligned} F_{0,\,\text{CRM}} &= F_1 + 2\,F_2 + 3\,F_3 + \ldots \\ &= \left(\lambda \mathrm{e}^{-\lambda} + 2\,\frac{\lambda^2}{2}\mathrm{e}^{-\lambda} + 3\,\frac{\lambda^3}{6}\mathrm{e}^{-\lambda} + \ldots\right) \cdot R_{\text{out}} \\ &= \lambda \mathrm{e}^{-\lambda} \Bigg(\underbrace{1 + \lambda + \frac{\lambda^2}{2} + \ldots}_{\mathrm{e}^{\lambda}} \Bigg) \cdot R_{\text{out}} \\ &= \lambda \cdot R_{\text{out}} \end{aligned} \tag{1.40}$$

The analogue calculation for TRM is similar (see Appendix D.4), but the probability has to be multiplied with the averaged trigger rate R_{trig} to conclude on the flux:

$$F_{0,\,\text{TRM}} = (1 + \lambda) \cdot R_{\text{trig}} \tag{1.41}$$

To get a better feeling for the spectral changes produced by pile-up, a software tool *PileItUp* which calculates the impact of pile-up to a given input spectrum was written. The software takes every bin of the input spectrum as an individual radiation source and calculates the pile-up of this component with itself and with all other sources. This approach is correct if all photons of different bins are uncorrelated. This is true for spectra with sharp lines (line width $\leq$ bin width). For a continuous spectrum, the relation between events of different bins has to be investigated thoroughly. Nevertheless, the tool gives an impression how pile-up works on continuous spectra. *PileItUp* can be configured to simulate CRM and TRM. The calculation depth is fixed to 3-fold pile-up. Figure 1.25 shows three representative examples produced with *PileItUp*.

1.3.3. Noise

In the following context, noise is classified as unknown, random fluctuations superimposed on a signal. The random nature makes it impossible to correct for noise. Indeed, noise is what remains after subtracting all known artifacts from a signal. In spectroscopy a low level of noise is important for:

- **Line identification:** energetic transitions in atoms or nuclei define very sharp energies.* Instrumental noise can make line emissions so broad that discrete energy lines cannot be resolved individually and a blurred continuum-like spectrum appears.
- **Reconstruction of the line shape:** effects that broaden line emissions can be reconstructed, if the instrumental line broadening due to noise is smaller than the line broadening effects of the source. The relativistically broadened iron line in the proximity of a compact object is a prominent example for line shape analysis.
- **Sensitivity:** noise influences the sensitivity for line detection, as a broad line spreads over a large background range and the peak becomes less significant.

Fano noise n_F, the noise associated with the stochastic generation of electron-hole pairs, has already been introduced in Section 1.2.1. Besides this, electronic noise n_e is a major contributor to the total noise n_tot. Considering only these two sources of noise, it is

$$n_\mathrm{tot} = \sqrt{n_\mathrm{F}^2 + n_\mathrm{e}^2} \tag{1.42}$$

as Fano noise and electronic noise are uncorrelated. Discussions on noise can be oriented on several aspects like the physical origin of noise, the spectral distribution of noise or the kind of noise representation in an equivalent circuit. See Tab. 1.3 for a comprehensive overview of the following discussion and Spieler [2005, § 1.10] or Lowe and Sareen [2013, § 1.10] for more details.

The **physical origin** of electrical noise are fluctuations of the electrical current due to velocity fluctuations and due to number fluctuations of charge carriers (mainly electrons). The three most important manifestations of noise in semiconductor detector systems are: thermal noise, shot noise, and trapping noise. In thermal noise, thermal motions of the conductive material couple to the current of charge carriers via collisions and result in charge carrier velocity fluctuations. Shot noise represents the uncorrelated, stochastic flow of individual electrical charges and results in a number fluctuation of charge carriers. In semiconductor detector systems, leakage current, i.e. the current through a reversed biased diode, is the most dominant source for shot noise. Trapping noise is another manifestation of number fluctuations caused by the stochastic nature of trapping and detrapping of charge carriers.

* The natural line width is quantum mechanically defined via the energy-time-uncertainty $\Delta E\,\Delta t_\mathrm{life} \approx \hbar$. Additionally, this line width ΔE broadens, as atom collisions effectively reduces the natural life time t_life. Both effects result in a Lorentzian line profile. Thermal movement within the light emitting medium results in an Doppler broadening with a Gaussian profile.

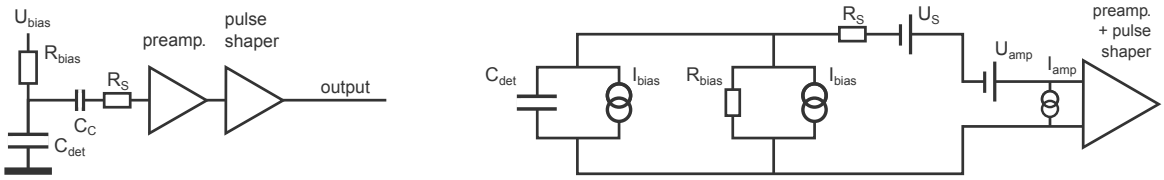

Figure 1.26. A typical detector front-end circuit (left) and its equivalent circuit for noise analysis (right), according to Spieler [2005].

The **spectral distribution** of noise, i.e. the noise power per unit bandwidth, can be flat (white noise) or decreasing with frequency (pink noise). The spectral distribution of pink noise is proportional to $1/f^{\alpha}$ with $0.5 \leq \alpha \leq 2$. Independent of the value of α, pink noise is often called $1/f$ noise.

A typical detector front-end circuit with its **equivalent circuit** for noise analysis is shown in Fig. 1.26. The different noise sources are modeled either with a current source parallel to the amplifier input or with a voltage source in series with the amplifier input. The noise caused by the detector leakage current I_{bias} is modeled with a current source. To model thermal noise, the configuration of the respective resistor is important: thermal noise of serial resistors can be modeled with a serial noise voltage source, while thermal noise of a parallel resistor is modeled with a parallel noise current source. So, the bias resistor works as current noise source while the series resistor R_{s} is modeled as voltage noise source.

To study noise quantitatively, it is useful to express all sources of noise in terms of equivalent noise charge (*ENC*). The *ENC* in units of elementary charge, states the amount of signal electrons that would result in a signal equal to this noise. With this concept, the contributions of different noise sources at different places in the readout chain can be compared effectively. According to Spieler [2005, Eq. (1.34)] the electronic noise n_{e} in terms of *ENC* can be modeled with the current noise contribution n_{c}, the voltage noise n_{v}, and the pink noise n_{pink}. Current and voltage noise are a function of the shaping time t_{shape}, a time constant characteristic for the used pulse shaper:

$$n_{\mathrm{e}} = \sqrt{n_{\mathrm{c}}^2 + n_{\mathrm{v}}^2 + n_{\mathrm{pink}}^2} \tag{1.43}$$

Table 1.3. Noise sources and their classifications. $\Delta\vec{v}$ corresponds to velocity fluctuations and $\Delta\rho_{\mathrm{N}}$ corresponds to fluctuations in the number density of charge carriers.

	thermal noise	shot noise	trapping noise
physical origin	$\Delta\vec{v}$	$\Delta\rho_{\mathrm{N}}$	$\Delta\rho_{\mathrm{N}}$
spectral shape	white	white	pink (1/f)
equivalent circuit	parallel & serial	parallel	-

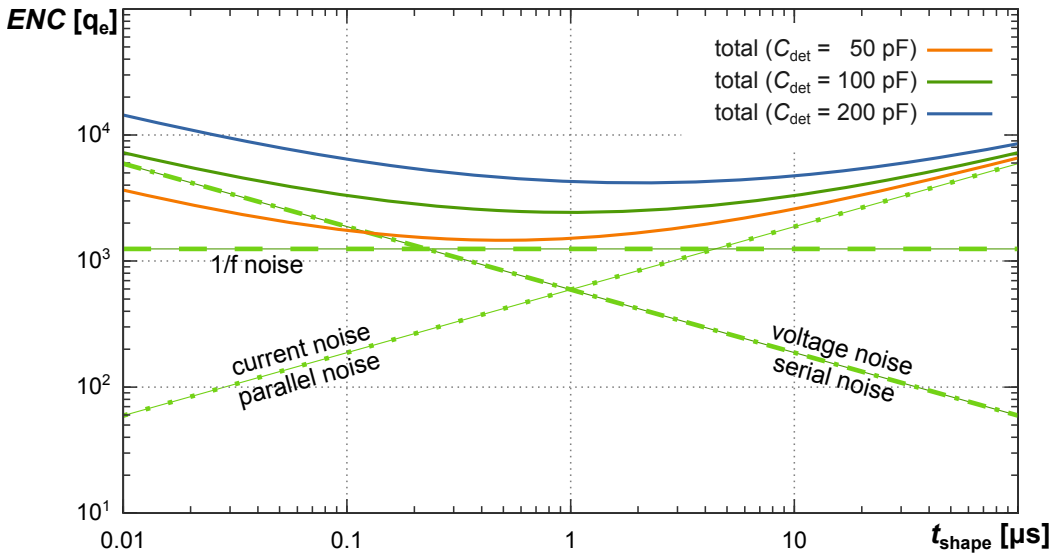

Figure 1.27. Equivalent noise charge *ENC* in units of the elementary charge q_e as function of the shaping time t_{shape} according to Eq. (1.43) to (1.46). The plots are using the following parameters: $I_{bias} = 100\,pA$, $T = 100\,K$, $R_{bias} = 1\,G\Omega$, $i_{na} = 10\,fA/\sqrt{Hz}$, $F_i = F_v = 0.9$, $R_s = 1\,\Omega$, $e_{na} = 1.0\,nV/\sqrt{Hz}$, $F_{vf} = 4$, and $A_f = 10^{-12}\,V^2$. The total *ENC* is plotted for different detector capacitances C_{det}. For $C_{det} = 100\,pF$ the current-, voltage-, and 1/f noise contributions are also shown.

$$n_c^2 = \left(2\,q_e\,I_{bias} + \frac{4k_BT}{R_{bias}} + i_{na}\right) F_i\,t_{shape} \tag{1.44}$$

$$n_v^2 = \left(4k_BTR_s + e_{na}^2\right) F_v \frac{C_{det}^2}{t_{shape}} \tag{1.45}$$

$$n_{pink}^2 = F_{vf}\,A_f\,C_{det}^2 \tag{1.46}$$

Here, q_e is the elementary charge, k_B the Boltzmann constant, i_{na} and e_{na} the current and voltage noise contribution of the amplifier, F_i, F_v, and F_{vf} shape factors determined by the pulse shaper, A_f the noise coefficient for pink noise, and C_{det} the detector capacitance. Figure 1.27 shows the equivalent noise charge as a function of the shaping time for different detector capacitances. It can be seen that:

- The 1/f noise is independent of the shaping time.
- The opposing shaping time dependence of current- and voltage noise results in an optimal shaping time for best noise performance.
- A smaller detector capacitance reduces the noise for all shaping times and shifts the optimal shaping time to smaller values.

In conclusion, the detector noise can be reduced by using a detector with a small capacitance (which reduces voltage noise and 1/f noise), a small leakage current (which reduces current noise), and by choosing an optimized shaping time for the system. For detectors with a very low capacitance of $C_{det} \approx 50\,fF$ noise values of $ENC \approx 1\,q_e$ are reported [Holl et al., 2003].

1.4. CANDELA setup

The test setup CANDELA (cadmium silicon detector laboratory) consists of two detector systems, a low energy detector (LED) placed in front of a high energy detector (HED). Since 2008, CANDELA has been used to develop and test analogue and digital readout electronics, power supply electronics, detector operation, heat management, and software based data analysis for the LED and the HED individually. The mechanical and electrical setup housing both detector systems was almost* completely designed and developed during this work. CANDELA extended its functionality continuously up to the present status which is presented in the next two sections. Individual detector performance of the LED and the HED are presented in § 2 and 3.

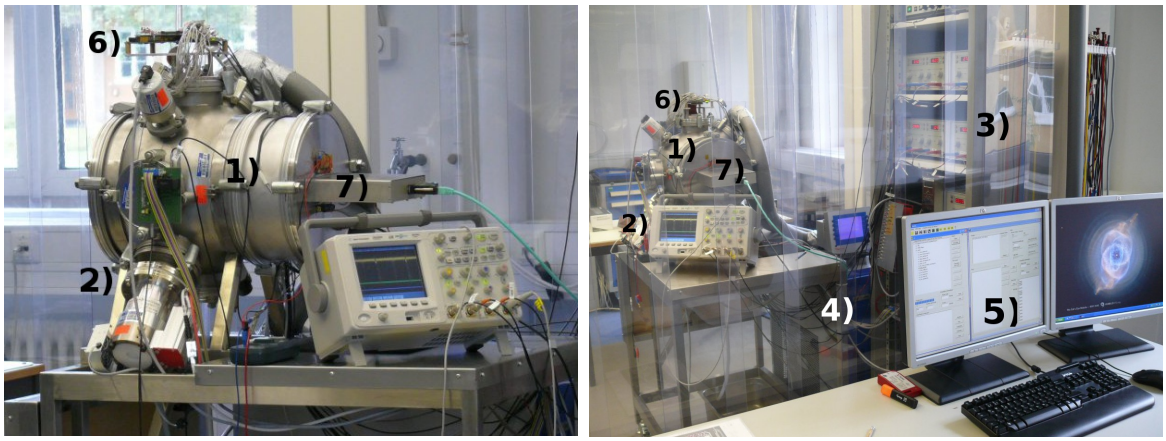

Figure 1.28. CANDELA: a laboratory to test a stacked detector system. The components that can be seen are: 1) vacuum vessel, 2) turbomolecular pump, 3) power supply rack, 4) heat exchanger, 5) PC with the command software Idef-X, 6) D3C PCB, 7) HED PCB. The whole setup is underneath a clean air tent.

1.4.1. The mechanical setup

The mechanical setup is designed to include the LED and the HED within an adjustable distance of $5 \leq d \leq 15\,\text{mm}$ between the two detector surfaces. Furthermore, both detectors must be cooled to a minimal temperature of $T = -40°\text{C}$ which requires to evacuate the setup or to establish a dry atmosphere. The detectors can be irradiated with different sources that can be shielded during operation. Images of the setup are shown in Figs. 1.28 and 1.29.

Cooling system

Both detector units are cooled via a heat exchanger which cools liquid ethanol down to a minimal working temperature of about -80°C. The minimal possible temperature

*This does not hold for the HED printed circuit board (PCB) and for the two vacuum PCBs, even though their functionality and layout are known and understood.

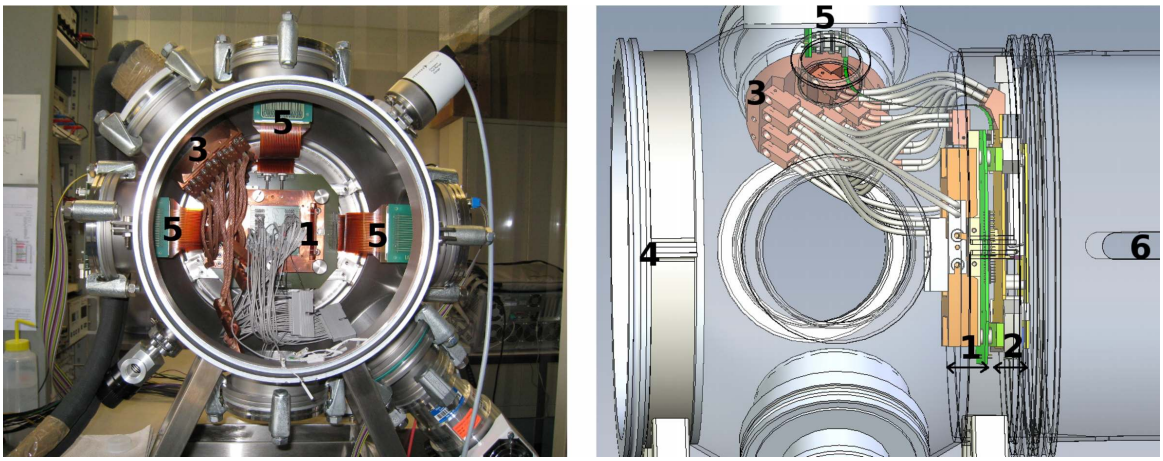

Figure 1.29. Left: a look inside CANDELA with opened front flange.
Right: The LED (1) is located 1 cm to the left of the HED (2). The cooling system (3) cools both detectors. The radioactive sources are located on the front flange (4). The electrical connections to the LED and to the HED are in the positions (5) and (6).

of the cooling fluid depends on the water content of the used ethanol. The viscosity of the fluid rises with increasing water content and the cooling system cannot reach its minimal temperature of -80°C if the cooling fluid is too viscous. The water content of the ethanol increases with each cooling cycle, as air moisture resublimates inside the cooling system, melts during the uncooled phases, and dilutes the alcohol. The water content of the ethanol is measured regularly and the cooling fluid is exchanged if the ethanol concentration is below 90 %.

The cold alcohol flows in spirally winding tubes through a cylinder of copper, the coldfinger, which serves as interface to the vacuum vessel. Both detectors are in thermal contact to this cold finger via copper cables. The chamber can be evacuated to a pressure of $P_{\mathrm{min}} \approx 10^{-7}$ mbar via a combination of a piston pump and a turbomolecular pump. The evacuation prevents condensation of air moisture at cold surfaces and simulates conditions that approximate the expected environment in space.

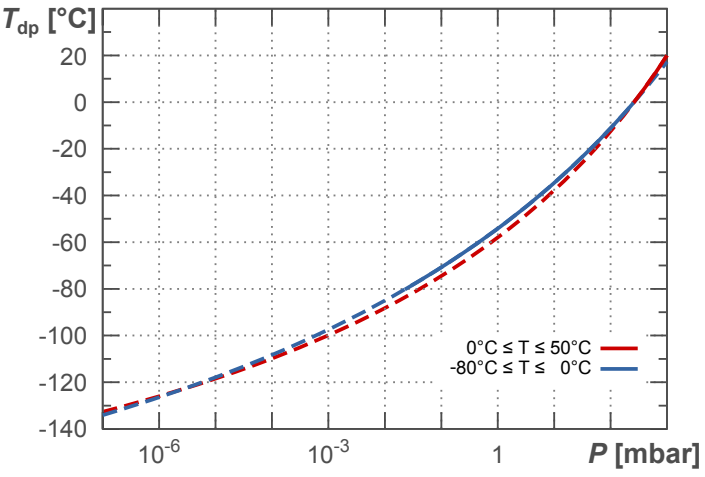

Figure 1.30. Dew point temperature T_{dp} as function of pressure. Solid lines indicate the temperature range the approximations are optimized for (maximal error: 0.14 %). Data: [Buck, 1981, Tab. 2].

The dew point temperature T_{dp} is a function of the pressure P and can be calculated with the Magnus formula

$$P_{\mathrm{s}}(T) = a \cdot \mathrm{e}^{\frac{b\,T}{c+T}} \tag{1.47}$$

which approximately calculates the saturation pressure P_{s} of water at the temperature T. For different temperature regions the parameters a, b, and c can be optimized to match experimental results. Condensation or desublimation starts if the pressure at a given temperature is larger than the saturation pressure. The calculations shown in Fig. 1.30 assume an air moisture of 100 % at a room temperature of $T = 20°\mathrm{C}$. This conservative estimations shows that a pressure of $P \lesssim 10^{-2}\,\mathrm{mbar}$ is necessary to prevent icing at $T = -80°\mathrm{C}$. With the minimal vessel pressure $P_{\mathrm{min}} \approx 10^{-7}\,\mathrm{mbar}$ the minimal setup temperature without icing is $T_{\mathrm{min}} \approx -130°\mathrm{C}$.

Alternatively to the operation in vacuum, a nitrogen gas supply system can be used to operate both detectors in a cold, dry atmospheric pressure environment. This allows to study the effects of convective cooling of the detector system. A set of temperature sensors (Pt-100) and hygrometers is installed to measure the setup conditions during operation.

To shield the large detector area of the LED (about $10\,\mathrm{cm}^2$) from the warm infrared radiation of the vessel, a copper cylinder which is in thermal contact with the cold finger is placed in front of the LED, see Fig. 1.31.

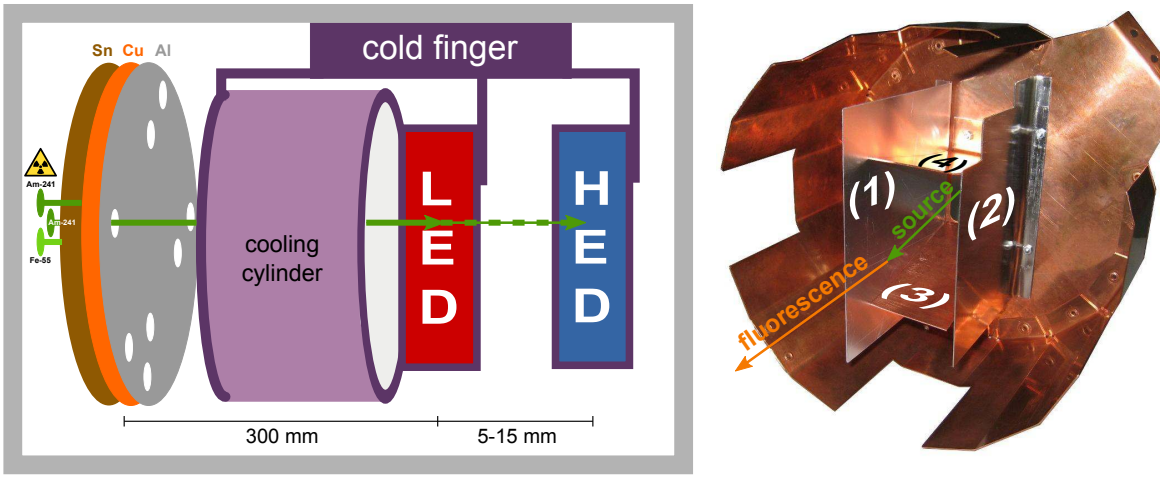

Figure 1.31. Left: CANDELA in a schematic view. The three radioactive sources (green) can be blocked or unblocked with a rotatable absorber wheel.
Right: Photo of the cooling cylinder with fluorescence sheets: Al (1), Ti (2), Cu (3+4).

Radiation sources

The test setup can be equipped with three radioactive sources which can be opened individually. The shutter mechanism is constructed as a rotatable wheel with holes in it. The wheel is made of 2 mm tin, 2 mm copper, and 2 mm aluminium to absorb a large fraction of the source radiation. The alternating materials are chosen in a way to shield the fluorescence radiation produced in the absorber: the copper absorbs the tin fluorescence and the aluminium absorbs the copper fluorescence. The decreasing flux in combination with a decreasing fluorescence yield for lighter elements results in an almost complete shut-off of the sources for a closed shutter position.

In the current configuration an iron (Fe-55) source with an activity of $A = 5.59\,\mathrm{MBq}$ and two americium (Am-241) sources with $A_1 = 1.66\,\mathrm{kBq}$ and $A_2 = 2.82\,\mathrm{MBq}$ serve as calibration and radiation sources. Table 1.4 shows the emitting radiation with respect to energy and intensity according to Firestone et al. [1999].

Additional sheets of aluminium, titanium, and copper are positioned in a way that they can be irradiated by the Fe and Am sources and emit fluorescence radiation towards the LED and the HED, see Fig. 1.31. Fluorescence and source lines are plotted in Fig. 1.32 convolved with Fano noise of a silicon detector. The intensities are relative to the most intensive line of the respective source and can be translated into absolute intensities with the source activity and the distance of the sources (300 mm to the LED, 310 mm to the HED). To calculate the absolute intensities of the fluorescence lines, a calculation similar to the one presented in Section 1.2.1 is needed.

Depending on the resolution of the detector system, separate neighboring lines are not resolved individually and the effective energy of the multiplet will be close to the mean value weighted by the relative intensity of the components. Lines within 100 eV are combined which can result in intensities greater than 100 %.

Table 1.4. Radioactive sources and fluorescence emission.

E [keV]	I [%]	origin
	Al	
1.487	150	Al-$K_{\alpha\,1,2}$
	Ti	
4.509	150	Ti-$K_{\alpha\,1,2}$
4.932	15	Ti-$K_{\beta\,1,3}$
	Fe-55	
5.895	150	Mn-$K_{\alpha\,1,2}$
6.490	17	Mn-$K_{\beta\,1,3}$
	Cu	
8.041	151	Cu-$K_{\alpha\,1,2}$
8.905	17	Cu-$K_{\beta\,1,3}$
	Am-241	
11.87	0.66	Np-L_{l}
13.76	1.07	Np-$L_{\alpha 2}$
13.95	9.60	Np-$L_{\alpha 1}$
15.86	0.15	Np-L_{η}
16.11	0.18	Np-$L_{\beta 6}$
16.82	2.50	Np-$L_{\beta 2}$
17.06	1.50	Np-$L_{\beta 4}$
17.51	0.65	Np-$L_{\beta 5}$
17.75	5.70	Np-$L_{\beta 1}$
17.99	1.37	Np-$L_{\beta 3}$
20.78	1.39	Np-$L_{\gamma 1}$
21.10	0.65	Np-$L_{\gamma 2}$
21.34	0.59	Np-$L_{\gamma 3}$
21.49	0.29	Np-$L_{\gamma 6}$
26.35	2.40	Am-241
33.20	0.13	Am-241
43.42	0.07	Am-241
59.54	35.9	Am-241

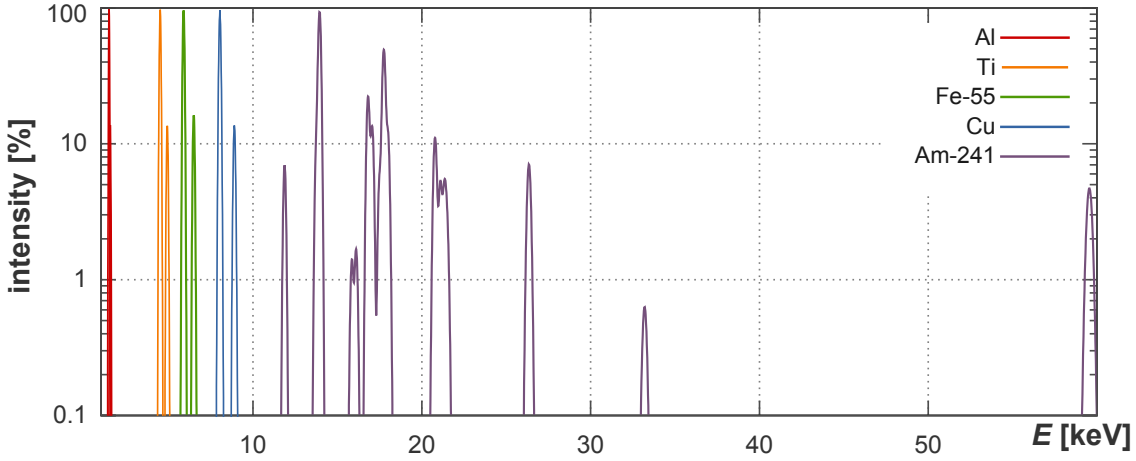

Figure 1.32. Spectrum of all fluorescence (Al, Ti, Cu) and source (Fe-55, Am-241) lines. All lines are folded with a Gaussian shape. The width of the Gaussian is equivalent to the Fano noise in silicon at the respective line energy. All intensities are relative to the strongest line of each source and not comparable between different sources.

1.4.2. The electrical setup

In terms of supply voltages and electrical signals the LED and the HED are two completely detached subsystems. The LED and the HED systems are both consisting of an outer board connected to all supply voltages and to the readout and control interface, and an inner board housing the detectors. The LED is connected to the left, right, and top side of the vessel, while the HED is connected to the backside.

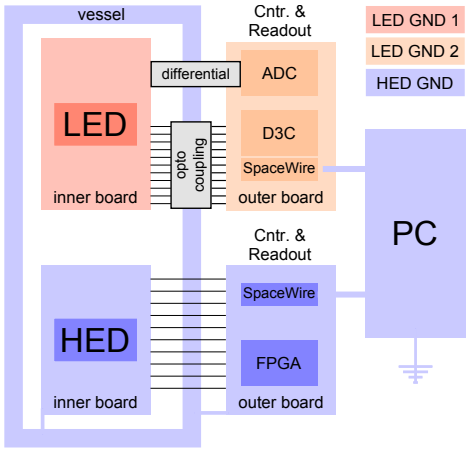

Figure 1.33. Grounding scheme.

The LED inner- and outer board have two different ground levels and communicate with each other via optically coupled units (digital signals) or via a differential signal (analogue detector data). As SpaceWire is also a differential communication, the LED outer board and the PC ground, which is common to the earth potential, are not connected. In contrast, the HED system uses the PC ground for its inner and outer board and connects the stainless steel vessel to it as well. For such a ground level which is distributed over a relatively long distance (a few meters in our example) it is absolutely necessary to prevent ground loops as such loops are working as induction loops and induce noise into the system.

The different ways of grounding the two detector systems are based on the different origins of the two systems, the semiconductor laboratory in Neuperlach for the LED and the CEA in Saclay for the HED, but set an ideal basis for the combined detector system, as electrical interference between both systems is almost not possible.

1.4.3. SpaceWire communication

SpaceWire is a serial, full-duplex, point-to-point communication link with a variable speed between 2 Mbit/s and 400 Mbit/s*. It is based on data strobe encoded, low voltage differential signaling (LVDS), which result in low noise and in a very good skew and jitter tolerance. The SpaceWire standard is defined by the European cooperation for space standardization in ECSS-E-ST-50-12C (31 July 2008).

Both detector units are commanded via SpaceWire and send their data via the same SpaceWire connection. A personal computer adapted with a SpaceWire PCI board serves as command interface and data storage. The PCI board can send and receive information via four independent SpaceWire channels in parallel. A software tool *Idef-X* allows to send commands via ASCII coded text files and stores the received data binary coded. Additionally, Idef-X allows to use simple programming structures like loops or wait states. The PCI board and the Idef-X software tool are built by the CEA, Saclay. See Fig. 1.34 for the graphical user interface of Idef-X.

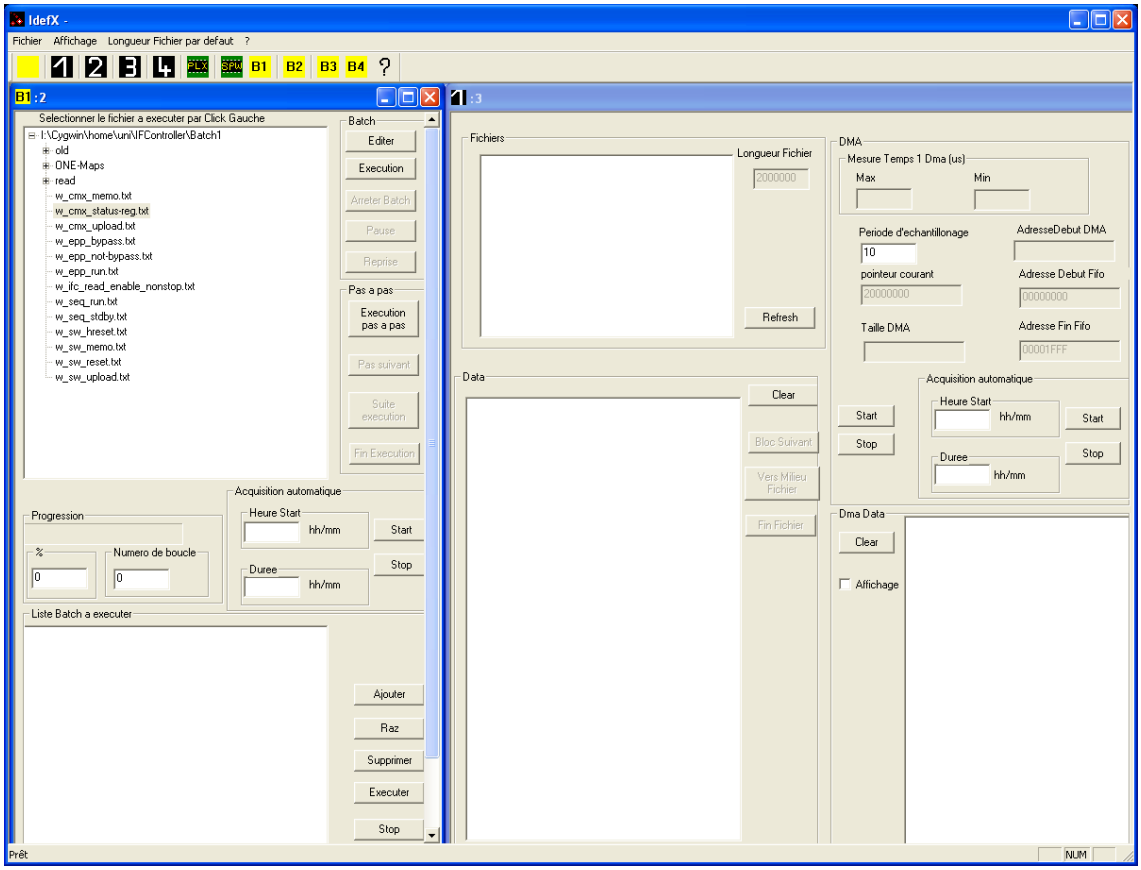

Figure 1.34. Graphical user interface of Idef-X. Commands summarized in batch files can be selected and sent (left window). The right window shows all incoming data.

* The maximal SpaceWire communication speed is approximately equal to the maximal speed of USB-2.0 (480 Mbit/s).

2. The LED: a Si DEPFET detector

The low energy detector (LED) of the CANDELA setup is realized by a 64 x 64 pixel DEPFET matrix, designed and produced by the Max-Planck-Institute Semiconductor Laboratory (HLL) in Neuperlach. Physical properties of the detector material silicon and their implications for radiation measurements are briefly presented in the next section. Sections 2.2 and 2.3 explain the technological concept of a DEPFET-pixel and the arrangement of the pixels in the detector matrix. For the operation of the LED, a real-time event preprocessing is essential and realized by the digital camera controller chip (D3C), introduced in Sect. 2.5. An offline data analysis is performed subsequent to the real-time data preprocessing. The strategies behind the analysis and the required software tools are introduced in Sect. 2.7. The spectroscopic performance of the LED and the different analysis modes are presented in Sect. 2.8. A short summary in Sect. 2.9 completes the description of the LED.

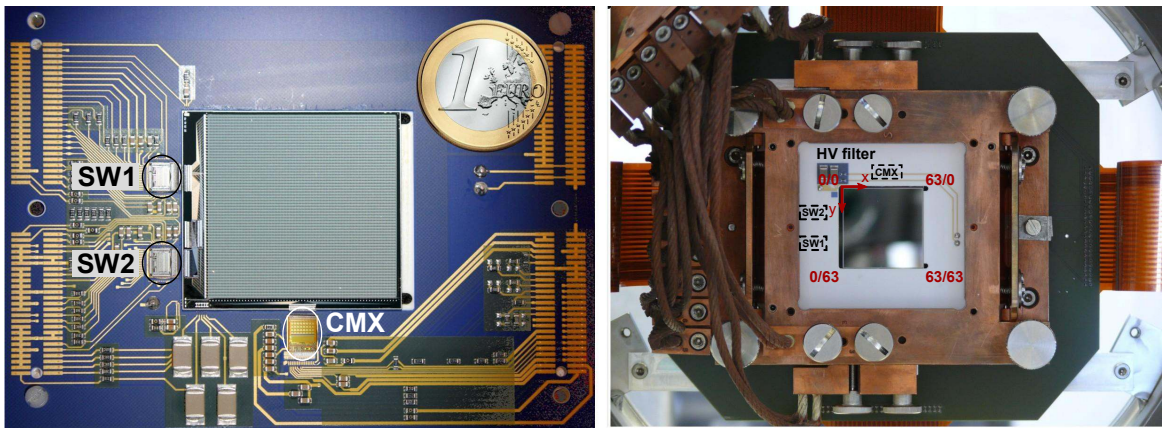

Figure 2.1. The low energy detector: a silicon based DEPFET matrix.
Left: front view of the DEPFET hybrid *SX-1*. A one euro coin is superimposed to show the dimensions of the LED. The two switcher chips SW1 (gate and clear gate) and SW2 (clear) control the operation of the detector matrix. The CAMEX readout chip (CMX) serves as charge amplification and multiplexing unit.
Right: in the CANDELA configuration, the LED is irradiated from its unstructured back side. Reflections on the highly polished detector back contact may give a false impression on the image. The high voltage low-pass filter (HV filter) is located close to the detector back contact. The detector is conductively cooled by a copper mask which is in contact with a heat exchanger (top left). The convention for the x- and y-direction used in the data analysis (Sect. 2.7) is shown in red. The positions of the CAMEX and SWITCHER chips on the front side are indicated.

2.1. Properties of Si-based detectors

While the first semiconductor transistors were made of germanium, silicon is the most used semiconductor material for microelectronics today. Compared to germanium, silicon based radiation detectors require only moderate cooling because of the wider band gap of $E_{\mathrm{G,\,Si}} = 1.12\,\mathrm{eV}$ compared to $E_{\mathrm{G,\,Ge}} = 0.67\,\mathrm{eV}$. Silicon is an indirect semiconductor with diamond cubic crystal structure that can be produced with very low crystal defects and very high purity (11N purity = 99.999 999 999 % purity).

The energy range of silicon based X-ray detectors starts typically around 100 eV and ends around 15 keV, depending on the detector thickness. Electrical noise that is increasing for lower energies and the decreasing cross section for photoelectric absorption at increasing energies define these two energy limits.

2.2. The DEPFET pixel structure

Sideward depletion

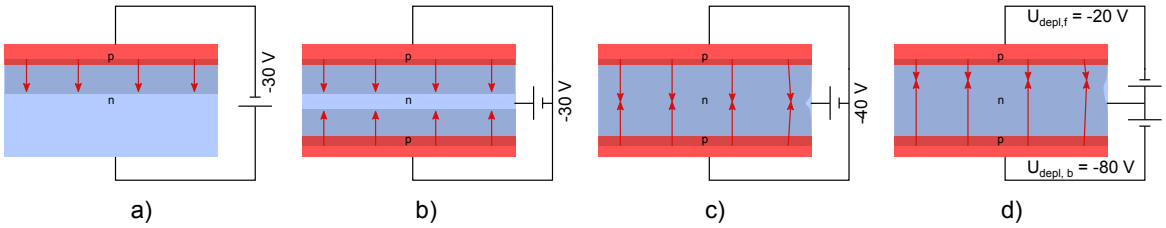

Figure 2.2. Sideward depletion: the red arrows show the drift direction for electrons. A depleted (dark area) pn structure (a) becomes depleted from two sides in a pnp structure (b). Increasing the depletion voltage results in a fully depleted substrate (c). Different depletion voltages result in an asymmetric field structure (d).

The depletion depth d of a reverse biased pn-diode is proportional to the square root of the depletion voltage: $d \sim \sqrt{U_{\mathrm{depl}}}$. Thicker substrates that are advantageous to detect high energy photons, require a quadratic increase of the depletion voltage to be fully depleted. However, increasing dark currents diminish the detector performance for large depletion voltages and voltage break downs can even destroy the detector. Hence, the depletion voltage and therefore the detector thickness are limited.

The LED is a fully depleted detector that uses the principle of sideward depletion [Gatti, 1984]. This principle is based on the idea to double the thickness of a fully depleted detector with two pn structures. In the following this is explained on the example of a pnp structure, see Fig. 2.2. The depletion regions of two opposing pn structures (the front and the back side) merge and form a fully depleted substrate at a critical depletion voltage $U_{\mathrm{depl,\,c}}$. If the front and back side depletion voltages $U_{\mathrm{depl,\,f}}$ and $U_{\mathrm{depl,\,b}}$ are equal, a potential minimum for electrons is created in the center of the substrate $z = d/2$. For $U_{\mathrm{depl,\,f}} > U_{\mathrm{depl,\,b}}$ this potential minimum can be shifted to the front side and vice versa.

Macro pixel

Extended pixel structures can be realized by using the sideward depletion technique with a ring-like structured front side. In the case of the LED, the back side depletion voltage is constant ($U_{\mathrm{depl,\,b}} \approx -80\,\mathrm{V}$), but the front side depletion voltage is stepwise increased ($-50\,\mathrm{V} \leq U_{\mathrm{ring}} \leq -5\,\mathrm{V}$) towards the most central ring. This way, a potential cone is formed which directs signal electrons to the center of the pixel, close to the front side.

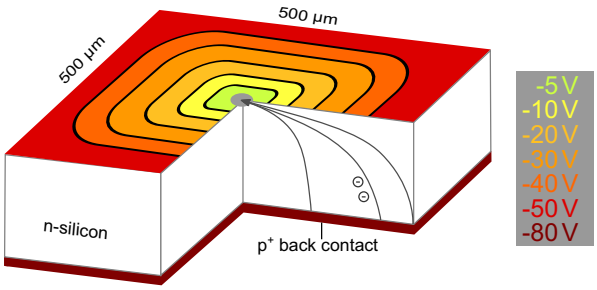

Figure 2.3. Scheme of a LED macro pixel. The cone shaped potential directs all electrons to the pixel center.

Figure 2.3 shows a schematic drawing of the LED macro pixel structure with the applied depletion voltages. The concept of macro pixels allows to vary the pixel size from about $50\,\mathrm{x}\,50\,\mu\mathrm{m}^2$ to several square millimeters [Zhang et al., 2006] and to use a compact detection mechanism directly integrated in the pixel center, the DEPFET cell.

The DEPFET cell and its detection principle

A DEPFET (depleted field effect transistor) cell is the elementary detection unit of the LED. It uses the principle of sideward depletion with an integrated transistor-detector configuration, first mentioned by Kemmer and Lutz [1987]*. A field effect transistor (FET 1) serves as a sensor and amplifier and is implemented as a p-channel field effect transistor (enhancement MOSFET type) with a circular gate structure, see Fig. 2.4. On the side of the ring structure a second FET (depleted n-channel MOSFET) is implemented to clear all signal charges after readout.

During operation, the electrons of the signal charge cloud drift to the central front side of a pixel following the macro pixel potential. At the potential minimum an additional n^+ depleted region enhances the attractivity for the

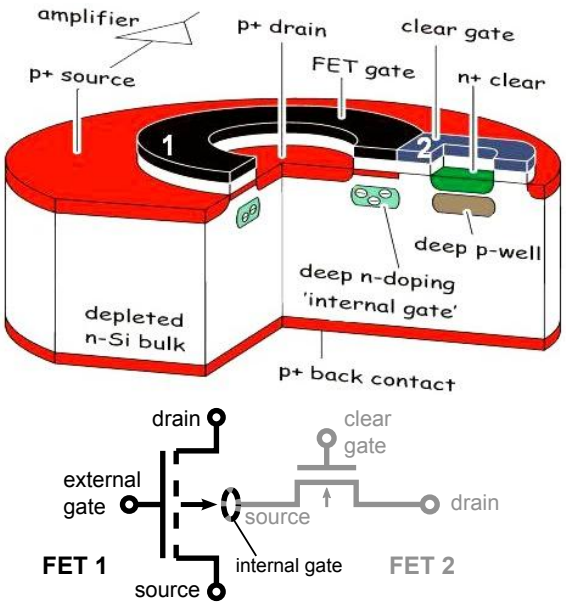

Figure 2.4. The DEPFET structure (top) allows charge storage, an amplified readout, and a discharge mechanism. It consists of two field effect transistors: one for signal amplification and readout (bottom, black) and the other for discharging the signal charge (bottom, gray).

*In this paper the basic working principle is described, although the term *DEPFET* is never used.

electrons and serves as storage region. This internal gate is positioned underneath the external gate of the first FET. The conductivity of the first FET, i.e. the conductivity between its source and its drain connection, is influenced by both gates in the same way: the more negative the potentials of the gates, the more holes* are accumulated between source (p-type) and drain (also p-type). At some point,† holes become the majority charge carriers in the FET channel and the formerly p^+np^+ structure becomes p^+pp^+, i.e. conductive.

To measure the signal charge the external gate is set on a constant negative level which must be larger than the threshold voltage‡ of the FET so that inversion takes place. The charge in the internal gate Q_{ig} influences the conductivity between source and drain in a proportional way. For a gate of 5 µm length and a first FET current of $I_{\mathrm{SD}} = 100\,\mu\mathrm{A}$, Wölfel [2007] calculated a first FET gain of

$$g_{\mathrm{q}} = \frac{\Delta I_{\mathrm{SD}}}{Q_{\mathrm{ig}}} \approx 300\,\mathrm{pA/q_e}. \tag{2.1}$$

Here, $\mathrm{q_e}$ is the elementary charge. In the actual configuration, ΔI_{SD} is not measured directly, but with a source-follower readout a constant current source tries to push a constant current I_{SD} through the first FET (FET 1) and the change in the source potential ΔU_{S} that is necessary to drive I_{SD} is measured. With the transconductance§ g_{m} of the FET, it is

$$\Delta U_{\mathrm{S}} = \frac{g_{\mathrm{q}}}{g_{\mathrm{m}}} \cdot \Delta Q_{\mathrm{ig}}. \tag{2.2}$$

For a DEPFET detector similar to the LED, Treis et al. [2006] reported a charge-voltage-gain of $\frac{g_{\mathrm{q}}}{g_{\mathrm{m}}} = 4\,\frac{\mu\mathrm{V}}{\mathrm{q_e}}$. After measuring ΔU_{S} the discharge of the internal gate is achieved with a second FET (FET 2) that builds a channel between the internal gate and the clear contact, the clear channel. Signal electrons from the internal gate drift along this channel to an attractive clear contact. To prevent charge loss through this contact during signal integration it is shielded statically by a p^+-well. The clear channel can be opened and closed dynamically via a clear gate switching structure.

See Table 2.1 for a summary of the gate, clear gate, and clear potentials in their active and inactive state. See also Fig. 2.5 for a pixel readout sequence.

Table 2.1. Applied potentials to operate a DEPFET cell of the LED.

$U_{\mathrm{gate,\,on}}$	$U_{\mathrm{gate,\,off}}$	$U_{\mathrm{clear\ gate,\,on}}$	$U_{\mathrm{clear\ gate,\,off}}$	$U_{\mathrm{clear,\,on}}$	$U_{\mathrm{clear,\,off}}$
-2.5 V	+5.0 V	3.1 V	-2.7 V	+16 V	-0.3 V

* These holes are the minor charge carriers of the n-doped substrate and not the holes generated during photon absorption.

† This is called *inversion*: in an n-doped substrate a region forms that behaves like a p-doped region.

‡ The threshold voltage is the gate voltage at which the FET starts to build a conductive channel between source and drain.

§ The transconductance is the ratio of the output current variation to the input voltage variation.

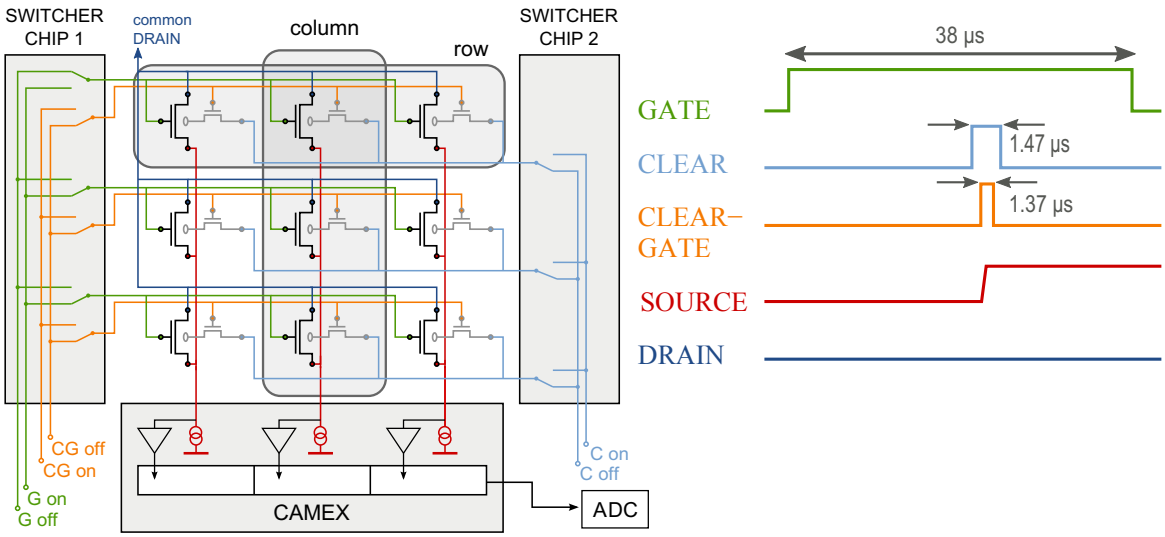

Figure 2.5. Left: a schematic wiring of all gate (G), clear gate (CG), and clear (C) contacts in a 3 x 3 DEPFET pixel matrix. The switching of the individual rows between the active (on) and inactive (off) potentials is achieved via two SWITCHER chips. The CAMEX readout chip is connected column wise to the source contacts of the first FETs. **Right:** readout scheme for one detector row. The drain potential is $U_{\text{drain}} = -5\,\text{V}$. The source potential depends on the charge in the internal gate: $U_{\text{drain}} < U_{\text{source}} < 0\,\text{V}$.

2.3. The DEPFET matrix

To operate the 4096 pixels of the LED with an acceptable effort in readout electronics, the individual DEPFET pixels can be wired in a way that many pixels (one row) can be processed in parallel. Figure 2.5 shows an exemplary wiring of nine pixels in a 3 x 3 matrix. The gate, clear gate, and clear contacts are all wired row wise and can be set to an active and an inactive potential also row wise. The device that controls these potentials, the SWITCHER chip, is presented in Section 2.3.1. The sources of the first FETs are wired column wise to a readout channel of the CAMEX chip, see Section 2.3.2 for more details on the readout chip. All first FET drains are connected to a common drain contact.

This way, a row can be selected with an active gate potential (gate on) while all other rows are switched off (gate off). The current source in each readout channel tries to push I_{SD} through all first FETs in the respective column but is only affected by the pixel of the active row.

After measuring the signal charge, the clear potential is activated and the clear channel is opened shortly after the clear pulse. This prevents charge injection from the clear contact through the clear channel into the bulk material. Even though the clear pulse is following, a fraction of this injected charge can stay in the bulk and distort the following readout. For the same reason (but even more important as no clear pulse is following) the clear channel is closed before the clear is made inactive.

After the readout of one row, the next row can be selected by deactivating the

(external) gate of the actual row and activating the gate of the next row. The next row must not be necessarily the local neighbor. In the *full frame mode* all rows are read out successively up to the end of the detector matrix; then the readout starts again with the first row. Compared to charge coupled devices (CCDs) the readout mode of DEPFETs is much more flexible. In the *window mode*, only the first 16 rows are read out successively. This enhances the time accuracy of the detection from 2.4 ms to 0.6 ms. In principle, the window mode could be focused on a smaller region of the matrix, starting at any row number. Even a readout of several different windows or a *shuffled mode* where a full frame readout is shuffled in between a series of window readouts is possible (but not implemented in the current setup) with this matrix configuration. Compared to CCDs, the advantages of the DEPFET matrix layout are:

- The *in-pixel-amplification* reduces electronic noise effects that are coupling into the detector signal before it reaches the readout chip.
- A reduced readout capacitance allows low noise amplification, see Section 1.3.3.
- No readout artifacts caused by large scale charge transfers, like trapping effects.
- The readout mode is configurable and faster.

2.3.1. SWITCHER chips

Two SWITCHER chips are used to control the electrical potentials of the gate, the clear gate, and the clear structures. The elementary unit of a SWITCHER chip can be represented by a device with two analogue inputs (*hi* and *low*) that are directed to one analogue output (*out*) controlled by its state (on or off), see Fig 2.6. An additional input (*sel*) can select or deselect the elementary unit. If deselected, the unit is in its off state; if selected, it is in its on (On = 1) or off state (On = 0), depending on the On-signal. A polarity signal (*pol*) defines whether the on or off state refers to a hi or low output or vice versa.

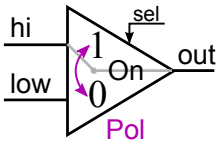

sel	On	state
1	1	on
1	0	off
0	1	off
0	0	off

Figure 2.6. Switcher unit.

The SWITCHER chip consists of a status unit and a switching unit. The main part of the switching unit is the SWITCHER matrix, 128 elementary units arranged in two columns, A and B, and 64 rows. The *hi*, *low*, *pol*, and *On* inputs are connected column wise while the *sel* inputs are connected row wise, see Fig. 2.7. The 64 outputs of each column are each connected to a contact of a DEPFET matrix row. The wiring for SWITCHER 1 and 2 is: A1 → gate contacts, B1 → clear gate contacts, A2 → not used, and B2 → clear contacts. A matrix counter in combination with an address decoder selects one matrix row after another in steps of the XCK signal which is generated by the sequencer (Sect. 2.5.1). The status unit is used to configure the switcher chips in terms of readout direction and signal polarity.

For a window readout mode, the matrix counter can be set to zero with a *reset* signal. A window mode starting at an arbitrary row number is not supported with this version of the SWITCHER chip.

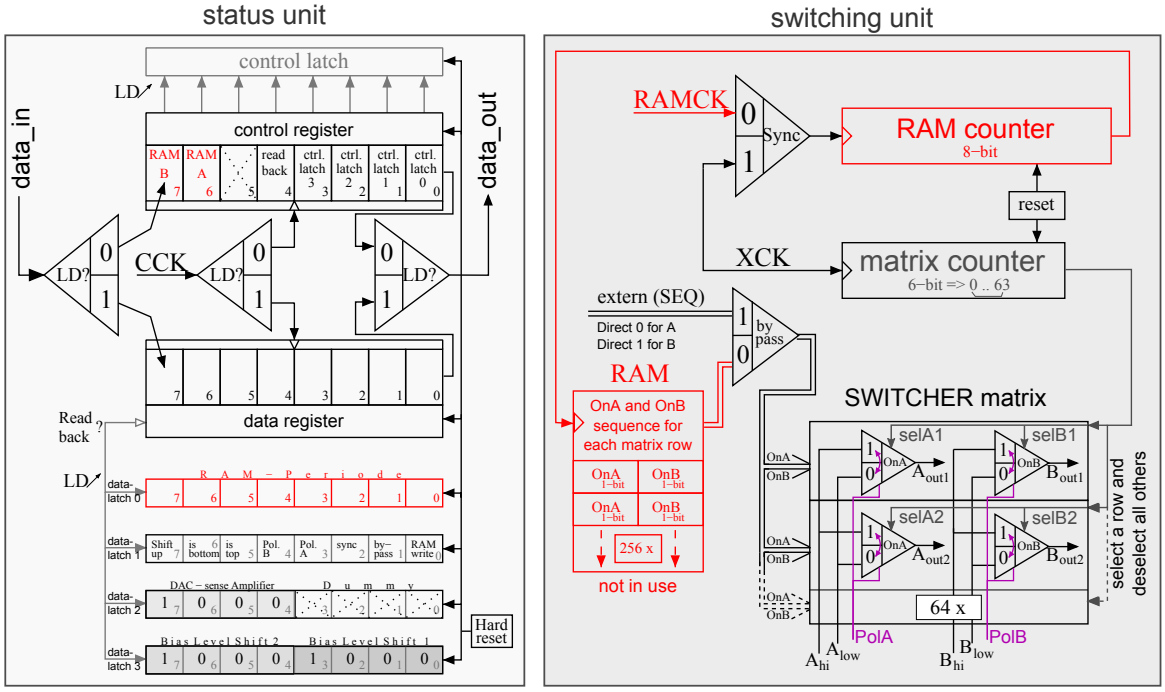

Figure 2.7. The SWITCHER chip consists of two units, a status unit (left) and a switching unit (right). The red colored parts are features not used in the CANDELA configuration.

2.3.2. CAMEX readout chip

The CAMEX (charge amplification and multiplexing) readout chip amplifies the detector signals, performs a correlated double sampling (CDS), and multiplexes the 64 input signals to one single analog-to-digital converter (ADC). The chip consists of 64 readout channels, each connected to the common source contact of a detector column so that a selected detector row (active gate) can be read out in parallel. A block diagram of one readout channel is shown in Fig. 2.8. According to this scheme, the readout sequence can be described in the following way:

1. The **current source** tries to push a constant current through the connected FET and the source voltage is set proportional to the conductivity of the FET which is again proportional to the signal charge in the internal gate.

2. This source potential is directed to a **JFET amplifier** by closing the S_{in} switch. The gain is defined as $g = \frac{C_{in}}{C_{f1}}$ (R_1 opened).

3. The switches S_1 to S_8 are closed and opened successively in the following **CDS filter**. The amplified gain voltage charges the capacitors C_1 to C_8. During this phase the R_2 switch is closed so that the capacitors become charged with respect to $V_{ref\,V}$.

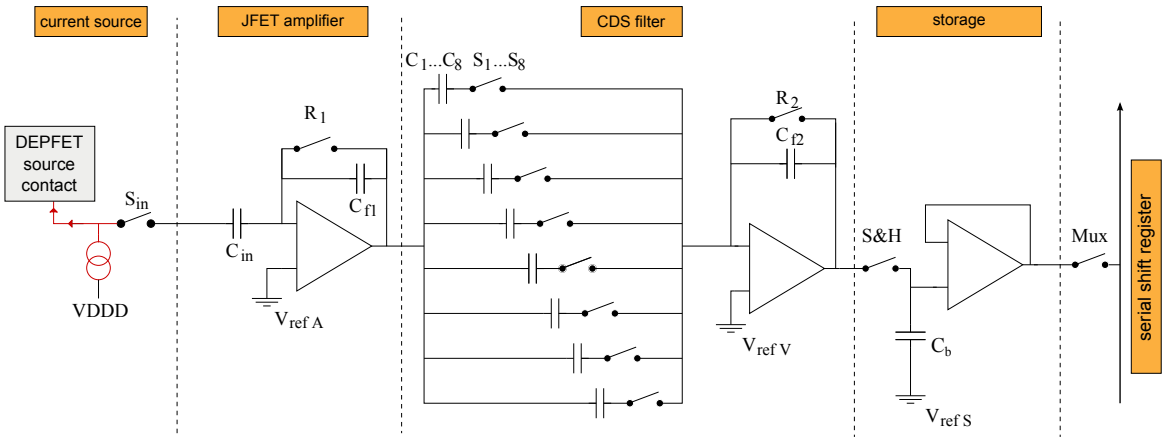

Figure 2.8. Block diagram of one of 64 CAMEX readout channels. Each channel is connected to a detector column. The Mux register serializes the output of all channels to an ADC.

4. S_{in} is opened and the detector is decoupled from the readout chip. The **clear process** of the DEPFET row starts.
5. After the clear process has finished, a **reference signal** of the DEPFET pixel with an empty internal gate is recorded in the same way with the difference, that R_2 is now open. The difference between the signal voltage which is still buffered in C_1 to C_8 and the incoming reference potential charges the capacitor C_{f2}. This **eight-fold correlated double sampling** reduces statistical fluctuations due to its eight-fold sampling and enhances the signal accuracy, as only the differences between the signals and the baseline signals are measured.
6. By closing the S&H switch the signal is transferred to another capacitor C_b which serves as a **buffer**. A following impedance converter sends the signal to an ADC when the Mux switch of the corresponding readout channel is closed.

This sequence, the opening and closing of the switches S_{in}, S_1 to S_8, R_1, R_2, and S&H, is defined by a CAMEX internal control register. Four different gain modes and a test mode operation can be controlled with an on-chip status register.

Misfits

A photon entering a pixel during the readout process results in a corrupted pulse height.

- If a photon enters before the clear process is executed but after the CDS has started, its energy is measured too low, as some empty samples are averaged with some samples including the event. Such events enhance the low energy background.
- If a photon hits a pixel after the clear process but before the CDS is completed, the measured pulse height becomes negative. These events which are named *misfits*, can be easily distinguished from "true" events by their energy value and will be rejected during data analysis.

2.4. Analog-to-digital conversion

Digitization is done with the analog-to-digital converter (ADC) *AD6645* from ANALOG DEVICES. This ADC converts an analogue differential input signal into a parallel, 14 bit digital output signal with a possible conversion rate between 30 MSPS* and 80 MSPS. The conversion starts with each ADC clock cycle ($\mathrm{clk_{ADC}}$) automatically. The pipeline based conversion takes about 3.5 clock cycles to be finished and is indicated by the ADC with a *data_ready* signal.

Adjustment stage

The CAMEX output signal has a common mode of about 1.4 V with an offset of 0.2 V and a voltage range of roughly ±0.8 V, see Fig. 2.9 for a visualization. The ADC input is centered at 2.4 V with a maximal voltage swing of ±0.55 V. An adjustment stage similar to Fig. 2.9 is used to shift the CAMEX output signal into the input range of the ADC so that almost the total 14 bit resolution can be used.

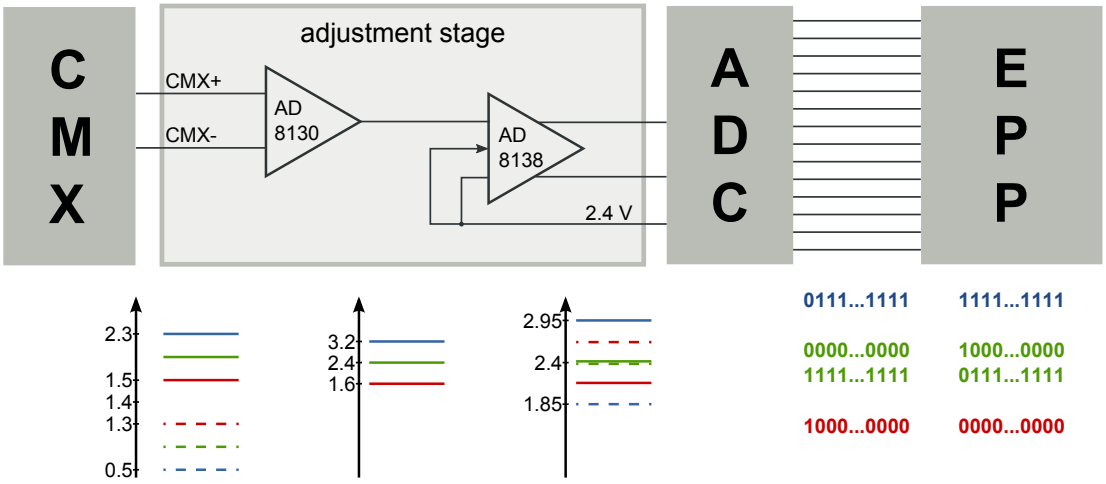

Figure 2.9. Scheme of the signal digitization for a zero (red), mid-range (green), and maximal detector signal (blue). The positive parts of differential signals are printed with bold lines, while the negative parts are printed with dashed lines. All CAMEX (CMX) signals are centered around a common-mode voltage of 1.4 V with an offset of 0.2 V. The AD8130 converts the differential signal to a single ended one in a way that a mid-range signal is centered at 2.4 V. As the negative input of the following differential-to-differential amplifier AD8138 is also put on this potential, a mid-range detector signal leaves the adjustment stage as a differential signal at 2.4 V with zero amplitude. The ADC number representation of this zero is coded as two's complement. Detector signals with lower (higher) energies are coded negative (positive). The amplification of the AD8138 is adjusted to match the 0.55 V input range of the ADC. The event preprocessor (EPP, see Sect. 2.5.2) flips the most significant bit to convert the two's complement representation into an unsigned 14 bit value which can be processed further.

*MSPS = mega samples per second.

It is important to recognize that the gain level of the CAMEX* g_{cmx} and the gain of the adjustment stage g_{adj} are acting in two different ways. The CAMEX gain defines a maximal energy $E_{\mathrm{max}}(g_{\mathrm{cmx}})$ that can be detected and assigns it to a signal with the maximal CAMEX output voltage. The adjustment stage matches the CAMEX output range to the ADC input range. Increasing the CAMEX gain cuts the energy spectrum at $E_{\mathrm{max}}(g_{\mathrm{cmx}})$ and enhances the energy resolution below this cutoff energy as the signals get more amplified. If the gain of the adjustment stage is set too high, it cuts the high energy part of the spectrum as well, but the resolution at lower energies increases only slightly as a result of a decreased digitization noise† and not caused by an increased amplification. If g_{adj} is too low, the digitization noise is higher than necessary, as the full 14 bit resolution is not used. See Fig. 2.10 for a schematic representation of the interaction between CAMEX, adjustment stage, and ADC.

The ideal case of an adjustment stage that perfectly matches the ADC input cannot be realized, as gain variations of different CAMEX channels result in different $E_{\mathrm{max}}(g_{\mathrm{cmx}})$ as well.

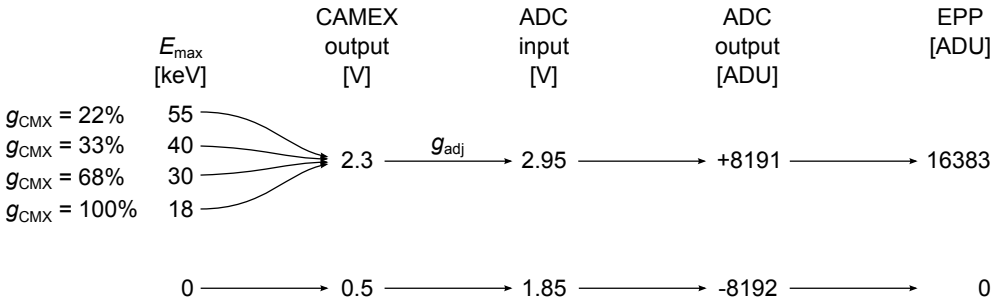

Figure 2.10. Interaction between CAMEX, adjustment stage, and ADC. The CAMEX gain level g_{CMX} assigns a maximal measurable input energy E_{max} to the maximal CAMEX output level. The gain of the adjustment stage shifts the CAMEX output range to match the ADC input range. The signed ADC output is converted to an unsigned value within the EPP.

2.5. D3C: a detector readout- and control electronics

The digital camera controller chip (D3C) consists of a detector configuration and operation unit (SEQ), a data preprocessing unit (EPP), and a SpaceWire command interface (IFC). See Fig. 2.16 for a schematic representation of these units with their internal and external connections between each other and to other parts of the LED system. All three units are combined into a *VIRTEX-4* field-programmable gate array (FPGA) from *XILINX* that runs with a system frequency of 100 MHz. The three subunits are explained in the next three sections.

* There are four internal gain stages, that can be set by the status register.

† The digitization noise describes the error that is made if a continuous signal is put in discrete bins. It is the roughness that occurs by approximating a continuous function with a step function.

2.5.1. Sequencer SEQ

The sequencer (SEQ) configures the SWITCHER chips and the CAMEX chip, i.e. it writes the status registers of the two SWITCHER chips and the control and the status register of the CAMEX chip. This initialization is done during each start up of the LED. For detector operation, the SEQ controls the following signals (see also Fig. 2.11):

- **SWITCHER signals:** the digital gate (*1DIR1*), clear gate (*1DIR0*), and clear signals (*2DIR1*,) of the SEQ are transformed to the analogue gate, clear gate, and clear potentials within the SWITCHER chips. The *XCK* signal of the SEQ increments the matrix counter which selects the actual detector row for readout. See Sect. 2.3.1 for more details.
- **CAMEX signals:** the *SCLK* signal of the SEQ loops through the CAMEX control register and controls the readout sequence. The *MUX_IN* signal initiates the output of the first CAMEX channel by setting the first bit of the Mux register. The *MUX_CLK* signal increments the Mux register by one which selects the next, neighboring CAMEX channel. See Sect. 2.3.2 for more details.
- **ADC signals:** a fast *PIX_CLK* signal of the SEQ clocks the ADC. The selected ADC requires no further signal for operation. See Sect. 2.4 for more details.
- **EPP signals:** the *PIXEL_CLK* signal of the SEQ indicates that a new pixel value is ready to be processed by the EPP (Sect. 2.5.2). In the current configuration the signal is much slower than the conversion rate of the ADC (defined by *PIX_CLK*). The difference results from the minimal ADC conversion rate of 30 MHz which is considerably higher than the current pixel readout frequency of approximately 1.68 MHz.

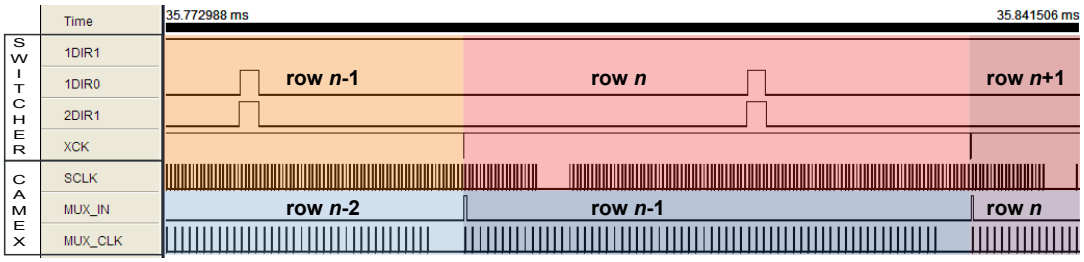

Figure 2.11. SEQ-signals for the LED operation sequence of two detector rows. The gate signal (1DIR1) is constantly high, as it is not switched off during the readout of one row. XCK switches to the next row and defines the operation time interval (reddish) for one row. See also Fig. 2.5 for a detailed view on the gate, clear gate and clear signals (be aware that Fig. 2.5 shows a switched gate signal, as it focuses on the readout of one row). The processed output signals of the CAMEX are buffered in the sample and hold stage, so that the next row can be processed, while the actual row is multiplexed to the ADC (light blue).

2.5.2. Event preprocessor EPP

A frequent continuous readout of a pixelated detector results in a large amount of recorded data. In the current, moderately fast configuration of the LED the data rate R_{data} is

$$R_{\text{data}} = 410\,\frac{\text{frames}}{\text{s}} \cdot 4096\,\frac{\text{pixels}}{\text{frame}} \cdot 14\,\frac{\text{bit}}{\text{pixel}} \approx 23.5\,\text{Mbit/s}. \tag{2.3}$$

Comparing R_{data} with the maximal downlink rate R_{dl} of currently operating X-ray satellites like XMM-Newton ($R_{\text{dl}} = 69.4\,\text{kbit/s}$) or CHANDRA ($R_{\text{dl}} = 1024\text{kbit/s}$) reveals that an on-board data preprocessing is unavoidable for satellites with fast detectors that are operated in a continuous readout mode. A considerable data reduction can be achieved by event building: on average, only a few pixels in a detector frame that is frequently read out are hit by a photon. The majority of the pixels are not hit by any photon. In the following, these pixels are named *empty* pixels, while the pixels hit by a photon are named *events*. Be aware, that events can consist of more than one pixel due to charge sharing, see Sect. 1.3.1.

The amount of data can be reduced by transmitting events and rejecting empty pixels. The data reduction capability can be estimated with the input output ratio $\lambda = R_{\text{in}}/R_{\text{out}}$ introduced in Eq. (1.32). The probability for empty pixels

$$P_{\text{e}} = \text{e}^{-\frac{R_{\text{in}}}{R_{\text{out}}}} \tag{2.4}$$

equals the data reduction capability.* The probability for pile-up

$$P_{\text{pu}} = 1 - \text{e}^{-\frac{R_{\text{in}}}{R_{\text{out}}}} - \frac{R_{\text{in}}}{R_{\text{out}}} \cdot \text{e}^{-\frac{R_{\text{in}}}{R_{\text{out}}}} \tag{2.5}$$

shows that the data reduction is efficient in the case of unlikely pile-up, see Fig. 2.12.

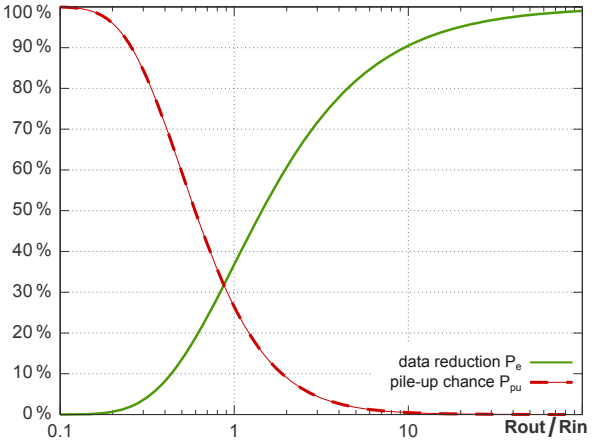

Figure 2.12. Pile-up chance and data reduction capability due to event building as function of the output rate R_{out} in terms of the input rate R_{in}. The data reduction and the pile-up chance are calculated according to Eq. (2.4) and Eq. (2.5). At $R_{\text{out}} = 10\,R_{\text{in}}$ ($\lambda = 0.1$), the pile-up chance is $P_{\text{pu}} \approx 0.47\,\%$ and the data reduction is $P_{\text{e}} \approx 90.5\,\%$.

For the LED, event building is realized through a fast, FPGA based event preprocessor (EPP) [Schanz et al., 2009] that is capable to process one detector row within 2 µs. This fast processing is achieved by a data processing structure which follows a pipeline design, see Fig. 2.13. The output of a detector system operating in a continuous readout mode followed by a subsequent event building is similar to a system operating in a triggered readout mode. In the same way as the triggered readout needs one or several trigger criteria, the EPP event building is based on criteria to distinguish between an empty pixel and an event:

* The difference between the event size (64 bit) and the size of a pixel pulse height (14 bit) is neglected.

- **Energy range:** The detected energy must exceed a low energy threshold E_{erg}. This is the main criterion for data reduction as all empty pixels and all misfits are rejected. The choice of E_{erg} is critical, as if it is chosen too low, noise enters the system and the data reduction gets less efficient. If E_{erg} is chosen too high, the spectrum is cut off at its low energetic end and parts of split events can get lost. To reduce the latter effect, a neighbor threshold $E_{\mathrm{nbr}} < E_{\mathrm{erg}}$ is introduced. If the signal of a pixel exceeds the energy threshold, the signals of all neighboring pixels are compared to E_{nbr} and not to E_{erg}.

  Pixel individual fluctuations due to noise or design related* differences require that both, E_{erg} and E_{nbr} must be applied pixel individually. The arrays that store these values are named *energy-threshold map* and *neighbor-threshold map*.

  An optional high energy threshold E_{MIP} enables to reject events that are most likely not a result of photon interactions but of interactions with charged particles. These minimal ionizing particles (MIPs) are, most likely, not stopped within the detector, but enter and leave it and deposit energy along their track. The stopping power can be approximated with [Amsler, 2007, Eq. (357)]

$$\frac{\mathrm{d}E}{\mathrm{d}x} = 2\,\frac{\mathrm{MeV/cm}}{\mathrm{g/cm^{-3}}} \cdot \rho \tag{2.6}$$

  which equals approximately 400 keV/mm for silicon. So, LED pixels which are affected by MIPs have most likely a saturated output signal and can be rejected with a high energy threshold that is set slightly below† the maximal output signal. All neighbors of a MIP trace are rejected as well, as they are possibly affected by charge sharing.

- **Pattern recognition:** as only the four split types of Fig. 1.20 are a possible result of a photon interaction, all events with different patterns can be rejected. The pattern recognition algorithm is optimized for fast operation with the trade-off that it does not reject illegal diagonal splits. This must be done subsequently with the offline data analysis. The pattern recognition is also necessary to apply the neighbor threshold and to find legal split events. The summation of the split parts is postponed to the offline analysis, as the loss of information coming from an EPP internal pattern summation, is not in relation to the data reduction.

- **Bad map:** some of the LED pixels are not responding to radiation (*cold pixels*) or give signals even without incoming radiation (*hot pixels*). Especially hot pixels that match the energy criteria can result in a large data rate. These pixels can be marked as bad pixels which are not further processed. The information is stored in the bad map inside the EPP, see Fig. 2.13. Within the EPP, neighbors of bad pixels are treated as legal pixels, but they receive a special treatment in the offline analysis, see Sect. 2.7.3.

* Each DEPFET pixel has its own preamplifier within the pixel.

† E_{MIP} is a global threshold for all pixels. The maximal output signal of different pixels differs due to variations of the internal pixel FETs and due to variations of different CAMEX channels.

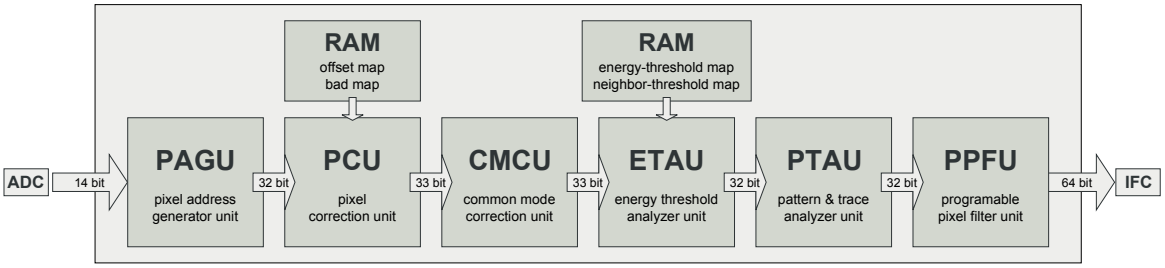

Figure 2.13. The EPP pipeline structure: in the PAGU each digitized signal is attributed an x- and y-coordinate according to its position in the data stream. The PCU subtracts the offset and can flag pixels as "bad". The CMCU calculates and subtracts the common mode. The energy range is checked in the ETAU according to the energy-threshold and neighbor-threshold map. The pattern distribution of valid events are finally checked in the PTAU. During the pipeline processing events are not rejected but flagged as valid or invalid. The PPFU filters all events according to these flags.

Besides the event building, the EPP must also perform some corrections that can only be done or that must be done at this early stage of data processing:

- **Offset correction:** a pixel individual offset value, stored in the *offset map*, is subtracted from the raw data. The offset correction cannot be postponed to the offline analysis because of the following common-mode correction.
- **Common-mode correction:** small variations in the supply voltage of the CAMEX chip result in measurable variations of the bias level in all CAMEX channels. As one detector row is processed in parallel, the common mode can be calculated as the median of the offset subtracted detector row, assuming that more than half of all pixels of this row are empty pixels. After calculating the common mode, it is subtracted from each pixel of the row, see Fig. 2.14. The common-mode calculation and correction must be done for each row separately.

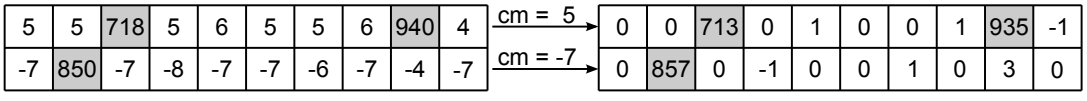

Figure 2.14. Common-mode correction for two rows with 10 pixels each. After the offset subtraction (not shown), the energies of empty pixels are distributed around zero superimposed with the common mode (cm) (left). The cm is calculated as median of each row and subtracted from each pixel of the row (right). Events are shown in gray.

- Additional **event information** is added. As the continuous data stream is disrupted by event building, each event gets a time-stamp (t_sec and t_subsec) and its x- and y-coordinate (xpos and ypos). Together with the event energy (erg) and several flags (f) used for internal event processing, the EPP output is:

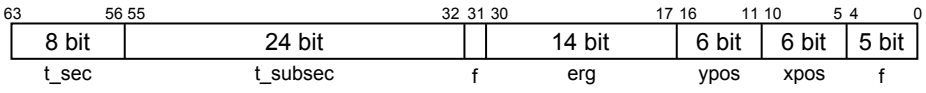

(2.7)

Bypass mode

In addition to the event building mode, the EPP can be set into a bypass mode in which all pixel signals are transmitted unprocessed. This allows to study the statistical properties—mainly the offset and the noise distribution (see also Sect. 2.6 and 2.7)—of empty pixels which are rejected in a normal operation mode. Because of the additional time, position, and flag information, the data rate is even larger than calculated with Eq. (2.3) and cannot be transmitted to the PC. To ensure a data structure consisting of complete frames, the D3C buffers eight full detector frames (4096 pixel each), waits until these frames are completely transmitted, and starts to fill the buffer again as soon as the first pixel of a new frame is processed. In bypass mode, 97 % of the data are lost during these waiting and transmitting states; the effective frame rate is about 12 frames per second.

2.5.3. Interface controller IFC

The interface controller (IFC) provides the SpaceWire interface of the LED system to a personal computer which represents a spacecraft command unit, see Section 1.4.3. All commands necessary for detector operation are stored in batch files, see Tab. 2.2.

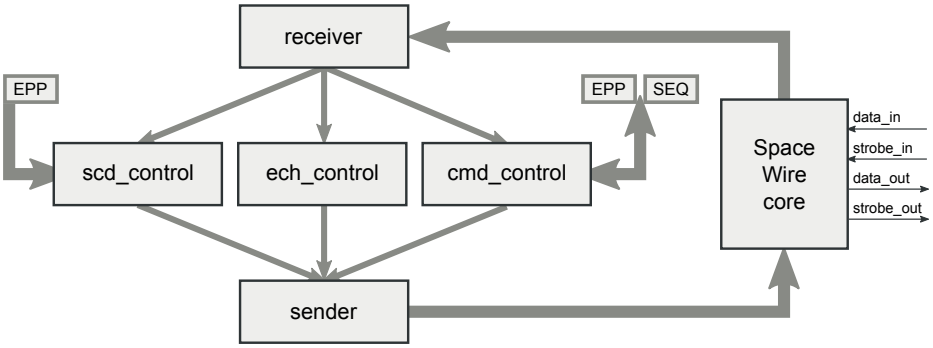

Figure 2.15. The IFC: the SpaceWire core encodes the SpaceWire stream. The receiver reads the address of the packets and directs the data or commands to the science (scd) control unit, the echo (ech) control unit, or the command (cmd) control unit. The scd control unit reads the EPP data output, the cmd control unit sends/receives commands and data to/from the SEQ and the EPP via an SPI connection.

The open source *SpaceWire light* core* from *OpenCores* is used as SpaceWire encoder-decoder. As the SpaceWire communication is packet oriented, the IFC has to unwrap incoming packets in a *receiver* unit and wrap new packets in a *sender* unit. All packets consist of three parts: an address byte indicating where the data are going to or coming from, the data (arbitrary length), and an end-of-packet (0x100) or an error-end-of-packet (0x101). The IFC has three sources of data: scientific data from the LED in the format of Scheme (2.7) (address = 0x35). Register data from the D3C: all registers (offset-, energy-threshold, neighbor-threshold maps, CAMEX status and

* Version 20110709; `http://opencores.org/project,spacewire_light`.

control register, SWITCHER status register) are readable (address = 0x34). In an 'echo-modus' data received via SpaceWire can be transmitted back to the PC. This modus is used to diagnose SpaceWire communication (address = 0x20). Figure 2.16 shows all mentioned parts of the LED system and their interconnections.

Table 2.2. LED operation commands: the necessary operation commands are shown approximately in the order of application. Additional commands are used to read the status of the setup and to debug the system.

command name	meaning
w_cmx_status	write the status register of the CAMEX chip to the SEQ
w_cmx_memo	write the control register of the CAMEX chip to the SEQ
w_cmx_upload	the SEQ writes the CAMEX control and status register
w_sw_status	write the SWITCHER status register to the SEQ
w_sw_hreset	hard reset for the SWITCHER chip: clear all registers
w_sw_upload	the SEQ writes the SWITCHER status register
w_sw_reset	reset the matrix counter of the SWITCHER chip
w_epp_bypass	set the EPP in bypass mode
w_xxx_map	upload a new EPP offset map (xxx = date of measurement)
w_xxx_nmap	upload a new EPP neighbor-threshold map (xxx = date)
w_xxx_emap	upload a new EPP energy-threshold map (xxx = date)
w_epp_not-byp	sets the EPP in full processing mode
w_epp_run	start the operation of the EPP
w_seq_run	start the operation of the SEQ
w_seq_stdby	stop the operation of the SEQ
w_ifc_re_ns	set a permanent read command to the IFC (recording data)

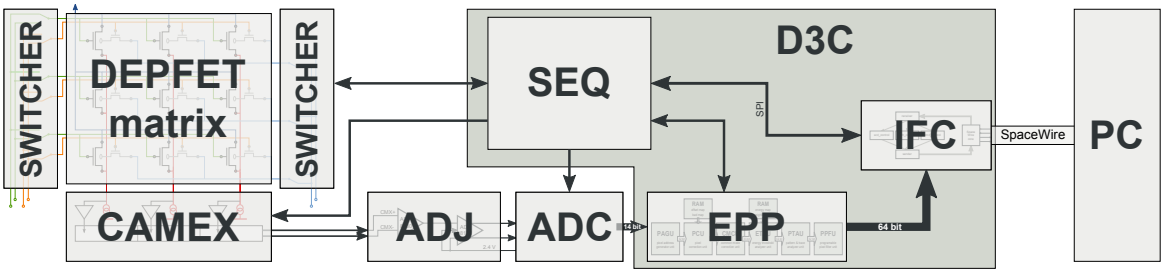

Figure 2.16. The LED system consists of the **detector hybrid** (DEPFET matrix § 2.3, SWITCHER controller chips § 2.3.1, and CAMEX readout chip § 2.3.2), the **digitization unit** (adjustment stage *ADJ* and *ADC* § 2.4), and the **D3C** (SEQ § 2.5.1, EPP § 2.5.2, and IFC § 2.5.3).

2.6. LED operation

In order to operate the LED a distinct sequence of steps (illustrated in Fig. 2.17) has to be performed. Evacuating the vacuum vessel takes between several hours and one day depending on the cleanliness of all objects inside the vacuum vessel. At a pressure below 10^{-2} mbar the cooling can be started without any risk of condensation, see again Fig. 1.30. Cooling all relevant parts of the system takes approximately three hours.

The operation of the detector requires several different voltage levels to be set in the correct order, see Appendix B for the complete power up sequence. First, the CAMEX is switched on and its status and control registers are updated. Then a similar procedure is executed for the SWITCHER chips. After starting the EPP (bypass mode) and the SEQ, the detector matrix voltages (active and inactive gate, clear gate, and clear potentials) can be adjusted. As the SWITCHER and the CAMEX chips are heating the detector matrix, it takes minimum one hour to establish a constant detector temperature, see Fig. 2.39 for measurements of the temperature influenced LED offset and noise drift during the first five hours of operation.

When the system is in thermal equilibrium, approximately 200 dark frames, i.e. measurements without detector irradiation, are recorded. These full frame, dark images are used to create the *offset*, *energy-threshold*, and *neighbor-threshold maps* offline, see Sect. 2.7. A preliminary *bad1 map* consisting of noisy and hot pixels will be constructed as well. After uploading these maps to the EPP and setting the EPP in its normal operation mode, the LED is irradiated homogeneously with a radioactive source (flat-field measurement) to find cold pixels. A *bad2 map* consisting of hot, cold, and noisy pixels is created and uploaded to the EPP. From now on, the LED system is ready for scientific measurements.

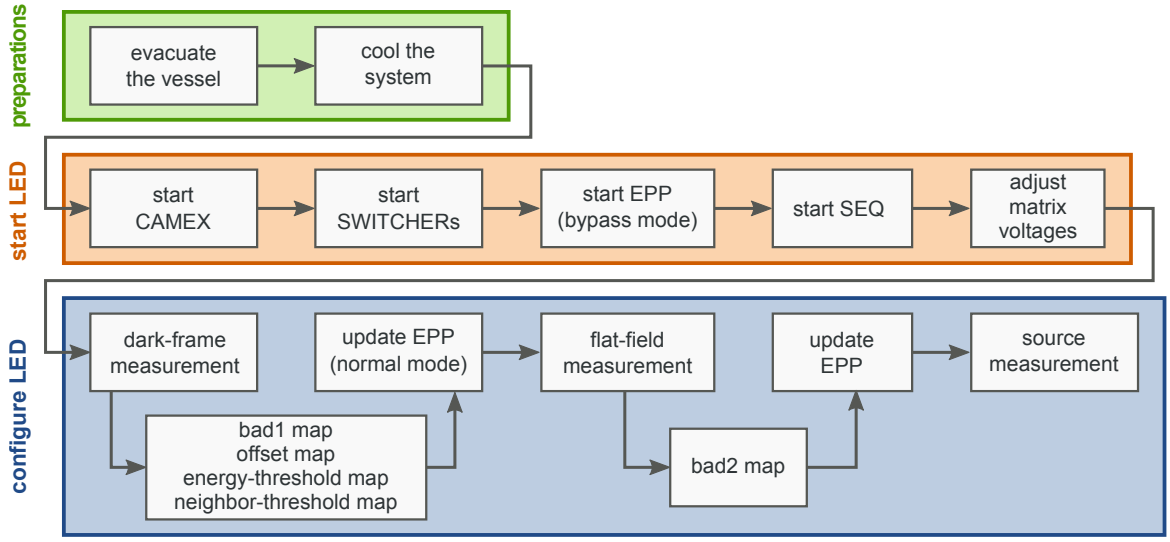

Figure 2.17. Summary of the different steps that are necessary to operate the LED. After detector cooling, the LED can be powered on and the different EPP lookup tables can be calculated with dark-frame and flat-field measurements.

2.7. Offline data analysis

The data recorded by the Idef-X software are stored in binary files (extension: *.tm) of 2 MB size each and are concatenated using the operating system command `copy`*. The LED data are stored in data packets consisting of

- 1 byte address of the packet: 0x35 indicates LED data.
- 8 byte EPP data packet according to Scheme (2.7).
- 1 byte + 1 bit: the additional bit indicates the end of the packet: 0x100.

Analyzing LED data means effectively analyzing the data of 4096 detectors, as each pixel has its own preamplifier unit, the pixel internal MOSFET. Making use of a pixel individual analysis is a key concept of all following steps which can be divided in three units: the analysis of dark-frame measurements, of flat-field measurements, and of scientific observations.

2.7.1. Analyzing dark-frame measurements

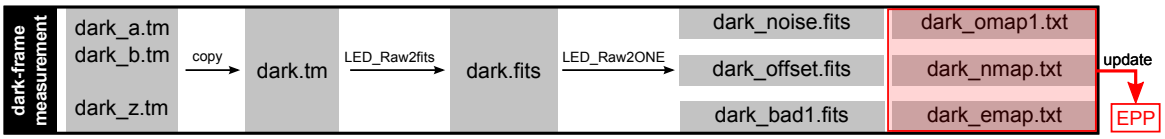

Figure 2.18. LED offline data analysis of dark frames: the recorded dark frames dark_a.tm - dark_z.tm are concatenated to dark.tm and converted into the fits format. LED_Raw2ONE generates the offset, noise, and bad1 map. Batch instruction files (ending *.txt) which update the offset, the energy-threshold, and the neighbor-threshold lookup tables of the EPP are created as well.

Dark frame measurements are used to determine the offset and the noise of each pixel, i.e. the offset map and the noise map. The EPP uses the offset map to process a bias free signal via offset subtraction. The noise map is used to conclude on the energy-threshold and neighbor-threshold maps. In order to measure dark frames, all radioactive sources inside the vacuum vessel have to be closed and the event preprocessing must be bypassed. In this *EPP bypass-mode* all detector pixels are processed.

The initial binary data format of the dark frames is converted into the fits-image format by the program `LED_Raw2fits`. Further on, another program, `LED_Raw2ONE`, then generates an offset, a noise, and a bad map according to the procedures described in the following paragraph. All dark frames are filtered for MIP events via an upper threshold and only the frames without MIP events, called good frames, are considered for the following calculations.

* For a Windows operating system, this is: `copy \b *.tm name.tm`. The terms *dark*, *flat*, or *data* are used to name the resulting output file.

Let f be the frame index ($1 \leq f \leq N$) with N equal to the number of good frames, i the pixel index ($0 \leq i \leq 4095$), and $pha_{f,i}$ the pulse height signal of pixel i in frame f. The **offset map** *offset* is calculated as pixel individual average of all frames N

$$offset_i = \frac{\sum_{f=1}^{N} pha_{f,i}}{N}. \tag{2.8}$$

A common-mode correction is not necessary for the offset-map creation, because the common mode is averaged out if N is chosen sufficiently large ($N > 100$). After the pixel individual offset is subtracted, the pulse heights of each pixel fluctuate around $PHA = 0\,\mathrm{ADU}$ with a Gaussian distribution. The **noise map** *noise* is calculated as the pixel individual root mean square variation of the offset subtracted pixel values

$$noise_i = \sqrt{\frac{\sum_{f=1}^{N} \Big(CM(pha_{f,i} - offset_i)\Big)^2}{N}}. \tag{2.9}$$

Here, $CM(...)$ indicates the common-mode correction. See Fig. 2.19 for a representative example of an offset and noise map.

The creation of the **bad1 map** is an iterative process. A pixel is declared as a *bad pixel* if its offset and noise values are outside of a tolerated offset and noise range. These so-called *bad limits* ($\mathrm{offset}_{\mathrm{min}}$, $\mathrm{offset}_{\mathrm{max}}$, $\mathrm{noise}_{\mathrm{min}}$, $\mathrm{noise}_{\mathrm{max}}$) are chosen on the basis of the offset and noise maps. The bad map is constructed with `LED_Raw2ONE` in combination with the bad limits which are passed as program arguments. Figure 2.21 shows the bad map constructed on the basis of the offset and noise maps of Fig. 2.19.

In addition to the fits formatted offset, noise, and bad maps, `LED_Raw2ONE` creates also ASCII based batch files. These instruction files are used to upload the **offset, neighbor-threshold, and energy-threshold lookup tables** of the EPP. Each of these lookup tables is 16 bit wide; the 14 bit offset values and the bad flags are joined to one lookup table, the `dark_omap.txt`. Bits 0 to 13 contain the offset values, bit 14 is not used and bit 15 represents the bad flag of the corresponding pixel. The energy-threshold map `dark_emap.txt` is calculated as a multiple m_{e} of the noise map

$$energy_i = m_{\mathrm{e}} \cdot noise_i. \tag{2.10}$$

The neighbor-threshold map `dark_nmap.txt` is calculated as a multiple m_{n} of the noise map

$$neighbor_i = m_{\mathrm{n}} \cdot noise_i. \tag{2.11}$$

The noise values calculated according to Eq. (2.9) are identical to the Gaussian standard deviations σ, assuming a Gaussian distribution. With the default values $m_{\mathrm{e}} = 5$ and $m_{\mathrm{n}} = 4$, the probability to detect an event falsely due to noise is less than

$$P_{\mathrm{E}} \leq 5.8 \cdot 10^{-7} \tag{2.12}$$

and the probability to detect a split event falsely due to noise is less than

$$P_{\mathrm{N}} \leq 6.4 \cdot 10^{-5}. \tag{2.13}$$

Both, m_{e} and m_{n} are call parameters of `LED_Raw2ONE`.

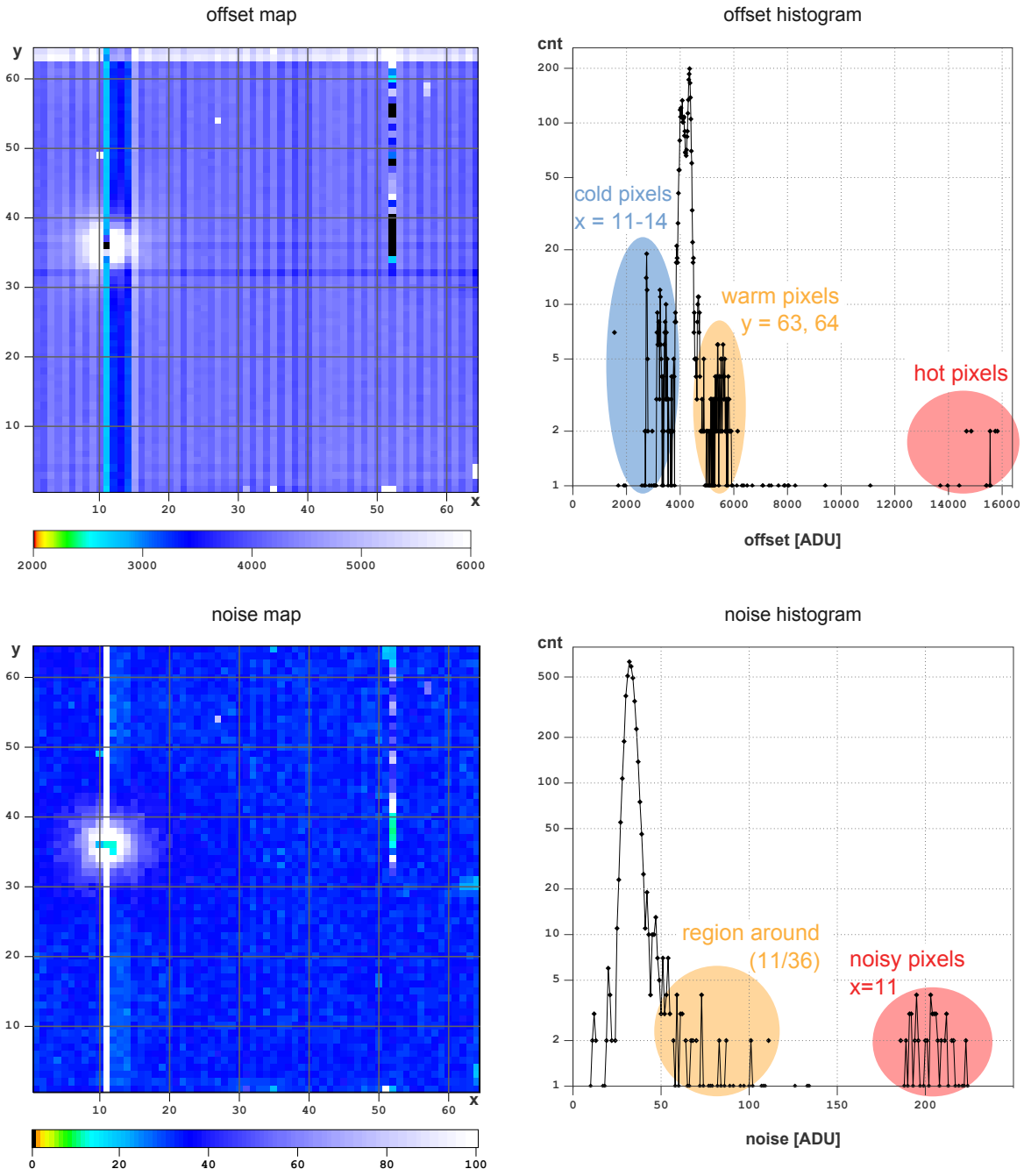

Figure 2.19. Offset and noise maps (left) and their distributions (right). A manufacturing defect at pixel (11/36) causes a detector malfunction within a region of about 4 pixels radius and in the complete 11th column. See also the corresponding bad map1 in Fig. 2.21. The measurement is done with the gain mode $g_{\mathrm{cmx}} = 62\,\%$.
Top: offset map with offset distribution. The offset shows a column-wise variation due to the different CAMEX readout channels. The columns 11-14 have an unusual low offset (not *cold* but *cool* pixels), while the pixel offsets of the rows 63 and 64 are higher than average (warm pixels); hot pixels are located around the pixel (11/36).
Bottom: noise map with noise distribution. The noise map clearly shows the distribution of noisy pixels (white). The noise distribution peaks at 32 ADU. The noisy pixels have a noise value of about 200 ADU.

2.7.2. Analyzing flat-field measurements

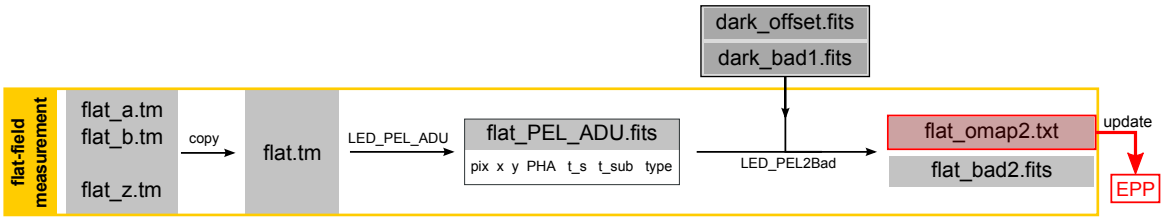

Figure 2.20. LED offline data analysis of a flat field measurement: the recorded flat fields flat_a.tm - flat_z.tm are concatenated to flat.tm. LED_PEL_ADU generates a pixel event list in a fits-table format. LED_PEL2Bad identifies cold pixels and hot pixels of type 2 and updates the bad map. The dark_offset.fits and dark_bad1.fits files were created in the previous dark-frame analysis. The batch instruction file flat_omap2.txt is updated with the new bad map.

After the offset, neighbor-threshold, and energy-threshold lookup tables are updated and the EPP mode is switched from its bypass to the normal operation mode, event preprocessed data are no longer frame based, but event based which means that only those pixels are processed that are associated with a photon event. See Sect. 2.7.3 for more information on the data structure of pixel events. A flat field measurement, i.e. a homogeneous irradiation of the whole detector, is used to identify pixels with a unusual low count rate which are called cold pixels.

With dark frame measurements, a preliminary bad map `dark_bad1` consisting of hot and noisy pixels has already been constructed in Sect. 2.7.1. Figure 2.21 shows the bad map constructed from the same measurement as shown in Fig. 2.19. The corrupt pixel at position (11/36) passed all offset and noise limits. Cold pixels like this can be identified by irradiating the LED homogeneously and creating a hit map. A hit map is a two dimensional histogram of a pixel event list showing the number of events over the x- and the y-positions on the detector. Pixels with count rates that lie far outside of the statistical fluctuations can then be identified as cold or hot pixels. The left part of Fig. 2.22 shows an LED hit map for a homogeneous detector irradiation with Fe-55 and Am-241. Prior to that measurement, the EPP was updated with the offset, energy-threshold, neighbor-threshold, and bad maps of Fig. 2.19 and 2.21.

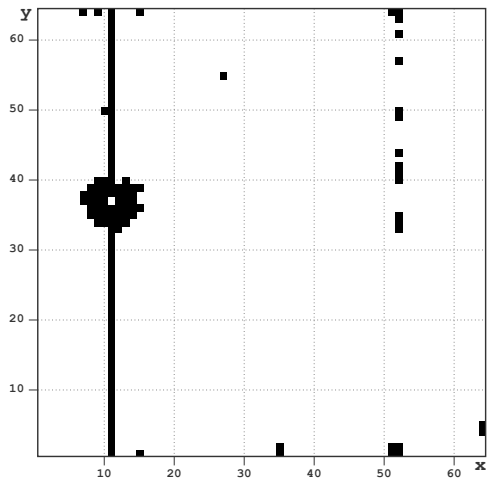

Figure 2.21. Bad-map (bad pixels are black) constructed with the offset and noise map of Fig. 2.19 with the limits (in ADU): $\text{offset}_{\text{min}} = 1500$, $\text{offset}_{\text{max}} = 6500$, $\text{noise}_{\text{min}} = 10$, $\text{noise}_{\text{max}} = 100$.

`LED_PEL2Bad` takes a pixel event list as input and calculates the pixel individual hits N_i and the average counts per pixel N_{avg}. i is the pixel index ($0 \leq i \leq 4095$). All pixels with

$$N_{\text{avg}} - s_1 \sqrt{N_{\text{avg}}} < N_i < N_{\text{avg}} + s_2 \sqrt{N_{\text{avg}}} \tag{2.14}$$

are considered to be good pixels; all others are identified as bad pixels and added to the bad map. The confidence intervals can be adjusted with the parameters s_1 and s_2. Typically $s_1 = s_2 = 7$ is chosen. The filter according to Eq. (2.14) is implemented with an additional check for hot pixels as some pixels that appear normal in dark frame measurements show an unusual high count rate in irradiated measurements. To distinguish the different types of hot pixels, hot pixels observed with dark frames are in the following classified as type 1 while hot pixels observed with irradiated measurements are labeled as type 2. `LED_PEL2Bad` identifies bad pixels according to Eq. (2.14) and adds them to the preliminary bad1 map `dark_bad1.fits` to generate the final bad map `flat_bad2.fits` (center of Fig. 2.22). As the bad flag is written into the EPP offset map, the original `dark_offset.fits` is also needed as input to create the final EPP batch command file `dark_omap2.txt`.

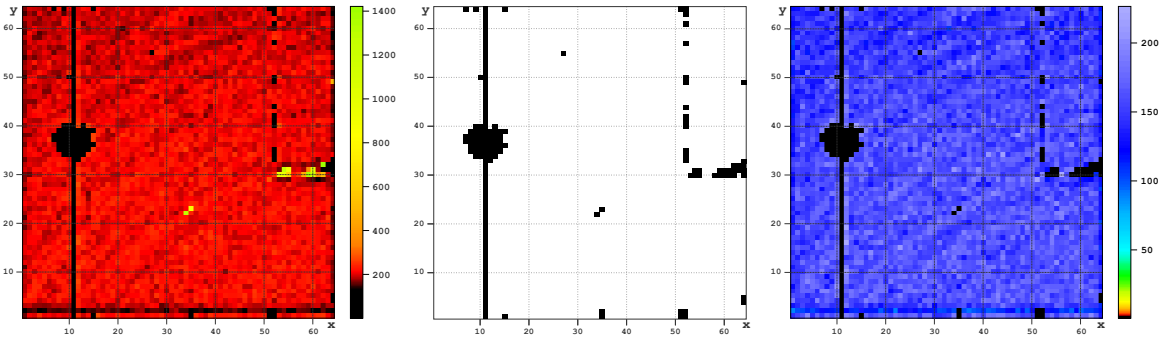

Figure 2.22. Left: hit map for a one minute flat-field measurement with Fe-55. A cold pixel at (11/36) and 7 others around (64/31) can be identified because of their low event counts. Hot pixels of type 2 are visible in yellow (> 500 hits): one at (64/49), two around (34/22), and 13 around (59/30). Compare also with the bad1 map in Fig. 2.21. **Center:** bad2 map including hot pixels (type 1 + 2), cold pixels, and noisy pixels. **Right:**. hit map obtained after updating the EPP with the bad map2; all remaining good pixels have a nearly homogeneous hit distribution.

For the presented flat-field measurement (Fig. 2.22 (left)), `LED_PEL2Bad` identifies 8 cold pixels and 16 hot pixels of type 2. The hot and cold pixels are not randomly distributed over the whole detector but agglomerate as point-like structures. While bad pixels with a column-like structure indicate a defect in the corresponding CAMEX readout channel and row-like structures indicate a malfunction in the corresponding SWITCHER channel, point-like structures can be explained with crystal defects that spread over several pixels. After uploading the bad2 map to the EPP, the LED is in its normal operation mode. A hit map measured in this configuration is shown in Fig. 2.22 (right). A homogeneous hit distribution with a superimposed, faint, wave-like structure can be seen. The reason for this structure is still under study.

2.7.3. Analyzing scientific observations

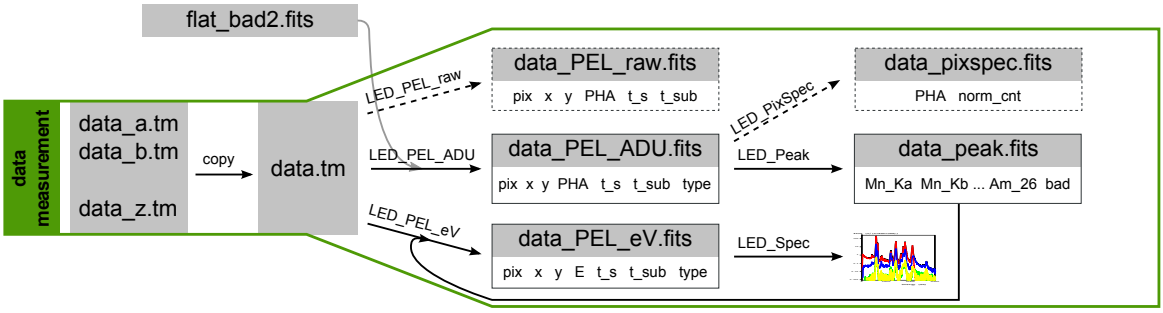

Figure 2.23. LED offline data analysis of a scientific measurement: the recorded data data_a.tm - data_z.tm are concatenated to data.tm. LED_PEL_ADU generates a pixel event list in a fits-table format. The flat_bad2.fits file was created in the previous flat-field analysis. LED_Peak identifies the position of calibration lines which are used to calculate the pulse-height-to-energy transformation which is done by LED_PEL_eV. Finally, LED_Spec generates the energy spectrum. The dashed parts are optional steps used for debugging or for parameter estimation.

In order to analyze scientific measurements* the offset values, the bad flags, the energy thresholds, and the neighbor thresholds of the EPP must be configured appropriately as described in the last two sections. All following data analysis procedures are based on the concept of a pixel event list (PEL). In a PEL each event is listed in one row and the column entries list the properties of the events.

A direct conversion of EPP data for debugging purposes is done via `LED_PEL_raw`. The resulting PEL consists of the pixel number pix, the x-position x, the y-position y, the pulse height PHA, and the event time consisting of a seconds and a subseconds counter entry t_s and t_sub. `LED_PEL_ADU` subtracts additionally the time stamp of the first event from the time stamps of all events and corrects for overflows of the seconds counter to produce a continuous time line which starts at zero for the first recorded event. Furthermore, split events are recognized and summed to one event. To keep record of the different distributions of charge sharing, 14 split types (see Fig. 2.24) are introduced and the split-type number is added to the PEL.

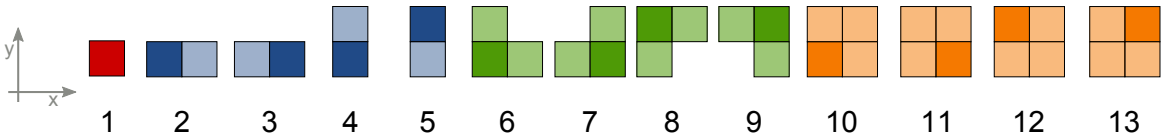

Figure 2.24. Split types: the color strength represents the relative amount of charge. The multiple double, triple, and quadruple splits are introduced to save the orientation of the split. An equal distribution of the patterns 2-5, 6-9, and 10-13 is expected and measured (see Sect. 2.8).

*Here, measurements that use an appropriately configured EPP are named scientific measurements.

Analyzing pixels around bad pixels

Bad pixels give no reliable information about their signal. Events in the close proximity of bad pixels have to be analyzed in a special way as charge sharing with the bad pixel and illegal event patterns (due to pattern pile-up or MIP traces including the bad pixel) cannot be detected. Figure 2.25 shows a bad pixel with its surroundings. Events located in the field$_3$ region are not influenced by the bad pixel and can be analyzed as described before. This is also true if the events split into field$_2$. Events in field$_2$ and field$_1$ can be affected by the bad pixel depending on their position, their split type and their pattern orientation.

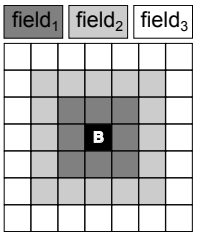

Figure 2.25. Regions surrounding a bad pixel.

In the following, it is assumed that pixel-diagonal charge sharing is not possible without generating a triple or a quadruple event. The original idea to handle neighbors of bad pixel is to reject all events which have their main energy within field$_1$. Figure 2.26 illustrates a number of possible scenarios resulting from this rejection algorithm. In principle, a rejection algorithm can accept legal events (A), accept (possibly) illegal events (B), reject legal events (C and D) and reject illegal events (E and F). All events rejected in case C have their main energy in a corner pixel of field$_1$. An exception of the rule for these 4 singles, 8 doubles (horizontal and vertical splits), 4 triples, and 4 quadruples enhances the efficiency of the detector without any negative impact.

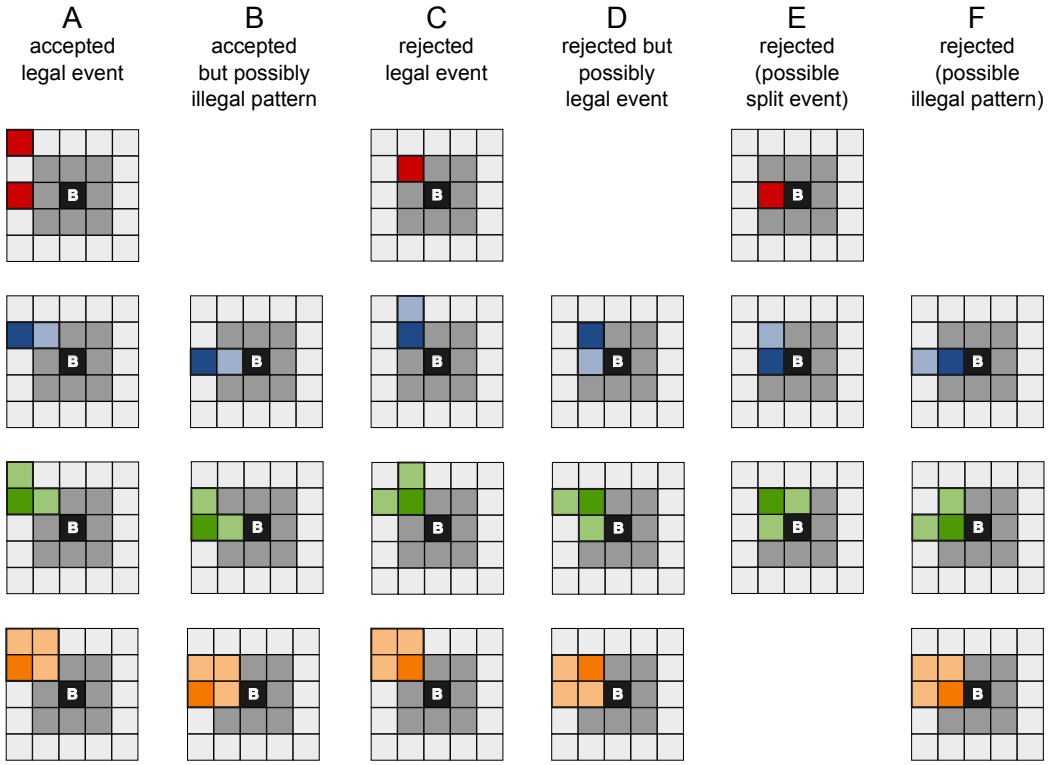

Figure 2.26. Pattern types near bad pixels and their classification for the top left region of a bad pixel. The color strength represents the relative energy of the event.

More critical is the question if events of cases B or D (possible undetected pattern pile-up) should be rejected or accepted, respectively. Rejecting events of case B decreases the counting statistics but increases the quality of the events. On the other hand, accepting events of case D increases the counting statistics but results in possibly corrupt events. How to balance the efficiency of the detector against the event quality can be decided for each observation individually. The properties of the radiation source (flux, spectral shape, variability), the properties of the observation (scientific goals, observation time), and the properties of the detector (amount of bad pixels, background flux, probability for pile-up or for split events) are all relevant factors for deciding if case B should be rejected or case D should be accepted.

The pattern recognition provided by `LED_PEL_ADU` and `LED_PEL_eV` can be adjusted with call parameters to accept and to reject events matching the cases A, B, C, and D. See Sect. 2.8.1 for consequences of the different analyzing methods on the measured spectrum and on the detection efficiency.

Energy calibration

The current energy calibration is based on a spectral line identification (`LED_Peak`) in the spectrum of a calibration measurement in combination with interpolation (`LED_PEL_eV`) between the calibration lines: in the case of CANDELA, the Fe-55 and Am-241 line emissions and the expected Al-, Ti-, and Cu-fluorescence lines can* be used for calibration, see Fig. 1.32 and Tab. 1.4. The lines of the calibration spectrum give a direct relation between the measured pulse heights [ADU] and the corresponding line energy [keV]. A cubic spline interpolation† based on these reference points is used to transform all pulse heights to energy units.

`LED_Peak` is used to find the peak energies of the expected spectral lines in a calibration measurement. The corresponding pixel individual PHA-peak values are written into the file `data_peak.fits`. Figure 2.27 shows that the pixel individual spread of the calibration lines can be larger than the distance between two neighboring lines. To guarantee a correct detection of all calibration lines, `LED_Peak` searches for the most dominant lines, calculates rough pulse-height-to-energy transformations, and uses these calculations to estimate and detect the position of the fainter lines. The peak finding algorithm checks the identified lines for their pulse height and for their flux which have to be in specific ranges of acceptable values. The ranges of tolerance are different for each chosen CAMEX gain g_{CMX}. If the line identification fails, the line position is considered to be corrupt and the line is not used for calibration of the corresponding pixel signals. If several lines within the same pixel are corrupt, the pixel is flagged bad for calibration.

* Dependent on the counting statistics of the calibration measurement and the used CAMEX gain mode g_{cmx}, not all fluorescence lines are used for calibration.

† A cubic spline interpolation connects a sample of data points in a smooth way. A cubic polynomial is fitted between each neighboring pair of data points and a smooth transition between each polynomial is stipulated.

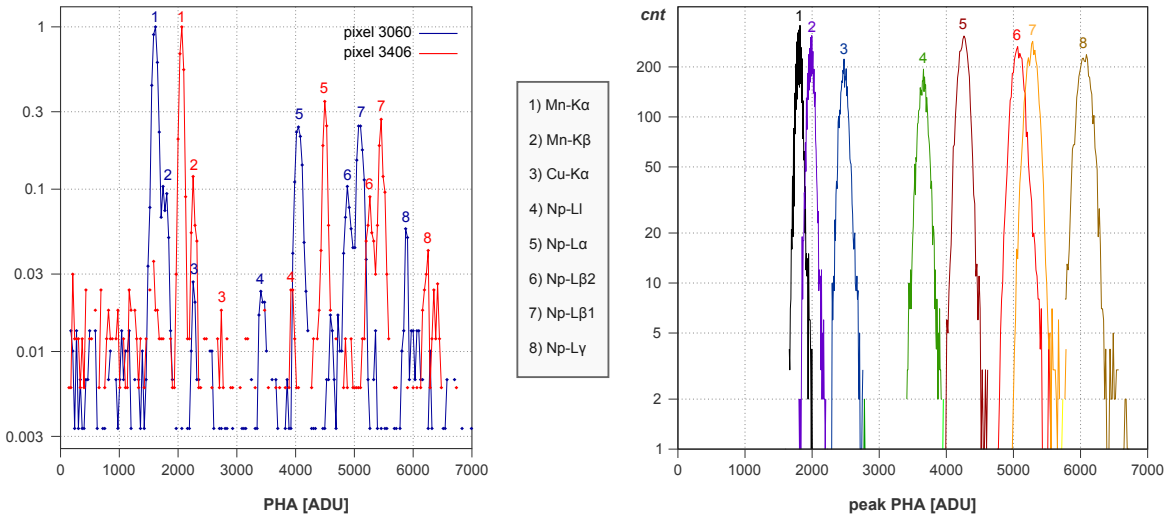

Figure 2.27. The diagrams show the pixel individual pulse height spectra and the distribution of all detected line positions. The numbers label the calibration lines which are listed between the diagrams. Each calibration line has a line specific energy which is observed in different pixels at (possibly) different pulse heights.
Left: single event spectra for two different pixels normalized to their Mn-K_α flux.
Right: the histogram of all detected calibration lines of all pixels shows that the pulse heights of the calibration lines spread more for higher line energies. Example: the Np-L_α line is observed in the range $4000 \leq PHA[ADU] \leq 4625$ and most likely at 4264 ADU.

For proper line identification, the calibration measurement must have a high counting statistics, as the line identification is done pixel individually and only single events are considered. A sufficiently large sample of Mn-K_α and Mn-K_β events originating from the Fe-55 source ($A = 55.9$ MBq) is detected within a few minutes: a 6:36 min Fe-55 measurement results in about 10 million LED events which is on average more than 2400 events per pixel. To observe a pixel individual source- and fluorescence spectrum from the Am-241 source ($A = 2.36$ MBq) takes a measurement time of about 2.5 hours.

`LED_PEL_eV` is similar to `LED_PEL_ADU` but transforms the ADU-values to eV-values with a cubic spline interpolation based on the calibration lines which are recorded in `data_peak.fits`. If some calibration lines are missing, the interpolation is performed with the remaining reference points. By this approach, a noisy pixel with faint, hardly detectable calibration lines can still be calibrated with its more prominent lines but for a pixel with a better energy resolution the full calibration spectrum can be used.

The pulse-height-to-energy transformation cannot be done on the basis of the PEL created by `LED_PEL_ADU` as split events must be calibrated pixel individually. Instead, the original measurement `data.tm` is used to create the energy based PEL (`data_PEL_eV.fits`), which, in combination with the data handling software fitsview *fv*, is used for further data analysis. As operations on large tables are relatively slow with *fv*, an additional program `LED_Spec` is used to calculate the spectra consisting solely of single, double, triple, and quadruples.

2.8. Results

The most important results for the LED study can be summarized with a discussion of the observed spectra. Before addressing the spectral properties, i.e. the energy range of observation and the spectral resolution, results of the bad pixel analysis are presented. The split ratios η of the event energy between adjacent pixels are investigated in detail as an understanding of their distributions is important to understand the spectral properties of the LED. Using the split ratio distributions, an alternative way of pile-up suppression and an analysis to study the shape of the signal charge cloud is presented.

2.8.1. Bad pixel analysis

A measurement with the Fe-55 and Am-241 sources is analyzed, using six different ways of treating neighbors of bad pixels. In the first analysis mode, neighbors of bad pixels are analyzed like normal pixels. In this case, all events of the classes A to F (see Fig. 2.26 for the definition of the classes) are accepted. The total hits observed with this analysis mode (580 197 events) are used as a reference value of 100 % detection efficiency in the following. The hit map is shown in Fig. 2.22 (right).

The low energetic noise measured at 1500 ADU (2200 eV) is reduced by 25.5 % if the event classes E and F are rejected, which is named the A+B+C+D analysis mode. This benefit comes with a 6.2 % reduced detection efficiency. Increasing the level of event rejection further decreases the detection efficiency of the LED only slightly (see Tab. 2.3) and the spectral shape remains nearly unaltered (see Fig. 2.28, right).

In summary, the large size of the LED pixels results in a large fraction of single events (about 80 % of all events) and makes the analysis susceptible for the bad classes C and E. Taking the low energetic noise and the detection efficiency into consideration favours the analysis modes A+B+C+D, A+B+C, and A+C. The differences between these modes are however marginal. All further analysis results were obtained in the A+C mode.

Table 2.3. Detection efficiency of different bad pixel analysis modes. The classes A to F are defined in Fig. 2.26. (r), (l), and (c) is short for (right), (left), and (center).

	A to F	A to D	A + B + C	A + C	A + B	A
abs. cnt.	580197	544128	543082	541589	533465	531995
rel. cnt. [%]	100	93.8	93.6	93.3	91.9	91.7
see Figure	2.22 (r)	-	2.28 (l)	-	2.28 (c)	-

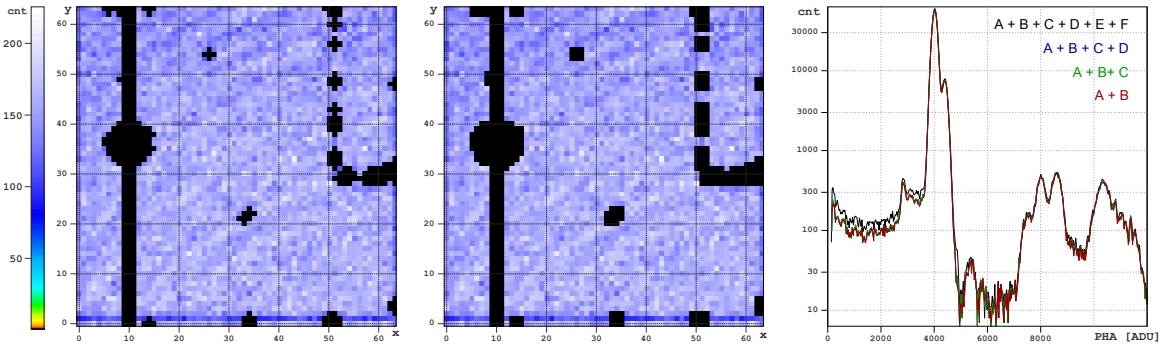

Figure 2.28. Analyzing neighbors of bad pixels with different analysis modes. See Fig. 2.26 for the definitions of the cases A to F. See also Tab. 2.3.
Left: hit map for the accepted classes A, B, and C (D, E, and F are rejected).
Center: hit map for the accepted classes A and B (C, D, E, and F are rejected).
Right: raw spectrum of Fe-55 and Am-241 (without pixel individual gain correction). Analyzing neighbors of bad pixels like normal pixels (analysis mode A+B+C+D+E+F) results in an increased low energetic noise level. Spectral differences due to the acceptance or rejection of the bad classes B, C, and D are marginal in case of the LED.

2.8.2. Split events

The split ratio $\eta_n = q_n/q_0$ introduced in Eq. (1.30) can be analyzed with the program `LED_PEL_s` which creates a pixel event list including all pixel information of a split event and not just the resulting energy sum. The fractional pulse height (related to the total pulse height of the event) is calculated for each pixel as well. A triple event is, for example, recorded with the following information: split type = 8, $PHA = 5000\,\mathrm{ADU}$, consisting of:

$$\begin{aligned}
&\text{pixel at } (x_1/y_1) \text{ with } PHA = 3000\,\mathrm{ADU}\ (60\,\%)\\
&\text{pixel at } (x_2/y_2) \text{ with } PHA = 1500\,\mathrm{ADU}\ (30\,\%)\\
&\text{pixel at } (x_3/y_3) \text{ with } PHA = \ 500\,\mathrm{ADU}\ (10\,\%).
\end{aligned}$$

An Fe-55 measurement with about 6.3 million events is used to analyze the split ratio η_1. The total split distribution in this measurement is: 80.2 % singles, 16.9 % doubles, 0.4 % triples, and 0.4 % quadruples. The remaining events (2.1 %) are rejected as illegal patterns*. Distributions of the split ratio η_1 for the different split types (see Fig. 2.24 for the definition of the split types) are presented in Fig. 2.29 (left).

The distributions of double events as a function of the split ratio η_1 are shown as sum of all double subtypes and for each double subtype (type 2, 3, 4, and 5) individually. As expected, the differences between these subtypes are marginal which is a strong evidence for a symmetric charge sharing† within the detector. A similar symmetry was observed for the triple and quadruple subtypes. The figure shows only the sum of all triple and quadruple subtypes (types 6, 7, 8, 9, and 10, 11, 12, 13) for clarity.

* Illegal patterns that are not rejected by the EPP are diagonal splits and triple events which have their most energetic pixel on the edge of the pattern and not in the center of it.
† The symmetric charge sharing should not be mixed up with a symmetric charge cloud. An asymmetric charge cloud can result in an averaged, symmetric charge charing.

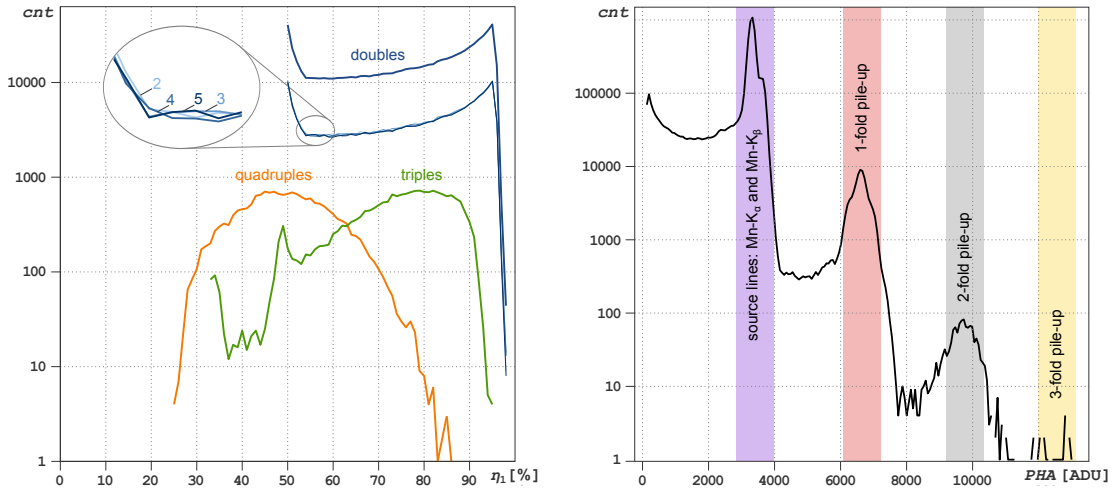

Figure 2.29. Charge split analysis of an Fe-55 measurement ($\sim$6.3 million events). **Left:** split ratio distribution η_1 for double, triple, and quadruple events. For doubles, the distribution of the four possible subtypes (2, 3, 4, and 5) and their sum are shown. For triples and quadruples only the sum of the respective subtypes are shown. **Right:** summarized pulse height spectrum of all pixels for the Fe-55 measurement. Pile-up of the Mn-K$_\alpha$ and Mn-K$_\beta$ emission lines can be identified by the pulse height and is observed up to the 3rd order.

A split that concentrates a large fraction of the signal charge in one pixel and shares only a small fraction of the total signal charge with its neighboring pixels results in a split ratio close to 100 %. A low split ratio indicates a homogeneously distributed split. By definition of η_1, the minimal split ratios for doubles, triples, and quadruples are 50 %, 33 %, and 25 %. See Sect. 2.8.7 for an analysis of the maximal split ratios.

In the case of pattern pile-up two, or more, signal-charge clouds build one event. To study the properties of charge sharing of a single charge cloud, the events must be corrected for pattern pile-up. The pulse height spectrum of the considered measurement is shown in Fig. 2.29 (right). The Fe-55 source lines and their 1- and 2-fold pile-ups are clearly visible. 3-fold pile-up is indicated by a few events.

Figure 2.30 shows the split ratio distributions for different pile-up multiplicities. The pile-up identification is based on criteria for the pulse height. Events without pile-up are selected via $PHA < 5000\,\mathrm{ADU}$, whereas 1- and 2-fold pile-ups are selected via $5000\,\mathrm{ADU} < PHA < 8000\,\mathrm{ADU}$ and $8000\,\mathrm{ADU} < PHA < 11000\,\mathrm{ADU}$, respectively.

The shape of the double and triple distributions are strongly affected by pile-up. Double events without pile-up tend to concentrate their charge into one pixel. Therefore, double, 1-fold pile-ups are likely to appear like an equally divided double event ($\eta_1 = 50\,\%$). In the same way, all other combinations of charge splits and pile-ups can explain the observed distributions (see the indicated event patterns within Fig. 2.30).

In cases of triple and quadruple events, not only the split ratio $\eta_1 = q_1/q_0$ but also the ratios η_2, η_3, and (only for quadruples) η_4 are interesting. Figure 2.31 shows these distributions for triples and quadruples. As shown there, triples tend to split very

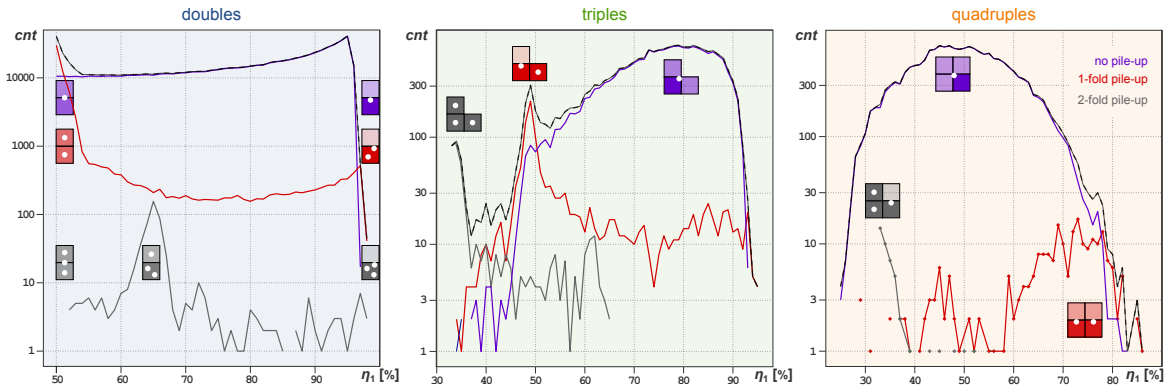

Figure 2.30. Split ratio distribution η_1 for double (left), triple (center), and quadruple events (right). Events without pile-up, 1-fold pile-up, and 2-fold pile-up are shown in violet, red, and gray. The sum of all distributions is shown in black dashed lines and is identical to those shown in Fig. 2.29 (left). Symbolic split patterns with indicated charge clouds (white circles) explain the underlying physical process. The horizontal position of these patterns matches η_1. The vertical position is arbitrary. The figures show that pile-up influences the split ratio distribution η_1 mainly in specific regions of η_1 which are different for double, triple, and quadruple events.

inhomogeneously and the η_2 and η_3 split ratios, i.e. the q_2 and q_3 signal charges, are on average very low. The smallest signal charge q_4 of a quadruple event is on average larger than the smallest signal charge q_3 of a triple event! Therefore, effects acting on small signal charges, like a wrong energy calibration at low energies, are more dominant for triples than for quadruples. This effect can be directly seen in Fig. 2.33 and is discussed in Fig. 2.32.

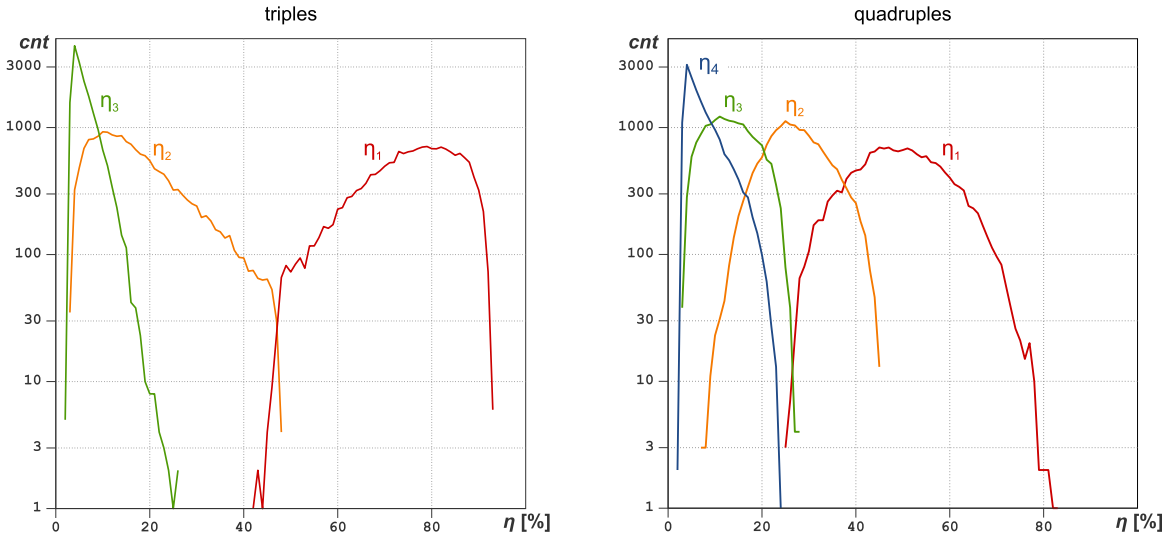

Figure 2.31. Distributions of pile-up free ($PHA < 5000$ ADU) triples and quadruples. Triples split on average more inhomogeneously (like for example $\eta_1 = 80\,\%$, $\eta_2 = 15\,\%$, $\eta_3 = 5\,\%$) than quadruples (like $\eta_1 = 50\,\%$, $\eta_2 = 25\,\%$, $\eta_3 = 13\,\%$, $\eta_4 = 12\,\%$).

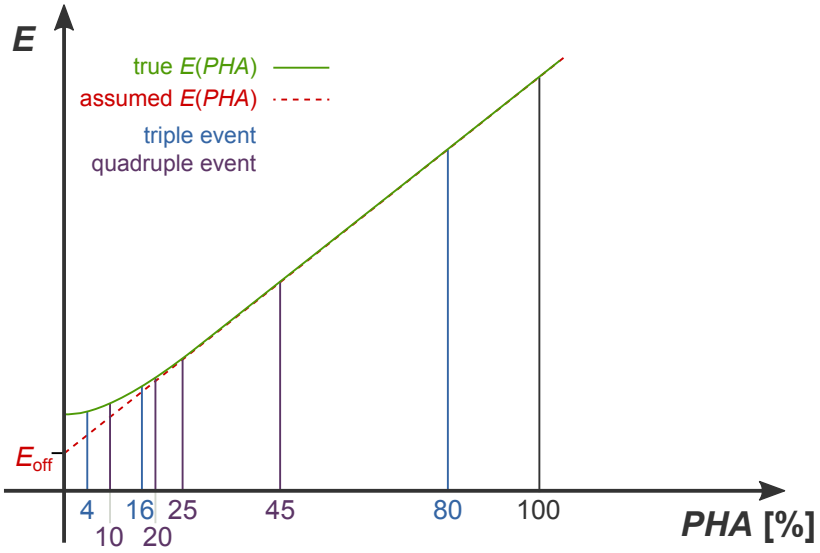

Figure 2.32. The figure shows the effect of an erroneous pulse-height-to-energy relation on split events. The pulse heights are stated as fractions of the total single-event pulse height (black). A triple event (blue) with $\eta_1 = 80\,\%$, $\eta_2 = 16\,\%$, and $\eta_3 = 4\,\%$ is more affected by a mismatched pulse-height-to-energy relation as a quadruple event (violet) with $\eta_1 = 45\,\%$, $\eta_2 = 25\,\%$, $\eta_3 = 20\,\%$ and $\eta_4 = 10\,\%$. The energy offset E_{off} is explained in Sect. 2.8.3.

Pile-up rejection

Even though individual pile-up events cannot be detected directly, they show their presence in the split ratio distributions. This can be used for an efficient pattern pile-up reduction: pattern pile-up can be turned off by rejecting all split events. But, depending on the detector geometry this can reduce the detector efficiency dramatically. Using the split ratio distribution, pattern pile-up can be suppressed by rejecting only those patterns with a split ratio which is more likely for pile-up as for normal splits; see again Fig. 2.30. In case of the considered Fe-55 measurement, selecting only double events with $\eta_1 > 52\,\%$, triples with $\eta_1 > 51\,\%$, and quadruples with $\eta_1 < 78\,\%$ rejects in total 81 548 events. 49 606 of the rejected events are pile-up events and 31 942 are pile-up free events. As all pile-up events (79 566) and pile-up free events (4 511 574) are known for this measurement due to their pulse heights, this approach reduces the number of pile-up events by 62.3 % while reducing the number of pile-up free events only by 0.71%. These numbers will change for other pixel geometries, observed fluxes, and especially for other spectral distributions of the observed source. The presented method identifies pile-up in a spectrum that is dominated by line emission and enables to reject pattern pile-up effectively which allows to resolve spectral structures that are overlaid by pile-up events.

2.8.3. Energy offset

In the case of an Fe-55 calibration, the Mn-K_α emission line is the calibration line with the lowest energy. To apply a pulse-height-to-energy transformation for pulse heights that are smaller than the pulse height of Mn-K_α an additional calibration point at $PHA = 0\,\mathrm{ADU}$ is necessary, the energy offset E_{off}.

E_{off} is chosen manually in an iterative process: the Mn-K_α peaks of single, double, triple, and quadruple events of the measured energy spectrum, should ideally all peak at the line energy of Mn-K_α. If the pulse-height-to-energy transformation is incorrect for energies smaller than Mn-K_α, the double, triple, and quadruple peak positions are shifted as they are a sum of multiple small pulse heights or energies, respectively.

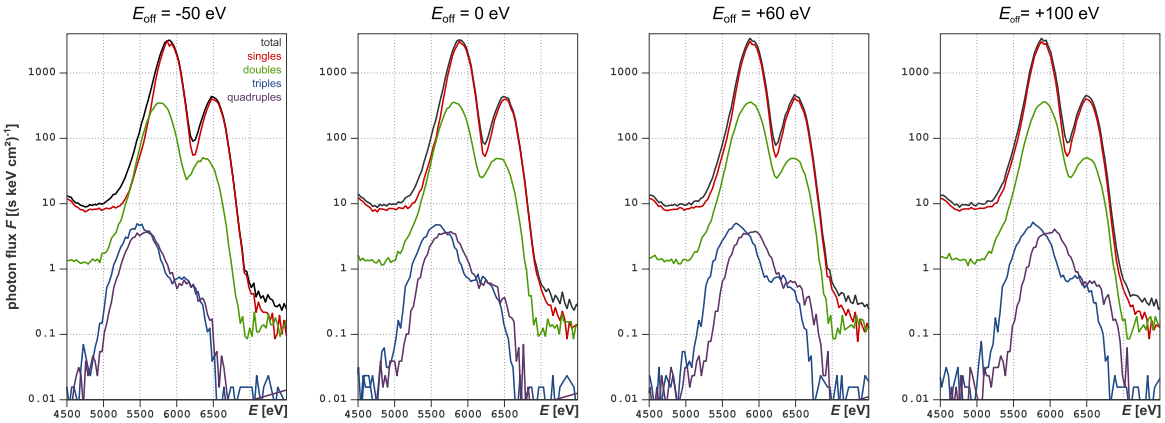

Figure 2.33. Spectra of the Mn-K_α and Mn-K_β lines generated with different energy offsets E_{off}. $E_{\mathrm{off}} = +60\,\mathrm{eV}$ is chosen as the optimal value because it corrects the position of the double event spectrum. See Fig. 2.32 for a discussion on the triples and quadruples.

Figure 2.33 shows spectra generated with different energy offsets E_{off}. The choice of the best energy offset E_{off} is based on the Mn-K_α peak position for doubles. The fact that triple and quadruple events are misaligned even if the peaks of the single and double events match shows that the pulse-height-to-energy relation is not just biased by E_{off} but also non-linear. To account for the nonlinearity, two additional, artificial reference points could be introduced and used to shift the triple and quadruple peaks.

The circumstance that the Mn-K_α peak of triple events is always positioned at lower energies than the corresponding quadruple peak gives a hint on the pulse-height-to-energy relation at small energies. The split ratio distributions introduced in Sect. 2.8.2 show that triple events split mainly into one large part and two very small parts, while quadruples split more homogeneously. A pulse-height-to-energy relation similar to the one presented in Fig. 2.32 can explain that split events are observed with a diminished energy and that this effect is most prominent for triples.

The following analysis adjusts E_{off} in a way to optimize the peak position of the double events. This strategy is motivated as double events are about two orders of magnitude more prominent than triples or quadruples at these low energies. Additional parameters to adjust the triple and quadruple peaks are not introduced. The

misalignments of the triple and quadruple peaks are in the order of 200 eV.

2.8.4. Spectral properties of the LED

For each of the four CAMEX gain settings two spectra are obtained, one with Fe-55 and another one with Am-241. Each measurement consists of about $5 \cdot 10^6$ events. The resulting Fe-55 and Am-241 spectra are combined for each CAMEX gain to one spectrum with the program `LED_spec_add`. See Fig. 2.35 for the spectra and Tab. 2.4 for a summary of the spectroscopic properties. The minimal detectable energy E_{min} is defined by the EPP energy threshold map which is constructed as the 5-sigma deviation of the pixel individual dark signals. Even though the mean pulse height noise in units of ADU decreases with a decreasing CAMEX gain g_{cmx}, the energy noise in units of eV increases as the eV-per-ADU gain factor increases as well. E_{min} is defined as the low energetic cutoff of the energy spectrum, see Fig. 2.34. The figure also shows that the low energy background noise is slightly lower for increasing gains.

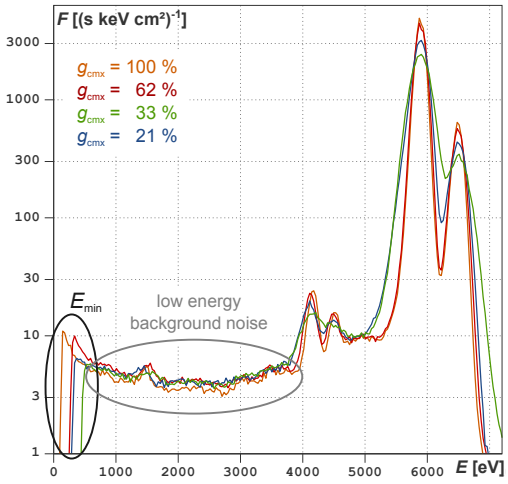

Figure 2.34. Low energetic part of the LED spectrum (all type of patterns) for different gains g_{cmx}.

Photons with an energy exceeding the maximal detectable energy E_{max} saturate the CAMEX output and result in a broadened peak *end-s* at the right end of the single event spectrum. For double events an *end-d* peak located at the double energy of the *end-s* peak exists for the same reason; see for example the peaks numbered 18 and 24 at the spectrum with $g_{\mathrm{cmx}} = 62\,\%$ in Fig. 2.35. E_{max} is detected as the low energetic tail of the *end-s* peak.

Table 2.4. Summary of the spectroscopic properties of the LED for different CAMEX gains g_{cmx}: the mean offset $\bar{o}$, the mean noise $\bar{n}$, the minimal and maximal observable energy E_{min} and E_{max}, and the energy resolution (FWHM) at Mn-K$_\alpha$ (ΔE_1), 26.4 keV (ΔE_2), and 59.5 keV (ΔE_3). s, d, t, q, is short for the single, double, triple, and quadruple event fraction observed with an Fe-55 source.

g_{cmx} [%]	$\bar{o}$ [ADU]	$\bar{n}$ [ADU]	E_{min} [eV]	E_{max} [keV]	ΔE_1 [eV]	ΔE_2 [eV]	ΔE_3 [eV]	E_{off} [eV]	s [%]	d [%]	t [%]	q [%]
100	4409	42	144	10	168	-	-	-50	79.5	18.3	0.59	0.55
62	3802	32	336	19	198	-	-	+30	80.7	17.3	0.46	0.43
33	3568	23	368	33	267	342	-	+60	83.9	14.5	0.25	0.19
21	3292	20	528	>60	342	344	352	-50	84.3	14.2	0.18	0.17

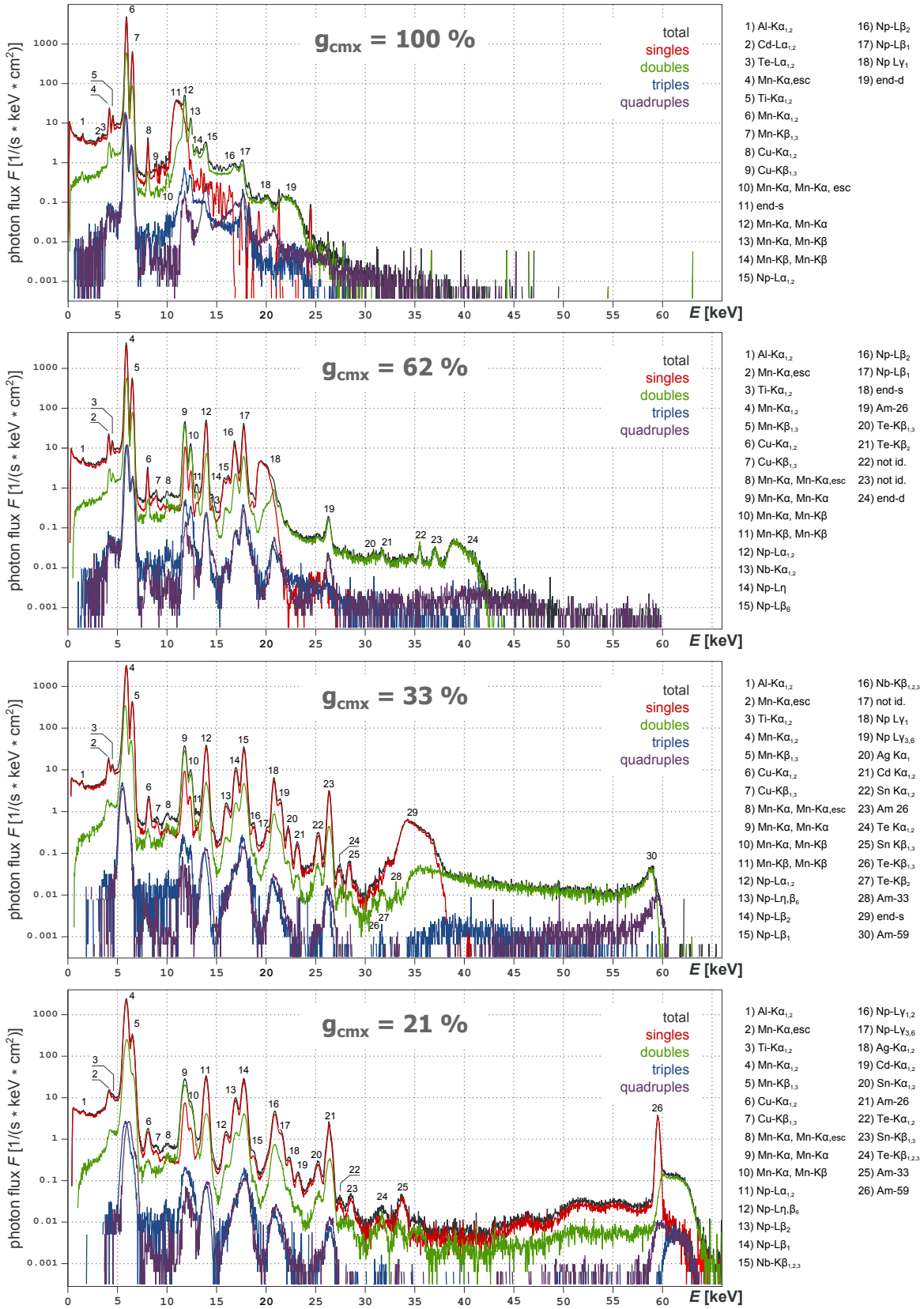

Figure 2.35. LED spectra observed with different gain modes g_{cmx}.

For the measurements presented in Fig. 2.35 the Mn-K$_\alpha$ line at 5.9 keV, the Am line at 26.4 keV (Am-26) and the Am line at 59.5 keV (Am-59) are fitted with a Gaussian line profile to obtain their energy resolution. With $g_{\mathrm{cmx}} = 21\,\%$, the measured energy resolution of $\Delta E = 352\,\mathrm{eV}$ (FWHM) at $E = 59.54\,\mathrm{keV}$ results in a spectroscopic resolution R of

$$R_{59} = \frac{\Delta E}{E} \approx \frac{1}{169}. \qquad (2.15)$$

The Fano-limit of $\Delta E = 344\,\mathrm{eV}$ (FWHM) at $E = 59.54\,\mathrm{keV}$ (see again Fig. 1.13) shows only marginal space for improvements at this energy. The peak-to-background ratio described in Fig. 2.36 is measured as $P/B = 93:1$.

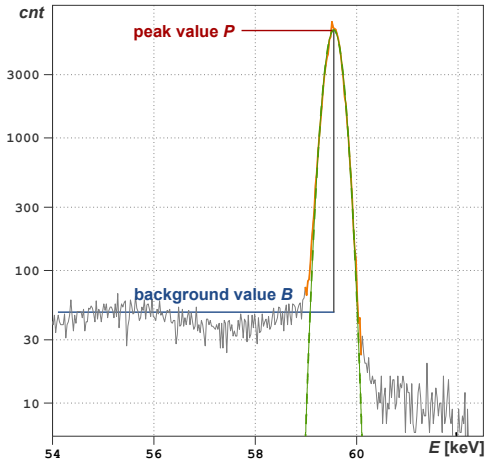

Figure 2.36. The Am-59 peak at 59.54 keV shows an energy resolution of $\Delta E = 352\,\mathrm{eV}$ (FWHM) and a peak-to-background ratio of $P/B = 93$.

In the maximal gain-mode $g_{\mathrm{cmx}} = 100\,\%$, the relative energy resolution is observed slightly worse. The measured energy resolution of $\Delta E = 168\,\mathrm{eV}$ (FWHM) at 5.9 keV results in a spectroscopic resolution of

$$R_{5.9} \approx \frac{1}{35}. \qquad (2.16)$$

The Fano limit of $\Delta E = 118\,\mathrm{eV}$ (FWHM) at 5.9 keV shows that the LED energy resolution at low energies is good but not at the possible limits. The degraded resolution at low energies can possibly be explained with the ratio between signal charges and dark current noise or with other intrinsic detector noise (like noise of the gate voltage). Studies at different detector temperatures could help to clarify this issue.

The low energetic part of the LED spectrum: $E \leq 6\,\mathrm{keV}$

The Mn-K$_{\alpha\,\mathrm{esc}}$, Al-K$_{\alpha\,1,2}$, and Ti-K$_{\alpha\,1,2}$ fluorescence lines are already clearly visible for $g_{\mathrm{cmx}} = 33\,\%$ and for higher gain modes. Operating the LED with the maximum CAMEX gain $g_{\mathrm{cmx}} = 100\,\%$ reveals also the cadmium, tin, and tellurium L$_\alpha$-fluorescence lines, see Fig. 2.37. Because of the high low-energy background, a line identification without any prior knowledge would be difficult. However, knowing the elements with strong K_α fluorescence lines in the setup allows to identify the expected, corresponding L$_\alpha$ lines which can then be used to check the energy calibration. The observed energies E are obtained on the basis

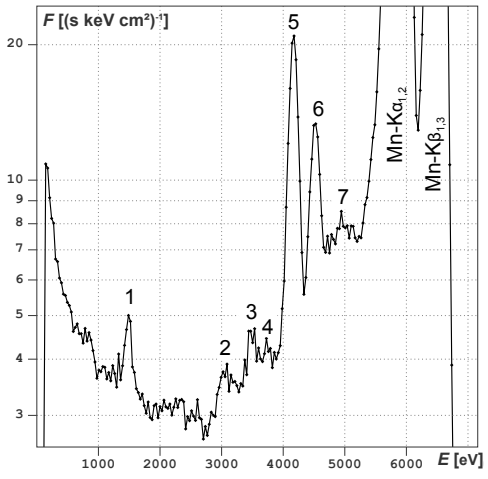

Figure 2.37. Zoomed spectrum of an Fe-55 and Am-241 irradiated measurement with maximum gain $g_{\mathrm{cmx}} = 100\,\%$. The peaks are listed in Tab. 2.5.

of a spectrum with a bin width of 32 eV. The bin including the local maximal flux, i.e. the peak, is averaged with its four neighboring bins weighted with their flux. Table 2.5 shows that the difference ΔE between the observed energy E and the line emission energy E_0 is in the order of a few ten electron volts in this energy range.

Table 2.5. Systematic error of low energetic fluorescence lines of Fig. 2.37. ΔE is the difference between the true line energy E_0 and the observed energy E; $g_{\mathrm{CMX}} = 100\,\%$.

	Al-$K_{\alpha\,1,2}$	Cd-$L_{\alpha\,1,2}$	Sn-$L_{\alpha\,1,2}$	Te-$L_{\alpha\,1,2}$	Mn-$K_{\alpha,\,\mathrm{esc}}$	Ti-$K_{\alpha\,1,2}$	Ti-$K_{\beta\,1,3}$
E_0 [eV]	1487	3133	3443	3768	4155	4509	4932
E [eV]	1493	3085	3475	3732	4186	4519	4955
ΔE [eV]	+6	-48	+32	-36	+31	+10	+23
Fig. 2.37	1	2	3	4	5	6	7

The high energetic part of the LED spectrum: $E > 6$ keV

As outlined in the previous section, the peak position of fluorescence and source lines which are not used as reference points can be used to check the energy calibration. The results for $g_{\mathrm{cmx}} = 21\,\%$ are presented in Tab. 2.6. For energies below 30 keV, the systematic error of the energy seems to be well below 100 eV. In this energy range, six calibration lines (Mn-K_α, Mn-K_β, Np-L_α, Np-$L_{\beta\,1}$, Np-$L_{\gamma\,1}$, Am-26) plus the energy offset E_{off} determine the pulse height to energy calibration in a way that no event has an energetic distance to the next reference point of more than $\Delta E_{\mathrm{cal}} = 3737$ eV. For energies $E > 30$ keV, only the two reference lines Am-26 and Am-59 can be used for calibration which explains the increased systematical error of the Am-33 line.

Table 2.6. Systematic error of high energetic fluorescence lines observed with $g_{\mathrm{CMX}} = 21\,\%$. ΔE is the difference between the true line energy E_0 and the observed energy E. ΔE_{cal} is the energetic distance to the next calibration line.

		Cu-$K_{\alpha\,1,2}$	$2 \cdot$ Mn-$K_{\alpha\,1,2}$	Np-$L_{\eta\,\beta 6}$	Np-$L_{\beta\,2}$	Nb-$K_{\beta\,1,2,3}$
E_0	[eV]	8041	11790	15996	16840	18656
E	[eV]	8086	11799	15970	16927	18702
ΔE	[eV]	+45	+9	-26	+87	+46
ΔE_{cal}	[eV]	1551	0	1754	910	906
		Cd-$K_{\alpha\,1,2}$	Sn-$K_{\alpha\,1,2}$	Te-$K_{\alpha\,1,2}$	Sn-$K_{\beta\,1,3}$	Am-33
E_0	[eV]	23108	25193	27377	28471	33196
E	[eV]	23216	25252	27447	28548	33594
ΔE	[eV]	+108	+59	+70	+77	+398
ΔE_{cal}	[eV]	2324	1152	1032	2126	6851

2.8.5. Comparison with a Geant4 simulation

In order to understand the spectral properties of the LED and its interaction with the HED in more detail, a Geant4* based simulation was performed by S. Pürckhauer as part of a diploma thesis. The simulation assumes a simplified geometry of the CANDELA setup consisting of the radioactive sources, the source shieldings, the LED, the HED, and the copper cooling mask in the correct dimensions; see Pürckhauer [2015] for more details on the simulation.

The simulation records the energies deposited inside a silicon layer due to photon interactions and modifies the recorded energies to match a Fano limited energy resolution. Figure 2.38 shows the simulated spectra in comparison with the measured one. Four noticeable spectral features shall be discussed:

- **Compton edge:** photons that interact inside the LED via the Compton effect result in a scattered photon and a Compton electron. While the scattered photon can escape from the silicon crystal, the Compton electron deposits, most likely, all its kinetic energy E_{kin} inside the LED. If the initial photon (with the energy E_0) is Compton backscattered, E_{kin} gets maximal and is called the Compton edge E_{C},

  $$E_{\mathrm{C}} = \frac{2E_0^2}{m_{\mathrm{e}}c^2 + 2E_0}. \tag{2.17}$$

  The energy spectrum of the Compton electrons is almost flat (slightly reduced at $E_{\mathrm{C}}/2$) with a cutoff at E_{C}. Each emission line of the Fe-55 and Am-241 sources produces a different Compton-electron spectrum. The 59.5 keV line emission of Am-241 has the largest cross section for Compton interaction with a Compton edge at

  $$E_{\mathrm{C},59} \approx 11.24\,\mathrm{keV}. \tag{2.18}$$

  In the simulated spectrum the Compton edge is visible at $E_{\mathrm{C,\,sim}} = 11.14\,\mathrm{keV}$ with a sharp flux decrease from $0.3\,(\mathrm{s\,keV\,cm^2})^{-1}$ to roughly $0.012\,(\mathrm{s\,keV\,cm^2})^{-1}$. In the measured spectrum the Compton edge is superimposed with the Np-$\mathrm{L_l}$ line and with an enhanced background noise of $F \approx 0.3\,(\mathrm{s\,keV\,cm^2})^{-1}$ and therefore not noticeable.

- **energy calibration errors:** the misalignment around 33 keV was already discussed in the last section. It is caused by a non-linear gain that is not corrected because of missing calibration points in this energy range. Additional to the systematic bias, the 33 keV line emission of Am-241 shows a reduced energy resolution because misalignments that are slightly different for each pixel are added up.

- **energy resolution:** Fig. 2.38 shows that a nearly Fano limited resolution is achieved at high energies. The width of the 59.5 keV line emission is almost

* Geant4 (Geometry and Tracking) is a Monte-Carlo based toolkit to simulate the interaction of particles and radiation with matter. For more information, see Agostinelli and GEANT4 Collaboration [2003].

identical for the simulation and for the measurement. At lower energies, the LED energy resolution is dominated by other noise sources, like for example dark-current noise. Broader peaks result also in reduced peak heights which explains the difference between the simulated and the measured peak heights at low energies.

- **background noise:** the simulation shows that a large part of the observed LED noise below 11 keV is caused by Compton scattered events. At E_C the simulated background noise $(0.3\,(\mathrm{s\,keV\,cm^2})^{-1})$ accounts for almost 100 % of the measured background noise. At energies between $11 \leq E\,[\mathrm{keV}] \leq 30$ the background noise is hard to identify because of the wealth of line emissions. For $30 \leq E\,[\mathrm{keV}] \leq 45$, the difference between the measured and the simulated background is less than one order of magnitude. The increasing noise in the measured spectrum for $E > 45\,\mathrm{keV}$ is caused by Compton reprocessed Am-59 photons on structures that are not present in the geometry of the simulation. The simulated peak near 53 keV shows the effect of Compton reprocessing: studying the traces of the corresponding events reveals that the events are all Compton scattered in the copper cooling mask of the LED and hit the HED with a scattering angle close to 90°. The energy loss through the Compton scattering (6.2 keV for a scattering at 90°) results in the simulated peak.

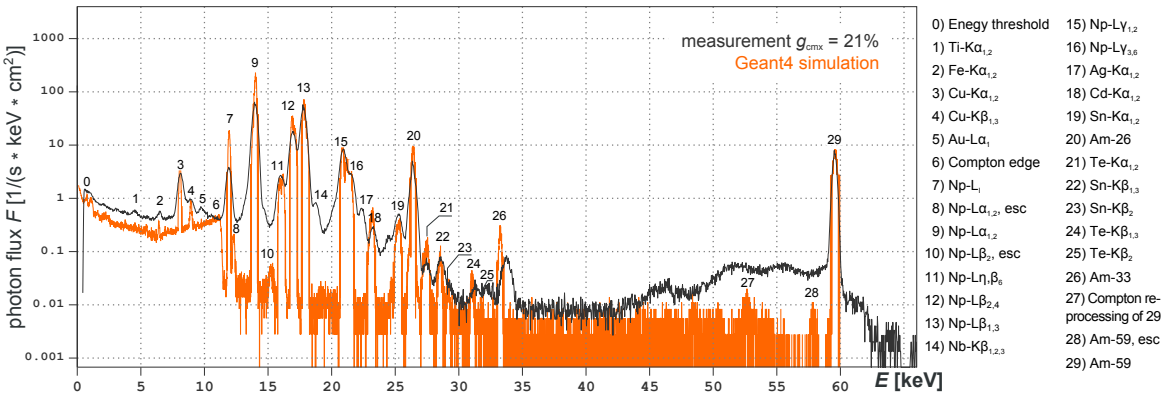

Figure 2.38. Comparison of the measured Am-241 spectrum (black) with a spectrum obtained with a Geant4 simulation (orange). The measurement is integrated over 2.5 hours; the simulation has an equivalent observation time of 50 minutes. The fluorescence lines with the numbers 1, 5, 14, and 17 are not visible in the simulation because the corresponding elements are not used in the simulated setup. The Compton edge (number 6) is clearly visible in the simulation. The peak number 27 results from Am-59 photons that are reprocessed by Compton scattering.

2.8.6. Temporal behavior of the LED

After power-on, the LED shows a time dependent increase of the pixel offset and the pixel noise for a time t_{var} which depends on the selected temperature setting T_{s} of the heat exchanger. The lower this temperature is chosen, the longer it takes to bring the LED into thermal equilibrium. For the minimum temperature setting of $T_{\mathrm{s,\,min}} = -80°\mathrm{C}$ it takes about $t_{\mathrm{var}} \approx 150$ minutes to reach thermal stability. Fig. 2.39 shows the pixel averaged offset and noise drift during the first 300 minutes of operation at $T_{\mathrm{s}} = -70°\mathrm{C}$. After about 50 minutes, the averaged offset is stable within a few ADU and the averaged noise within a fraction of one ADU. The offset and noise drift can be explained by the heating caused from the power dissipation of the CAMEX and SWITCHER chips which are positioned close to the detector matrix.

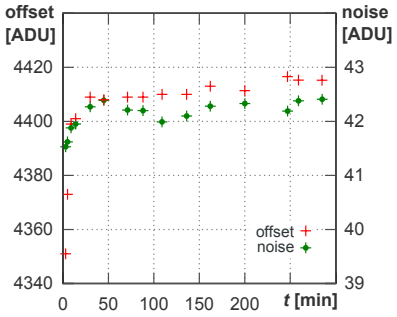

Figure 2.39. Averaged offset and noise drift during the first 300 minutes of operation.

2.8.7. Study of the charge cloud shape

In the following considerations, only pile-up free events are considered which can be achieved by applying a pulse height cutoff at $PHA = 5000\,\mathrm{ADU}$ on an Fe-55 measurement, see Fig. 2.29. The maximal split ratios $\eta_{1\,\mathrm{max}}$ for double, triple, and quadruple events are measured to be 97 %, 93 %, and 82 %, compare also Fig. 2.30. $\eta_{1\,\mathrm{max}}$ is related to the event detection thresholds which are saved in the neighbor-threshold map of the EPP. A maximum energy reduction by 3 % for doubles is in accordance with the used neighbor-threshold settings which predicts a maximal energy loss of 3.1 %*. Triples have roughly twice the detection threshold, as they split mainly on two sides, see Fig. 2.40. For quadruples, the detection threshold is more complicated as the two side splits, q_2 and q_3, and the edge split q_4 are of different magnitude. The relation between q_4 with q_2 and q_3 can be calculated for a spherical charge cloud with a geometrical approach, see Appendix D.5. According to this calculation it is

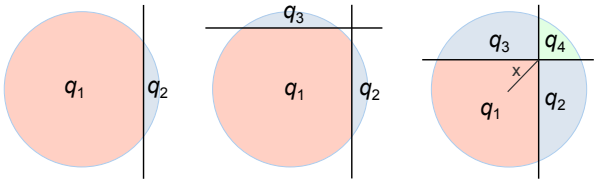

Figure 2.40. Double, triple, and quadruple splits and their fractional charges.

$$q_2 = q_3 \qquad \text{and} \qquad q_2 = m(x)\, q_4 \tag{2.19}$$

with a multiplication factor $m(x)$ that depends on the diagonal distance x between the center of the charge cloud and the corner of the pixel. Figure 2.42 shows $m(x)$ and the maximal split ratio $\eta_{1\,\mathrm{max}}(x)$.

* The neighbor threshold is calculated as 4σ variation of the dark measurements. In the discussed measurement, the averaged neighbor threshold is $4 \cdot 26\,\mathrm{ADU} = 104\,\mathrm{ADU}$ which is 3.09 % of the observed Mn-K$_\alpha$ pulse height (3365 ADU).

It is not possible to reconstruct the observed maximal split ratio for quadruples $\eta_{1\,\max} = 82\,\%$ with this calculation. To construct such a high split ratio, the diagonal distance x must be in the order of the charge cloud radius which results in an extremly high multiplication factor. Taking the observed charge loss of 18 % requires $m = 2.5$ as muliplication factor ($(2 \cdot 2.5 + 1) \cdot 3\,\% = 18\,\%$). Assuming a spherical geometry, $m = 2.5$ results in a diagonal distance of $x/r \approx 0.43$. At this distance the split ratio is only $\eta_{1\,\max}(0.43) \approx 47\,\%$ which is far away from the observed $\eta_{1\,\max} = 82\,\%$.

The presented model assumes a spherical, homogeneously distributed charge cloud. Considering a more realistic charge cloud with a density profile that decreases with the distance to the center of the cloud even magnifies the observed discrepancy. Introducing an elliptical charge cloud, q_4 could be increased without increasing q_2 and q_3 that much. Figure 2.41 shows an illustration of an elliptically shaped charge cloud with $q_2 = q_3 \approx 3 \cdot q_4$ and $\eta_1 \approx 78\,\%$.

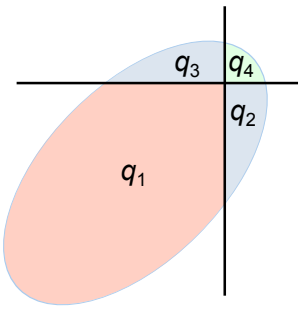

Figure 2.41. Model of an elliptical charge cloud.

The low statistics of the split ratio distribution near $\eta_{1\,\max}$ makes a detailed study of the charge cloud shape difficult. This, and the analytical complexity caused by an elliptically shaped charge cloud model favors a study by using a simulations approach. With such an approach not only $\eta_{1\,\max}$, but the whole shape of the split ratio distribution η_1 could be further investigated. It is beyond the scope of the present study to perform such a simulation.

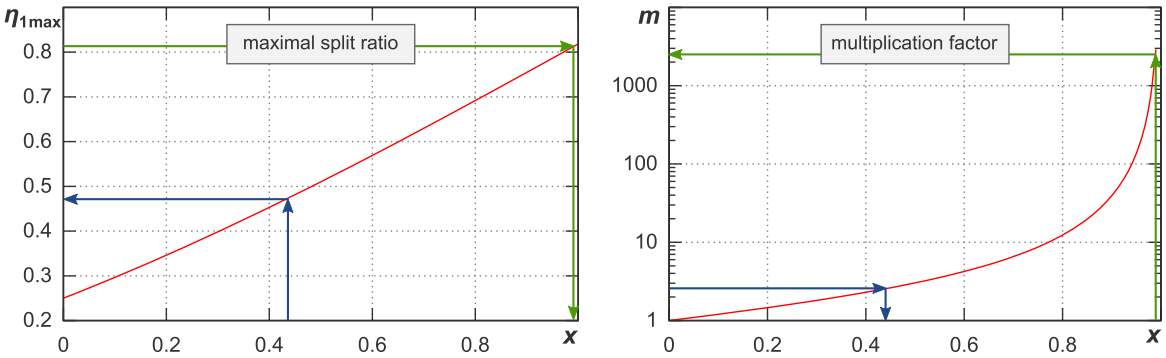

Figure 2.42. Calculating the maximal split ratio assuming a spherical charge cloud: the graphs of the maximal split ratio $\eta_{1\,\max}$ (left) and the multiplication factor m (right) are a function of the diagonal distance x between the center of the charge cloud and the corner of the pixel. x is stated in units of the charge cloud radius r. The observed $\eta_{1\,\max} = 0.82$ requires $x \approx r$ which results in a large multiplication factor of $m > 1000$ (green lines) and an unrealistic low detection threshold of $18/(2 \cdot 1000 + 1)\,\%$. On the other hand, $m = 2.5$ (which fits to the observed detection threshold of 3 %) results in $\eta_{1\,\max} \approx 0.47$ (blue lines).

2.9. Summary

The LED study as part of this thesis contains both, a part that has a hardware related concern and a contribution in detector related data analysis.

The **hardware part** included the construction work of the LED lab setup as well as the adjustment of the ADC and the enhancement of the digital camera controller chip (D3C). The latter required some sophisticated modifications of the VHDL-based FPGA firmware and a thorough and extensive testing of the D3C by utilizing state of the art electronic data logging equipment.

For the **data analysis study** an analysis software consisting of several programs was developed, tested, and operated in order to quantify the spectroscopic characteristics of the LED and its setup. In summary, the most important step in the analysis was the pixel individual energy calibration which had to be performed with great accuracy. The upper edge of the energy range of the LED is variable between 10 keV and >60 keV with an energy resolution of $\Delta E = 168\,\text{eV}$ (FWHM) at 5.9 keV and $\Delta E = 352\,\text{eV}$ (FWHM) at 59.5 keV. Systematic effects were observed to be less than 100 eV at $E < 30\,\text{keV}$. At higher energies, more calibration lines will be needed to quantify and correct the remaining systematic effects.

The studies concerning **neighboring bad pixels** and the split ratio distributions were central parts of the performed analysis of LED data. The special analysis of neighbors of bad pixels is important for the LED as it has many bad pixels and, consequently even more pixels neighboring bad pixels. This analysis may become a matter of practical interest for other (pixel based) detectors which experienced an increase of bad pixels during their space mission lifetime.

Analyzing the **split ratio distributions** enables an alternative way to suppress pile-up and to study the charge cloud shape inside the detector. The pile-up suppression is capable to reduce pile-up on a variable extent which allows to adjust the analysis to individual needs and to optimize the tradeoff between pile-up rejection and detection efficiency. The measured pile-up suppression of 62.3 % with an efficiency loss of merely 0.71 % shows the capabilities of this method.

The studies concerning the charge cloud shape are just at the beginning, but the analysis of the maximal split ratio of quadruple events clearly shows that the idea of a spherical charge cloud distribution has to be questioned.

3. The HED: a CdTe-detector

The high energy detector (HED) is materialized by an 8 x 8 pixel CdTe hybrid detector module called Caliste-64 designed and produced by the CEA[2]* in Saclay, France [Meuris et al., 2008, 2009]. Figure 3.1 shows the module and its integration in the HED setup. An introduction to CdTe-based detectors is presented in the first four sections. Intrinsic properties of CdTe that are crucial for the understanding of the detector properties are discussed in Sect. 3.1. In Sect. 3.2, the phenomenon of crystal polarization and its impact on spectroscopic measurements is introduced. A quantitative analysis of the polarization effect and its temporal evolution is given in Sect. 3.3 and Sect. 3.4. The next two sections are focused on the hardware configuration of Caliste-64 (Sect. 3.5) and the offline data processing analysis (Sect. 3.7). The resulting spectroscopic performance of the HED and conclusions on its operational stability are presented in Sect. 3.8.

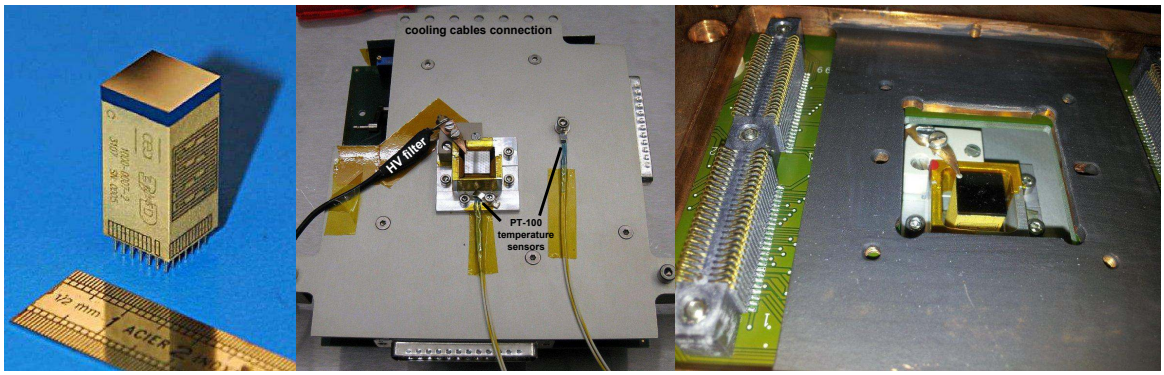

Figure 3.1. Left: Caliste-64, an 8 x 8 pixel CdTe detector with integrated readout electronics. The module size is 10 x 10 x 20 mm^3. Image: Meuris et al. [2009].
Center: Caliste-64 installed in the HED vacuum PCB. The aluminium plate is used for cooling and is connected via copper cables to the cold finger. The module is surrounded by an aluminium cooling funnel and is in thermal contact to it via cooling pads. The HV filter is implemented as an RC low-pass filter and included in the high voltage connection cable, as close as possible to the cathode of the crystal. Pt-100 temperature sensors measure the temperature of the aluminium plate and the aluminium funnel.
Right: the HED is installed 10 mm behind (in terms of the direction of irradiation) the LED which is not installed in this image. The LED is in direct contact to the large, black cooling mask. The HED cooling pads are not installed in this image.

* The *Commissariat à l'énergie atomique et aux énergies alternatives* (CEA[2]) is a French government-funded technological research organization.

3.1. The CdTe band structure

CdTe is a direct semiconductor consisting of cadmium and tellurium in a zincblende structure*. Several energy levels are located within the large band gap of $E_G \approx 1.47\,eV$. Besides substitutional defects†, vacancy defects, interstitial defects‡ and antisite defects§ form midgap levels at different energies. This section focuses only on deep acceptor levels (DALs) originating from Cd vacancies, as they are key to understand the polarization effect of CdTe. Because of the lower vapor pressure of Cd compared to Te, Cd vacancies originate during crystal growth and spread homogeneously over the whole crystal. The number density¶ n_T of the Cd vacancies and the distance between their energy level E_T and the top of the valence band E_V have typical values of $n_T = 4.56 \cdot 10^{12}\,cm^{-3}$ and $E_T - E_V = 0.69\,eV$ [Toyama et al., 2006]; see the band diagram of CdTe in Fig. 3.2.

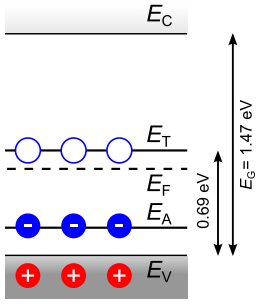

Figure 3.2. Band diagram of p-type CdTe with acceptor levels at E_A.

3.1.1. The HED, a CdTe-Al Schottky device

The HED is built as a Pt-CdTe-Al Schottky device. This means that the 1 mm thick CdTe crystal is contacted on one side by a common platinum layer and on the opposite side by pixelated aluminium contacts. In principle, metal-semiconductor junctions can create ohmic and Schottky contacts. For the HED, the high work function of platinum (5.65 eV) results in an ohmic contact while the lower work function of aluminium (4.28 eV) produces a Schottky contact [Michaelson, 1977].

At the Schottky contact charges are redistributed until the Fermi levels of the metal and of the semiconductor are identical. This results in an intrinsic band bending of the semiconductor's conduction band‖ (with energy E_C), the deep acceptor level (E_T), the acceptor level (E_A) and the valence band (E_V), by an amount of ΔE_F, the difference between the Fermi levels of the unconnected metal and the semiconductor, see Fig. 3.3.

The band bending creates a region without free charge carriers but with fixed space charges. The space charge number density n_{ion} is a result of shallow and deep ionized acceptor levels. Assuming a constant space charge density within the depletion region, the depletion width W in the semiconductor can be calculated as [Sze, 1981, 3.2.2]

$$W = \sqrt{\frac{2\epsilon_0\epsilon_r}{q_e\, n_{ion}}\left(U_{bi} - U - \frac{k_B T}{q_e}\right)} \tag{3.1}$$

* The zincblende structure consists of two atom types arranged as regular tetrahedrons in a way that the closest neighbors of an atom are always atoms of the other type.
† In a substitutional defect, impurities are placed on the position of a Cd or Te atom.
‡ In an interstitial defect, an atom is placed outside the crystal lattice.
§ In an antisite defect, a Cd atom is at the place of a Te atom, or vice versa.
¶ Deep acceptor levels are associated with charge traps. Therefore, the index 'T' is used.
‖ Band bending occurs also in the metal but the Debye length is so short that all charges tunnel through the barrier.

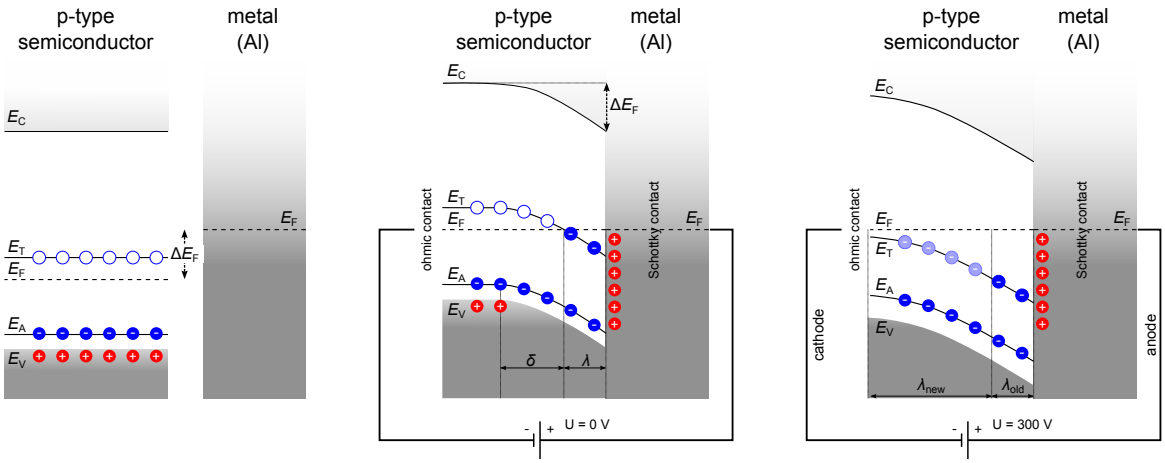

Figure 3.3. Illustration of band bending in a Schottky p-semiconductor contact. The vertical direction represents energy levels, while the horizontal direction represents the spatial distance rectangular to the Schottky contact layer.
Left: metal and semiconductor without interaction have different Fermi levels E_F.
Center: in contact, the Fermi level of the semiconductor is pulled-up to the Fermi level of the metal. Far away from the Schottky contact all levels in the semiconductor are shifted by ΔE_F, while they keep their energy level directly at the contact. This results in a "normal" band bending of width δ and of an additional bending of width λ because of new ionized states. $\delta + \lambda$ defines the space charge region.
Right: applying a reverse voltage to the Schottky contact enhances the band bending. Now, all deep acceptor levels are below the Fermi level and can get ionized with time. The additional ionized states are colored in pale blue.

with the dielectric constant for CdTe $\epsilon_r = 10.2$ [Madelung, 1982], the elementary charge q_e, the built-in voltage $U_{bi} \approx \Delta E_F/q_e$, the external voltage U, and the thermal voltage $k_B T/q_e \approx 1/40\,V$ at $T = 300\,K$. In semiconductor detectors, the applied external voltage is much higher than the built-in or the thermal voltage. This leads to the following approximation:

$$W[\mathrm{mm}] \approx 33578 \cdot \sqrt{\frac{-U[\mathrm{V}]}{n_{ion}[\mathrm{cm}^{-3}]}} \qquad \text{for } U \ll -10\,V \tag{3.2}$$

In the case of a reverse biased crystal, a rough estimation of n_{ion} can be obtained by assuming that the concentration of ionized charges equals the concentration of free charge carriers* $n_{ion} \approx n_{free}$. With $n_{ion} \approx 10^8\,cm^{-3}$ and $U = 300\,V$, the depletion

* The free charge carrier concentration n_{free} for elementary semiconductors (like Si or Ge) is equal to the doping concentration. For semiconductor compounds like CdTe the case is more difficult because different native defects compensate each other [Biswas and Du, 2012]. The easiest way to estimate n_{free} is to measure the resistivity (Funaki et al. [1999] reports $\rho \approx 10^9\,\Omega$cm for a CdTe crystal grown by traveling heater method as used for the HED crystal) and to calculate the free charge carrier concentration with the help of the hole mobility $\mu_h = 100\,cm^2/(Vs)$ (Tab. 1.1) and the elementary charge q_e to $n_{free} = (\rho \mu_h q_e)^{-1} \approx 6.3 \cdot 10^7\,cm^{-3}$.

width $W \approx 58\,\text{mm}$ becomes much larger than the detector thickness $d = 1\,\text{mm}$. In summary, these numbers show that if only the free charge carriers contribute to the density of ionized charges, a fully depleted CdTe crystal can be achieved easily, even with low depletion voltages. The phenomenon of crystal polarization shows that this is not the case.

3.2. The phenomenon of crystal polarization

Since the early 1970's (e.g. Bell [1974], Malm and Martini [1974]) it is observed that CdTe based radiation detectors are not stable under operational conditions. The observed effects are the following:

- decrease of the **counting rate**: the detector seems to lose quantum efficiency over time. From an observational point of view, the spectral flux becomes smaller during the time of observation.
- decrease of the **charge collection efficiency** (CCE): the spectrum is shifted to lower pulse heights (energies) during the time of observation.

The decrease of the CCE starts directly after the depletion of the crystal with a very small spectral shift of $\sim$10 eV/h if the detector is cooled to a temperature of $T = 0°\text{C}$ [Meuris et al., 2011]. After the polarization time t_{pol}, the flux starts to decrease and the spectral shift becomes so prominent that the detector is no longer usable as a spectroscopic device. A short reset of the depletion voltage restores the initial performance. Therefore, the phenomenon is known as bias induced polarization effect. The term *polarization* arises from accumulated space charge inside the CdTe crystal i.e. the crystal is electrically polarized. Crystal polarization is caused by the Fermi level crossing of deep acceptor levels which originates from the following two effects:

- **enhanced band bending:** the depletion voltage U bends all states in the semiconductor to lower levels. Especially the deep acceptor levels can be bent under the Fermi level and contribute to n_{ion}, see Fig. 3.3 (right).
- **increase of the Fermi level** due to the depletion voltage U. This effect is described in Matz and Weidner [1998] and can be understood as the reverse process of lowering the Fermi level with p-doping. In a depleted semiconductor without photoionization, free charge carriers can only be generated thermally. This results in an equal amount of majority and minority charge carriers (with densities p and n). The intrinsic condition $p = n$ is approached so that the Fermi level under biased conditions $E_{\text{F}_{\text{bias}}}$ will increase with respect to its unbiased value E_{F_0} according to [Sze, 1981, 1.4.3, Eq. (47)]

$$E_{\text{F}_{\text{bias}}} = E_{\text{F}_0} + \text{k}_\text{B}T \cdot \ln\left(p_0/p_{\text{bias}}\right) \approx E_{\text{F}_0} + 90\,\text{meV}. \tag{3.3}$$

  This calculation assumes a temperature $T = 15\,°\text{C}$, an intrinsic majority charge density $p_0 = 6 \cdot 10^7\,\text{cm}^{-3}$, and a majority charge density under biased conditions $p_{\text{bias}} = 1.6 \cdot 10^6\,\text{cm}^{-3}$.

Both effects result in deep acceptor levels that are located below the Fermi level, i.e. that are likely to become ionized by capturing electrons and enhance n_{ion}. To understand why these effects can cause the polarization effect Eq. (3.1) serves as a first intuitive view.* The increase of the space charge number density n_{ion} reduces the depletion width proportional to $1/\sqrt{n_{\text{ion}}}$. So, a fully depleted detector volume can become partially depleted if a large fraction of the deep acceptor levels becomes ionized.

To understand the effects of crystal polarization, the electric field inside the crystal must be investigated in more detail. Figure 3.4 illustrates qualitatively the electric field distribution inside a medium of thickness d with an applied depletion voltage U; see the following section for a quantitative calculation. In the ideal case, the electric field is constant and signal charge separation is uniform† in the whole medium, i.e. independent of the absorption depth z (case a) in Fig. 3.4).

The Schottky band bending and the additional band bending by ionized deep acceptors amplify the electric field close to the anode because of the space charge in that region. The field at the cathode must be reduced correspondingly to conserve the voltage U:

$$\int_0^d E(z)\,\mathrm{d}z = U = \text{const.} \tag{3.4}$$

The detector becomes polarized if a part of the crystal has a vanishing electric field and cannot longer contribute to signal generation (case c) in Fig. 3.4).

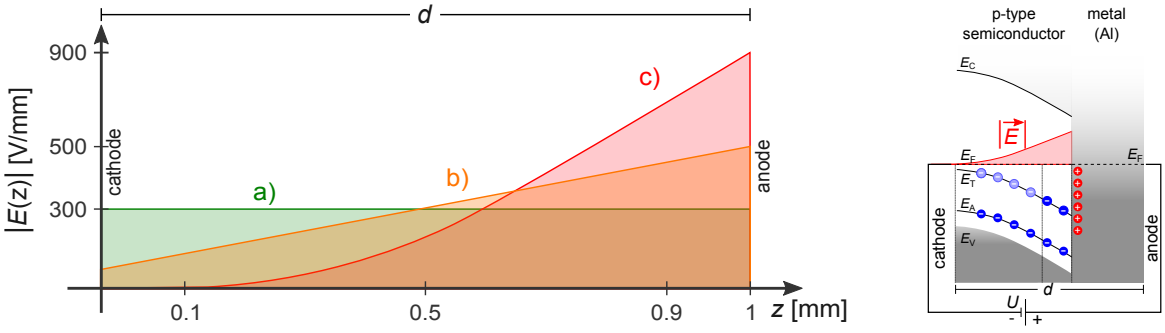

Figure 3.4. Qualitative diagram of different electric field distributions in a 1 mm thick detector. The cathode is located at $z = 0$ mm and the readout anode at $z = 1$ mm. The depletion voltage is $U = 300$ V in all cases. The Schottky contact of Fig. 3.3 with indicated electric field (red) is shown on the right.
a) Ideal case: constant electric field in the complete detector volume.
b) Electric field distribution according to the Schottky contact.
c) Electric field distribution of a Schottky contact in a polarized medium. The detector becomes insensitive near the cathode ($z < 0.1$ mm).

* Eq. (3.1) only applies for a constant distribution of n_{ion} under equilibrium conditions. Both assumptions are not valid for a polarized CdTe crystal.

† This does not imply a uniform signal generation. Despite the constant electric field, the contribution of signal charges to the detector output signal depends on the absorption depth z because of charge trapping that differs for electrons and holes. See Sect. 1.3 for details on this issue.

3.3. The polarization effect: a quantitative view

As shown in the previous section, crystal polarization is caused by the ionization of deep acceptor levels that changes the amount of space charge and hence the electric field distribution. The following calculations assume a detector consisting of a CdTe crystal (with the space charge number density n_{ion}) which is depleted by the voltage U. A quantitative investigation of crystal polarization can be done in four steps.

1. Assume a space charge density ρ.
2. Calculate the electric field E.
3. Calculate the charge collection efficiency CCE.
4. Find a model for the space charge density evolution with time, see Sect. 3.4.

The **space charge density** $\boldsymbol{\rho}$ must be known or assumed in a reasonable way. A uniform distribution of ionized acceptors can be assumed*:

$$\rho = -\mathrm{q_e} n_{\mathrm{ion}} \tag{3.5}$$

The resulting **electric field** $\boldsymbol{E}$ can be calculated with Poisson's equation:

$$\Delta\Phi = -\vec{\nabla}\vec{E} = -\frac{\rho}{\epsilon_0 \epsilon_{\mathrm{r}}} \tag{3.6}$$

With $a = \mathrm{q_e} n_{\mathrm{ion}}/(\epsilon_0 \epsilon_{\mathrm{r}})$ Matz and Weidner [1998] calculated the penetration depth of the electric field

$$z_{\mathrm{E}} = \sqrt{2U/a} \tag{3.7}$$

and the electric field E as:

$$E(z) = 0 \qquad | \, z \leq d - z_{\mathrm{E}},\ z_{\mathrm{E}} \leq d \tag{3.8}$$

$$= a\,(z - d + z_{\mathrm{E}}) \qquad | \, z > d - z_{\mathrm{E}},\ z_{\mathrm{E}} \leq d \tag{3.9}$$

$$= a\left(z - \frac{d}{2}\right) + \frac{U}{d} \qquad | \, z_{\mathrm{E}} > d \tag{3.10}$$

The electric field distribution within the detector medium depends on the width d of the crystal, the applied depletion voltage U, and the space charge density which is represented by the number of ionized acceptors n_{ion}. The crystal is fully depleted if $z_{\mathrm{E}} > d$ (Fig. 3.5, green), i.e. for large depletion voltages and for a small number of ionized acceptors. If $z_{\mathrm{E}} < d$ (Fig. 3.5, red) the electric field vanishes near the cathode and the detector is insensitive in this region.

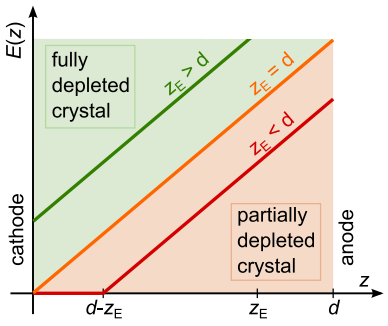

Figure 3.5. The electric field E assuming uniformly ionized acceptors.

* This holds if all acceptors within a region $0 \leq z \leq z_{\mathrm{E}}$ are ionized and the region is free from charge carriers. The charge density is then created by uncompensated deep acceptors [Stallinga, 2009, § 1.5.2].

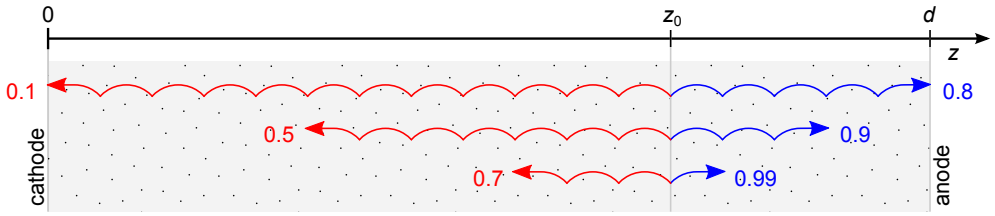

Figure 3.6. Representation of the modified Hecht equation (Eq. (3.12)). The rippled lines represent the traveling of an electron (blue) or a hole (red), starting at z_0. The (fictional) numbers at the end of each line are the probabilities ρ_h and ρ_e that the charge can travel the distance $|z - z_0|$. See also the left part of Fig. 3.7.

The **charge collection efficiency** (*CCE*) can be calculated with the help of the Shockley-Ramo theorem which states that the detector signal is generated by drifting signal charges; see Sect. 1.3 for details. The mean drift lengths for electrons and holes

$$L_\mathrm{e} = \mu_\mathrm{e}\tau_\mathrm{e}E \qquad \text{and} \qquad L_\mathrm{h} = \mu_\mathrm{h}\tau_\mathrm{h}E \tag{3.11}$$

depend on the mobility-lifetime product $\mu\tau$ and the electric field E. The *CCE* can be calculated with a modified version of the Hecht equation*:

$$Q_\mathrm{det}(z_0) = \frac{Q_0}{d}\left\{ \underbrace{\int_0^{z_0} \underbrace{\exp\left[-\int_z^{z_0} \frac{\mathrm{d}z'}{L_\mathrm{h}(E(z'))}\right]}_{\rho_\mathrm{h}(z)} \mathrm{d}z}_{d_\mathrm{h}} + \underbrace{\int_{z_0}^{d} \underbrace{\exp\left[-\int_{z_0}^{z} \frac{\mathrm{d}z'}{L_\mathrm{e}(E(z'))}\right]}_{\rho_\mathrm{e}(z)} \mathrm{d}z}_{d_\mathrm{e}} \right\} \tag{3.12}$$

Because of charge trapping, the measured charge Q_det is smaller than the signal charge Q_0 which is originally generated in a distance z_0 from the cathode. The charge collection efficiency is defined as $CCE = Q_\mathrm{det}/Q_0$. Equation (3.12) becomes Eq. (1.20) for a constant electric field E.

Figure 3.6 explains the idea of Eq. (3.12) graphically. Charge trapping has to be considered as a statistical process and can only be studied in the context of averaged values. The drifting of holes (index h) and of electrons (index e) contributes to the total signal according to their individual mean drift lengths L_h and L_e and must be considered separately. In Eq. (3.12) the innermost integrals over z' take the z-dependence of the mean drift lengths $L_\mathrm{h}(E)$ and $L_\mathrm{e}(E)$ into account. The exponential terms in color, the signal length distributions $\rho_\mathrm{h}(z)$ and $\rho_\mathrm{e}(z)$, are the probabilities that a drifting charge carrier reaches the depth z. The signal lengths d_h and d_e, calculated by integrating these distributions over all possible drift lengths, can be interpreted as averaged drift lengths. In this sense, the *CCE* is proportional to the area under the signal length distributions $\rho_\mathrm{h}(z)$ and $\rho_\mathrm{e}(z)$, see Fig. 3.7 (left).

The signal length distributions and the charge collection efficiency can be calculated† by inserting Eq. (3.11) and Eqs. (3.7 - 3.10) in Eq. (3.12):

* In the original publication, Hecht [1932] shows the dependence of the *CCE* on the drift length. Kubicki et al. [1994] extend the theory to non-uniform electric fields.

† This calculation can be found in Matz and Weidner [1998]. Be aware of a typing error in their Eq. (9).

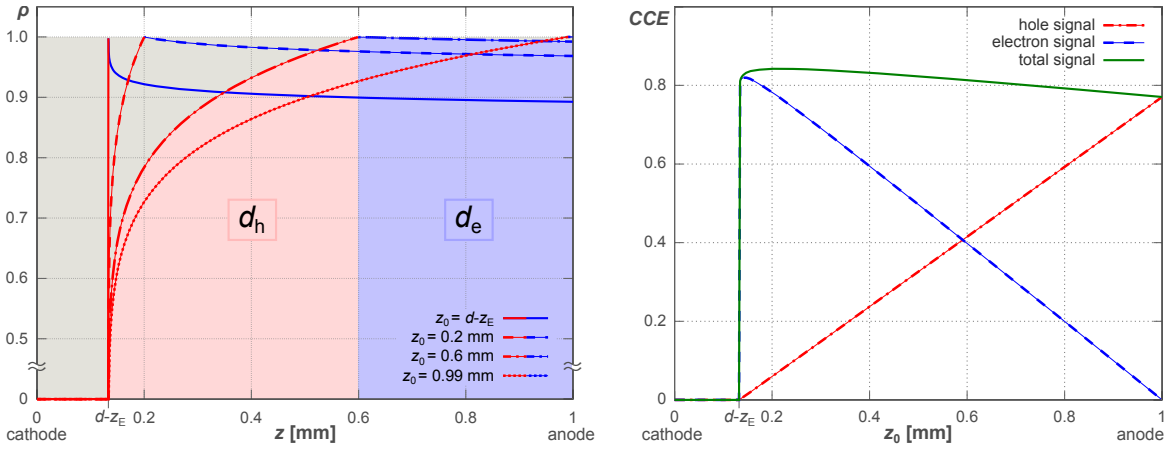

Figure 3.7. Calculated charge collection efficiency for a 1 mm thick CdTe detector with a depletion voltage of $U = 300\,\mathrm{V}$, mobility-lifetime products of $\mu_\mathrm{h}\tau_\mathrm{h} = 10^{-4}\,\mathrm{cm^2/V}$, $\mu_\mathrm{e}\tau_\mathrm{e} = 10^{-3}\,\mathrm{cm^2/V}$, and a trap density of $n_\mathrm{ion} = 0.1 \cdot n_\mathrm{T} = 4.5 \cdot 10^{11}\mathrm{cm^{-3}}$. The electric field penetrates the crystal from the anode ($z = 1\,\mathrm{mm}$) up to $d - z_\mathrm{E} = 0.133\,\mathrm{mm}$.
Left: signal length distribution ρ as a function of the crystal depth z for four different photon absorption depths z_0. In the case $z_0 = 0.6\,\mathrm{mm}$, the signal lengths for holes d_h and for electrons d_e are indicated as red and blue areas. The ratio between the colored area $d_\mathrm{h} + d_\mathrm{e}$ and the gray area (range: $0\,\mathrm{mm} \le z \le 1\,\mathrm{mm}$ and $0 \le \rho \le 1$) equals the charge collection efficiency.
Right: charge collection efficiency as a function of the signal generation depth z_0. Charge deposited in the undepleted region $0 \le z \le d - z_\mathrm{e}$ recombines directly because of the vanishing electric field. In the active region $d - z_\mathrm{e} < z \le 1\,\mathrm{mm}$, the total *CCE* is only weakly dependent on z, despite the very different contributions of electron and hole signals.

$$CCE(z) = 0 \qquad \big|\, z \le d - z_\mathrm{E},\ z_\mathrm{E} \le d \tag{3.13}$$

$$= \frac{1}{d}\left\{ \frac{\mu_\mathrm{e}\tau_\mathrm{e}a}{\mu_\mathrm{e}\tau_\mathrm{e}a - 1}\left[z_\mathrm{E}\left(\frac{z - d + z_\mathrm{E}}{z_\mathrm{E}}\right)^{1/(\mu_\mathrm{e}\tau_\mathrm{e}a)} - z + d - z_\mathrm{E}\right] + \right.$$

$$\left. \frac{\mu_\mathrm{h}\tau_\mathrm{h}a}{\mu_\mathrm{h}\tau_\mathrm{h}a + 1}\left[z - d + z_\mathrm{E}\right]\right\} \qquad \big|\, z > d - z_\mathrm{E},\ z_\mathrm{E} \le d \tag{3.14}$$

$$= \frac{1}{d}\left\{ \frac{\mu_\mathrm{e}\tau_\mathrm{e}a}{\mu_\mathrm{e}\tau_\mathrm{e}a - 1}\left[\left(\beta + \frac{d}{2}\right)\left(\frac{\beta - d/2 + z}{\beta + d/2}\right)^{1/(\mu_\mathrm{e}\tau_\mathrm{e}a)} - z + d/2 - \beta\right]\right.$$

$$\left. \frac{\mu_\mathrm{h}\tau_\mathrm{h}a}{\mu_\mathrm{h}\tau_\mathrm{h}a + 1}\left[\beta - d/2 + z - (\beta - d/2)\left(\frac{\beta - L/2}{\beta - L/2 + z}\right)^{1/(\mu_\mathrm{h}\tau_\mathrm{h}a)}\right]\right\}$$

$$\big|\, z_\mathrm{E} > d \tag{3.15}$$

$$\text{with } a = \frac{\mathrm{q_e}n_\mathrm{ion}}{\epsilon_0\epsilon_\mathrm{r}},\ \beta = \frac{U}{ad} \text{ and } z_\mathrm{E} = \sqrt{\frac{2\epsilon_0\epsilon_r U}{\mathrm{q_e}n_\mathrm{ion}}}. \tag{3.16}$$

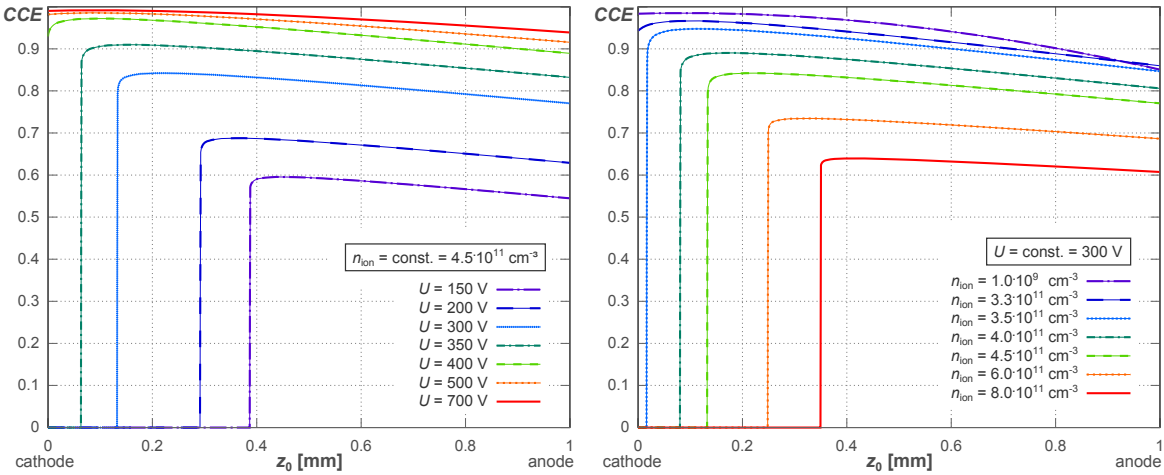

Figure 3.8. The charge collection efficiency *CCE* according to Eqs. (3.13 - 3.16) as function of the signal generation depth z_0 for different depletion voltages U (left) and trap densities n_{ion} (right). More details can be found in the description of Fig. 3.7.

Figure 3.7 (right) shows the charge collection efficiency for a partially depleted detector, which is maximal for photon absorptions close to $z = d - z_{\mathrm{E}}$. In this representative example, the *CCE* varies less than 10 % for different photon absorption depths within the depleted volume. The influence of crystal polarization on the *CCE* depends on the β-parameter defined in Eq. (3.16) which depends in turn on the ratio U/n_{ion}. Figure 3.8 shows the *CCE* for different depletion voltages U and acceptor densities n_{ion}. A large value of β is favorable for spectroscopic measurements because of the following reasons:

- At small values of β, the crystal can be only partially depleted. Radiation absorbed in the undepleted volume creates signal charges that recombine directly and can not be detected. A decreasing value of β reduces the quantum efficiency of the detector and results in a decreasing observed flux.
- The *CCE* in the depleted detector volume decreases for lower values of β, irrespective of whether the detector is fully depleted or not. As a consequence, mono-energetic photons are detected with smaller pulse heights for decreasing values of β.
- For small values of β, the low energetic part of the spectrum degrades more strongly as the high energetic part. The polarization effect is more pronounced for low energy photons, because their shorter penetration depths result in an interaction near the entrance window (cathode) where the electric field is weak or even vanishes.

Experimentally observed crystal polarization showing all three mentioned effects is presented in Fig. 3.28. The β-factor can be increased by using thinner crystals which diminishes the quantum efficiency of the detector at high energies or by increasing the depletion voltage which increases also the dark-current noise. The third important quantity to increase β, the crystal temperature, is discussed in the next section.

3.4. Timing evolution of crystal polarization

According to Eq. (3.2) an original concentration of ionized charges of $n_{\mathrm{ion},0} \approx 10^8\,\mathrm{cm}^{-3}$ (see the footnote on page 99 for details of the calculation) results in a theoretical depletion width of $W \approx 58\,\mathrm{mm}$ for $U = 300\,\mathrm{V}$, i.e. the detector is fully depleted. Doing the same calculation assuming that all deep acceptors are ionized $n_{\mathrm{ion}} = n_{\mathrm{T}} \approx 10^{12}\,\mathrm{cm}^{-3}$ [Toyama et al., 2006] results in a strong polarized crystal which is only partially depleted with a depletion width of $W = 0.58\,\mathrm{mm}$.

Fortunately, it takes some time to ionize all deep acceptors. The fact that the Fermi level is above the deep acceptor level does not mean that all levels are ionized immediately, but that a large fraction of it will be ionized under equilibrium conditions. The polarization time t_{pol} states how fast the system approaches equilibrium. After t_{pol} a fraction of the deep acceptor levels is ionized and the electric field is deformed in a way that it vanishes close to the cathode. The characteristic time constant τ_{i} that governs the ionization rate of the deep acceptors is given by [Toyama et al., 2006]

$$\tau_{\mathrm{i}} = \frac{1}{n_{\mathrm{V}}\,\sigma\,v_{\mathrm{h}}} \cdot \mathrm{e}^{\frac{E_{\mathrm{T}}-E_{\mathrm{V}}}{\mathrm{k_B}T}} \tag{3.17}$$

with the cross section for deep acceptor ionization σ, the thermal velocity of holes v_{h}, and the Boltzmann constant $\mathrm{k_B}$. For a given temperature T, this time constant depends on the effective density of states for the valence band n_{V} and on the energy difference between the deep acceptor level E_{T} and the top of the valence band E_{V}. Assuming that no deep acceptors are ionized at the moment the depletion voltage is applied ($t = 0$), the number density of ionized deep acceptors n_{ion} can be calculated via

$$\frac{\mathrm{d}n_{\mathrm{ion}}}{\mathrm{d}t} = \frac{n_{\mathrm{T}} - n_{\mathrm{ion}}}{\tau_{\mathrm{i}}} \quad \Leftrightarrow \quad n_{\mathrm{ion}}(t) = n_{\mathrm{T}}\left(1 - \mathrm{e}^{-t/\tau_{\mathrm{i}}}\right) \tag{3.18}$$

If the depletion voltage is turned off, the deep acceptor levels are positioned above the Fermi level and deionization of the ionized deep acceptors starts. Deionization can be described with the time constant τ_{d} [Bell, 1974]

$$\tau_{\mathrm{d}} = \frac{1}{n_{\mathrm{V}}\,\sigma\,v_{\mathrm{h}}} \tag{3.19}$$

and occurs much faster than ionization because no energy barrier is involved in the process. With the initial number density of ionized deep acceptors $n_{\mathrm{ion},0}$ the temporal evolution of n_{ion} is

$$\frac{\mathrm{d}n_{\mathrm{ion}}}{\mathrm{d}t} = -\frac{n_{\mathrm{ion}}}{\tau_{\mathrm{d}}} \quad \Leftrightarrow \quad n_{\mathrm{ion}}(t) = n_{\mathrm{ion},0}\,\mathrm{e}^{-t/\tau_{\mathrm{d}}} \tag{3.20}$$

Elhadidy et al. [2007] shows n_{V} and v_{h} as a function of the temperature T:

$$n_{\mathrm{V}} = 4.829 \cdot 10^{15}\left((m_{\mathrm{h}}^*/m_{\mathrm{e}})\,T\right)^{3/2} \quad \mathrm{cm}^{-3}\mathrm{K}^{-3/2} \tag{3.21}$$

$$v_{\mathrm{h}} = 6.743 \cdot 10^{5}\sqrt{T/(m_{\mathrm{h}}^*/m_{\mathrm{e}})} \quad \mathrm{cm\,s}^{-1}\mathrm{K}^{-1/2} \tag{3.22}$$

The effective mass of holes in CdTe is reported with $m_h^* = 0.35\,m_e$ [Khlyap and Sydorchuk, 2001]. Using Eq. (3.21) and Eq. (3.22) with Eq. (3.17) allows to calculate the ionization time constant τ_i as a function of the temperature T for different ionization cross sections σ and acceptor depths $E_T - E_V$. The polarization time t_{pol}, defined as the time at which the electric field at the cathode starts to vanish, can be calculated with Eq. (3.18) and Eqs. (3.13 - 3.16). Figure 3.9 shows the calculated polarization time t_{pol} as a function of the temperature T for different ionization cross sections σ and acceptor depths $E_T - E_V$ assuming $U = 300\,V$ and $n_T = 10^{-12}\,cm^{-3}$.

In literature, values for the acceptor depth are reported with $0.60\,eV \leq E_T - E_V \leq 0.77\,eV$, see Meuris et al. [2011] and the references therein. Elhadidy et al. [2007] reports capture cross sections for near mid-gap levels of $\sigma \approx (10^{-15} - 10^{-17})\,cm^2$. The presented calculations allow to conclude on crystal parameters ($E_T - E_V$ or σ) by measuring the polarization time or to calculate t_{pol} for a given parameter set.

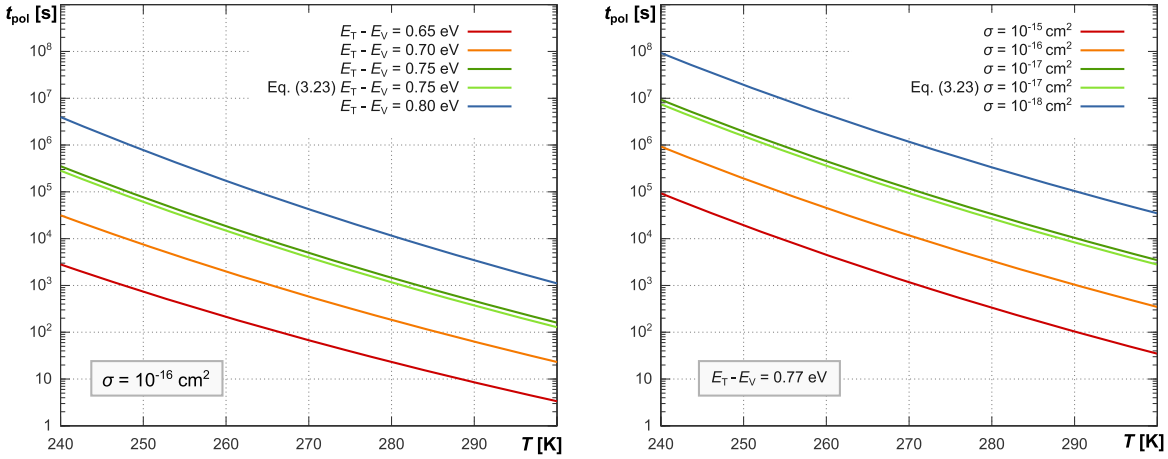

Figure 3.9. Polarization time t_{pol} as a function of the temperature T. The calculations are done with Eqs. (3.13 - 3.22) if not indicated otherwise. $U = 300\,V$, $d = 1\,mm$.

Besides the charge distribution presented in Eq. (3.5) more realistic and elaborate models can be studied with the same theoretical steps as presented. Toyama et al. [2006] suggested a $\lambda = 87\,\mu m$ thin permanently ionized region at the anode. In this region the deep acceptors are below the Fermi level, even in the unbiased case, see Fig. 3.3 (center). Meuris et al. [2011] calculated for this geometry the polarization time

$$t_{pol} \approx \frac{\tau_i}{d^2}\left(\frac{2\epsilon_r\epsilon_0}{q_e n_T}U - \lambda^2\right) \qquad \text{if } \frac{U}{d^2} \ll 10^3\,\frac{V}{mm^2} \tag{3.23}$$

which is also shown in Fig. 3.9. The temperature dependence in Eq. (3.23) is identical to the previous calculations as it depends solely on the ionization time constant τ_i. Equation (3.23) with Eq. (3.17) shows that the polarization time depends on material properties of CdTe (number density n_T and energy level E_T of the deep acceptors), the geometry of the detector (detector width* d), and the conditions of operation (temperature T and applied voltage U). See Fig. 3.30 for measured values of t_{pol}.

* In Meuris et al. [2011] it is also mentioned that contrary to Eq. (3.23) $t_{pol} \sim 1/d^3$ fits better to their experimental results.

3.5. Hardware configuration of Caliste-64

The high energy detector (HED) is realized by a 8 x 8 pixel hybrid detector called Caliste-64. The CdTe crystal is contacted on the photon entrance window with a common Pt-cathode and on the readout side of the crystal with pixel individual Al-anodes. The pixels are $900 \times 900\ \mu m^2$ in size with a 100 µm inter pixel gap surrounded by a 900 µm thick guard ring. See Fig. 3.10 for a sketch of Caliste-64. Each of the anodes is connected to a subsequent read-out channel* that performs a trigger analysis, signal shaping and amplification, as well as signal multiplexing. 16 read-out channels are combined in one of four ASICs† called *IDeF-X V1.1* that are directly underneath the CdTe crystal and form the electrical body of the camera. 49 input/output ports are used to establish the supply voltages, to configure parameters for detector operation (low-energy threshold, peaking time, disabling of pixels), and for signal output. See Meuris et al. [2009] for more details on Caliste-64.

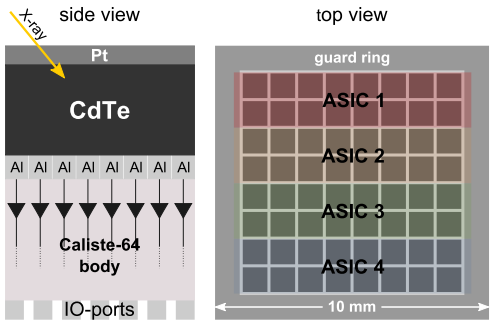

Figure 3.10. Caliste-64 in side view (not to scale) and top view (true to scale).

3.5.1. Readout process

Signal triggering and sampling

The HED operates in a triggered readout mode which means that the signal of a pixel is sensed‡ continuously and an event is detected if the pixel signal exceeds a low energy threshold. The readout process consists of a sequence of operations which are summarized in Fig. 3.11:

- **signal preamplification:** the charge sensitive preamplifier accumulates signal charges and dark currents. To prevent saturation, the resistor R_F discharges the feedback capacitor C_F continuously with a time constant τ_F.
- **pole-zero cancellation:** even though τ_F is much larger than the sampling time, the output of the preamplifier is no longer step like but exponentially decreasing which results in a baseline undershoot of the following pulse shaper output. Adding an additional resistor R_{pz} to the pulse shaper's differentiator corrects for this undershoot [Spieler, 2005, § 4.8.2] if

$$R_F C_F = R_{pz} C_{diff}. \tag{3.24}$$

* The term *Pixel* identifies the detector substructure of the crystal and is used for photon interactions, while *channel* identifies the readout electronics and is used in the context of signal processing.
† ASIC = application-specific integrated circuit.
‡ In this context, the term *sensed pixel signal* means that the charge is only compared to a threshold value but not measured accurately which is indicated by the term *sampling*.

- **pulse shaping:** the signal pulse is observed as a function of time. A Fourier transformation of the signal pulse shows that the signal power is also distributed at various signal frequencies (frequency space). To enhance the signal-to-noise ratio, the pulse shaper attenuates all frequencies that are not characteristic of the signal. In the easiest way, this is accomplished with a CR differentiator that attenuates all frequencies below the cutoff frequency $f_{\mathrm{c,\,low}} = 1/(2\pi R_{\mathrm{diff}} C_{\mathrm{diff}})$ followed by an RC integrator which attenuates all frequencies above

  $$f_{\mathrm{c,\,high}} = 1/(2\pi R_{\mathrm{int}} C_{\mathrm{int}}). \tag{3.25}$$

  Operations in frequency space change also the signal shape as a function of time, hence the name *pulse shaping*. The time constant of the integrator

  $$\tau_{\mathrm{int}} = R_{\mathrm{int}} C_{\mathrm{int}} \tag{3.26}$$

  defines the rise time of the pulse while the time constant of the differentiator $\tau_{\mathrm{diff}} = R_{\mathrm{diff}} C_{\mathrm{diff}}$ determines the pulse duration. In the case of Caliste-64, signal shaping is realized by a fourth order Sallen-Key-type shaper with an adjustable, global peaking time [Meuris et al., 2008].

- **peak detection and storage:** after the maximum of the pulse height is detected it is stored in an analog memory and multiplexed to a serial readout pin.

The detection mechanisms of the LED and the HED are fundamentally different. The LED operates in a continuous readout mode, i.e. the signal charge of the detector pixels are read out in continuous steps. Between the readout, the detector integrates all charges inside its sensitive volume. Dark currents result in an offset which must be first measured and later on subtracted from all data. See Sect. 2.7.1 for more details on the LED offset map. For the triggered readout mode of the HED, the continuous discharge of the preamplifier results in an offset free sampling.

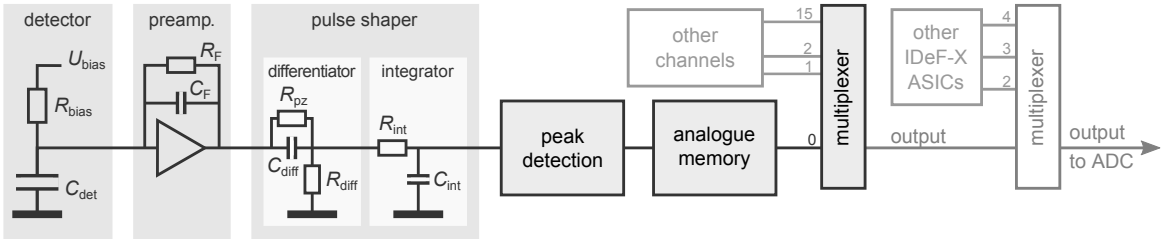

Figure 3.11. Simplified schematic diagram of a Caliste-64 readout channel (black) and its periphery (gray). The depleted CdTe crystal is shown as detector capacitance C_{det}. The charge sensitive preamplifier (preamp.) amplifies the signal pulse. A continuous reset is achieved via R_{F} and its resulting baseline undershoot is compensated by R_{pz}. The pulse shaper cuts the low frequent parts via the differentiator and the high frequent parts via the integrator out of the signal. The maximum of the signal peak is detected and stored in an analog memory. The multiplexing unit connects all 16 channels of one ASIC to one readout pin. The trigger mechanism is not shown in the figure.

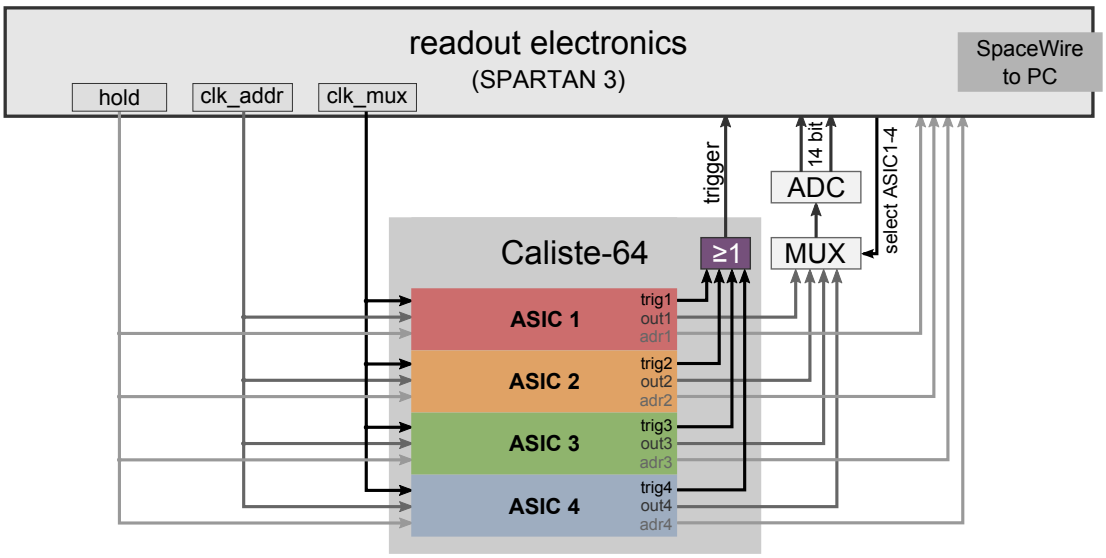

Figure 3.12. Simplified HED readout scheme: each ASIC has a common *hold*, *clk_addr*, and *clk_mux* input. The ASIC specific triggers *trig1* - *trig4* are joint within the Caliste body and constitute a global trigger. The signal outputs *out1* - *out4* are multiplexed into an ADC. See Fig. 3.13 for a temporal sequence of the shown signals.

The readout sequence of Caliste-64

If the measured signal of one channel exceeds the ASIC specific configurable threshold, the readout sequence between Caliste-64 and the readout electronics, a SPARTAN3 FPGA, is initiated. See Fig. 3.12 for a simplified readout scheme of the HED and Fig. 3.13 for a measured temporal sequence of the readout process.

1) **trigger:** a trigger signal indicates that an event occurred. The trigger threshold can be set ASIC individually. All four ASIC triggers are merged into a global trigger signal via an or-function of the ASIC specific trigger signals. Only the global trigger is connected to an output pin of Caliste-64.

2) **hold:** all ASICs wait a configurable, global lock time t_{lock}, during that the signal charge can evolve to its maximal value. After t_{lock}, Caliste-64 is set into a lock state where it holds its present state and is insensitive to new events.

3) **location:** the readout electronics checks how many and which channels have an active trigger by sending 16 pulses (*clk_addr*) and checking the response of each ASIC (*adr1* - *adr4*) in parallel. The number of all triggered channels is N.

4) **read-out:** the signal of each triggered channel is multiplexed to an ADC. The *clk_mux*, consisting of N pulses, steps through the analog memory of all four ASICS. The *select_ASIC1* - *select_ASIC4* signals are used to multiplex the different ASIC outputs to an ADC.

5) **reset:** after resetting all internal registers and buffers, Caliste-64 is ready to detect new events. The dead time t_{d} of the camera depends on the number of channels that have to be read out. For one channel it is $t_{\mathrm{d},1} \approx 66\,\mu\mathrm{s}$ while for all channels it is $t_{\mathrm{d},64} \approx 132\,\mu\mathrm{s}$, see Fig. 3.13.

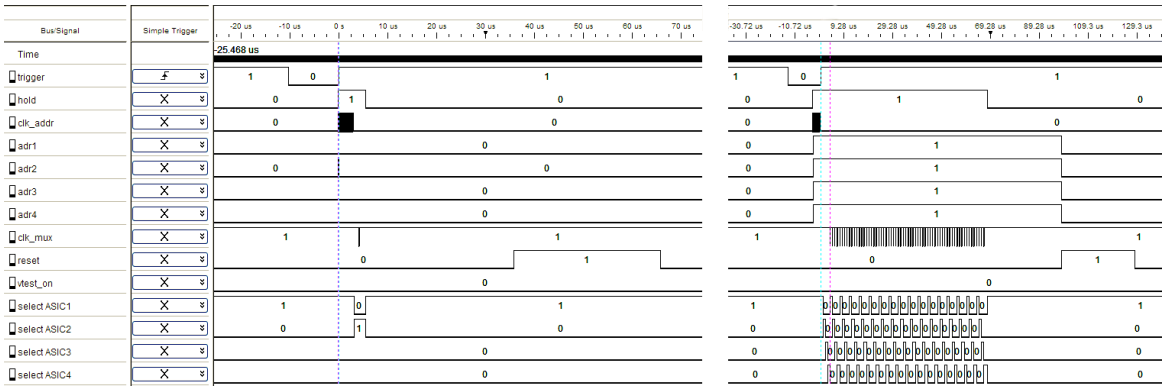

Figure 3.13. Temporal sequence of two HED readout processes following an external charge injection: the signals are labeled identical to those shown in Fig 3.12. The 16 pulses of *clk_addr* are not resolved in this image. In the left image, only one pixel has triggered. In the image on the right, all 64 pixels have triggered and are read out.

3.5.2. HED cooling environment

In order to operate the HED, crystal temperatures below 0°C are desirable to avoid crystal polarization within an observation time of several hours. Convective cooling in a cold, dry nitrogen atmosphere turned out to be efficient and allows crystal temperatures below 0°. A mounting plate and a cooling funnel around Caliste-64 (see Fig. 3.14), both made of aluminium, are in thermal contact with the cold finger of the CANDELA setup. For vacuum operation, the radiative cooling between Caliste-64 and the cooling funnel turned out to be insufficient and an additional conductive cooling system was introduced using thermal pads positioned between the cooling funnel and the Caliste-64 body. The material of the thermal pads must have the following properties: a high thermal conductivity, a low outgassing rate, a malleable consistency with gap filling characteristics, and an electrically isolating property. The silicone elastomer *Tpli 280* fulfills all requirements and is positioned between the Caliste body and the cooling funnel via Kapton tape. Pt-100 temperature sensors are positioned at the cooling funnel and the mounting plate to check the temperature conditions during detector operation. See Fig. 3.15 for a picture of the installed Caliste-64.

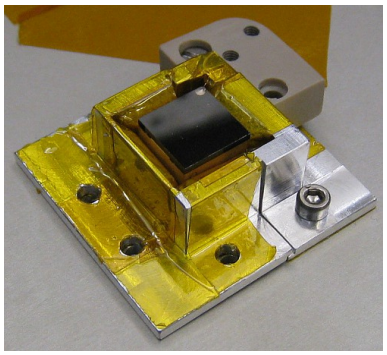

Figure 3.14. Caliste-64 with cooling plate and cooling funnel. The gap filling material is positioned between the Caliste body and the cooling funnel via Kapton tape (yellow).

3.5.3. HED high voltage connection

The high voltage connection, necessary for crystal depletion, is applied between the pixel individual Al-anodes and the common, planar Pt-cathode. The cathode is not connected via an I/O-pin of Caliste-64 but via an external copper pin that is pressed down on a conductive epoxy drop located at the edge of the cathode, see Fig. 3.15. This configuration enables an easy and safe demounting of Caliste-64. To suppress noise coupling into the detector signal via the high voltage connection, an RC-RC low-pass filter is installed within the HV coaxial cable as close as possible to the detector cathode. The HV connection is designed in a flat style to enable a close positioning of the HED and the LED.

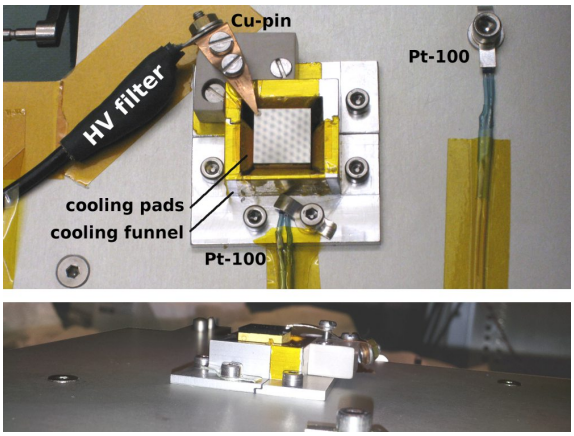

Figure 3.15. Caliste-64 with external high voltage (HV) pin connection. The low-pass filter, is located within the HV coaxial cable as close as possible to the detector cathode. The lower image shows the flat construction of the HV connection.

3.5.4. HED timing accuracy

HED events are tagged with a seconds counter and a subseconds counter. The subseconds counter is based on the system clock of the HED electronics ($f = 100\,\mathrm{MHz}$) and therefore increased in time steps of 10 ns. Considering the HED photon detection process reveals that the time accuracy is limited by other effects. The signal pulse results from drifting signal charges and has a duration that can be estimated for a constant electric field $|\vec{E}|$ via

$$t = s/(\mu \cdot |\vec{E}|) \tag{3.27}$$

with the drift distance s and the mobility μ (see Tab. 1.1). For a photon absorption near the cathode, i.e. for a pure electron drift, or for an absorption near the anode, i.e. for a pure hole drift, the corresponding pulse widths are $t_\mathrm{e} \approx 30\,\mathrm{ns}$ and $t_\mathrm{h} \approx 330\,\mathrm{ns}$, assuming $s = 1\,\mathrm{mm}$ and $|\vec{E}| = 300\,\mathrm{V/mm}$. Calculating the mean absorption depth $\bar{z}$ and the variation of the absorption depth Δz allows to estimate the mean signal duration $\bar{t}_\mathrm{drift}$ and the variation of the signal duration Δt_drift. The details of this calculation are summarized in Appendix D.6. The results, presented in Fig. 3.16, show that the mean drift duration is almost constant $\bar{t}_\mathrm{drift} = 80\,\mathrm{ns}$ for photon energies $E \geq 80\,\mathrm{keV}$ and the one sigma variation is less than 60 ns for all energies.

The event time tag is defined by the time of the event trigger. The trigger analysis is based on the output signal of the pulse shaper which has a typical peaking time of 10 µs. The delay between the photon absorption and the trigger time of the channel is defined as *time-walk* $\Delta t_\mathrm{w}(z_0, E, E_\mathrm{th}, t_\mathrm{p})$ which depends on the absorption depth of the photon z_0, the event energy E, the detection threshold E_th, and the peaking time of the shaper t_p, see Fig. 3.17. The *mean* time-walk $\overline{\Delta t_\mathrm{w}}(E, E_\mathrm{th}, t_\mathrm{p})$ is averaged over all

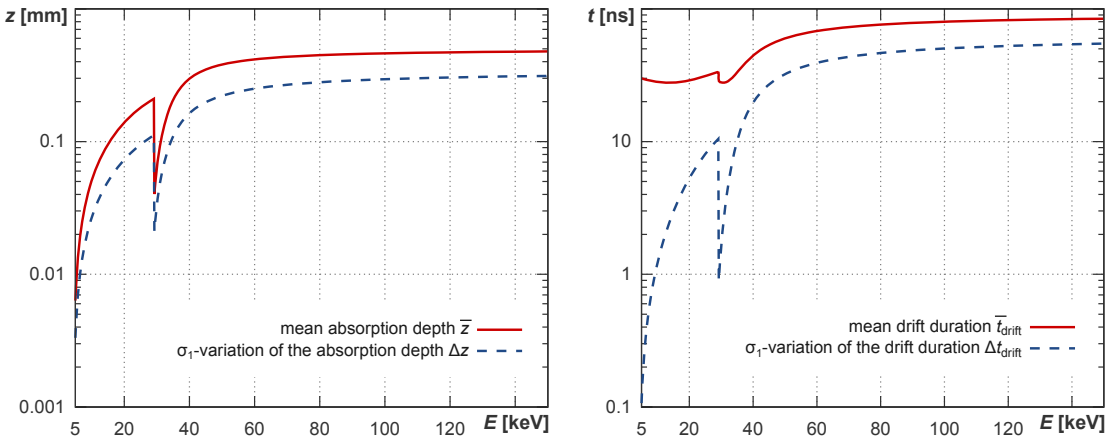

Figure 3.16. Calculated signal formation for the HED (see Appendix D.6). The X-ray mass attenuation coefficients for CdTe are approximated with the ones for tin and based on Hubbell and Seltzer [2007]. The K-edge of tin is located at 29.2 keV while for cadmium it is 26.7 keV and for tellurium it is 31.8 keV. The thickness of the detector substrate $d = 1\,\text{mm}$ and an electric field $|\vec{E}| = 300\,\text{V/mm}$ are assumed.
Left: for high energies ($E > 60\,\text{keV}$) the mean free path of a photon becomes considerably longer than the detector depth d and absorption becomes equally probable for all absorption depths, which results in a mean absorption depth $\bar{z} = d/2 = 0.5\,\text{mm}$. The one sigma variation of the absorption depth Δz is $\pm 0.34\,\text{mm}$ for $E \to \infty$.
Right: the mean drift duration is almost constant $\bar{t}_{\text{drift}} = 80\,\text{ns}$ for photon energies $E \geq 80\,\text{keV}$ and the one sigma variation is less than 60 ns for all energies.

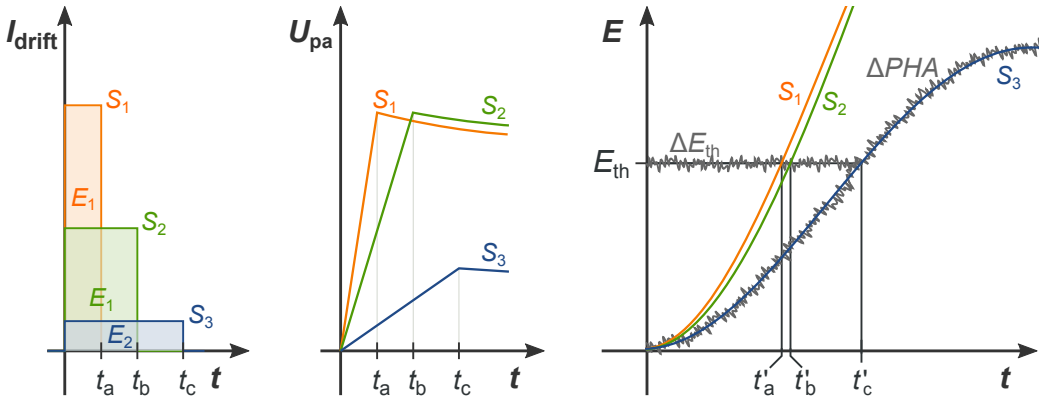

Figure 3.17. The effect of time-walk for three different signals: the signal S_1 (orange), with the energy E_1, is absorbed close to the cathode which results in a large fraction of fast electron drifts. The signal S_2 (green) has the same energy E_1 but is absorbed near the anode (large contribution of hole drifts). The energy of the signal S_3 (blue) is $E_2 < E_1$. The maximal output of the preamplifier U_{pa} is proportional to the signal energy and its rise time is defined by the drift durations t_{a}, t_{b}, and t_{c} of the signal charges to the detector electrodes. The rise times t_{a}, t_{b}, and t_{c} are reprocessed by the pulse shaper and produce the time-walks t'_{a}, t'_{b}, and t'_{c}. The noise of the trigger threshold ΔE_{th} and of the signal ΔPHA (only shown for S_3) are indicated in gray.

possible absorption depths. It can be measured or calculated—as function of E, E_{th}, and t_{p}—and all event times can be corrected for it. The fluctuations of the time-walk (i.e. the differences $\Delta t_{\mathrm{w}} - \overline{\Delta t_{\mathrm{w}}}$) depend on fluctuations of the drift duration $\Delta t_{\mathrm{drift}}$, on the signal noise ΔPHA, and on the noise of the trigger threshold ΔE_{th}, see Fig. 3.17. These fluctuations define the time inaccuracy of the measurement.

For Caliste-64 Meuris et al. [2009] measured with $t_{\mathrm{p}} = 9.6\,\mu\mathrm{s}$ a minimal mean time-walk of $2\,\mu\mathrm{s}$ ($E = 150\,\mathrm{keV}$, $E_{\mathrm{th}} = 2\,\mathrm{keV}$) and a maximal mean time-walk of $7\,\mu\mathrm{s}$ ($E = 10\,\mathrm{keV}$, $E_{\mathrm{th}} = 7\,\mathrm{keV}$). These measurements are based on external charge injection and do not consider fluctuations of the drift time $\Delta t_{\mathrm{drift}}$. The time inaccuracy due to electronic noise (ΔE_{th} and ΔPHA) is measured to be less than 150 ns for $E > 10\,\mathrm{keV}$ if the mean time-walk is subtracted correctly. The mean drift time $\bar{t}_{\mathrm{drift}}$ and the fluctuation of the drift time $\Delta t_{\mathrm{drift}}$ presented in Fig. 3.16 must be reprocessed by the pulse shaper to conclude on their exact contribution to the time-walk.

3.6. HED operation

Prior to the cooling of the setup, the vacuum vessel must be evacuated or flooded with dry nitrogen. To reach stable thermal conditions, it takes roughly one hour using a nitrogen atmosphere and more than 2 hours in vacuum. The power-up sequence of the HED consists of only three steps: turn on the digital supply voltage, turn on the high voltage for depletion, and configure Caliste-64 via a set of instructions which are listed in a batch command file with the following meanings:

- **enable/disable channels:** each of the 16 readout channels for each ASIC can be disabled. The trigger signal of a disabled channel is rejected and the signal data are not stored in the analog memory. In this way, pixels or channels can be tested individually and hot pixels can be switched off.
- **injection or normal operation mode:** an external signal pulse can inject charges into all readout channels via a common capacitive coupling. In this mode the readout channels are decoupled from the anodes to measure only the injected amount of charge. Charge injection enables to investigate the electrical characteristics of the readout channels. To address a single channel, all other channels have to be disabled.
- **set trigger threshold:** the trigger threshold can be chosen as an equivalent energy in the range $1\,\mathrm{keV} \leq E_{\mathrm{th}} \leq 7\,\mathrm{keV}$ in steps of 6.2 eV. These thresholds are rough estimates of the equivalent signal energy as each channel has a slightly different energy bias and signal amplification. The trigger threshold can be set for each ASIC and is identical for all channels of the ASIC.
- **configure the pulse shaper:** the peaking time of the pulse shaper can be chosen between $1.2\,\mu\mathrm{s}$, $2.4\,\mu\mathrm{s}$, $3.6\,\mu\mathrm{s}$, $4.8\,\mu\mathrm{s}$, $6.0\,\mu\mathrm{s}$, $7.2\,\mu\mathrm{s}$, and $9.6\,\mu\mathrm{s}$ which is (according to Eqs. (3.25) and (3.26)) equivalent to cutoff frequencies in the range $16.6\,\mathrm{kHz} \leq f_{\mathrm{c,\,high}} \leq 133\,\mathrm{kHz}$. The peaking time is collectively set for all channels of all four ASICS.

- **set reset time:** the reset delay between the end of the hold signal and the beginning of the reset signal can be chosen between 8-30 µs in steps of 10 ns. The duration of the reset pulse is identical to the reset delay (see Fig. 3.13).

3.7. Offline data analysis

During a measurement, the HED event data are stored in a collection of binary files, each of 2 MB size. After concatenating all files, the data can be analyzed with three small programs that were all developed in the framework of this thesis. Figure 3.18 shows the processing chain of a typical HED data analysis.

1. `HED_PEL_ADU`: the binary data of the detector are converted into a pixel event list in the fits table format. Each event consists of the following parameters:
   - the pixel number $0 \leq pix \leq 63$ and the x and y-positions of the event: $0 \leq pix_{\mathrm{x}} \leq 7$ and $0 \leq pix_{\mathrm{y}} \leq 7$. See Fig. 4.1 for the definition of the pixel positions in the x and the y-directions within the setup.
   - the pulse height value *PHA* of the event in units of ADU.
   - the event time consisting of a counter number for seconds and for subseconds. The time stamp of the first event is subtracted from all events so that the measurement starts at $t = 0$. Overflows of the seconds counter are recognized and corrected.
2. `HED_CAP` determines the pixel individual pulse height to energy transformation. See the following section for more details on the energy calibration.
3. `HED_CorGain` applies the energy calibration to the data. Results of energy calibrated HED measurements are presented in Sect. 3.8.

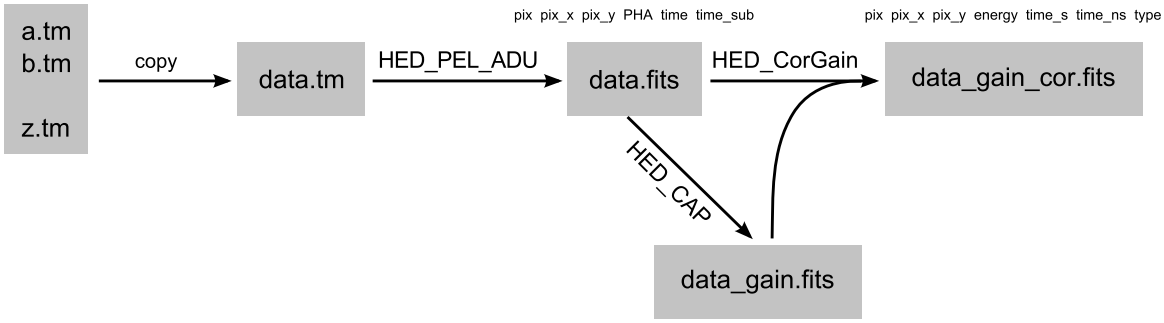

Figure 3.18. A typical HED data analysis starts with the concatenation of all measured files to one file (`data.tm`). `HED_PEL_ADU` converts this binary file into a pixel event list in the fits table format (`data.fits`). Based on a correlation algorithm, `HED_CAP` calculates the optimal parameters for the energy calibration and stores the pixel individual results in `data_gain.fits`. `HED_CorGain` applies the pulse-height-to-energy transformation according to these parameters.

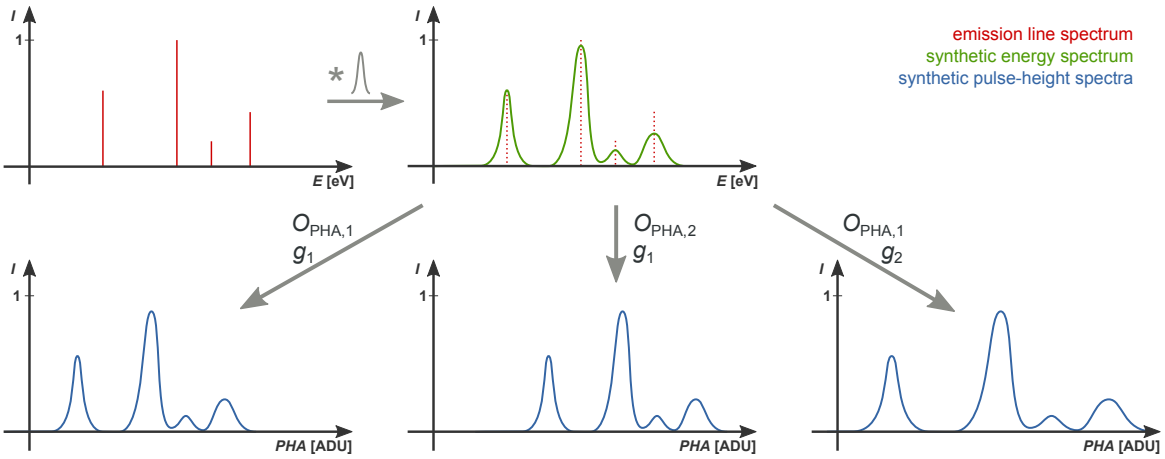

Figure 3.19. Creation of synthetic pulse-height spectra:
Top: the emission line spectrum (red), normalized to the intensity of the most dominant emission line, is convolved with the expected energy resolution and the quantum efficiency of the detector to create the synthetic energy spectrum (green). Both, the energy resolution and the quantum efficiency are a function of the energy.
Bottom: using different parametrizations for the energy-to-pulse-height relation results in different synthetic pulse height spectra. For a linear energy-to-pulse-height relation (like shown) the pulse-height offset O_{PHA} shifts the spectra to other pulse heights (left and center) while the gain g stretches or squeezes the spectra (left and right).

3.7.1. Energy calibration

As for the LED, a full energy calibration that assigns each pulse-height bin to a specific energy (or vice versa) is not accessible due to the limited presence of calibration lines. The energy calibration method CSI* which is used for LED data (see Sect. 2.7.3) can in principle also be used for an approximated HED energy calibration. In this section, an additional method for the energy calibration which can handle less significant calibration spectra, is presented. After describing the theoretical basis of this energy calibration via correlation (ECC)† technique, it is used to calibrate HED data using a linear and a non-linear pulse-height-to-energy relation. The differences between CSI and the linear and non-linear ECC are finally presented in Sect. 3.8.1.

Theoretical description of ECC

The ECC method is based on the idea to construct multiple, synthetic pulse-height spectra and to compare these spectra with the measured spectrum. The construction method that results in the best match has the parameter set to be used for energy calibration. ECC uses a parametrized energy-to-pulse-height relation to construct the **synthetic pulse-height spectra** in the following way:

* CSI = calibration via spline interpolation.
† The idea of the method is adopted from Irfu, CEA^2, Saclay.

1. The emission lines of the calibration sources have to be known in terms of energy and intensity. The intensities are normalized relative to the intensity of the strongest calibration line. See Fig. 3.19 (top left).

2. A synthetic energy spectrum, can be constructed by convolving each line emission with the expected resolution and quantum efficiency of the detector at this energy. See Fig. 3.19 (top center).

3. The energy-to-pulse-height relation $PHA(E \mid P)^*$ with the parameter set P is used to transform the synthetic energy spectrum into a synthetic pulse height spectrum S_{syn}, see Fig. 3.19 (bottom).

The last step is repeated for different parametrizations and each obtained synthetic pulse-height spectrum S_{syn} is compared with the measured pulse-height spectrum S_{obs} via a **correlation factor**

$$cor = \sum_{PHA=0}^{PHA_{\max}} S_{\mathrm{syn}}(PHA) \cdot S_{\mathrm{obs}}(PHA). \tag{3.28}$$

Here, S_{obs} is also normalized with respect to its maximal line strength. The summation in Eq. (3.28) runs over all discrete pulse height values which are defined by the resolution of the ADC. To check the quality of the parametrization, the optimal correlation factor can be estimated via

$$cor_{\mathrm{opt}} = \sum_{PHA=0}^{PHA_{\max}} \left(S_{\mathrm{obs}}(PHA)\right)^2 \tag{3.29}$$

and compared with the correlation factor obtained by Eq. (3.28).

The parameter set P that results in a correlation factor with the smallest difference to cor_{opt} is chosen as the best parametrization and can be used for the energy calibration which is done with the inverse energy-to-pulse-height relation

$$E(PHA \mid P) = PHA(E \mid P)^{-1}. \tag{3.30}$$

In practical applications the observed correlation factors cor are smaller than cor_{opt} because the synthetic spectrum is simplified and consists only of the most prominent emission lines but ignores other spectral features like a background continuum. Only if the energy resolution is estimated worse or if the quantum efficiency is estimated larger than the true values, cor can exceed cor_{opt}. In such a case the synthetic model should be reconsidered.

The advantage of the ECC method is that it is not restricted to line emissions. Other spectral features like continuum radiation or the pulse width can be used to construct the synthetic spectrum. The correlation factor of Eq. (3.28) includes more spectral information than the CSI method and ECC can therefore operate with spectra that have a lower counting statistics.

*Here, $(E \mid P)$ means that the energy E is the variable with the parameter set P.

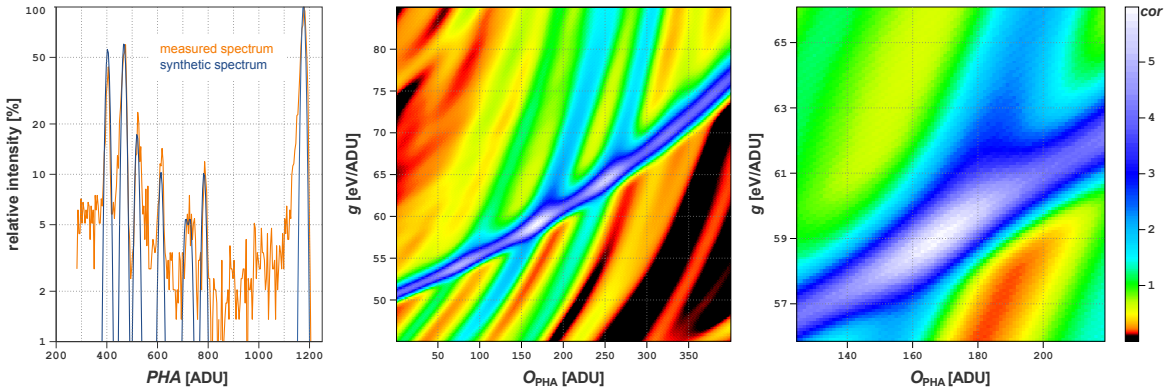

Figure 3.20. Linear ECC shown for the HED pixel number 1 irradiated with Am-241. **Left**: measured pulse-height spectrum (orange) in comparison to the synthetic spectrum with the highest correlation factor (blue).
Center: color coded correlation map as a function of the pulse-height offset O_{PHA} and the gain g. Three islands with large correlation factors are visible.
Right: the correlation map near the maximal correlation. The optimal parameters are $O_{\mathrm{PHA}} = 167\,\mathrm{ADU}$ and $g = 59.0\,\mathrm{eV/ADU}$ with a maximal correlation of $cor = 6.216$.

Linear pulse-height-to-energy relation

A linear pulse-height-to-energy relation is the simplest, non-trivial application of the ECC method and is explained in the following. For a linear pulse-height-to-energy relation the parameter set P consists of only two parameters, the gain g and the pulse-height offset* O_{PHA}. It is

$$E(PHA \,|\, P) = g \cdot (PHA - O_{\mathrm{PHA}}) \tag{3.31}$$

and

$$PHA(E \,|\, P) = \frac{1}{g} E + O_{\mathrm{PHA}}. \tag{3.32}$$

With Eq. (3.32) synthetic spectra can be constructed for different parameters g and O_{PHA}. The pulse-height offset O_{PHA} shifts the synthetic spectra to lower or higher pulse heights while the gain g stretches or squeezes the spectra (see Fig. 3.19). Figure 3.20 (center) shows the color coded correlation factors of a specific pixel (pixel number 1) as a function of g and O_{PHA}. This correlation map points out that large correlation factors are obtained for different combinations of the parameters g and O_{PHA} which is caused by the comb-like calibration lines of Am-241. The maximal correlation $cor = 6.216$ is obtained for $O_{\mathrm{PHA}} = 167$ ADU and $g = 59.0\,\mathrm{eV/ADU}$. The optimal correlation for the measured spectrum is $cor_{\mathrm{opt}} = 7.160$.

* To distinguish clearly between the offset value obtained as a mean value of dark frame measurements and the offset of an energy calibration, the latter is labeled with the index 'PHA'.

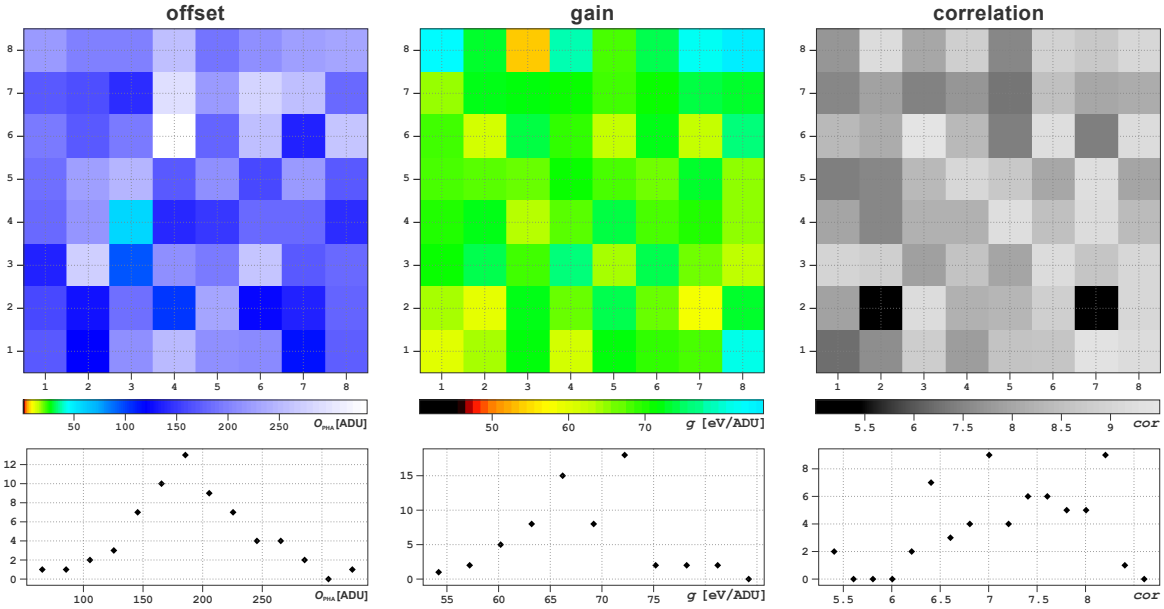

Figure 3.21. Linear ECC in case of an Am-241 calibration with 386 554 events. An offset shift of 100 ADU corresponds to an energy shift of at least 5.5 keV which shows the necessity for a pixel individual energy calibration.
Top: HED pixel maps for the pixel specific offset, gain, and correlation values.
Bottom: distributions for the offset, the gain, and the correlation factor of the 64 Caliste-64 pixels.

`HED_CAP_lin` computes pixel individual pulse-height spectra and calculates for each pixel the optimal parameters O_{PHA} and g for the energy calibration. Pixel individual offset, gain, and correlation values are presented in Fig 3.21. The offset and gain variations show that a pixel individual energy calibration is necessary to achieve spectroscopic measurements with an energy resolution better than a few keV.

Figure 3.22 shows the observed and the best synthetic spectrum obtained for pixel (2/4). Both, the offset and the gain are adjusted to match the most dominant line emissions. The mismatch between both spectra is most prominent at 700 ADU and is in the order of 1.4 keV. The mismatch is not the result of an erroneous determination of the offset O_{PHA} or gain g and cannot be corrected with a linear ECC. An additional distortion factor is required to match both spectra. The phenomenon of non-linear pulse-height-to-energy relations is observed in several pixels and is always linked with a reduced energy resolution of the

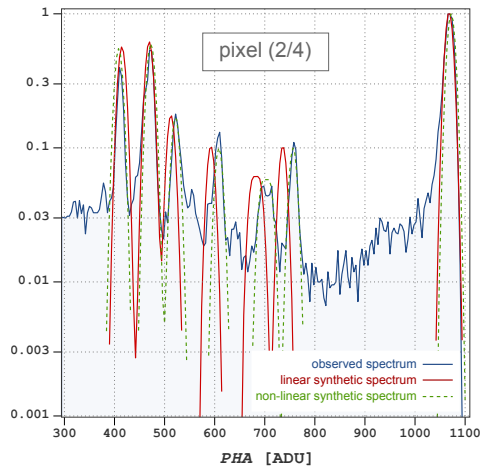

Figure 3.22. With a linear ECC, pixel (2/4) shows an uncorrectable mismatch between the observed and the synthetic spectrum. The non-linear ECC (green) is introduced in the next section.

59.5 keV emission line.

Non-linear pulse-height-to-energy relation

The ECC method can be extended to pulse-height-to-energy transformations that are based on more than two parameters. For the HED a non-linear pulse-height-to-energy relation according to

$$E = g \cdot (PHA - O_{\mathrm{PHA}})^d \tag{3.33}$$

which is equivalent to

$$PHA = (E/g)^{1/d} + O_{\mathrm{PHA}} \tag{3.34}$$

was studied. Here, the energy E of an event is calculated as a function of the pulse height PHA with a gain g and a pulse-height offset O_{PHA}. The distortion factor d enables to deviate from a linear energy calibration ($d = 1$) to one with an increasing slope ($d > 1$) and to one with a decreasing slope ($d < 1$).

`HED_CAP_nl` determines the pixel individual energy-to-pulse-height transformations according to Eq. (3.34) and calculates the parameters O_{PHA}, g, and d that result in the largest correlation factor *cor* according to Eq. (3.28). Pixel individual offset, gain, and distortion values are presented in Fig 3.23.

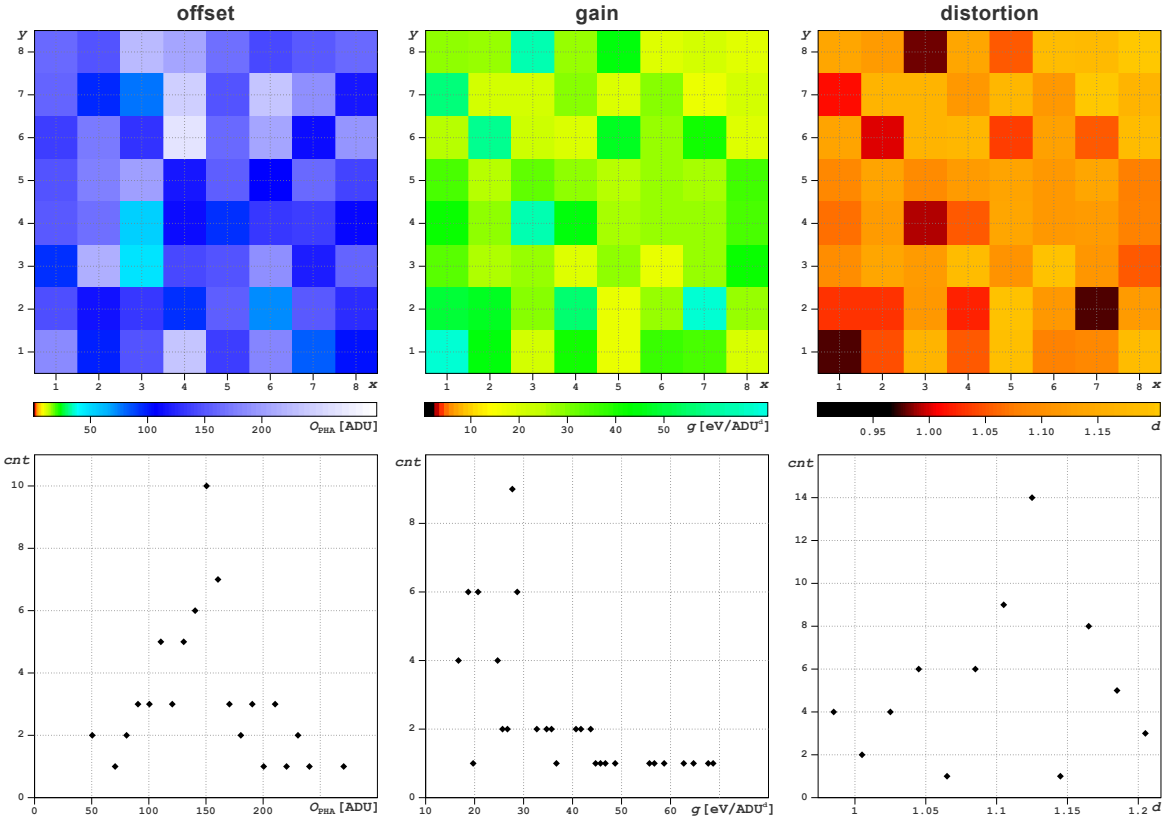

Figure 3.23. Non-linear ECC in case of an Am-241 calibration with 483 729 events. **Top:** HED pixel maps for the pixel specific offset, gain, and distortion values. **Bottom:** distributions for the offset, the gain, and the distortion factor. The gain g is not directly comparable to the gain presented for the linear ECC because its units are eV/(ADU^d). Four pixels have a distortion factor $d < 1$.

Energy calibration

In order to apply the pulse-height-to-energy transformation to the recorded data, the program `HED_CorGain` is used in two versions, one for a linear correction according to Eq. (3.31) and one for a non-linear correction according to Eq. (3.33). The program uses the pixel individual optimal parameters O_{PHA}, g, (and d) which are listed in `data_gain.fits` and stores the energy calibrated events as a new pixel event list into `data_gain_cor.fits`. See Fig. 3.18 for the data processing chain.

3.8. Results

The following analysis is based on a 100 minute irradiation of the HED with an Am-241 source (activity $A = 2.8\,\mathrm{MBq}$) which results in a total number of 1 033 456 triggered* events. The measurement was made in a dry nitrogen atmosphere ($P = 1\,\mathrm{atm}$), with a depletion voltage of $U = 300\,\mathrm{V}$, a pulse-shaper peaking time of $\tau_{\mathrm{int}} = 9.6\,\mu\mathrm{s}$, a trigger threshold of $E = 3\,\mathrm{keV}$, and a setting temperature of the heat exchanger of $T_{\mathrm{s}} = -45°\mathrm{C}$. The temperature of the cooling funnel was measured at $T_{\mathrm{cf}} = -1°\mathrm{C}$. The LED was deinstalled for this measurement.

After converting the binary data into a pixel event list, the event rate, the integrated hit map, and the pulse-height spectra of the measurement can be constructed with *fitsview* (see Fig. 3.24).

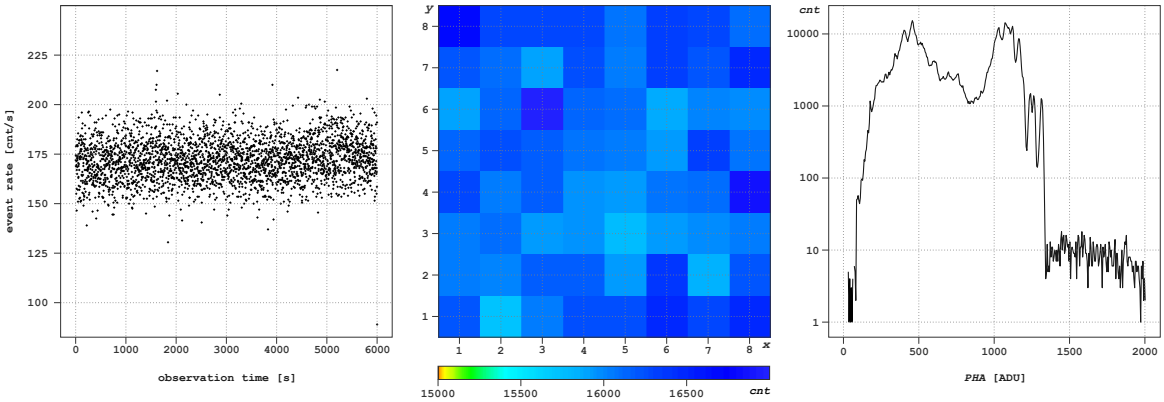

Figure 3.24. A 100 minute Am-241 measurement with a total of 1 033 456 events.
Left: the event rate as function of the time results in an averaged event rate of approximately 175 events per second. The fluctuations are in accordance with Poisson statistics.
Center: hit map of the total observation. The HED is irradiated homogeneously.
Right: pulse-height spectrum of all HED pixels. The Np-L_α line (13.9 keV) is positioned at $PHA \approx 450\,\mathrm{ADU}$, the 59.5 keV Am emission is at $PHA \approx 1100\,\mathrm{ADU}$. The spectral details are averaged out because of pixel individual variations between the pulse heights and the corresponding energies.

* The pattern recognition is not yet performed and split events are counted multiple times.

3.8.1. Comparing different methods for the energy calibration

The mentioned HED measurement is analyzed with different energy calibration methods. The analysis is focused on the spectroscopic resolution, on systematic errors of the energy, and on the low energy detection threshold which is detected as a steep decrease of the background flux. See Tab. 3.1 and Fig. 3.25 for the summarized results.

`HED_CAP_lin` is used to apply a **linear ECC** and calculate the pixel specific offset O_{PHA} and gain g parameters similar to those presented in Fig. 3.21. Transforming the pulse heights to energies (`HED_CorGain_lin`) results in the final pixel event list. Figure 3.25 (top) shows the resulting energy spectra for single, double, triple, and quadruple events. The misalignment between the single and double events indicates a systematic error in the energy calibration which is largest for small energies. The Np-L_α is observed at 13.8 keV with single events but at 11.5 keV with double events. The occurrence of negative energies (256 events) and the observed energy threshold of $E_{\mathrm{th}}^{\mathrm{obs}} = 635\,\mathrm{eV}$ (the trigger threshold set is to $E_{\mathrm{th}} = 3\,\mathrm{keV}$) indicates a systematic error of more than 2.3 keV for small pulse-heights.

A **non-linear ECC** performed with `HED_CAP_nl` and `HED_CorGain_nl` reduces the systematic errors; see Fig. 3.25 (center) for the corresponding energy spectrum. The double event spectrum matches the single event spectrum with a maximal deviation of $\Delta E = 0.53\,\mathrm{keV}$. Faint details like the Sn-K_β fluorescence emission can now be resolved. 52 events have a negative pulse height after the subtraction of O_{PHA}. Because of the exponential distortion factor d in Eq. (3.33), these events cannot be assigned with an energy and are therefore missing in the spectra.

A **CSI** based energy calibration is performed for comparison. `HED_Peak` finds the pixel specific pulse heights of the calibration lines (Np-L_α, Np-L_β, Np-L_γ, Am_{26}, $Am_{59}\,Cd_{esc}$, Am_{59}) and `HED_CorGain_peak` calculates the pulse-height-to-energy transformation. The resulting spectrum (see Fig. 3.25 (bottom)) is similar to the one obtained with a non-linear ECC. The misalignment between single and double event spectra is reduced to maximal $\Delta E = 0.45\,\mathrm{keV}$ and a faint Cu-K_α fluorescence emission is now indicated around 8 keV.

Table 3.1. Summary of the spectroscopic properties of the HED listed as: the number of events with a negative energy *NNE*, the observed energy threshold $E_{\mathrm{th}}^{\mathrm{obs}}$, and the energy resolution (FWHM) at 13.9 keV (ΔE_1) and 59.5 keV (ΔE_2). The difference between the true line energy E_0 and the detected line energy E is calculated via $\Delta = E - E_0$ for Np-L_α (Δ_{14}), Np-L_β (Δ_{18}), Np-L_γ (Δ_{21}), Am_{26} (Δ_{26}), Cd-K_α escape of Am_{59} (Δ_{36}), and Am_{59} (Δ_{59}). For all measurements the conditions are: $T_{\mathrm{CdTe}} = 10°\mathrm{C}$, $U = 300\,\mathrm{V}$, $t_{\mathrm{p}} = 9.6\,\mu\mathrm{s}$, and $E_{\mathrm{th}} = 3\,\mathrm{keV}$.

calibration	*NNE*	$E_{\mathrm{th}}^{\mathrm{obs}}$ [eV]	Δ_{14} [eV]	Δ_{18} [eV]	Δ_{21} [eV]	Δ_{26} [eV]	Δ_{36} [eV]	Δ_{59} [eV]	ΔE_1 [eV]	ΔE_2 [eV]
lin. ECC	256	635	-138	186	652	759	1344	-84	959	1024
nl. ECC	52	3600	66	-73	17	-4	124	-75	935	1023
CSI	102	3054	-40	67	-7	72	69	-9	933	1026

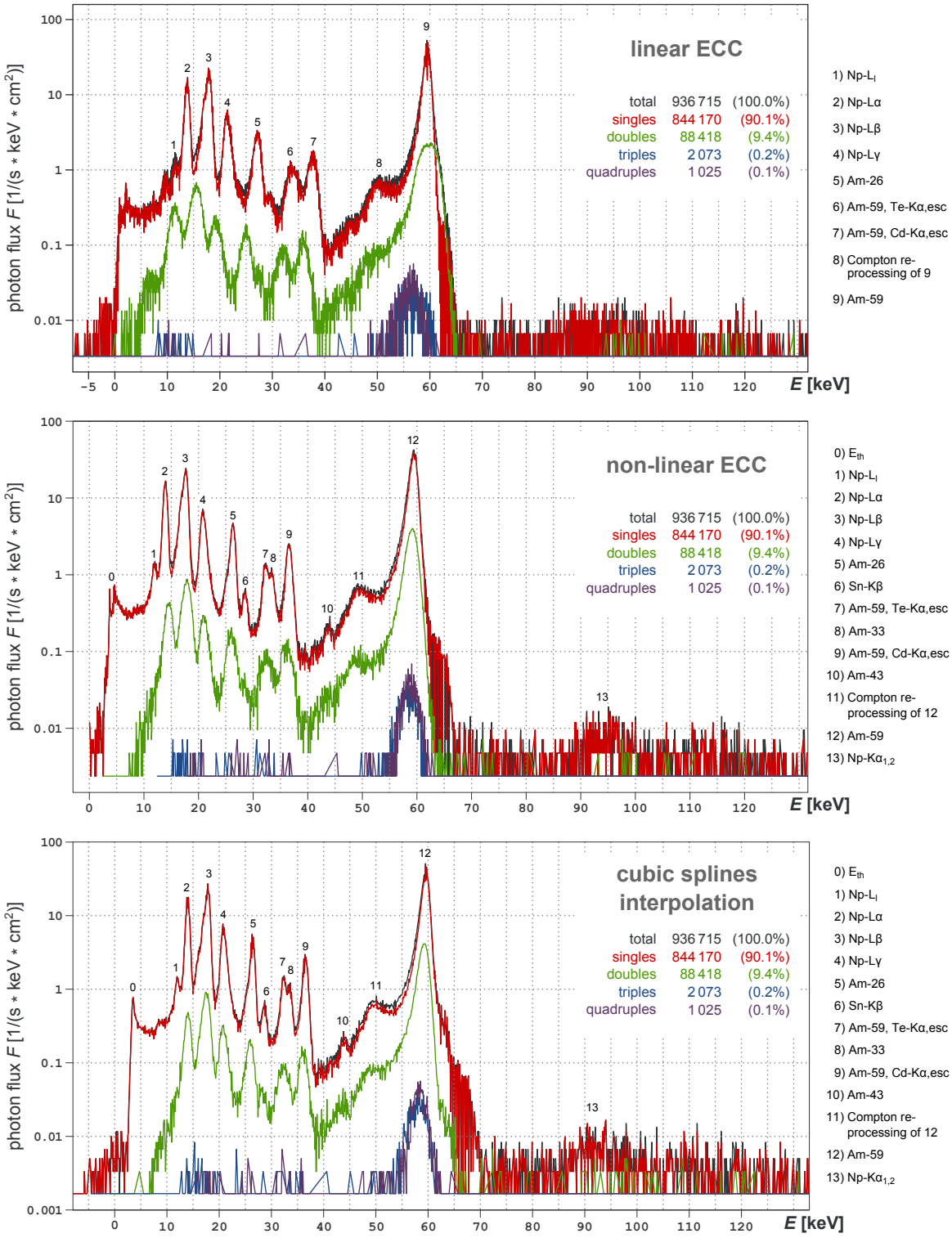

Figure 3.25. HED Am-241 spectra (bin size = 100 eV) of a 100 minute observation obtained with a linear ECC (top), a non-linear ECC (center), and a cubic spline interpolation (bottom). 1026 events are rejected because of an irregular pattern. The conditions of the measurement are: $T_{\mathrm{CdTe}} = 10°\mathrm{C}$, $U = 300\,\mathrm{V}$, $t_{\mathrm{p}} = 9.6\,\mu\mathrm{s}$, and $E_{\mathrm{th}} = 3\,\mathrm{keV}$.

3.8.2. Spectral properties of the HED pixels

The following discussion of the spectroscopic resolution of specific HED pixels refers to a non-linear ECC, but the results are similar for the linear ECC and the cubic spline interpolation technique. Figure 3.26 presents a pixel specific Gaussian line fitting of the 59.5 keV americium line emission. The mismatch between the fit and the true line position is for all pixels within +100 eV and −300 eV.

The spectrum of the pixel (8/8) is presented in Fig. 3.27 and shows some outlying properties. The epoxy drop and the copper pin, that are used to apply the depletion voltage to the crystal cathode, are positioned above this pixel (see Fig. 4.1) and form a thick, insensitive absorption layer. Photons can get Compton scattered in this layer and the scattered photon can be detected by the pixel (8/8) with a reduced energy. The statistical spread of the scattering process results in a reduced spectral resolution of the pixel ($\Delta E = 1430$ eV FWHM at 59.5 keV in contrast to the best pixel resolution of $\Delta E = 941$ eV FWHM at 59.5 keV), see Fig. 3.27.

If the scattering effect is large enough to shift the position of the line to lower energies, the energy calibration becomes incorrect and all photons that passed the dead layer without scattering are recorded with an excess energy. This explains the high energetic tail of pixel (8/8) and the overestimated line position of the fit at $E_0 = 59.621$ keV.

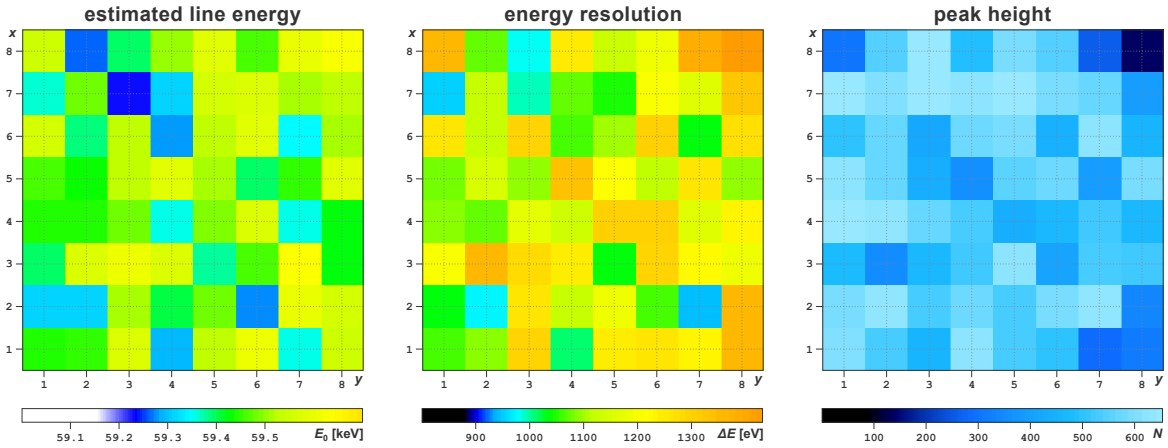

Figure 3.26. Pixel individual spectral resolution at 59.5 keV. The presented data are based on a non-linear ECC. The 59.5 keV Am-241 line is fitted by a Gaussian distribution with three free parameters: the central energy E_0, the width ΔE, and the peak height N. See Fig. 3.27 for pixel individual spectra of the pixels (7/2) and (8/8).
Left: the central energies of the fit E_0 and the true emission line have a maximal mismatch of +100 eV and −300 eV. For pixel (8/8) it is $E_0 = 59.621$ keV.
Center: the energy resolution, stated as full width at half peak maximum, is degraded at the corner pixel (8/8) of the detector where the high voltage contact is located.
Right: the peak height of the fit in units of counts. The reduced counts in pixel (8/8) result from absorptions in the high voltage contact pin.

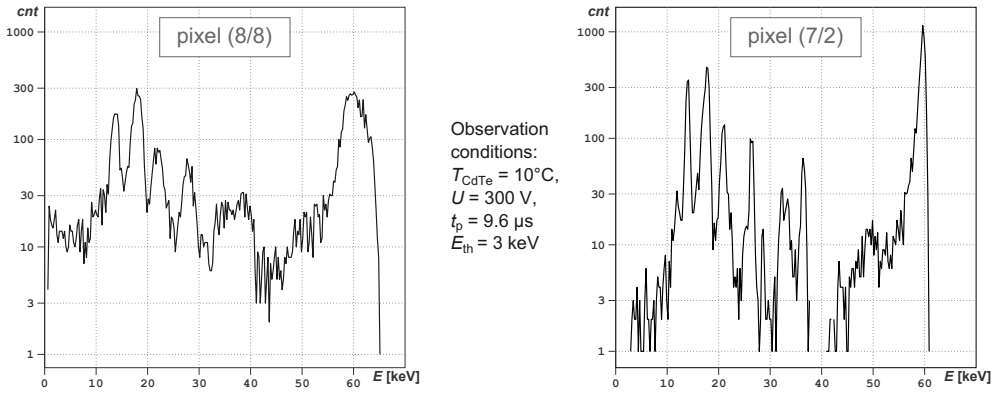

Figure 3.27. HED pixel spectra (bin size = 250 eV): the spectral shape of pixel (8/8) can be explained with Compton scattering in an inactive layer positioned above the pixel, which is formed by the high voltage contact. Pixel (7/2) is measured with the best pixel specific energy resolution of $\Delta E = 941\,\mathrm{eV}$ and is presented for comparison. Compare the counts at $E < 10\,\mathrm{keV}$ and at $E \approx 40\,\mathrm{keV}$.

3.8.3. Temporal stability of the HED

In the following, the bias induced polarization effect of CdTe and its impact on the stability of the HED operation is studied with a spectroscopic approach. To guarantee stable thermal conditions, the HED is operated in a nitrogen atmosphere at atmospheric pressure. The temperature is measured with two Pt-100 sensors located directly at the cooling funnel of the HED and at a distance of about 4 cm. The precision of the temperature measurement is estimated to be better than 1°C. A temperature difference between the measured temperature of the cooling funnel T_{cf} and the temperature of the CdTe crystal T_{CdTe} is assumed to be $\Delta T = +11\,\mathrm{K}$. The temperature difference results from the power consumption of the Caliste-64 ASICs (3 mW per channel, 200 mW in total [Meuris et al., 2009]) and the thermal coupling of the ASICs to the cooling funnel and to the CdTe crystal. The details of the analysis that allows to estimate the temperature difference ΔT are presented at the end of this section.

The data recording starts a few seconds after the depletion voltage is set and is restricted to the data of pixel (7/2). This approach does not allow to study pixel individual variations* of the polarization effects, but is adequate to study the impact of the temperature and the depletion voltage on crystal polarization. Figure 3.28 shows the evolution of an Am-241 spectrum within the first 8 ks of the observation. The temperature is measured at $T_{\mathrm{cf}} = 5°\mathrm{C}$ ($T_{\mathrm{CdTe}} = 16°\mathrm{C}$) and the depletion voltage is set to $U = 200\,\mathrm{V}$. The increasing crystal polarization reduces the detection efficiency and the charge collection efficiency by deforming the electric field inside the crystal. Parts in the crystal with a vanishing electric field become insensitive to radiation and, as a consequence, the measured flux is reduced. Other parts of the crystal, that are

* Analyzing 22 of the 64 pixels of Caliste-64, Meuris et al. [2011] report pixel individual differences in the peak drift with a maximal factor of two and differences in the polarization time of about 10 %.

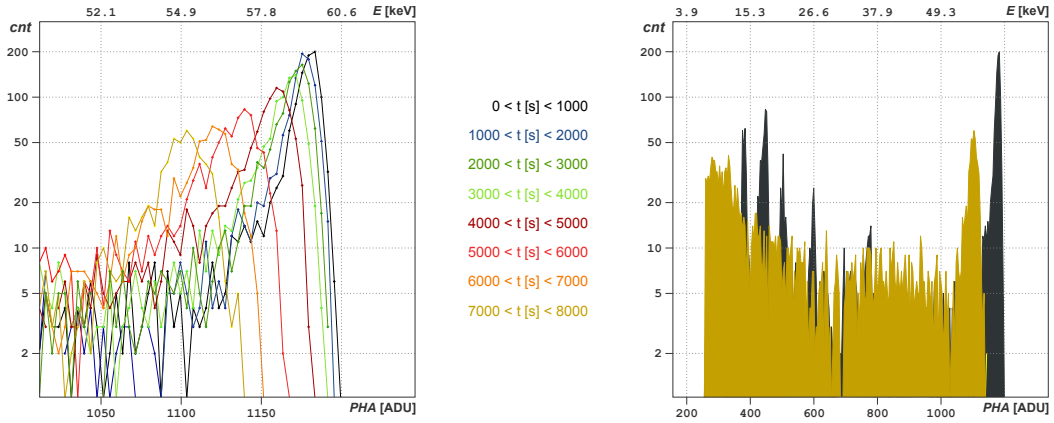

Figure 3.28. Crystal polarization in CdTe observed at $T_{\mathrm{CdTe}} = 16\,^{\circ}\mathrm{C}$ and $U = 200\,\mathrm{V}$. **Left:** zoomed view on the temporal evolution of the 59.5 keV emission line. The reduced detection efficiency and the reduced charge collection efficiency result in a decreasing peak that is drifting to lower energies with increasing observation time. **Right:** Am-241 spectra observed in the first (black) and the last (brown) 1000 seconds of the observation show that crystal polarization is most prominent at low energies as the averaged photon absorption is closer to the detector entrance window (cathode).

located closer to the anode, are sensitive to radiation but have a low electric field and therefore a low charge collection efficiency. The latter effect shifts the detected emission lines to lower energies.

In order to study the polarization effect more quantitatively, the peak positions of the 59.5 keV emission line is measured as a function of time. The exposed position of the line allows to detect the peak position by limiting the analysis to pulse heights within $1000\,\mathrm{ADU} \leq PHA \leq 1200\,\mathrm{ADU}$ and calculate a moving average of 400 seconds width of all events within this pulse-height range. Figure 3.29 shows that the decrease of the peak position, i.e. the decrease of the charge collection efficiency, starts directly after the depletion of the detector ($t = 0$). The initial peak drift $(\mathrm{d}E/\mathrm{d}t)_{\mathrm{i}} = -2238\,\mathrm{eV/h}$ changes to an intensive peak drift of $(\mathrm{d}E/\mathrm{d}t)_{\mathrm{p}} = -9185\,\mathrm{eV/h}$ once the polarization time is reached. These high values result from the high tem-

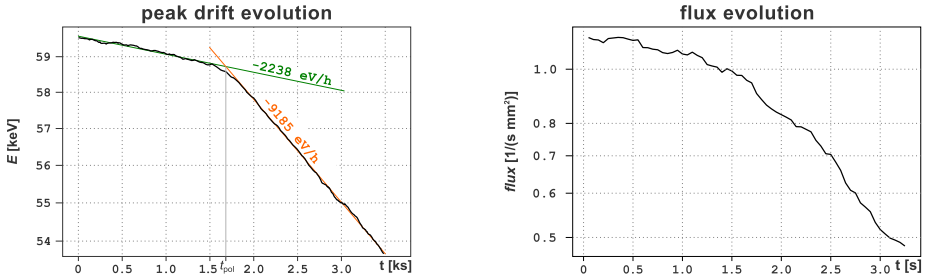

Figure 3.29. A quantitative measurement ($T_{\mathrm{CdTe}} = 26\,^{\circ}\mathrm{C}$, $U = 200\,\mathrm{V}$) of crystal polarization. After detector depletion, the peak position of the 59.5 keV line drifts by $(\mathrm{d}E/\mathrm{d}t)_{\mathrm{i}} = 2238\,\mathrm{eV/h}$. For $t > t_{\mathrm{pol}}$, the drift increases to $(\mathrm{d}E/\mathrm{d}t)_{\mathrm{p}} = 9185\,\mathrm{eV/h}$. At lower crystal temperatures the peak drift is much less: $(\mathrm{d}E/\mathrm{d}t)_{\mathrm{i}} < 1\,\mathrm{eV/h}$ and $t_{\mathrm{pol}} \approx 33\,\mathrm{h}$ are reported at $T_{\mathrm{CdTe}} = -8\,^{\circ}\mathrm{C}$ and $U = 300\,\mathrm{V}$ [Meuris et al., 2011]. The measured flux shows a similar temporal evolution as the peak drift.

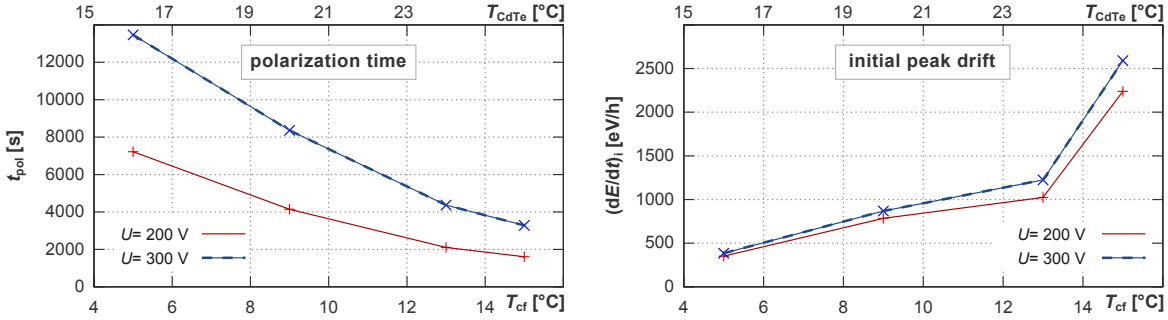

Figure 3.30. Polarization time t_{pol} and initial peak drift $(\mathrm{d}E/\mathrm{d}t)_{\mathrm{i}}$ as a function of the temperature. T_{cf} is the measured temperature at the cooling funnel and T_{CdTe} is the estimated temperature of the CdTe crystal. The polarization time and the initial peak drift are both strongly dependent on the temperature. Increasing the depletion voltages U increases the polarization time considerably but the peak drift only slightly.

perature of the CdTe crystal ($T_{\mathrm{CdTe}} = 26°\mathrm{C}$). A linear fit of the peak drifts $(\mathrm{d}E/\mathrm{d}t)_{\mathrm{i}}$ and $(\mathrm{d}E/\mathrm{d}t)_{\mathrm{p}}$ followed by a calculation of the time of their intersection point allows to determine the polarization time precisely, see Fig. 3.29 (left). The flux is obtained by summing all events within 50 seconds of observation and calculating a moving average. The fluctuations of the measured flux are too large to conclude on details of its temporal evolution, but a similar behavior to the peak drift evolution is indicated (see Fig. 3.29 (right)).

According to Eq. (3.23) crystal polarization depends on the crystal temperature and on the applied depletion voltage. The polarization time t_{pol} and the initial energy drift $(\mathrm{d}E/\mathrm{d}t)_{\mathrm{i}}$ at 59.5 keV are measured in the same way as described above for different temperatures and depletion voltages. Figure 3.30 summarizes the results. Matching these results with the polarization times reported in Meuris et al. [2011] results in the estimation of the temperature difference $\Delta T_{\mathrm{N2}} = +11\,\mathrm{K}$ between the cooling funnel and the CdTe crystal.

The operation of the HED is possible for crystal temperatures close to room temperature and below. The spectral properties of the HED benefit from decreasing temperatures in two ways: the polarization time increases and the peak drift during the observation decreases. The first effect allows to operate the detector on longer time scales and the latter effect increases the spectral resolution of the observation. Furthermore, the depletion voltage can be increased at low temperatures because of the diminished leakage current. The higher depletion voltage increases the peak drift only slightly but—according to Eq. (3.23)—the polarization time in a linear way .

Using a nitrogen atmosphere limits the set temperature of the heat exchanger to a minimum of $T_{\mathrm{s}} = -20°\mathrm{C}$ which results in a cooling funnel temperature of $T_{\mathrm{cf}} = 5°\mathrm{C}$ and a crystal temperature of $T_{\mathrm{CdTe}} = 16°\mathrm{C}$. At lower temperatures the heat exchange with the surface of the vacuum vessel increases strongly and vapor condensation at the outer layer of the vessel becomes an issue. For vacuum operation the minimal set temperature is $T_{\mathrm{s}} = -80°\mathrm{C}$ which results in $T_{\mathrm{cf}} = -45°\mathrm{C}$. The temperature difference is measured in the same way as for the operation in nitrogen. It increases to $\Delta T_{\mathrm{vac}} = 29\,\mathrm{K}$ because of the loss of the convective cooling flow via the nitrogen gas.

3.9. Summary

The embedded design of a 1 mm thick CdTe crystal with the very low noise IDeF-X ASICs results in a detector capable to perform spectroscopy and imaging in an energy range $2\,\mathrm{keV} \leq E \leq 100\,\mathrm{keV}$ and makes the HED an ideal addition to the LED.

The integration of the HED into CANDELA included a spectrum of tasks addressing the mechanical and electrical configuration. The cooling environment of the HED was optimized by rebuilding the cooling funnel and preparing a thermal contact between the cooling funnel and Caliste-64 via thermal pads. The high voltage contact of the planar HED cathode was reconstructed to allow a close position of LED and HED with a minimal distance of 5 mm.

The polarization effect of CdTe is a critical factor for the operation of the HED and was therefore studied in detail. The theoretical treatment allows to conclude on the influence of all relevant parameters and to estimate the duration of stability for different operation conditions. Via studies of the temporal evolution of spectroscopic measurements, not only the influence of crystal polarization on the operation stability and on the spectral resolution can be quantified, but also the crystal temperature—which cannot be measured directly with the used setup—can be recalibrated. The cooling capability of the HED is the limiting factor for stable HED operation on long time scales. Using a nitrogen atmosphere, stable operations are measured for time scales larger than 3.7 hours. With vacuum conditions, operation stability is limited to 2.5 hours with the present setup.

The triggered readout concept of the HED necessitates a different way of analyzing the measured data. As part of this thesis a data analysis software specific for HED observations was written, tested, and used to investigate the spectroscopic performance of the HED. In this process an alternative method for energy calibration was tested and further developed to account for non-linear pulse-height-to-energy relations. Applying a linear ECC results in systematic errors which can be larger than 1 keV. The non-linear ECC or the CSI technique have a comparable spectroscopic performance. The advantage of the non-linear ECC is founded in its capability to use all kinds of calibration spectra and that it is not limited to emission lines. Furthermore, because it is not concentrating on the line peaks, but on the whole line shape, it can operate with lower counting statistics than needed for the CSI technique.

The spectroscopic studies of the HED result in measured systematic errors smaller than 100 eV and a resolution of $\Delta E = 1023\,\mathrm{eV}$ (FWHM at 59.5 keV) for $T_{\mathrm{CdTe}} = 10°\mathrm{C}$. Meuris et al. [2009] report $\Delta E = 842\,\mathrm{eV}$ (FWHM at 59.5 keV) for $T_{\mathrm{CdTe}} = -10°\mathrm{C}$. The differences are mainly caused by the peak drift which is $\sim 60\,\mathrm{eV/h}$ at $T_{\mathrm{CdTe}} = 10°\mathrm{C}$ and below 1 eV/h at $T_{\mathrm{CdTe}} = -10°\mathrm{C}$, [Meuris et al., 2011, Fig. 11]. Despite the limiting cooling capabilities of CANDELA, the HED shows excellent spectroscopic results and a large quantum efficiency in the hard X-ray range which extends the spectro-imaging capabilities of the LED.

4. LED and HED in a stacked setup

The individual detector specifics of the LED and the HED were presented in Chapters 2 and 3. In the present chapter, the mutual influences of both detectors—mainly the absorption effect of the LED on the HED and fluorescence emission of the HED—are investigated in Sect. 4.2. Section 4.3 introduces the analytical steps which are necessary to study both detector units in one framework. The combined event analysis opens up new possibilities to use the stacked detector setup which are presented in Sect. 4.4.

4.1. The stacked setup

Figure 4.1 shows the positioning of the LED and the HED. The HED is positioned 10 mm behind the LED; both detector substrates are plane parallel and (almost) centered on each other. The HED is connected from the back* of the CANDELA setup and the LED is connected from the sides.

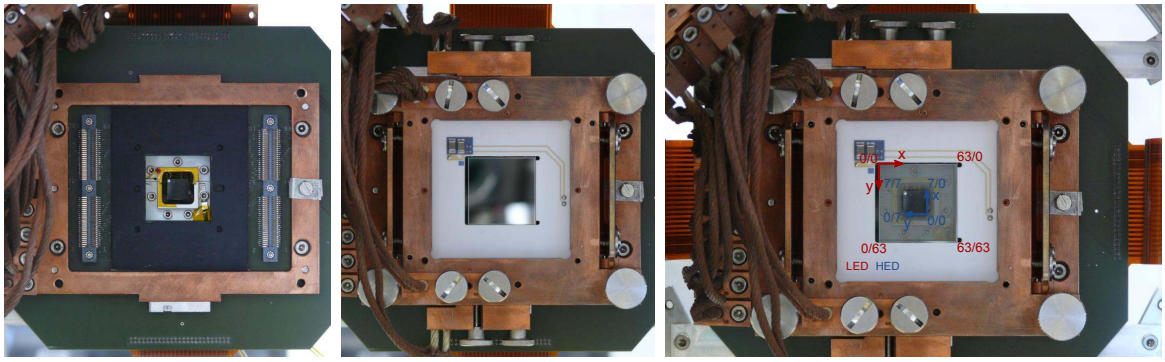

Figure 4.1. Front view on the setup with installed HED (left) and LED (center). Reflections on the highly polished detector surfaces may be misleading on these images. Right: the HED with a drawn, superimposed, semi-transparent LED image shows the alignment of the stacked detector setup. This is the perspective from which a ∼15 keV photon may "see" the setup. The orientation of the x- and y-directions of both detectors are not identical: the origin of the pixel numbering is on the top left corner for the LED but on the bottom right corner for the HED.

* The location of the radioactive sources are defined as the front of the CANDELA setup.

4.2. Mutual influence

The mutual influences that are discussed in this section can affect the imaging and spectral performance of the LED and the HED. Negative effects between the two detectors can be of thermal, electrical, and radiative origin and appear in the form of heating, signal crosstalk, flux absorption, and fluorescence emission. Positive effects that result from the stacked detector configuration are presented in Sect. 4.4.

A conductive thermal coupling between the LED ($P_{\mathrm{LED}} \approx 0.8\,\mathrm{W}$) and the HED ($P_{\mathrm{HED}} \approx 0.2\,\mathrm{W}$) is not possible because both detectors are only coupled by the common cold finger which is a large thermal reservoir.

In a nitrogen atmosphere convective heating between both detectors can increase the operating temperatures of both subsystems. A temperature influence between both detectors was studied via spectroscopy. The LED and the HED spectra are not influenced by the operation of the other detector. This is explainable by the good thermal coupling to the cold nitrogen gas. This analysis also shows that electrical crosstalk, i.e. a signal interference of one detector to the other detector is not existing.

Under vacuum conditions a radiative heat transfer is the only possible remaining thermal interaction between both detector subsystems. Using a set temperature of $T_{\mathrm{s}} = -60°\mathrm{C}$ and the maximal CAMEX gain $g_{\mathrm{cmx}} = 100\,\%$, an indirect temperature measurement is performed by comparing the offset and the noise of the LED (see Sect. 2.7.1) before and after the power up of the HED. The resulting temporal evolution of the pixel averaged offset and noise values are shown in Fig. 4.2. The LED offset increases by $\sim$1.0 % and the LED noise by $\sim$2.4 % if the HED is switched on. The thermal equilibrium is reached after approximately two hours. The offset change can be compensated with an updated offset measurement; the increase of the noise results in an equal increase of the energy uncertainty ΔE_{FWHM}, i.e. in a small decrease of the energy resolution.

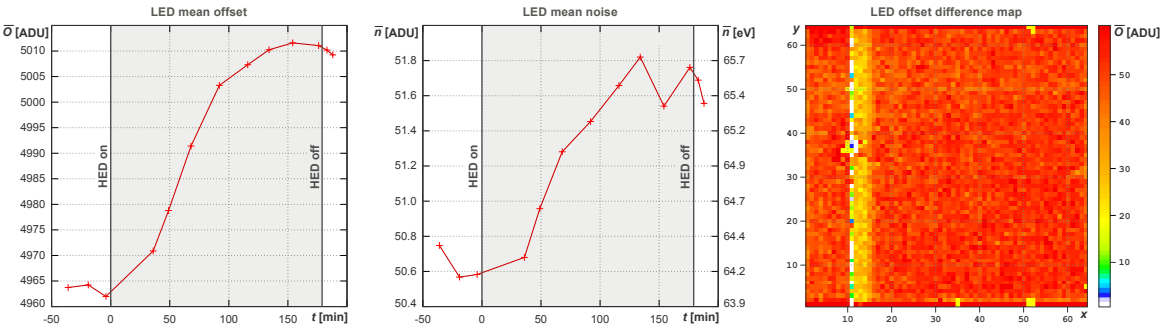

Figure 4.2. Evolution of the LED offset and noise after the HED is powered up. The offset and the noise of the LED increase because of radiative heating caused by the HED. The pixel averaged offset (left) increases by $\sim$45 ADU which can be corrected with an update of the offset map. The mean pixel noise (center) increases by roughly 1 ADU ($\sim$1.3 eV). The difference between the offset maps observed at $t = -4\,\mathrm{min}$ and at $t = 134\,\mathrm{min}$ (right) shows that the offset increases homogeneously over the LED pixel matrix (except for the known bad pixels).

Spectral changes

The presence of the HED influences the **LED spectrum** via cadmium and tellurium fluorescence lines, see Fig. 2.35. The L-fluorescence lines (Cd-$L_\alpha = 3.1\,\mathrm{keV}$, Te-$L_\alpha = 3.8\,\mathrm{keV}$) are indicated in Fig. 2.37; the more energetic K-fluorescence lines (Cd-$K_\alpha = 23.2\,\mathrm{keV}$, Te-$K_\alpha = 27.5\,\mathrm{keV}$) can be observed with the CAMEX gains $g_{\mathrm{cmx}} = 33\,\%$ and $g_{\mathrm{cmx}} = 21\,\%$. Figure 4.3 shows an LED hit map that is restricted to events with energies near ($\pm 200\,\mathrm{eV}$) Cd-K_α and Te-K_α. The central position of the HED is indicated by an increased counting statistics. The figure shows that fluorescence emission is oriented predominantly orthogonal to the surface of the CdTe crystal which can be explained with an increased self absorption at flatter emission angles. Using the two highest CAMEX gains, the LED spectrum is not influenced by cadmium or tellurium K-fluorescence lines because they are both out of the observing energy range of the detector ($E < 19\,\mathrm{keV}$).

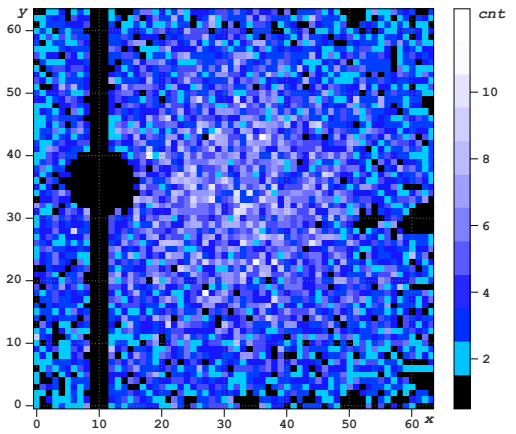

Figure 4.3. LED hit map observed in the energies Cd-$K_\alpha \pm 200\,\mathrm{eV}$ and Te-$K_\alpha \pm 200\,\mathrm{eV}$ in 10.8 ks.

The **HED spectrum** is practically not influenced by silicon fluorescence lines because of three reasons: first, the energy of the lines (Si-$K_\alpha = 1740\,\mathrm{eV}$) are typically below the trigger threshold* of the HED. Second, the silicon fluorescence yield is low ($y_{\mathrm{Si}} \approx 0.05$, see Fig. 1.11) which suppresses the generation of Si-fluorescence. Third, the LED absorbs radiation and re-emits fluorescence lines predominantly at its photon entrance side which is the opposite direction of the HED.

The photon absorption in the LED reduces the HED photon flux at low energies. Figure 4.4 shows the HED spectrum of Am-241 observed with and without installed LED. The spectra are almost identical at energies $E > 25\,\mathrm{keV}$ but differ at lower energies. The measurement with the installed LED, is additionally irradiated with Fe-55 which cannot pass through the LED. The observed flux reduction is caused by the quantum efficiency of the LED which drops sharply for $E > 10\,\mathrm{keV}$. See Fig. 4.4 (right) for a Geant4 simulation of the quantum efficiency of the LED and the HED in the stacked configuration [Pürckhauer, 2015]. Notable is the fact that the low energy background at $E < 10\,\mathrm{keV}$ is reduced by a factor of about 40 % if the LED is installed. This gives a hint on the composition of the low energy background; besides the events which are produced within the detector as a result of noise, a considerable ($\sim$40 %) part of the background must originate from K- and L-fluorescence photons that are generated by the irradiation of various elements within the CANDELA setup.

* The choice of the trigger threshold E_{th} depends on the noise level at the anodes of the Caliste-64 channels and is usually chosen as $E_{\mathrm{th}} = 3\,\mathrm{keV}$ within the CANDELA setup. The minimal selectable threshold is $E_{\mathrm{th}} = 1\,\mathrm{keV}$.

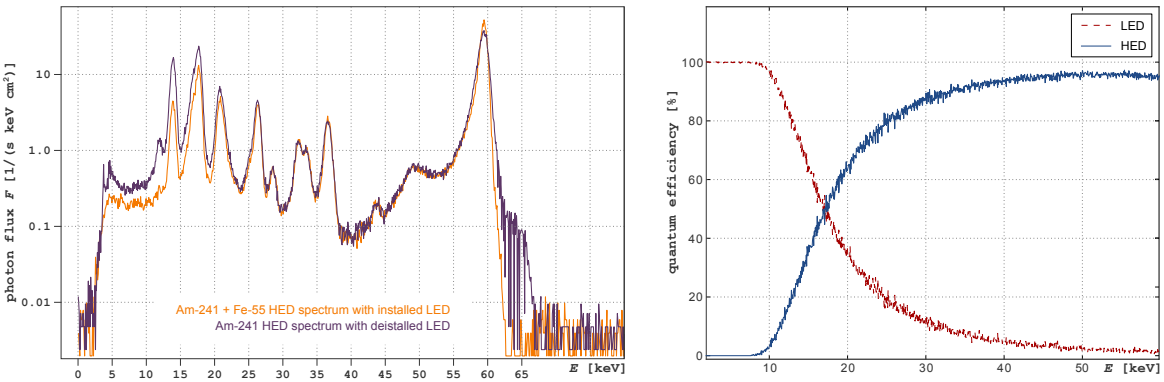

Figure 4.4. Left: HED spectrum observed with installed LED (orange) and without LED (purple). Only single events are used for the spectra. The conditions of the measurements are: $T_{\mathrm{CdTe}} = 10\,^{\circ}\mathrm{C}$, nitrogen atmosphere ($P = 1\,\mathrm{atm}$), a depletion voltage of $U = 300\,\mathrm{V}$, a peaking time of $t_{\mathrm{p}} = 9.6\,\mu\mathrm{s}$, and a trigger threshold of $E_{\mathrm{th}} = 3\,\mathrm{keV}$. Both spectra are calibrated with a non-linear ECC (see Sect. 3.7.1). The slightly better energy resolution with installed—but switched off—LED can be explained with a reduced temperature of the HED caused by the shielding of thermal radiation by the LED.
Right: Geant4 simulation of the quantum efficiency of the LED and the HED in the stacked detector configuration used in the CANDELA setup [Pürckhauer, 2015].

In summary, the (negative) mutual influences between the LED and the HED are marginal. Electrical crosstalk is not observed; heating effects of both detectors are measurable, but can be minimized with a proper operation of the detector system: the HED supply voltage must be switched on during the thermalization process of the LED, while the HED depletion voltage should be switched on only shortly before the measurement starts to prevent premature crystal polarization.

Spectral influences of both detectors are prominent: the HED spectrum is cut off below ∼10 keV and considerably reduced between 10 keV and 20 keV. The LED observes K- and L-fluorescence emission of cadmium and tellurium. All spectral effects become less important considering the designated operation modes for both detectors: the LED is intended to operate in a high gain mode ($g_{\mathrm{CMX}} = 100\,\%$ or $g_{\mathrm{CMX}} = 61\,\%$) and is therefore not influenced by Cd or Te K-fluorescence; the HED focuses on energies above 10 keV and is therefore not effected by silicon fluorescence.

4.3. Data analysis

In order to analyze LED and HED data in the same framework, the LED and HED pixel event lists (PELs) are combined into a common event list (CEL). In the CEL, the events are no longer positioned using pixel coordinates, but within a common coordinate system in units of millimeters. `PELs2CEL` is a software, written for this thesis, that builds a common event list using an LED and a HED pixel event list. The LED and HED PELs must be preprocessed as described in Sect. 2.7.3 and 3.7. The resulting CEL consists of the following entries:

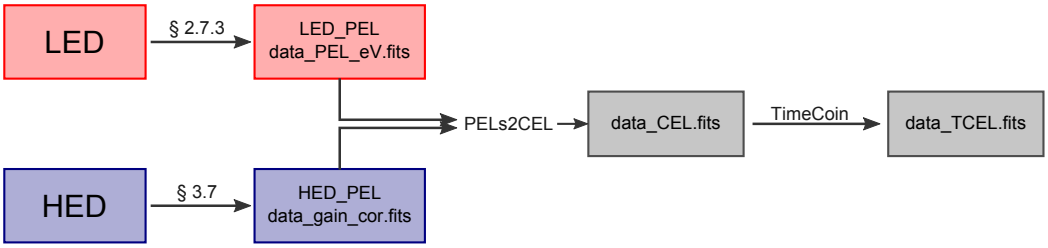

Figure 4.5. Structure diagram of the combined analysis of LED and HED data. The preprocessing of `data_PEL_eV.fits` and `data_gain_cor.fits` is sketched in Fig. 2.23 and Fig. 3.18. The `PELs2CEL` software combines these two pixel event lists and transforms the pixel coordinates into a common coordinate system. Another software, `TimeCoin`, filters the common event list for time coincident events.

- the **x-**, **y-**, and **z-positions** relative to a common coordinate system.
- the **energy** of the event.
- a common **time** coordinate.
- the **split type** of the event, defined according to Fig. 2.24.

The event energy is part of the LED and HED preprocessed PELs. The split types of the HED must be transformed to match the new directions of the common coordinate system. A sub-pixel resolution can be obtained for split events, if the center of mass of the split parts is calculated. In the current status of the setup this is not implemented but planned for future work. The transformation of the events into a common temporal and spatial coordinate system is discussed in detail in the following sections.

4.3.1. The common coordinate system

To correlate the two images observed by the LED and the HED, a common coordinate system is used. Besides imaging, the precise knowledge about the mutual positioning of both detector units is necessary for the analysis of LED-HED interactions, e.g. scattering effects. The center of the LED is chosen as origin of the common coordinate system (CCS) and the direction of the pixel rows and columns of the LED are chosen as the x- and y-directions of the CCS; see Fig. 4.6 for a sketch of the geometry.

In order to verify the positioning of both detectors, a structured shield, as shown in Fig. 4.7, is used to project an X-ray image on both detectors. The analysis of the resulting LED and HED hit maps shows the mutual positioning of both detectors in a rough way and is limited by the dimensions of the LED and HED pixels, 0.5 mm and 1.0 mm, respectively.

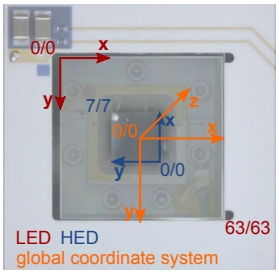

Figure 4.6. Coordinate systems of LED and HED.

To enhance the accuracy of the detector alignment, two optical images, one with the installed LED and the other one with the (solely) installed HED are used, similar as in Fig. 4.6. To minimize errors due to image distortions, the distance between the optical camera and the detectors is chosen as large

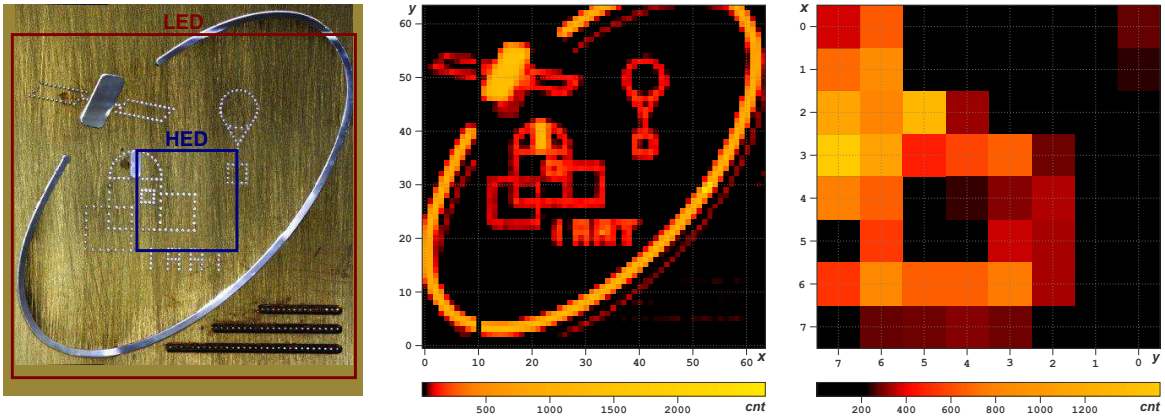

Figure 4.7. Left: brass shield with the IAAT logo in the dimensions 30 x 31 mm. The shield was installed horizontally flipped to match the LED x- and y-directions. The sizes of the LED and HED images are indicated.
Center: the LED hit map observed in 450 s with Fe-55 and Am-241. The shade like structure (red) of the ring (orange) results from the displacement between the Fe-55 and the Am-241 source. Column number 10 is set bad.
Right: the HED hit map observed in 1.4 ks with Fe-55. Be aware of the rotated coordinates.

as possible (∼2 m) and the detectors are placed in the center of the images. For the alignment of the images and the position measurements, standard image manipulating software* is used. The dimension of the HED (10 x 10 mm^2) and of the LED (32 x 32 mm^2) are used to transform the pixels of the optical camera (photo pixels) into lengths. The x- and the y-directions are calibrated individually to compensate for direction specific distortions or non-squared photo pixels which turned out to be not the case (the calibration factors are 14.910 x-photo-pixels/mm in contrast to 14.888 y-photo-pixels/mm). The uncertainty in the x- and y-directions is conservatively estimated to 2 photo pixels each, which results in $\Delta x = \Delta y \approx 0.13$ mm. The analysis of the optical images shows that the center of the HED is positioned at $x = -1.42$ mm and $y = -0.01$ mm and the direction of the pixel rows and pixel columns of the HED are slightly misaligned to the x- and y-directions of the CCS by 0.74°.

4.3.2. Timing

An accurate timing of LED and HED events is necessary to identify photons that interact in the LED *as well as* in the HED. The time delay caused by atomic transitions (µs to ns) or due to the limited speed of light (33 ps for a light traveling distance of 10 mm) are much shorter than the time accuracy of the CANDELA setup (2.44 ms). Therefore, scattering and fluorescence events are considered coincident in time. To identify **time coincidence**, the LED event time and the HED event time must be known relative to each other, but not absolute to another reference system.

* GIMP is used to align the images via (small) displacements and rotations. Inkscape is used to measure distances in the images.

Due to their heritage of different experiments, the LED and the HED subsystems are in the current configuration working with two individual chronometers that are both based on system clock counters. The LED and the HED system clocks are 100 MHz each, originating from two different oscillator circuits. This configuration has three difficulties.

1. LED and HED data have an offset in their timing. This **time offset t_0** results from the delay between the power up of both detector systems.

2. Small, constant differences in the frequency of the individual oscillators result in a **systematic error*** c_{sys} for the relative timing of both detector systems.

3. Variations in the frequency of the individual oscillators result in **additional uncertainties** of the time difference between both systems.

The timing offset and the systematic error can be recalibrated using a time variable source and observing the flux variations within the LED and the HED. In the simplest case, a manual opening and closing of the source shield can be used as flux variation. In the presented timing calibration the LED time t_{LED} is considered to be fix and only the HED time is recalibrated. The time offset can be corrected with a constant time shift t_0 and the systematic error is corrected with a correction factor c_{sys} according to

$$t^*_{\mathrm{HED}} = t_{\mathrm{HED}} \cdot (1 + c_{\mathrm{sys}}) + t_0. \tag{4.1}$$

Figure 4.8 shows the measured LED and HED flux as a function of the observation time. During the total observation time of 10.8 ks, the source shield was closed approximately each 15 minutes for a duration of 20 s. The opening and closing of the

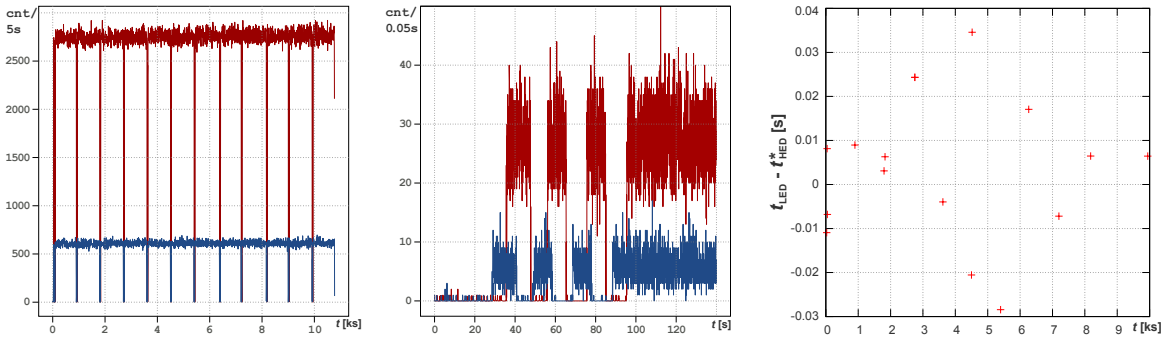

Figure 4.8. LED (red) and HED (blue) flux measurements in order to calibrate the timing of both subsystems. During 10.8 ks of observation, the Am-241 source is opened and closed several times (left). The zoomed image (center) of the measured counting rates for the LED and the HED shows a time offset of ∼7 s at the beginning of the measurement. The systematic time drift ($c_{\mathrm{sys}} \approx -6.8 \cdot 10^{-6}$) can be estimated by the evolution of this offset with increasing observation time. After correcting for both effects, the remaining relative timing error is in the order of several 10 ms (right).

* Here, the term *systematic error* does not mean that the error is constant but that it is determined. A time shift of 1 ms per hour is a systematic error.

Am-241 source is accomplished via a rotation of the source shield. Because of a projection effect during the rotation, the edges of the LED can be irradiated without irradiating the (smaller) HED. To correct for this effect, only the central $1\,\mathrm{x}\,1\,\mathrm{cm}^2$ part of the LED is further considered. The falling and rising edges of the LED and the HED flux are measured and t^*_{HED} can be fitted to t_{LED} according to Eq. (4.1) with the results: $t_0 \approx 7.004\,\mathrm{s}$ and $c_{\mathrm{sys}} = -6.8 \cdot 10^{-6}$. The timing inaccuracy is estimated via the residuals t_{LED} - t^*_{HED} and is in the order of several 10 ms (see Fig.4.8).

Timing calibration with fluorescence events

The timing accuracy can be improved dramatically by using fluorescence events for the timing calibration. A fluorescence photon that is emitted from the HED and detected in the LED represents two time coincident events that can be identified by their energy depositions. As Cd-K_α is the most prominent fluorescence emission of the HED it is used for the following calibration.

The LED pixel event list is filtered for Cd-K_α fluorescence events and the HED PEL is filtered for events of the Cd-K_α escape peak of the 59.5 keV americium emission line: during the measurement, 34 731 escape events were emitted by the HED and 8412 fluorescence events were detected by the LED. The difference results because of escape photons that do not hit the LED or that are not detected by the LED because of their large energy (23.2 keV).

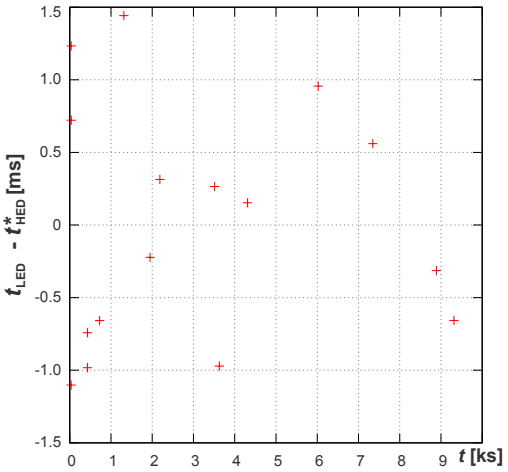

Figure 4.9. Timing calibration with coincident fluorescence events: the HED time is recalibrated according to Eq. (4.1) and the remaining residuals between the (fixed) LED time t_{LED} and the calibrated HED time t^*_{HED} is a measure of the timing inaccuracy which is less than ± 1.5 ms.

For the calibration, the LED time is assumed to be fix and the HED time is fitted to match the LED time. Figure 4.9 shows that the resulting residuals between the LED time and the recalibrated HED time are less than $\Delta t_{\mathrm{exp}} = \pm 1.5\,\mathrm{ms}$. The theoretical limit of the time accuracy can be estimated with the frame rate of the LED which is 410 frames/s = 2.44 ms/frame. Because of the very good timing capability of the HED, the HED time can be interpreted as an (almost) true event time. The delayed readout of the LED results in a negative time accuracy of $\Delta t_{\mathrm{th}} = -2.44\,\mathrm{ms}$. The recalibration, i.e. the fitting routine, shifts the HED time to minimize the magnitude of the absolute error and results in a theoretical time accuracy of $\Delta t_{\mathrm{th}} = \pm 1.22\,\mathrm{ms}$.

In summary, the timing of LED and HED events can be done roughly via the analysis of artificially induced flux variations. This first timing calibration helps to identify time coincident fluorescence and escape events which enables to perform a more accurate timing calibration with a measured accuracy of $\Delta t_{\mathrm{exp}} = \pm 1.5\,\mathrm{ms}$ which is close

to the theoretical limit of the system in its current configuration ($\Delta t_{\mathrm{th}} = \pm 1.22\,\mathrm{ms}$). For the future, an electronics based synchronization of the LED and the HED time counter via the already existing SpaceWire communication [Pinsard and Cara, 2008] is scheduled and will help to simplify the data analysis and to enhance the timing accuracy even further.

4.4. New possibilities to analyze stacked detectors

Besides the coverage of a broad energy range with one single telescope, a stacked detector setup enables new ways of data analysis and of observation.

Fluorescence events

At first sight, the detection of fluorescence emission is a disadvantage that comes with a stacked detector setup. But, a fluorescence event detected in detector A is correlated with the occurrence of an escape event in detector B. Such event pairs can be recognized via coincident time stamps and via the characteristic energy of the fluorescence emission. Combining both events has several advantages:

- reconstruction of the original energy: even if the reconstructed events suffer from enhanced noise due to the event sharing and will therefore be rejected for analysis methods that require the best spectral resolution possible, the reconstructed events help to measure the observed flux more accurately.

- subtracting fluorescence emission: the fluorescence event can be canceled out of the spectrum of detector A and faint spectroscopic structures can become visible.

- canceling the escape peak of the spectrum of detector B. Again, this allows to detect faint spectroscopic effects at the corresponding energy more precisely.

- the fluorescence event and the escape event are time coincident events that can be used to calibrate the relative timing between LED and HED (see Sect. 4.3.2).

As the fluorescence yield for CdTe is considerably higher than for silicon (see Fig. 1.11) the most likely scenario is the occurrence of an escape event in the HED followed by the detection of the fluorescence emission in the LED. The area that is covered by the LED and the quantum efficiency of the LED at the energy of the fluorescence emission ($\eta \approx 25\,\%$ at Cd-K_α) are both relevant factors to calculate the probability for the fluorescence detection. The stated quantum efficiency is a lower limit because of the close distance between HED and LED ($d = 10\,\mathrm{mm}$) and the large area of the LED ($32\,\mathrm{x}\,32\,\mathrm{mm}^2$), the fluorescence emission is likely to pass through the LED non-orthogonal, which enhances the possible interaction length of the photon. A ratio between LED fluorescence events and HED escape events of $7097/27866 \approx 25.4\,\%$ is measured for Cd-K_α fluorescence.

Compton reprocessing

Compton scattering can modify the LED and the HED spectra and can be differentiated into two processes: Compton forward scattering (CFS) describes the Compton scattering of an incident photon in the LED with a resulting scattering angle θ_{CFS} so that the scattered photon hits the HED. Compton backward scattering (CBS) refers to a Compton interaction in the HED with a scattering angle θ_{CBS} so that the scattered photon hits the LED. Assuming incident photons that are directed perpendicular to the detector surfaces, the possible scattering angles for the CANDELA setup geometry are $0° \leq \theta_{\mathrm{CFS}} \leq 64.5°$ and $115.5° \leq \theta_{\mathrm{CBS}} \leq 180°$. The energy of the scattered photon E' and of the Compton electron E_{e} can be calculated according to

$$E' = \frac{E_0}{1 + \frac{E_0}{511\,\mathrm{keV}}\left(1 - \cos\left(\theta\right)\right)} \tag{4.2}$$

$$E_{\mathrm{e}} = E_0 - E'. \tag{4.3}$$

Figure 4.10 shows the graphs of Eq. (4.2) and Eq. (4.3) as a function of the incident photon energy E_0 for all possible scattering angles θ in the case of CFS and CBS. The dominant emission line of Am-241, $E_0 = 59.5\,\mathrm{keV}$, results in

$$55.8\,\mathrm{keV} \leq E'_{\mathrm{CFS}} \leq 59.5\,\mathrm{keV}, \quad \text{and} \quad 48.3\,\mathrm{keV} \leq E'_{\mathrm{CBS}} \leq 51.0\,\mathrm{keV}, \tag{4.4}$$

$$0.0\,\mathrm{keV} \leq E_{\mathrm{e,\,CFS}} \leq 3.7\,\mathrm{keV}, \quad \text{and} \quad 8.5\,\mathrm{keV} \leq E_{\mathrm{e,\,CBS}} \leq 11.2\,\mathrm{keV}. \tag{4.5}$$

The colors indicate the detection in the LED (red) and in the HED (blue). In the case of CFS, the Compton reprocessing results in an enhanced low energy background for the LED and an additional low energy tail for each detected line in the HED spectrum.

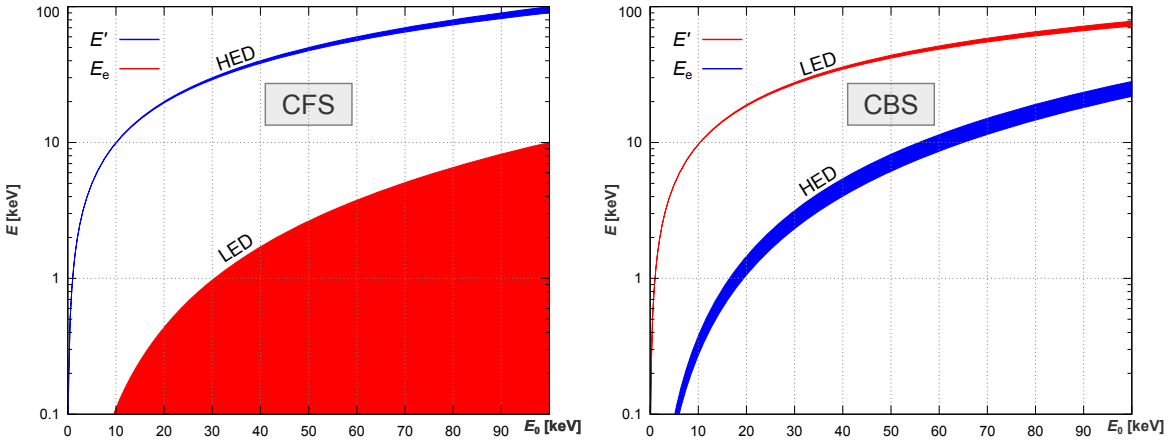

Figure 4.10. Compton forward scattering (CFS, left) and Compton backward scattering (CBS, right) calculated for the geometry of the CANDELA setup according to Eq. (4.2) and Eq. (4.3). The energy of the Compton electron E_{e} and of the scattered photon E' are deposited in the LED and the HED or vice versa, depending on the scattering being forwards or backwards directed.

The detector configuration of the CANDELA setup is suitable to detect Compton forward scattering in a wide energy range: for the LED, the low energy threshold and the high energy limit was measured to $E_{\mathrm{th}} = 144\,\mathrm{eV}$ and $E_{\mathrm{max}} > 60\,\mathrm{keV}$ (see Tab. 2.4) which results in a range of incident photon energies $11\,\mathrm{keV} \leq E_0 \leq 263\,\mathrm{keV}$ that can be detected with the CANDELA setup via CFS, see Fig. 4.10 (left). To detect Compton back scattering events is difficult because the trigger threshold of the HED $E_{\mathrm{th}} > 3\,\mathrm{keV}$, the energy range of the LED, and the quantum efficiency of the LED are not suited for such measurements, see Fig. 4.10 (right).

The detection of CFS events allows to reduce the background in the LED and the HED spectra. Furthermore, advanced analysis methods allow to build a Compton camera and a Compton polarimeter.

- **Compton camera:** the geometry of the Compton scattering can be used to trace the scattered photon back and to estimate its direction of arrival.
- **Compton polarimeter:** the dependency of the Compton scattering cross section on the polarization vector of the incident photon can be used to measure the degree and the angle of the incident radiation.

A detailed description of these two applications is given in the second part of this thesis.

4.5. Summary

In the stacked detector configuration, mutual influences between the LED and the HED affects the individual detector performances. A small increase of the average offset (+1 %) and noise level (+2.4 %) of the LED results from the mutual heating between both detectors. The LED spectrum is influenced by cadmium and tellurium fluorescence lines and the HED spectrum is cut off at energies below 10 keV because of the shielding effect of the LED. Compton forward scattering (CFS) in the LED effects the HED, but not vice versa, because Compton backward scattering in the HED occurs at energies that are mainly out of the detection range of the LED. Spectral changes caused by CFS are not observed with the HED which shines a light on the low statistical abundance of CFS. In the second part of this thesis the probability for CFS is calculated to $P \approx 6.1‰$ for $E_0 \approx 60\,\mathrm{keV}$, see Fig. 5.14.

The identification of time coincident events allows to compensate the negative mutual influences and can even be used to correct for effects that are not caused by the stacked configuration: the identification of fluorescence events in the LED allows to identify escape events in the HED; the rejection of such events suppresses fluorescence *and* escape peaks in the observed LED and HED spectra. Furthermore, Compton reprocessing makes it possible to build a Compton imaging camera and a Compton polarimeter.

Part II.

X-ray polarimetry

5. Applications for CANDELA

5.1. Overview

Besides the spatial distribution (imaging), the energetic distribution (spectroscopy), and the temporal distribution (timing) of electromagnetic radiation, the polarization is another quantity which is a characteristic of electromagnetic radiation. Electromagnetic polarization can be described with the concept of elliptical polarization, which implies linear and circular polarization as special cases. In the following, the term 'polarization' is used to refer to linear polarization. Polarization measurements provide access to two quantities, the degree of polarization P, which describes the relative amount of polarized photons to all observed photons, and the angle of polarization Ψ, which is the orientation of the electric field of the electromagnetic wave.

Polarization is characteristic to electromagnetic waves and is therefore present in the complete electromagnetic spectrum, ranging from radio waves to gamma radiation. Radio antennas are directly susceptible to polarization via their orientation and a simple polarization measurement can be obtained with two orthogonal antennas. In contrast, in the near infrared, optical and near ultraviolet regions, the polarization is not directly measured with the detectors, but with the help of special filters in front of the sensors. These filters modulate light depending on its angle of polarization, which results in an intensity variation that can be measured. The analysis of two distinct measurements obtained with orthogonal filter positions allows to conclude on the degree and the angle of polarization.

In the X-ray and gamma-ray regions, polarimetry is more subtle. The wavelengths are too short to be influenced by filters.* Instead, the fundamental interactions between light and matter are used to measure the polarization of the radiation. A comprehensive overview of the fundamental physics of the two most dominant interactions in the X-ray range—the photoelectric absorption and the Compton scattering—is given in Sect. 5.5. The expected efficiency of the CANDELA setup to detect Compton forward scattered events is calculated in Sect. 5.6 and its application as Compton camera and as Compton polarimeter are introduced in Sects. 5.7 and 5.8.

Even though imaging, spectroscopy and timing analysis need a large number of photons to obtain meaningful results, the orientation, the energy, and the arrival time of a *single* photon is defined clearly and can be measured individually. In contrast, the degree of polarization and the angle of polarization are quantities that are either not defined or not measurable for single photons which reveals that electromagnetic polarization can only be understood on a statistical level. The statistics that govern polarimetric measurements are therefore investigated in detail in Chapter 6.

*Polarimeters based on Bragg reflection use the compact, regular structure of crystals for X-ray polarimetry in the soft energy range of a few keV.

5.2. History of X-ray polarimetry

Astronomical observations using X-ray polarimeters started in 1968 using a Thomson-scattering X-ray polarimeter onboard an Aerobee-150 sounding rocket pointing on Sco X-1 [Angel et al., 1969]. In the observation time of only 70 seconds no polarization was observed. The first positive detection of polarized X-rays from an astrophysical source succeeded in 1971 with an Aerobee-350 sounding rocket experiment realized by the team of the Columbia University headed by Bob Novick [Novick et al., 1972, Weisskopf et al., 1972]. Using Thomson scattering and Bragg polarimeters,* they detected a polarization of the Crab Nebula with a degree of polarization $P = (15.4 \pm 5.2)\,\%$ and an angle of polarization $\Psi = 156° \pm 10°$ with a confidence level of 99.7 %. This observation confirmed the synchrotron emission mechanism of the source. A few years later, Weisskopf et al. [1976] observed again the Crab Nebula using graphite crystal X-ray polarimeters onboard the OSO-8† satellite and confirmed the previous results: $P = (15.7 \pm 1.5)\,\%$, $\Psi = 161.1° \pm 2.8°$ at 2.6 keV and $P = (18.3 \pm 4.2)\,\%$, $\Psi = 155.5° \pm 6.6°$ at 5.2 keV.

Up to now, the Crab Nebula is the only astrophysical object (except the sun) with a statistically significant detection of polarized X-ray emission. Silver et al. [1979] found upper limits $P \leq 13.5\,\%$ and $P \leq 60\,\%$ for the accreting X-ray pulsars Cen X-3 and Her X-1, using also the OSO-8 satellite.

In the recent years, more and more groups have become interested in X-ray polarimetry. Even though no telescope specialized for polarimetric measurements in the X-ray range is operating at the moment, existing telescopes are used with special analysis methods to search for polarization signatures in the observed X-ray data, see for example Lotti et al. [2012] (NuSTAR), Mizuno [2012] (ASTRO-H), Moran et al. [2013] (INTEGRAL), Chattopadhyay et al. [2014] (Astrosat).

5.3. Scientific motivation

Although the spatial, the spectroscopic, and the temporal resolution of observatories in the X-ray range made great improvements during the last decades, the models to explain the properties of astrophysical objects are often not unambiguous and several different models compete with each other. X-ray polarimetry can help to distinguish between these models if the models predict different outcomes for the degree of polarization and the angle of polarization. See Meszaros et al. [1988] and Krawczynski et al. [2011] for a detailed investigation on the expected impact of X-ray polarimetry for the analysis of compact objects.

The application of polarimetric analysis methods shall be illustrated with a prominent example: the observation of NGC 1068 [Antonucci and Miller, 1985] which made an important contribution to the unification of AGN. As described in Sect. 1.1.1,

* In their analysis, they combined the results of both detectors and assumed that the polarization of the source is independent of the energy band.

† OSO: orbiting solar observatory.

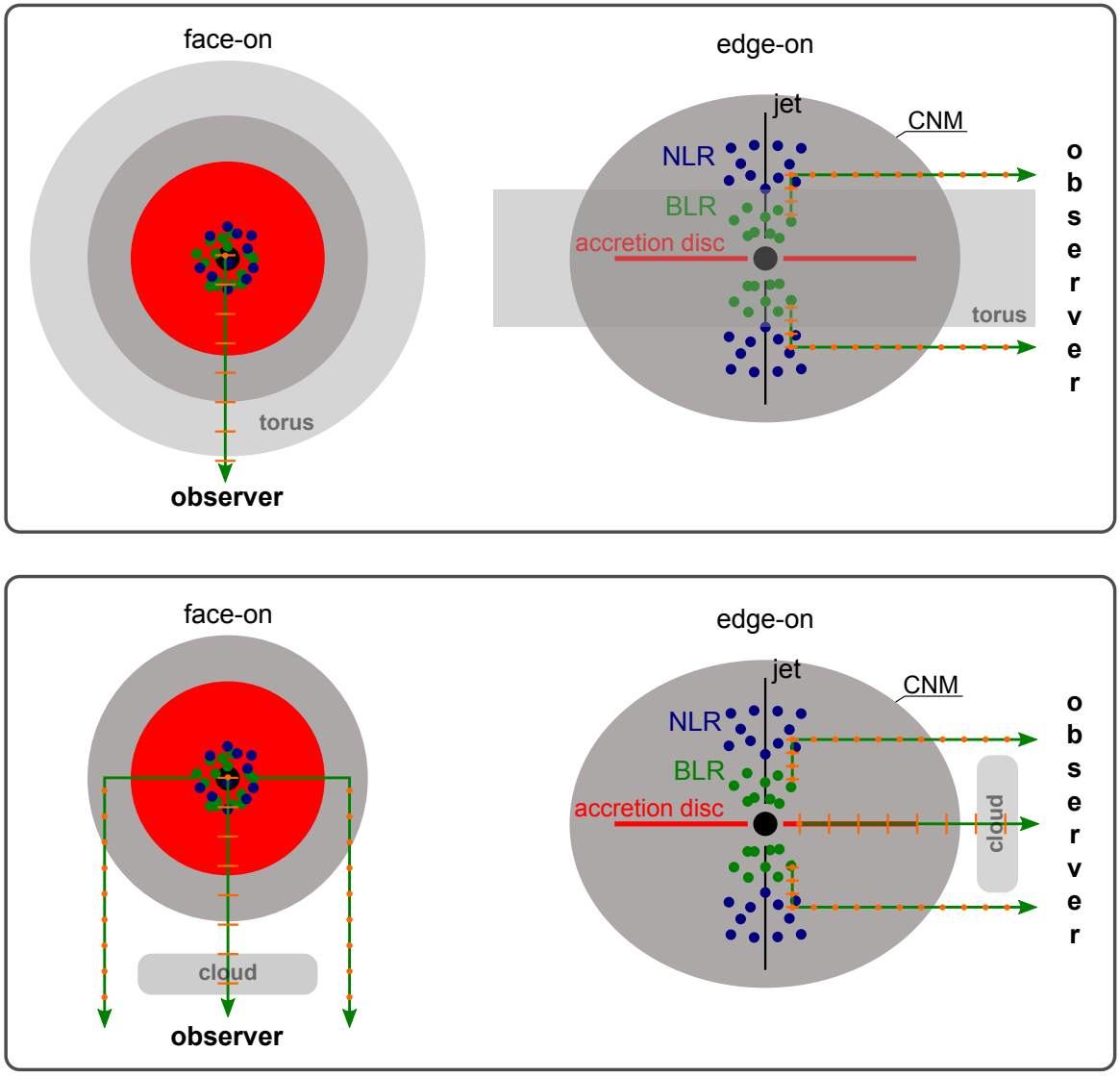

Figure 5.1. NGC 1068: a Seyfert II galaxy with a broad line region (BLR) that can be observed using a polarimetric analysis. The direction of the electric field of the emitted radiation is drawn with dots (orthogonal to the paper plane) and bars (parallel to the bars, in the paper plane) in orange.
Top: a toroidal structured thick medium (torus) obscures the nucleus and the BLR of the AGN. Initially unpolarized BLR emission is scattered at circum-nuclear material (CNM) in the direction of the observer. Only the scattering along the jet axis can escape the toroidal structure and results in an observed polarization which is perpendicular to the jet axis.
Bottom: with a cloud-like obscuring structure the scattered radiation can originate from all directions and the net-polarization is averaged out if the cloud cannot be spatially resolved. From an observer's view, the central scattered radiation (central green arrow in the image) is above and below the cloud in case of the face-on image and left and right of the cloud in case of the edge-on image.

Seyfert I galaxies are observed with narrow and broad line features, while Seyfert II galaxies show only narrow line features. Today it is believed that Seyfert I and II galaxies are both AGN observed under different viewing angles and that a thick torus absorbs emission from the broad line region if the AGN is observed edge-on. This AGN model is strongly supported by a polarimetric analysis* of the observation of NGC 1068. Antonucci and Miller [1985] restricted the analysis to polarized radiation in the optical band and observed thereby broad lines (a type I feature) in the Seyfert II galaxy NGC 1068. This proves that a (hidden) broad line region is also present in Seyfert II galaxies. The observation can be explained with scattering: the radiation of the broad line region are scattered into the line of sight of the observer by circum-nuclear material which has a larger extent than the obscuring torus, see Fig. 5.1 (top). In NGC 1068 this structure is believed to consist of free electrons in an ionized gas [Bianchi et al., 2012]. This weak signal became only observable after all the unpolarized light was cut out during the analysis.

Furthermore, the geometrical structure of the obscuring torus can be estimated with the observation. Figure 5.1 (bottom) shows a Seyfert II model that uses an obscuring cloud-like structure between the AGN and the observer to account for the hidden broad line region. In this model, the reflections at the circum-nuclear material should come from all directions around the cloud and the polarization of the observed radiation is averaged out. A toroidal structure is a simple model that predicts the observed polarization which is orthogonal to the direction of the AGN jet axis.

Even though this observation uses optical radiation, it demonstrates two principle possibilities for polarimetric analysis. The restriction of the analysis to polarized radiation allows to select only a small fraction of all photons that originates from a specific region or that have undergone a specific interaction. Thereby, faint polarized radiation that is concealed within the unpolarized radiation becomes visible. Second, the additional parameters P and Ψ allow to distinguish different astrophysical models. The models can be focused on the geometry of the observed object (as in the example of NGC 1068), or on the generation/reprocessing mechanisms of radiation. The latter are further investigated in the following section.

5.4. The generation of polarized radiation

Polarized radiation can be generated by various effects. The radiation processes that emit polarized radiation are:

- **synchrotron radiation:** the linear polarization of synchrotron emission in a uniform magnetic field was first studied by Westfold [1959]. Russell and Shahbaz [2014] summarize the recent studies on the polarization properties for more elaborate configurations. The basic production mechanism of synchrotron radiation results in radiation that is linearly polarized in the plane of the motion

* The polarization is observed in the optical, but the processes are similar for X-rays and the example also shows the possibilities for X-ray polarimetry.

of the charge particle. The degree of polarization depends on the energy of the radiation and increases from 2/3 at radio frequencies asymptotically to unity for higher energies [Westfold, 1959].

- **bremsstrahlung:** electrons that are polarized, i.e. that have an aligned orientation of the electron spins, emit linearly polarized bremsstrahlung if they are accelerated [Tashenov et al., 2013].

Besides the direct generation of polarized radiation it is also possible to reprocess radiation and to change thereby its polarization characteristics:

- **scattering:** if unpolarized radiation is scattered, the scattered radiation is partially polarized in an orthogonal direction to the scattering plane which is defined by the incident and the scattered radiation. The resulting degree of polarization depends on the scattering angle and is zero for forward and backward scattering and 100 % for orthogonal scattering angles. See also Fig. 5.1.

- **inverse Compton:** the polarization of inverse Compton scattering depends on the orientation of the electrons, on the momentum of the target photons, and on the polarization of the target photons. Krawczynski [2012] presents analytical and numerical calculations of the linear polarization properties of inverse Compton scattered radiation. He concludes that
  - inverse Compton scattering by non-thermal electron plasmas does not create polarization. An initially unpolarized beam stays unpolarized and an initially polarized beam reduces its degree of polarization after scattering.
  - the degree of polarization of the inverse Compton radiation depends on the degree but not the direction of the polarization of the target photons.

In contrast to the presented radiation processes, no polarization is assumed for blackbody radiation or for bremsstrahlung with unpolarized electrons. Furthermore, the possibility for the production of polarized radiation does not guarantee that a net-polarization can be observed. If the radiation emitting region has a symmetric shape, all polarization will be averaged out, see Fig. 5.1 (bottom). A symmetry breaking source structure is needed in addition to the mentioned production mechanisms.

5.5. The interactions of photons with matter

The interaction between light and matter depends on the energy of the radiation and the properties of the matter. In the X-ray region, photoelectric absorption and Compton scattering are the predominant types of interaction, whereas pair production becomes the dominant interaction in the gamma ray region. The probability P of a photon interaction within an interaction length d can be calculated with Beer's law to

$$P = 1 - \mathrm{e}^{-\mu \cdot d}. \tag{5.1}$$

The attenuation coefficient μ for silicon and cadmium telluride is shown in Fig. 5.2 for different photon interactions.

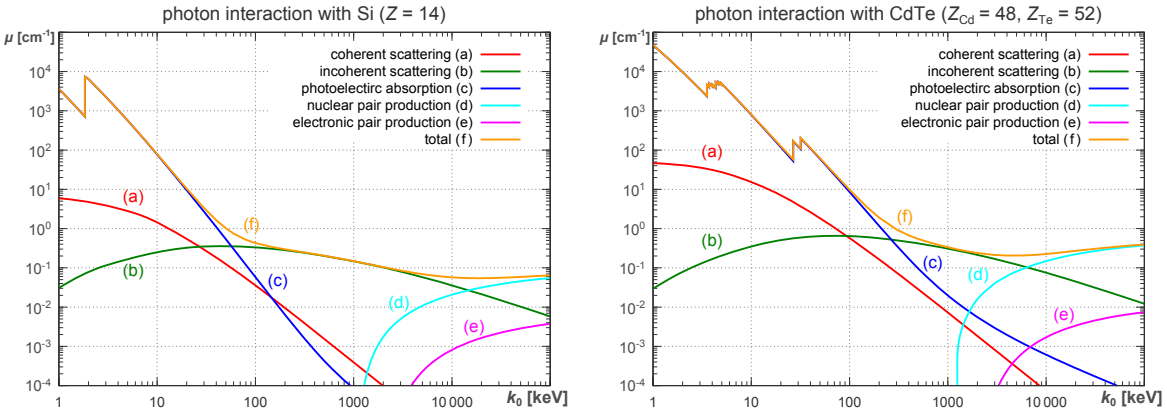

Figure 5.2. Attenuation coefficients for electromagnetic radiation from 1 keV to 100 MeV in silicon (left) and cadmium telluride (right). Photoelectric absorption is dominant up to about 100 keV, whereas Compton scattering (incoherent scattering) becomes dominant between 100 keV and 10 MeV. Coherent scattering only contributes in the transition region from photoelectric absorption to Compton scattering significantly to the total cross section. This transition region is shifted to higher energies for heavier elements, whereas the transition to pair production is shifted to lower energies for heavier elements. All data are taken from the XCOM Photon Cross Sections Database, see Gerward et al. [2001] and Berger et al. [2010].

5.5.1. Photoelectric effect

Photoelectric absorption refers to the interaction of an X-ray photon with a strongly bound electron*. If the photon energy is larger than the ionization energy of the electron, it can be absorbed and the atom becomes ionized. In the non-relativistic case with Born's approximation, the differential cross section $\frac{\mathrm{d}\sigma}{\mathrm{d}\Omega}$ for photoelectric absorption by a K-electron is [Heitler, 1954, § 21]:

$$\frac{\mathrm{d}\sigma_{\mathrm{PE}}}{\mathrm{d}\Omega} = \mathrm{r_e^2}\frac{Z^5}{137^4}\left(\frac{\mathrm{m_e c^2}}{k_0}\right)^{3.5}\frac{4\sqrt{2}\,\sin^2(\theta)\cos^2(\phi)}{(1-\frac{v}{\mathrm{c}}\cos(\theta))^4} \tag{5.2}$$

Here, $\mathrm{r_e}$ represents the classical electron radius, Z the atomic number of the interacting material, k_0 the energy of the incident photon, $\mathrm{m_e}$ the mass and v the velocity of the photoelectron, θ the scattering angle between the photon and the photoelectron and ϕ the azimuthal scattering angle between the electric field of the photon and the direction of the photoelectron, see Fig. 5.3.

In order to calculate the cross section for a photoelectric interaction with all electrons of an atom a factor of 2 must be introduced for the second K-electron. As experimental fact, all other electrons contribute with an additional factor of 5/4 [Heitler,

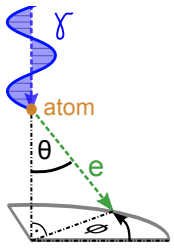

Figure 5.3. Terminology for the photoelectric effect.

* A free electron cannot absorb a photon. The strong binding to the nucleus is needed for momentum transfer.

1954]. Multiplying with these factors and integrating Eq. (5.2) over all scattering directions θ and ϕ results in the total cross section per atom

$$\sigma_{\mathrm{PE}}(k) = 5\sqrt{2} \cdot \sigma_{\mathrm{Th}} \cdot \frac{Z^5}{137^4} \cdot \left(\frac{\mathrm{m_e c^2}}{k_0}\right)^{3.5} \tag{5.3}$$

with the Thomson cross section

$$\sigma_{\mathrm{Th}} = \frac{8\pi}{3} \mathrm{r_e^2}. \tag{5.4}$$

Deviations from Born's approximation

Because of Born's approximation, Eq. (5.2) is only valid for photon energies k_0 much larger than the ionization energy I and a correction factor $f(\xi)$ has to be multiplied for the analysis near an absorption edge [Stobbe, 1930].

$$f(\xi) = 2\pi \sqrt{\frac{I}{k_0}} \cdot \frac{\mathrm{e}^{-4\xi\,\mathrm{arccot}(\xi)}}{1 - \mathrm{e}^{-2\pi\xi}}\,, \qquad \xi = \sqrt{\frac{I}{k_0 - I}} \tag{5.5}$$

The expression "near an absorption edge" is somewhat misleading. Figure 5.4 shows the correction factor $f(k_0)$ for photoelectric absorption in the K- and the L1-shell of silicon. Even at energies of 100 keV, which is about 50-times the energy of the K-edge, the photoelectric absorption is reduced by a factor of about a third with respect to Eq. (5.2) or (5.3).

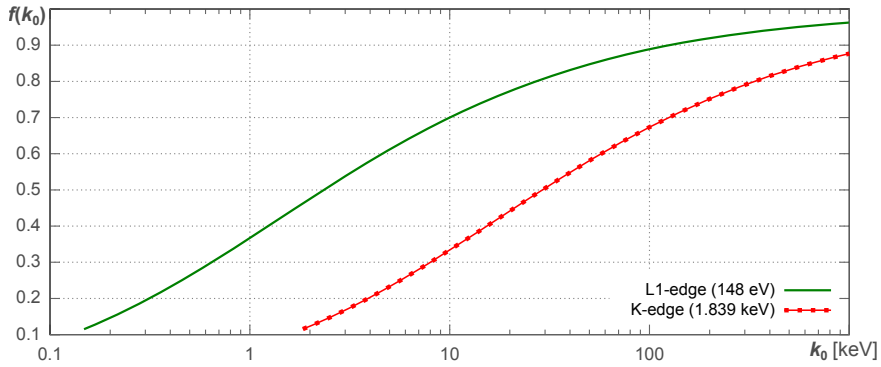

Figure 5.4. The correction factor $f(k_0)$ for photoelectric absorption in the K- and the L1-shell of silicon. Even for energies much greater than the absorption edges, photoelectric absorption is reduced significantly with respect to Born's approximation (Eq. (5.2)).

Altogether, the differential cross section for photoelectric absorption can be calculated with

$$\frac{\mathrm{d}\sigma}{\mathrm{d}\Omega} = 10\,\mathrm{r_e^2} \frac{Z^5}{137^4} \left(\frac{\mathrm{m_e c^2}}{k_0}\right)^{3.5} \frac{\sqrt{2}\,\sin^2(\theta)\cos^2(\phi)}{(1 - \frac{v}{c}\cos(\theta))^4} \cdot f(k_0) \tag{5.6}$$

and the total cross section with

$$\sigma_{\mathrm{PE}}(k) = 5\sqrt{2} \cdot \sigma_{\mathrm{Th}} \cdot \frac{Z^5}{137^4} \cdot \left(\frac{\mathrm{m_e c^2}}{k_0}\right)^{3.5} \cdot f(k_0). \tag{5.7}$$

Figure 5.5 (left) shows the differential cross section for a K-shell electron according to Eq. (5.2). Forward ($\theta = 0°$) and backward ($\theta = 180°$) emission of the photo electron is forbidden and an orthogonal emission ($\theta = 90°$) along the direction of the electric field of the absorbed photon ($\phi = 0°$ or $\phi = 180°$) is preferred.

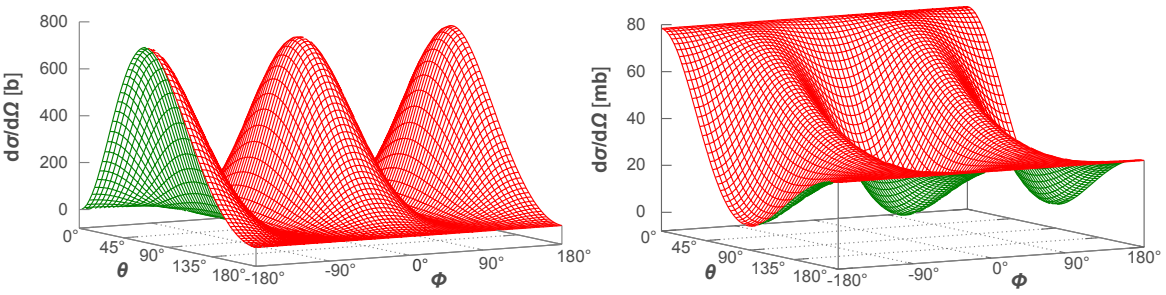

Figure 5.5. Left: differential cross section for the non-relativistic photoelectric effect with a K-shell electron in silicon for $k_0 = 10\,\mathrm{keV}$ according to Eq. (5.2).
Right: differential cross section for Compton scattering on free electrons for $k_0 = 200\,\mathrm{keV}$ according to Eq. (5.11).

5.5.2. Compton Scattering

Compton scattering is the inelastic scattering of a photon with a free or nearly-free* charged particle, mostly an electron. Using the conservation of energy and momentum results in a relation between the incident photon energy k_0, the scattering angle θ and the energy of the scattered photon k:

$$k(\theta) = \frac{k_0\,\mathrm{m_e c^2}}{\mathrm{m_e c^2} + k_0\,(1 - \cos(\theta))} \tag{5.8}$$

The energy of the electron can be calculated as

$$E_\mathrm{e} = k_0 - k(\theta) \tag{5.9}$$

$$= \frac{k_0^2(1 - \cos\,(\theta))}{\mathrm{m_e c^2} + k_0(1 - \cos\,(\theta))} \tag{5.10}$$

and is shown in Fig. 5.6 for different photon energies k_0.

The differential cross section for the interaction between a photon and a free electron is described by the Klein-Nishina formula and can be expressed in polar coordinates, see Appendix A:

$$\frac{\mathrm{d}\sigma_\mathrm{CS}}{\mathrm{d}\Omega} = \frac{1}{2}\mathrm{r_e^2}\left(\frac{k(\theta)}{k_0}\right)^2\left(\frac{k(\theta)}{k_0} + \frac{k_0}{k(\theta)} - 2\sin^2(\theta)\cos^2(\phi)\right) \tag{5.11}$$

* *nearly-free* means that the photon energy is much higher than the ionization energy of the material.

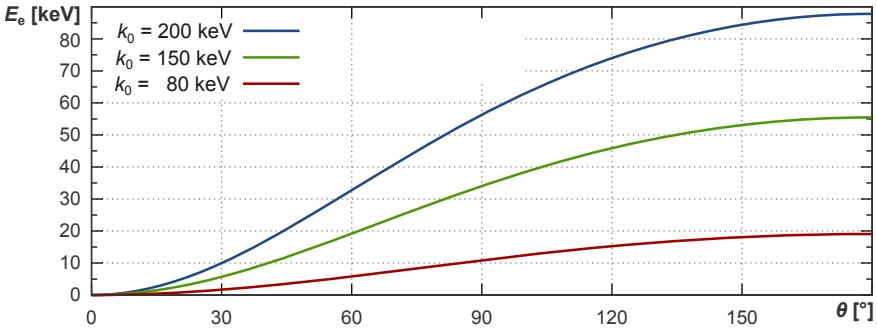

Figure 5.6. The energy of the Compton electron E_e depends on the energy of the incident photon k_0 and on the scattering angle θ. The relative energy transfer to the electron E_e/k_0 is larger for higher photon energies k_0.

Herein, r_e represents the classical electron radius, k_0 the energy of the incident photon, θ the scattering angle of the photon and ϕ the azimuthal scattering angle between the electric field of the incident photon and the direction of the scattered photon, see Fig. 5.7. The scattering angle of the electron and the polarization of the scattered photon are in the following not further investigated. See Heitler [1954, § 22] for an analysis. Figure 5.5 (right) shows a surface plot of the differential cross section for Compton scattering on free electrons.

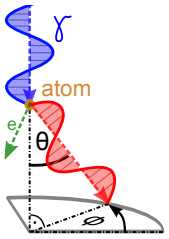

Figure 5.7. Terminology of Compton scattering.

An integration of the differential cross section over the azimuth angle ϕ results in the θ-differential cross section which is a function of θ:

$$\sigma_{\mathrm{CS},\theta}(k_0,\theta) := \int_0^{2\pi} \frac{\mathrm{d}\sigma_{\mathrm{CS}}}{\mathrm{d}\Omega}\,\mathrm{d}\phi = \frac{\mathrm{d}\sigma_{\mathrm{CS}}}{\sin(\theta)\,\mathrm{d}\theta} = \pi \mathrm{r}_e^2 \left(\frac{k(\theta)}{k_0}\right)^2 \left(\frac{k(\theta)}{k_0} + \frac{k_0}{k(\theta)} - \sin^2(\theta)\right) \quad (5.12)$$

The $\sin(\theta)$ in the denominator of Eq. (5.12) accounts for the geometrical reduction of the solid angle for $\theta \to 0°$ and $\theta \to 180°$. The total cross section σ_{CS} can be calculated by integrating Eq. (5.12) over θ which results in [Heitler, 1954, § 22, Eq. (45)]

$$\sigma_{\mathrm{CS}}(k_0) = \frac{3}{4}\sigma_{\mathrm{Th}} \left\{ \frac{1+x}{x^3} \left[\frac{2x(1+x)}{1+2x} - \ln(1+2x) \right] + \frac{1}{2x}\ln(1+2x) - \frac{1+3x}{(1+2x)^2} \right\} \quad (5.13)$$

with

$$x = k_0/(\mathrm{m_e c^2}). \quad (5.14)$$

Figure 5.8 shows the cross section for the θ-differential cross section and the total cross section. Compton scattering is most likely forward directed. The asymmetry between forward and backward scattering increases with the photon energy k_0. The total cross section is only slightly dependent on the energy k_0.

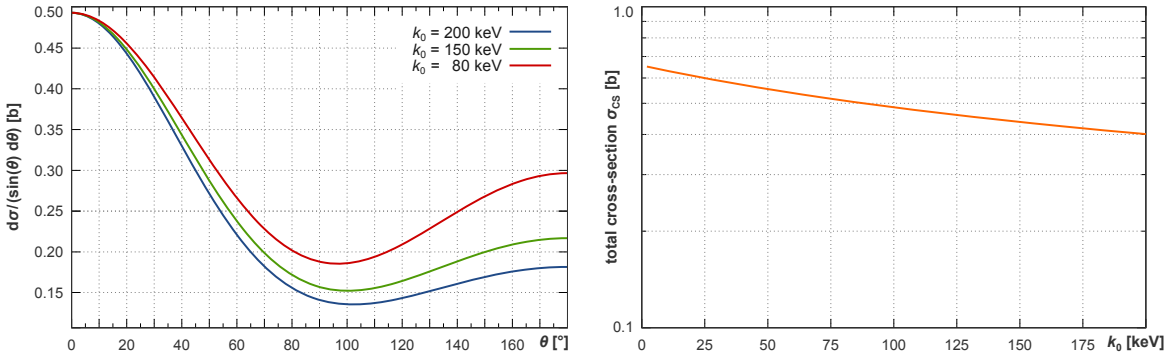

Figure 5.8. Left: θ-differential cross section for Compton scattering according to Eq. (5.12). See also Fig. 5.5 (right) for the (fully) differential cross section.
Right: total cross section for Compton scattering according to Eq. (5.13).

The incoherent scattering factor S

The Klein-Nishina formula describes the differential cross section for Compton scattering on a free electron. If the photons are scattered on atoms, the formula must be multiplied with an incoherent scattering factor S which states the amount of electrons of an atom that contribute to the scattering. To distinguish Compton scattering on free electrons and Compton scattering on atoms, the latter is in the following labeled *incoherent scattering*. The incoherent scattering factor S depends on the momentum transfer Δp between photon and electron, which is

$$\Delta p = \frac{\sin(\theta/2)}{\mathrm{hc}} \cdot k_0. \tag{5.15}$$

For large momentum transfers (i.e. large scattering angles θ and large photon energies k_0) all electrons contribute to the incoherent scattering: $S \to Z$. Hubbell et al. [1975] present tabulated, theoretical values for $S(\Delta p)$, see Fig. 5.9. For silicon, a fit $\hat{S}$ is calculated to

$$\hat{S}(k_0, \theta) = 14 \cdot \frac{1 - \exp(-0.18\,(k_0\,\sin\,(\theta/2))^{0.87})}{1 + 7.19 \cdot \exp(-3.11\,k_0\,\sin\,(\theta/2))}. \tag{5.16}$$

The ansatz of the fit is motivated by no physical idea but as an analytical approximation to the tabulated values. The differential cross section for incoherent scattering

$$\frac{\mathrm{d}\sigma_{\mathrm{IS}}}{\mathrm{d}\Omega} = \frac{\mathrm{d}\sigma_{\mathrm{CS}}}{\mathrm{d}\Omega} \cdot \hat{S}(k_0, \theta) \tag{5.17}$$

is shown in Fig. 5.10 (left). The θ-differential cross section can be calculated using the result of Eq. (5.12)

$$\sigma_{\mathrm{IS},\,\theta}(k_0, \theta) := \frac{\mathrm{d}\sigma_{\mathrm{IS}}}{\sin(\theta)\,\mathrm{d}\theta} = \frac{\mathrm{d}\sigma_{\mathrm{CS}}}{\sin(\theta)\,\mathrm{d}\theta} \cdot \hat{S}(k_0, \theta) \tag{5.18}$$

and is shown in Fig. 5.10 (right). The total cross section for incoherent scattering must be recalculated via

$$\sigma_{\mathrm{IS}}(k_0) = \int_0^{\pi} \sigma_{\mathrm{IS},\,\theta}(k_0, \theta) \cdot \sin(\theta)\,\mathrm{d}\theta \tag{5.19}$$

which is done numerically. See Fig. 5.11 for the resulting cross section σ_{IS}.

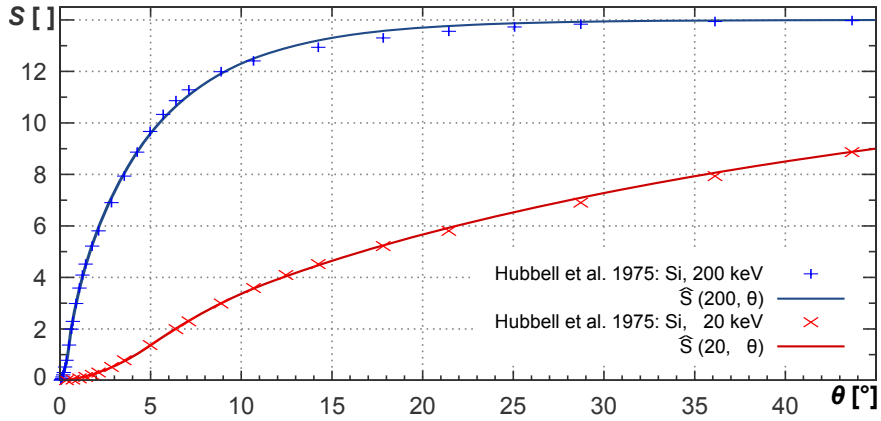

Figure 5.9. The incoherent scattering factor S for Compton scattering in silicon as a function of the scattering angle θ. The tabulated values from Hubbell et al. [1975] are shown with the corresponding fits $\hat{S}$ according to Eq. (5.16).

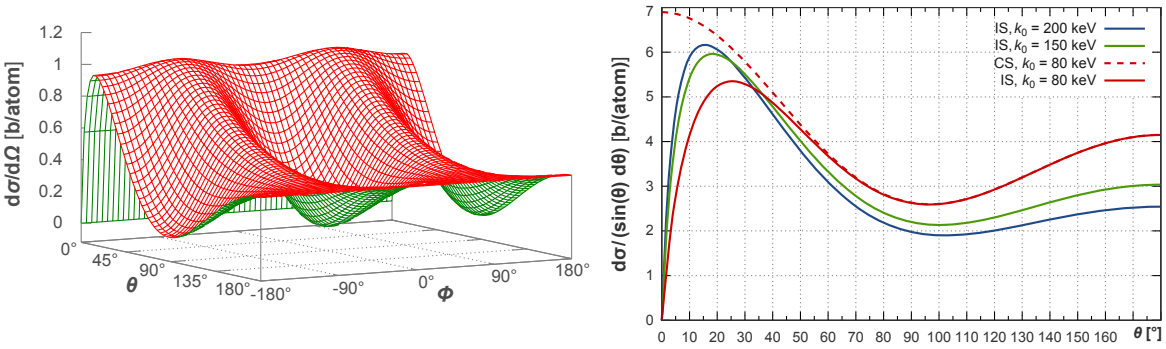

Figure 5.10. Left: differential cross section for incoherent scattering in silicon for $k_0 = 200\,\text{keV}$ according to Eq. (5.17). Compared to the differential cross section for Compton scattering (Fig. 5.5 (right)), the cross section is reduced at small scattering angles θ.
Right: θ-differential cross section for incoherent scattering according to Eq. (5.18). For $k_0 = 80\,\text{keV}$, the cross section for Compton scattering multiplied with the number of electrons per Si-atom ($Z = 14$) is printed as dashed line. At small scattering angles θ, forward scattering can be more probable for higher energetic photons as for lower energetic ones: for higher energies, the decreasing Klein-Nishina cross section is more than compensated by the increasing number of available electrons per atom.

5.5.3. Pair production

The occurrence of pair production has an energy threshold of $E > 1022\,\text{keV}$ and is therefore out of the X-ray range; it is shortly introduced for the sake of completeness. Pair production describes the phenomenon that a high energy photon can produce an electron-positron pair in the vicinity of a nucleus. The nucleus is needed for

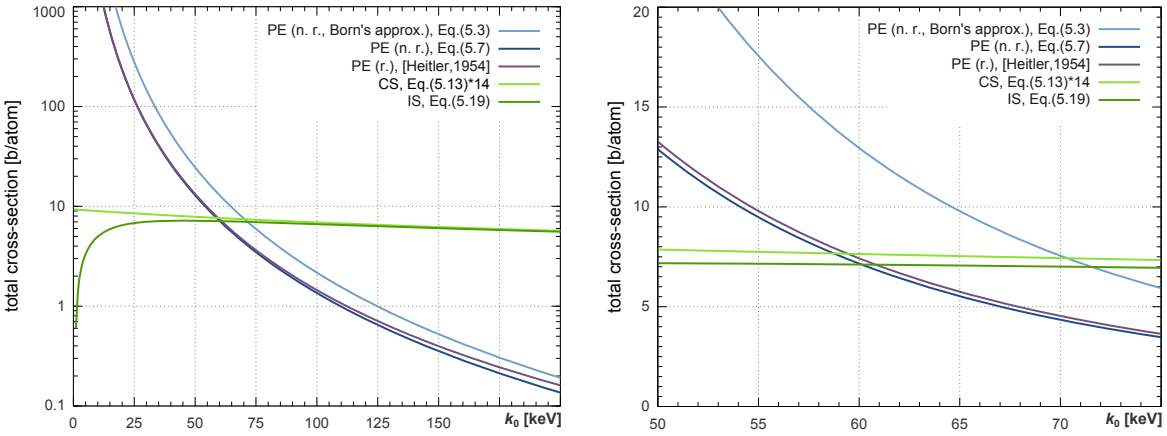

Figure 5.11. Graphs of the analytic expressions for the total cross sections for the photoelectric effect (PE) and Compton scattering (CS) in the case of silicon. Born's approximation is according to Eq. (5.3). The differences between the non-relativistic (n. r.) calculation (Eq. (5.7)) and the relativistic (r.) calculation [Heitler, 1954, § 21, Eq. (17)] for the photoelectric effect are only minor for $k_0 < 100\,\mathrm{keV}$. Incoherent scattering (IS, according to Eq. (5.19)) is significantly reduced compared to Compton scattering (Eq. (5.13) multiplied with 14 to account for the number of electrons per silicon atom) for small energies $k_0 \lesssim 50$. The zoom (right) shows that photoelectric effect and Compton scattering are equally probable at $k_0 \approx 61\,\mathrm{keV}$ which fits to the measured attenuation coefficients μ_{PE} and μ_{CS} of Fig. 5.2 which are equal for $k_0 \approx 57\,\mathrm{keV}$.

momentum conservation. The cross section is calculated in Heitler [1954, § 26, Eq. (6)]:

$$\frac{\mathrm{d}\sigma}{\mathrm{d}\theta_+\,\mathrm{d}\theta_-\,\mathrm{d}\phi\,\mathrm{d}E_+} = -\frac{\mathrm{e}^4 Z^2}{2\pi 137}\frac{p_{\mathrm{s}+}p_{\mathrm{s}-}}{k_0^3 q^4}\left(\frac{p_{\mathrm{s}+}^2(4E_-^2-q^2)}{(E_+-p_{\mathrm{c}+})^2}+\frac{p_{\mathrm{s}-}^2(4E_+^2-q^2)}{(E_--p_{\mathrm{c}-})^2}+\right.$$
$$\left.\frac{2p_{\mathrm{s}+}p_{\mathrm{s}-}\cos(\phi)(4E_+E_-+q^2-2k_0^2)}{(E_+-p_{\mathrm{c}+})(E_--p_{\mathrm{c}-})}+\frac{2k_0^2(p_{\mathrm{s}+}^2+p_{\mathrm{c}-}^2)}{(E_+-p_{\mathrm{c}+})(E_--p_{\mathrm{c}-})}\right) \quad (5.20)$$

Here, $p_{\mathrm{s}} = p\sin(\theta)$ and $p_{\mathrm{c}} = p\cos(\theta)$ with the momentum p and the energy E. The + and - index represent the positive and negative charged particle, i.e. the positron and the electron. The momentum transfer to the nucleus is $q = k_0 - p_+ - p_-$. The scattering angle $\theta_\pm$ is measured with respect to the direction of the incident photon whereas ϕ is the angle between the gamma-electron-plane and the gamma-positron-plane, see Fig. 5.12.

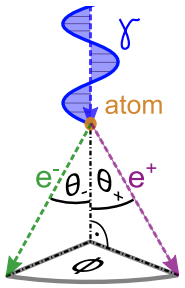

Figure 5.12. Terminology for pair production.

5.6. The sensitivity of CANDELA for Compton forward scattering

This section describes two possible applications for a stacked detector setup, a Compton camera and a Compton polarimeter. Because both applications are based on Compton scattering, the general investigation of Compton scattering of Sect. 5.5.2 is further studied for the specific case of Compton forward scattering within the CANDELA setup. This investigation can be divided into five parts:

1) Incoherent scattering in the LED

The probability P_{LED} that a photon interacts in the LED via incoherent scattering can be calculated with the incoherent scattering cross section σ_{IS} of Eq. (5.19) in combination with Beer's law (Eq. (5.1)):

$$P_{\mathrm{LED}}(k_0) = 1 - \exp(-\sigma_{\mathrm{IS}}(k_0) \cdot n_{\mathrm{Si}} \cdot d_{\mathrm{LED}}) \tag{5.21}$$

With the number density of $n_{\mathrm{Si}} = 5.0 \cdot 10^{22}$ Si-atoms/cm^3 and the detector thickness $d_{\mathrm{LED}} = 0.045\,\mathrm{cm}$, P_{LED} can be calculated as a function of the incident photon energy k_0; see Fig. 5.14 for the graph of $P_{\mathrm{LED}}(k_0)$.

2) Transportation in the LED

The incident or the scattered photon can be absorbed in the LED via the photoelectric effect. The probability P_{track} that a photon is not absorbed in the LED can be calculated with the photoelectric cross section σ_{PE} of Eq. (5.7) in combination with Beer's law (Eq. (5.1)):

$$P_{\mathrm{track}}(k_0) = \exp(-\sigma_{\mathrm{PE}}(k_0) \cdot n_{\mathrm{Si}} \cdot d_{\mathrm{LED}}) \tag{5.22}$$

This calculation neglects that the added track length of the incident photon track and of the scattered photon track are larger than the detector thickness d_{LED} if $\theta > 0°$. For large scattering angles θ, Eq. (5.22) overestimates the transparency of the LED. See Fig. 5.14 for the graph of $P_{\mathrm{track}}(k_0)$.

3) Interaction of the Compton electron in the LED

The spectral distribution of the Compton recoil electrons that are detected in the LED, can be calculated with the θ-differential cross section for incoherent scattering $\sigma_{\mathrm{IS},\,\theta}(k_0, \theta)$ according to Eq. (5.18) and the inverse function of Eq. (5.10), i.e. the scattering angle θ as function of the energy of the Compton electron:

$$\theta(E_{\mathrm{e}}) = \arccos\left(1 - \frac{E_{\mathrm{e}}\,\mathrm{m_e c^2}}{k_0^2 - k_0\,E_{\mathrm{e}}}\right) \tag{5.23}$$

Figure 5.13 (left) shows the Compton electron spectrum calculated via $\sigma_{\mathrm{IS},\,\mathrm{E_e}}(k_0, \theta(E_{\mathrm{e}}))$ for $k_0 = 200\,\mathrm{keV}$. The non-linear transformation between the electron energy E_{e} and

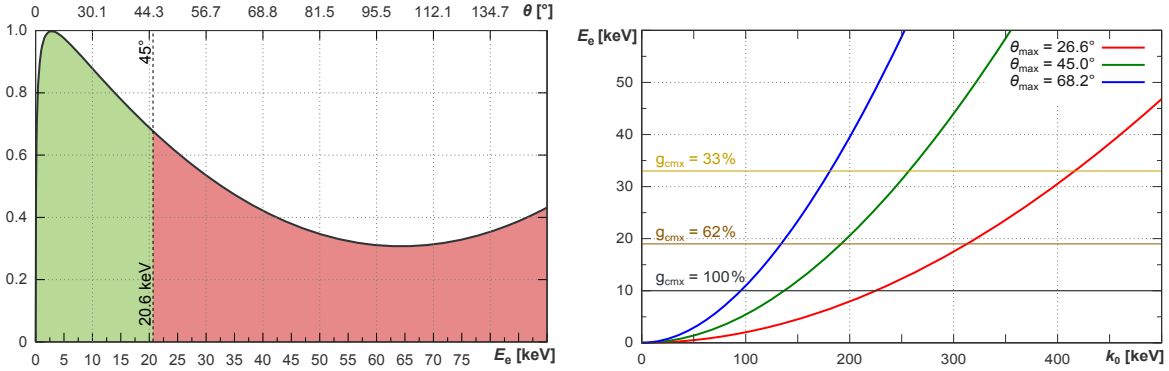

Figure 5.13. Left: the Compton electron spectrum for $k_0 = 200\,\text{keV}$. The spectrum is normalized to a maximal intensity of one. With the current configuration $\theta_{\text{max}} = 45°$, the Compton scattering in the direction of the HED results in $E_\text{e} \leq 20.6\,\text{keV}$. The ratio between the green area and the total area (green and red) is—similar to Eq. (5.26)—the probability that a photon is scattered into the HED.
Right: the maximal Compton electron energy E_e is shown as a function of the photon energy k_0 calculated for different maximal scattering angles θ_{max}. The high energy thresholds of the LED are shown for the three highest CAMEX gains. For $g_{\text{CMX}} = 21\,\%$ only an upper limit $E_{\text{max}} > 60\,\text{keV}$ is known.

the scattering angle θ results in a deformed spectrum compared to the θ-differential cross section; see the scaling of the two x-axes in the Fig. 5.13 (left).

Because of the low mean free path lengths of electrons in the LED (see Sect. 1.2.1), the detection efficiency of a Compton electron is assumed with 100 %. In order to measure the energy of the incident photon—as a summation of the LED and the HED event energies—the electron detection in the LED must be energy dispersive. The maximal observable energy of the LED (E_{max} in Tab. 2.4) limits the detectable energy range of the incident radiation. In this context *detectable* means a detection via Compton forward scattering with a LED event energy that is lower than E_{max}. The detectable energy k_0 depends on the used gain factor of the CAMEX g_{CMX} and on the maximal scattering angle θ_{max}. In the current configuration, with a distance between LED and HED of $d = 10\,\text{mm}$, the maximal scattering angle is $\theta_{\text{max}} \approx 26.6°$* but, with smaller distances d, the maximal scattering angle can be increased. To test the configurations

$$\theta_{\text{max}} = 45° \quad (d = 5\,\text{mm}) \tag{5.24}$$

and

$$\theta_{\text{max}} \approx 68.2° \quad (d = 2\,\text{mm}) \tag{5.25}$$

is scheduled for the future. The following theoretical analysis considers all three configurations. Figure 5.13 (right) shows the energy of the Compton electron E_e as a function of the photon energy k_0 for the mentioned values of θ_{max}.

* In the following, the orthogonal to the detector surface projected center of the HED onto the LED is assumed as interaction point for the Compton scattering.

4) Emission direction of the scattered photon

The probability P_θ that the scattered photon hits the HED can be calculated as the ratio

$$P_\theta(k_0, \theta_{\min}, \theta_{\max}) = \frac{\int_{\theta_{\min}}^{\theta_{\max}} \sigma_{\mathrm{IS},\,\theta}(k_0, \theta)\,\mathrm{d}\theta}{\int_{0}^{\pi} \sigma_{\mathrm{IS},\,\theta}(k_0, \theta)\,\mathrm{d}\theta} \tag{5.26}$$

which is the cross section for a scattering in the direction of the HED normalized to the total cross section; see also Fig. 5.13 (left). In the following, $\theta_{\min} = 0°$ is assumed, but see Sect. 5.8.2 for a discussion of $\theta_{\min} > 0°$. The numerically obtained result of Eq. (5.26) is shown in Fig. 5.14.

5) Interaction of the scattered photon in the HED

The probability P_{HED} that a photon interacts in the HED (with the detector thickness $d_{\mathrm{HED}} = 1\,\mathrm{mm}$) via photoelectric absorption can be calculated similar to Eq. (5.21) as

$$P_{\mathrm{HED}}(k_0) = 1 - \exp(-\sigma_{\mathrm{PE,\,r}}(k_0) \cdot n_{\mathrm{CdTe}} \cdot d_{\mathrm{HED}}). \tag{5.27}$$

The number density n_{CdTe} of cadmium or tellurium atoms is calculated with the averaged molar mass $\overline{m}_{\mathrm{CdTe}} = 120\,\mathrm{g/mol}$ and the density $\rho_{\mathrm{CdTe}} = 5.85\,\mathrm{g/cm^3}$ to

$$n_{\mathrm{CdTe}} = \rho_{\mathrm{CdTe}}/\overline{m}_{\mathrm{CdTe}} = 2.92 \cdot 10^{22}\,\mathrm{atoms/cm^3}. \tag{5.28}$$

The cross section $\sigma_{\mathrm{PE,\,r}}$ is calculated as the relativistic cross section for the photoelectric effect of a K-electron [Heitler, 1954, § 21, Eq.(17)] in combination with the correction factor introduced in Eq. (5.5) and with an additional factor of $2 \cdot 5/4$ that accounts for the residual electrons per atom.

The calculation assumes that the photon looses no energy during the Compton scattering in the LED, which is only true for $\theta = 0°$. At larger scattering angles, Eq. (5.27) underestimates the quantum efficiency of the HED because of the energy loss during the Compton scattering and because of the increased apparent crystal depth for non-orthogonal detector irradiation.

Discussion on the detector efficiency

The total probability to detect a Compton forward scattered event with the CANDELA setup is defined as the detector efficiency ϵ and can be obtained via

$$\epsilon(k_0, \theta_{\min}, \theta_{\max}) = P_{\mathrm{LED}}(k_0) \cdot P_{\mathrm{track}}(k_0) \cdot P_\theta(k_0, \theta_{\min}, \theta_{\max}) \cdot P_{\mathrm{HED}}(k_0). \tag{5.29}$$

Figure 5.14 shows the efficiency ϵ with its constituents for the configuration $\theta_{\min} = 0°$ and $\theta_{\max} = 45°$ as a function of the photon energy k_0. Graphs of the detector efficiency for the actual configuration ($\theta_{\max} = 26°$), for the intended configuration $\theta_{\max} = 68°$, and for the theoretical limit $\theta_{\max} = 90°$ (ignoring Compton back scattering) are also shown. The detector efficiency ϵ is the probability that a Compton event occurs in the LED *and* that it can be detected in the HED. The properties of ϵ are:

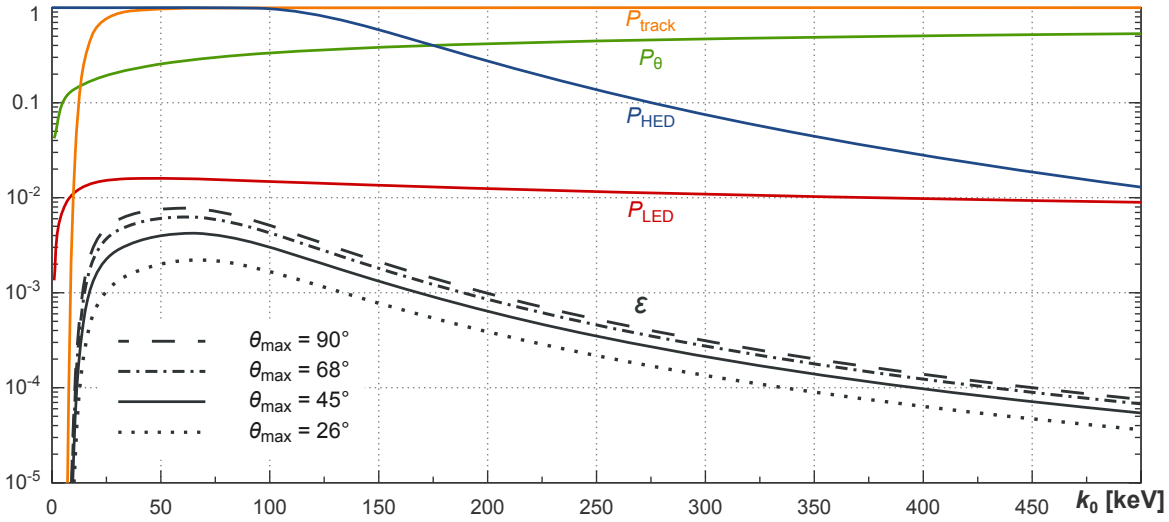

Figure 5.14. The probability to detect a Compton forward scattered event with the CANDELA setup is a function of the energy k_0 of the incident photon. P_{LED}, P_{track}, P_θ (with $\theta_{\max} = 45°$), P_{HED}, and ϵ are calculated according to the equations (5.21), (5.22), (5.26), (5.27), and (5.29). The total probability ϵ to observe a Compton forward scattered event is shown for the three configurations $\theta_{\max} = 26°$, $\theta_{\max} = 45°$, and $\theta_{\max} = 68°$ and for the theoretical limit $\theta_{\max} = 90°$. For $\theta_{\max} = 68°$, the highest efficiency $\epsilon = 6.1\,‰$ is obtained for a photon energy of $k_0 \approx 60\,\mathrm{keV}$.

- At low energies ($E < 10\,\mathrm{keV}$), the efficiency to detect Compton events is zero because the photons interact in the LED mostly by photoelectric absorption.
- At medium energies ($10\,\mathrm{keV} < E < 100\,\mathrm{keV}$), the sensitivity is mainly limited by P_{LED} which is almost independent of the photon energy k_0.
- At high energies ($E > 100\,\mathrm{keV}$), the spectral change of the detector efficiency is determined by the decreasing quantum efficiency of the HED.
- Only P_θ depends on the geometry of the setup ($\theta_{\min}$ and $\theta_{\max}$). The efficiency improves most if small maximal scattering angles are increased and saturates for $\theta_{\max} \to 90°$; compare the large increase of ϵ from $\theta_{\max} = 26°$ to $\theta_{\max} = 45°$ with the small increase obtained by the change $\theta_{\max} = 68° \to \theta_{\max} = 90°$.
- The energy of the radiation, that results in the maximal detector efficiency, decreases slightly if $\theta_{\max}$ is increased.
- For $\theta_{\max} = 68°$, the maximal efficiency $\epsilon = 6.1\,‰$ is obtained at $k_0 \approx 60\,\mathrm{keV}$.

The presented calculation does not consider the increased track lengths in the LED and the HED for scattering angles $\theta > 0°$. This effect lowers P_{track} at small energies and increases P_{HED} at large energies k_0. Furthermore, the neglected energy loss of the scattered photon increases P_{HED} additionally. As a consequence of these effects, the energy k_0 with the highest efficiency ϵ will be shifted to higher energies compared to the presented values.

5.7. CANDELA as a Compton camera

Since the first concepts of Compton imaging [Schönfelder et al., 1973] the idea of imaging hard X-rays or soft gamma-rays by analyzing Compton events, is investigated by several groups with COMPTEL aboard the Compton Gamma-Ray Observatory [Schöenfelder et al., 1993] beeing the most prominent example in astronomy. The CANDELA setup with its stacked detector configuration can be used as a Compton camera as well. This section describes the phenomenological principle of a Compton camera and refers to Maier et al. [2014,b] for a more detailed and analytical treatment.

The working principle of a Compton camera is, in the case of the CANDELA setup, Compton forward scattering as described in Sect. 5.6. Figure 5.15 illustrates the basic idea of the camera. In contrast to a Compton telescope, the Compton camera assumes a *local* source, i.e. a source that emits divergent radiation. The source photons are Compton scattered in the LED and the scattered photons are detected in the HED. Considering the photon path backwards allows to conclude on the position of the source. The energy deposition in the LED and in the HED, E_{LED} and E_{HED}, result in the energy k_0 of the incident photon via

$$k_0 = E_{\mathrm{LED}} + E_{\mathrm{HED}}. \tag{5.30}$$

The fact that the detected energy in the LED represents the energy of the Compton electron ($E_{\mathrm{LED}} = E_{\mathrm{e}}$) allows to calculate the scattering angle θ according to Eq. (5.23). The LED and HED interaction points define an interaction direction (z' in Fig. 5.15); because the azimuth angle ϕ of the Compton scattering is unknown, a single Compton scattered event allows only to conclude on a cone of possible source directions around the z'-axis. The projection of this *Compton cone* on an auxiliary plane S, which lies in a distance D parallel to the surface of the LED, results in an ellipse of possible source positions. The Compton ellipses of several Compton scattered events intersect in the source position if the distance D matches the true distance between LED and source.

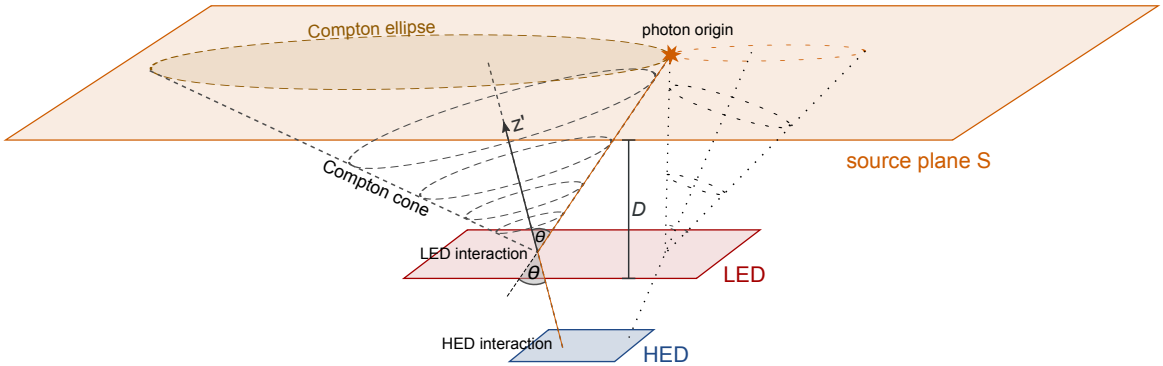

Figure 5.15. Illustration of a Compton camera. A photon, Compton scattered in the LED into the HED, can be projected back to a cone of possible origins. The cones of several photons with the same origin intersect in one point, the photon origin.

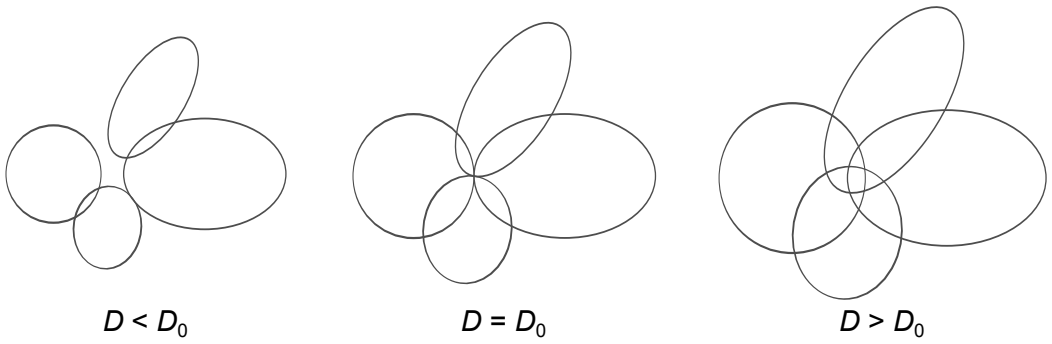

Figure 5.16. Illustration of Compton cones that are projected onto a source plane S which is positioned in a distance D to the LED. The resulting Compton ellipses cannot intersect in a common point if the true distance of the source D_0 is larger than D (left) or smaller than D (right). Only if the source plane is chosen in the correct distance to the LED all Compton ellipses can intersect in one point (center).

If D is chosen too small, the Compton ellipses do not intersect and if D is chosen too large they intersect on multiple points, see Fig. 5.16. The source distance D can be obtained by constructing the Compton ellipses for different values of D and selecting the distance D that results in an n-fold intersection point, whereby n equals the number of the observed Compton events. Inaccuracies enter into the described reconstruction process due to errors in the position measurement of the LED events and the HED events; this results in an erroneous pointing direction of the Compton cones. Additionally, errors in the scattering angle θ are caused by the limited energy resolution of the LED and the HED which causes an incorrect opening angle of the Compton cone. Nevertheless, the source distance can be estimated as the distance that results in a maximum of intersection points of Compton ellipses. In this way, the Compton camera enables a reconstruction of all three spatial dimensions which is an astonishing performance for a device without additional focusing or absorbing structures.

5.8. CANDELA as a polarimeter

Beside the use as a Compton camera, the stacked detector setup can also be operated as an X-ray Compton polarimeter. The expected performance of CANDELA to work as a Compton polarimeter is investigated in this section. See Chapter 6 for a detailed introduction into the statistics of such a polarimetric measurement.

The detection principle of a Compton polarimeter is based on the azimuthal asymmetry of the Compton scattering process*. The azimuthal distribution of the differential cross section for incoherent scattering is illustrated in a polar plot in Fig. 5.17 (left). Therein, the azimuth angle ϕ is measured between the plane containing the

* This asymmetry is equal for Compton scattering and for incoherent scattering. Therefore, the term *Compton* scattering is often used, even if the physical process is incoherent scattering.

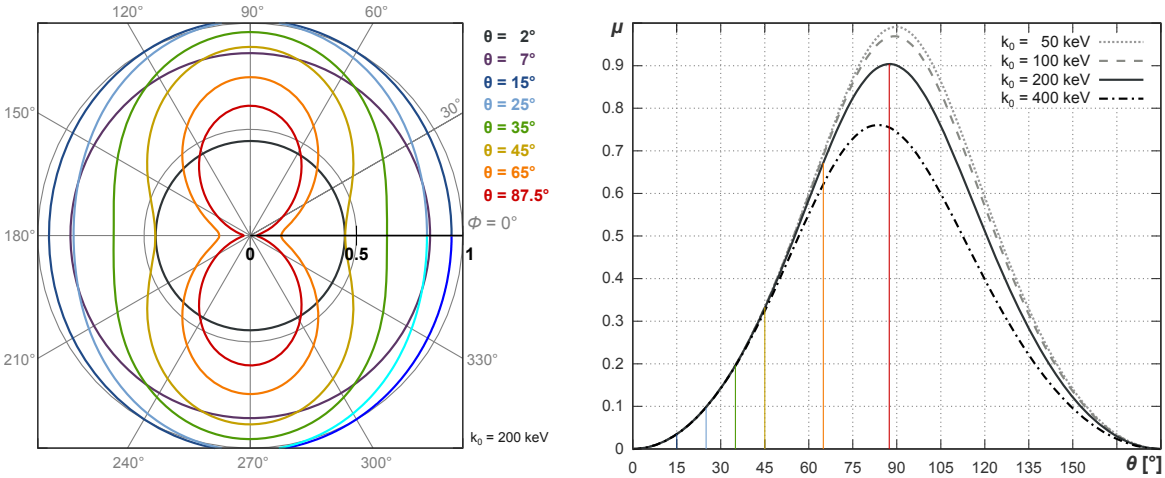

Figure 5.17. Left: Polar plot of the differential cross section for incoherent scattering in silicon for $k_0 = 200\,\mathrm{keV}$ according to Eq. (5.11). The scattering angle θ is color coded and ranges from nearly forward scattering ($\theta = 2°$) to an almost orthogonal scattering ($\theta = 87.5°$). The azimuthal angle ϕ is the variable of this plot and ranges from 0° to 360° (printed in gray). The radial distance between the function lines and the center of the image represents the magnitude of the differential cross section which ranges from 0 to ∼1 b/atom.
Right: the modulation factor μ as a function of the scattering angle θ according to Eq. (5.31). For high photon energies k_0, the maximum of the modulation function is slightly shifted to smaller values than 90°. For $k_0 = 200\,\mathrm{keV}$, the maximal modulation $\mu_{\max} \approx 90.4\,\%$ is obtained at $\theta \approx 87.5°$.

electric field of the incident photon and the plane containing the incident photon trajectory and the scattered photon trajectory. The plot shows that for small scattering angles θ the differential cross section is low (because of the incoherent scattering factor S) and almost symmetric in ϕ; each azimuthal angle is (almost) equally probable. For large scattering angles, the scattered photon is predominantly emitted in the direction perpendicular to the electric field of the incident photon ($\phi = 90°$) and reduced in the direction of the electric field ($\phi = 0°$). This dependency of the azimuthal scattering angle ϕ on the direction of the electric field of the incident photons enables to conclude on the orientation of the electric field of the incident photons, i.e. to measure their polarization.

5.8.1. The modulation factor

The modulation factor μ is defined as the ratio

$$\mu(k_0,\theta) = \frac{\frac{\mathrm{d}\sigma_{\mathrm{IS}}}{\mathrm{d}\Omega}(k_0,\theta,\phi=90°) - \frac{\mathrm{d}\sigma_{\mathrm{IS}}}{\mathrm{d}\Omega}(k_0,\theta,\phi=0°)}{\frac{\mathrm{d}\sigma_{\mathrm{IS}}}{\mathrm{d}\Omega}(k_0,\theta,\phi=90°) + \frac{\mathrm{d}\sigma_{\mathrm{IS}}}{\mathrm{d}\Omega}(k_0,\theta,\phi=0°)} = \frac{\sin^2(\theta)}{\frac{k}{k_0} + \frac{k_0}{k} - \sin^2(\theta)}. \qquad (5.31)$$

The incoherent scattering factors S in Eq. (5.31) cancel, i.e. the modulation factors for Compton scattering and for incoherent scattering are identical. The modulation

factor describes the maximal extent of the azimuthal asymmetry. Therefore, the most probable scattering direction ($\phi = 90°$) and the most unlikely direction ($\phi = 0°$) for Compton scattering are used for Eq. (5.31). The graphs of Eq. (5.31) show that the modulation factor has a maximum close to $\theta = 90°$ and that the modulation factor is decreasing for increasing photon energies k_0, see Figure 5.17 (right).

5.8.2. Optimizing the sensitivity of the polarimeter

Besides the detection efficiency (Sect. 5.6, Fig. 5.14), the modulation factor is another important quantity that describes the performance of a polarimeter. In the case of Compton forward scattering, the modulation factor increases with the scattering angle θ. An ideal Compton polarimeter uses therefore a maximal scattering angle of $\theta_{\text{max}} \approx 90°$. It is important to note that the scattering angles of polarimeters are not fixed to a single value but consist of a range of scattering angles $\theta_{\text{min}} \leq \theta \leq \theta_{\text{max}}$, see Fig. 5.18 (left). This averages the modulation and the effective modulation factor $\overline{\mu}$ can be calculated as

$$\overline{\mu}(k_0) = \frac{1}{\theta_{\text{max}} - \theta_{\text{min}}} \cdot \int_{\theta_{\text{min}}}^{\theta_{\text{max}}} \mu(k_0, \theta)\, \mathrm{d}\theta. \tag{5.32}$$

The choice of θ_{min} is not trivial, because an increase of θ_{min} increases the effective modulation factor but decreases the efficiency to detect Compton scattered events.

The detector efficiency is calculated in Eq. (5.29) as a product of several terms. Using the approximations discussed in Sect. 5.6 (neglecting the increased path lengths in the detectors and the energy loss during the scattering) only P_θ—the probability

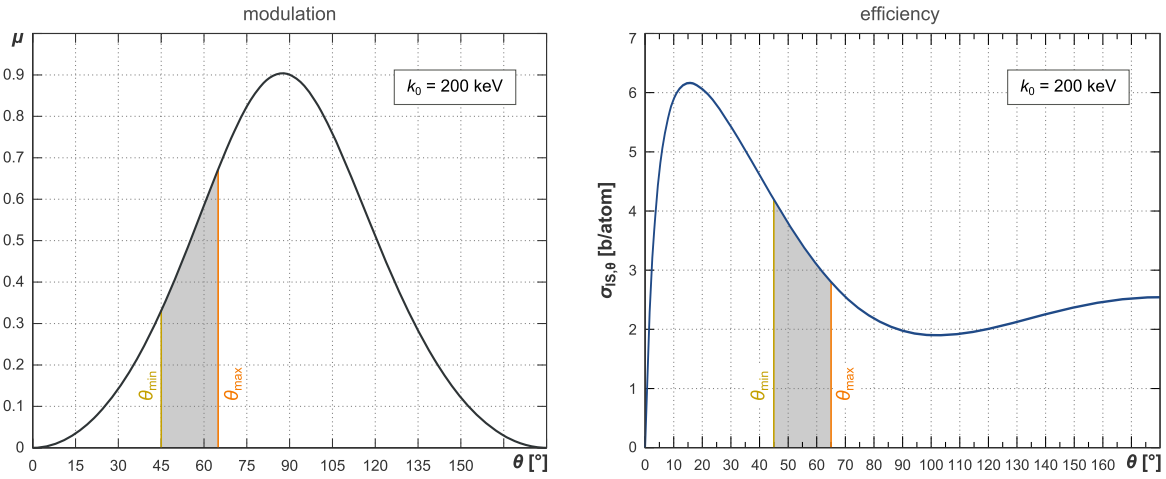

Figure 5.18. Left: the effective modulation factor $\overline{\mu}$ is averaged for the possible scattering angles $\theta_{\text{min}} \leq \theta \leq \theta_{\text{max}}$ according to Eq. (5.32).
Right: the detector efficiency ϵ (Eq. (5.29)) is proportional to P_θ which can be calculated according to Eq. (5.26) as the ratio of the gray indicated area to the total area of the θ-differential cross section $\sigma_{\text{IS},\theta}$.

that a scattered photon hits the HED—is a function of the scattering angle θ. This means that the θ-dependency of the detector efficiency ϵ is solely determined by P_θ. Figure 5.18 (right) shows the θ-differential cross section for incoherent scattering for $k_0 = 200\,\mathrm{keV}$. In order to achieve a maximal efficiency, the gray indicated area must be as large as possible. Scattering angles near $\theta = 90°$ result in a minimal efficiency, but in a maximal modulation factor and a maximal efficiency ($\theta \approx 15°$) results in low modulation factors.

The best compromise between a high effective modulation factor $\overline{\mu}$ and a large detector efficiency ϵ can be obtained by minimizing the minimum detectable polarization (MDP)*. Muleri and Campana [2012] showed that the MDP is minimized if the *quality factor*

$$q = \overline{\mu} \cdot \sqrt{\epsilon} \tag{5.33}$$

is maximized which is achieved with a minimal scattering angle

$$\theta_{\mathrm{min}}^{\mathrm{opt}}(\mathrm{deg}) \approx 0.57 \cdot \theta_{\mathrm{max}}(\mathrm{deg}). \tag{5.34}$$

θ_{min} and θ_{max} can be defined by the geometry of the setup or due to optimizations like Eq. (5.34). For the case of the CANDELA setup, θ_{max} is defined by the geometry of the stacked detector setup and can be increased with a reduced distance between the LED and the HED. $\theta_{\mathrm{min}} = 0°$, but in order to optimize the detector sensitivity, only those events with a scattering angle

$$\theta > \theta_{\mathrm{min}}^{\mathrm{opt}} \tag{5.35}$$

should be considered for the data analysis.

Table 5.1 shows the expected performance of the CANDELA setup for polarimetric measurements with a photon energy of $k_0 = 200\,\mathrm{keV}$. The geometrical configuration of the setup has a large impact on its polarimetric performance. In the current configuration the maximal modulation factor, obtained at $\theta = \theta_{\mathrm{max}}$, is less than 11.13 % and the effective modulation, obtained for $\theta_{\mathrm{min}}^{\mathrm{opt}} \leq \theta \leq \theta_{\mathrm{max}}$, is less than 7 %. With

Table 5.1. Expected performance of CANDELA as a Compton polarimeter: the maximal modulation factor μ_{max}, the effective modulation factor $\overline{\mu}$, the probability P_θ, the impact of the configuration to the sensitivity $\overline{\mu}\sqrt{P_\theta}$, and the sensitivity gain compared to the current configuration are shown. All values are calculated for $k_0 = 200\,\mathrm{keV}$.

configuration	θ_{max}	$\theta_{\mathrm{min}}^{\mathrm{opt}}$	μ_{max} [%]	$\overline{\mu}$ [%]	P_θ [%]	$\overline{\mu}\sqrt{P_\theta}$ [%]	sensitivity gain
current	26.6°	15.2°	11.13	6.98	14.11	2.62	1.0
A	45.0°	25.7°	33.07	20.61	22.88	9.86	3.8
B	68.2°	38.9°	72.66	47.61	29.79	25.99	9.9
optimum	90.0°	51.3°	90.08	73.16	33.92	42.61	16.3

* The minimum detectable polarization is a quantity that defines the sensitivity of a polarimeter; the lower the MDP the better the sensitivity, see Sect. 6.2 for the exact definition of the MDP.

the intended configuration "B", the setup achieves a maximal modulation of 72.66 % and an effective modulation of 47.61 %. Compared to the current configuration, this represents a sensitivity gain of almost a factor 10.

5.9. Summary

X-ray polarimetry is based on the fundamental interactions of light with matter and uses the photoelectric effect or Compton scattering. To perform a polarimetric measurement with a stacked detector system is a difficult but promising task; it is difficult because the detector setup is not intended to work as a polarimeter and the configuration of the setup is not designed for that application. But, because of the same reason it is also promising because an already existing detector system can be operated as a polarimeter.

The analysis of the detection efficiency for Compton scattered events shows that a Compton camera or a Compton polarimeter is usable in a wide energy range from several 10 keV up to a few 100 keV. The efficiency is mainly limited by the cross section for incoherent (Compton) scattering which is nearly independent of the energy k_0 and the atomic number Z. In the CANDELA setup the maximal detection efficiency for Compton scattered events is 6.1 ‰, obtained at a photon energy of $k_0 \approx 60\,\mathrm{keV}$.

Besides the efficiency for Compton scattering, the ratio between Compton scattering and photoelectric absorption should be as high as possible for the scattering material. The probability for Compton scattering in silicon at 200 keV is 36-times higher compared to the probability for the photoelectric effect. This reduces the absorption of the incident or the scattered photon in the silicon crystal and minimizes photoelectric induced background in the LED. The reduced background helps to identify time coincident events between the LED and the HED. The combination of two different detector materials allows to use the low-Z silicon crystal as a target for Compton scattering and the high-Z cadmium telluride crystal as an effective absorber for the high energetic scattered radiation via photoelectric absorption.

The operation of CANDELA as a Compton camera may serve as a first application of the stacked setup in the current configuration. For the polarimetric analysis, the calculations show that the sensitivity to polarimetric measurements can be increased by a factor of 10 if the distance between the LED and the HED is reduced from 10 mm to 2 mm. The design of the CANDELA setup allows to change this distance with a small effort.

6. Statistics in polarimetric measurements

The working principle of all X-ray polarimeters is the angular (in azimuthal angle ϕ) dependence of the basic interactions between radiation and matter, introduced in Sect. 5.5. The emission direction of the secondary particles—the electrons for photoelectric absorption, the scattered photons for Compton scattering or the electron-positron emissions for pair creation—allows to reconstruct the degree and the angle of polarization of the primary photons.

In the following chapter, analysis methods for linearly polarized radiation are performed with a frequentist and with a Bayesian approach. Additional Monte Carlo simulations serve as validation of the theories and as an intuitive way of understanding the applied statistics. A synopsis of Sect. 6.2 and 6.3 can be found in Maier et al. [2014,a].

6.1. Basic parameters and terminology

Numerous variables and parameters will be introduced in the following sections. Table 6.1 serves as an overview of the used terminology.

Table 6.1. The applied terminology for a variable X is the following: x_0 labels the true value of X, $\hat{x}$ is the estimated value, and x is the observed value.

Name	symbol	range	explanation	definition
degree of polarization	P	$[0, 1]$	fraction of photons with equal angle of polarization	Eq. (6.3)
modulation amplitude	a	$[0, 1]$	observed signal asymmetry	Eq. (6.2)
signal-to-noise ratio	p	$\mathbb{R}_0^+$	measurement statistics	Eq. (6.10)
min. detectable pol.	P_{md}	$\mathbb{R}^+$	detection sensitivity	Eq. (6.19)
angle of polarization	Ψ	$(-\pi/2, \pi/2]$	direction of the pol. vector	
scattering angle	ϕ	$[0, 2\pi)$	azimuthal scattering angle	
probability density	$\rho_{\mathrm{p},\Psi}$	$\mathbb{R}_0^+$	bivariate density in p & Ψ	Eq. (6.12)
rice distribution	ρ_{p}	$\mathbb{R}_0^+$	univariate density in p	Eq. (6.14)
probability density	ρ_{Ψ}	$\mathbb{R}_0^+$	univariate density in Ψ	Eq. (6.34)
distribution width	σ_{c}	$\mathbb{R}^+$	statistical fluctuation	Eq. (6.9)
distribution width	σ_n	$\mathbb{R}^+$	confidence intervals	Sect. 6.2.3

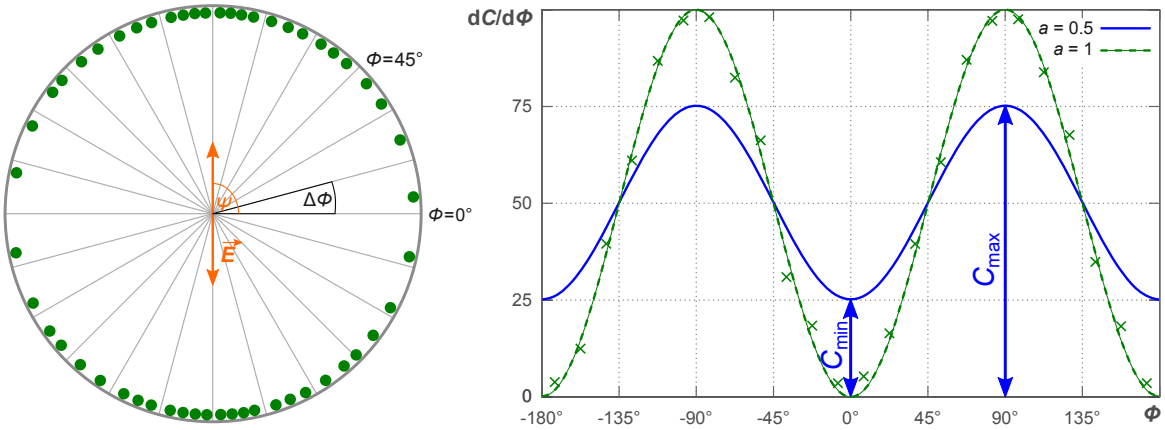

Figure 6.1. Schematic count distribution in a polarimeter based on the photoelectric effect. The horizontal direction is chosen as direction of reference with $\phi = 0°$. The angle of polarization is $\Psi = 90°$ as indicated with the orange arrow.
Left: each point represents an event. The distribution is binned with $\Delta\phi = 15°$.
Right: the summed events per bin $\Delta C/\Delta\phi$ can be fitted with the azimuthal density function of Eq. (6.1). The modulation amplitude a is obtained as best fit parameter and shown for $a = 100\,\%$ (green) and $a = 50\,\%$ (blue). The definition of the modulation amplitude (Eq. (6.2)) is illustrated for $a = 50\,\%$.

6.1.1. The $\frac{\Delta C(\phi)}{\Delta\phi}$-distribution

In the case of photoelectric or Compton interaction the $\cos^2(\phi)$-dependency of the differential cross section—see Eq. (5.2) and Eq. (5.11)—results* in a positive π-periodic signal† of counts ΔC per $\Delta\phi$-interval. In the case of photoelectric interaction, the maximal count rate is in the direction of the electric field of the primary photons, while it is orthogonal to this direction for Compton scattering, see Fig. 5.5. An infinitesimally small ϕ-binning leads to the continuous azimuthal density function $\frac{\mathrm{d}C(\phi)}{\mathrm{d}\phi}$. In the case of photoelectric interaction, $\frac{\mathrm{d}C(\phi)}{\mathrm{d}\phi}$ can be parametrized [Elsner et al., 2012] as

$$\frac{\mathrm{d}C(\phi)}{\mathrm{d}\phi} = \frac{C}{2\pi}\left(1 + a\cos\left(2\left(\phi - \Psi\right)\right)\right) \tag{6.1}$$

with the total number of counts C, the **modulation amplitude** $\boldsymbol{a}$ and the polarization angle Ψ. All angles are related to an arbitrary but fixed reference direction ($\phi = 0°$) of the instrument. Knowing the orientation of the polarimeter allows to transform the polarization angle to any reference frame. A corresponding $\frac{\mathrm{d}C(\phi)}{\mathrm{d}\phi}$-distribution for Compton scattering can be modeled with a sine instead of a cosine function or by adding additional $\pi/2$ to Ψ. To achieve a joint theoretical description for photoelectric and Compton polarimeters Eq. (6.1) is taken as common basis and Ψ is shifted by $+\pi/2$ in the case of Compton scattering. The modulation amplitude is defined as

* As a result of the trigonometric identity: $\cos^2(x) = \frac{1+\cos(2x)}{2}$.
† In literature, this is often called 'a 2ϕ signature'.

$$a := \frac{C_{\max} - C_{\min}}{C_{\max} + C_{\min}} \qquad 0 < a \leq 1 \tag{6.2}$$

with the maximal number of counts $C_{\max}$ and the minimal number of counts $C_{\min}$ per ϕ-interval. Instead of calculating the modulation amplitude with Eq. (6.2) it can also be obtained as best fit parameter of the measured ϕ-dependent counts with Eq. (6.1), see Fig. 6.1.

The modulation amplitude for 100 % linearly polarized light is called **modulation factor μ**. It represents the maximal ϕ-modulation that can be produced by a polarimeter and is therefore a key parameter to describe the performance of the instrument. Besides the possibility of measuring the modulation factor μ, it can also be calculated, see Sect. 5.8. The **degree of the observed polarization P** can now be obtained as

$$P = \frac{a}{\mu}. \tag{6.3}$$

Polarimetric analysis for X-ray radiation is done by fitting the azimuthal density function of Eq. (6.1) to experimental data points in the $\frac{\Delta C(\phi)}{\Delta \phi}$-plot. The fitting-parameters are the modulation amplitude a and the polarization angle Ψ. Knowing the modulation factor μ and the orientation of the polarimeter allows to determine the degree of polarization P and the angle of polarization Ψ. Polarization measurements require a sufficiently large set of detected events. It is impossible to detect the polarization of a single photon with the techniques presented in this thesis.*

6.1.2. The Stokes parameters

The Stokes parameters I, Q, U, and V were originally defined by George G. Stokes in 1852 and rediscovered by Chandrasekhar [1950]. Besides the degree of polarization P and the angle of polarization Ψ, the normalized Stokes parameters $q = Q/I$ and $u = U/I$ are an alternative way to describe linearly polarized radiation. They are defined as normalized intensity differences in four specific directions, which are labeled as $0°, 45°, 90°$, and $135°$:

$$q = \frac{I_{0°} - I_{90°}}{I_{0°} + I_{90°}} \tag{6.4}$$

$$u = \frac{I_{45°} - I_{135°}}{I_{0°} + I_{90°}}. \tag{6.5}$$

The intensities I_x are directly measurable as the radiation power behind an x-oriented ideal polarizer. The degree of polarization P and the angle of polarization Ψ can be calculated on the basis of the normalized Stokes parameters q and u as

$$P = \sqrt{(q^2 + u^2)} \tag{6.6}$$

$$\Psi = {}^1\!/_2 \cdot \arctan\left({}^u\!/_q\right). \tag{6.7}$$

For a detailed study of repeated measurements of normalized Stokes parameters and the manifold ways how to combine these measurements, see Clarke et al. [1983].

*For all I know, it is impossible to detect the polarization of a single photon at all.

6.1.3. The bivariate probability density function $\rho_{\mathrm{p},\,\Psi}$

The degree and the angle of polarization are both affected by statistical fluctuations. Statistical considerations on linearly polarized radiation can be performed on the basis of Gaussian distributed Stokes parameters, see Quinn [2012] and on the basis of a noise affected modulation signal (Eq. (6.1)).

For the latter case, the work by Elsner et al. [2012] is especially interesting because it shows not only that the resulting* probability density function†

$$\rho_{\mathrm{a},\Psi}(a,\Psi \mid a_0,\Psi_0)\,\mathrm{d}a\,\mathrm{d}\Psi \overset{a_0\ll 1}{\approx} \frac{a}{\pi\sigma_\mathrm{c}^2}\exp\left(-\frac{(a-a_0)^2+aa_0(2\sin(\Psi-\Psi_0))^2}{2\sigma_\mathrm{c}^2}\right)\mathrm{d}a\,\mathrm{d}\Psi \tag{6.8}$$

is consistent with the well-accepted standard expression—see Quinn [2012]—but it also gives an expression for the count-related distribution width σ_c which is defined by the number of source and background counts C_S and C_B as

$$\sigma_\mathrm{c} = \sqrt{2(C_\mathrm{S}+C_\mathrm{B})}/C_\mathrm{S}. \tag{6.9}$$

The bivariate probability density (Eq. (6.8)) represents the probability of measuring a modulation amplitude within $[a, a+\mathrm{d}a]$ and an angle of polarization within $[\Psi, \Psi+\mathrm{d}\Psi]$, while the true values are a_0 and Ψ_0. See Fig. 6.2 for a graphical representation of Eq. (6.8). The figure clearly shows that the modulation amplitude is positive definite. Unpolarized light will always result in a positive modulation amplitude. With an increasing degree of polarization, the probability density function transforms into a double Gaussian distribution, centered around the true values a_0 and Ψ_0. In the limit $a_0 \ll 1$, the uncertainties in determining the modulation amplitude a are almost independent of the modulation amplitude itself. By contrast, the orientation of the polarization becomes sharper with increasing a_0. For very high degrees of polarization, two aspects must be additionally considered:

- the approximation $a_0 \ll 1$ does not hold and Eq. (22) in Elsner et al. [2012] must be integrated numerically‡ over ϕ and then be normalized by a two-dimensional numerical integration over a and Ψ. Figure 6.2 (E+F) shows that for moderate polarizations this results only in a small change of the probability density function. For very high degrees of polarization, the corrected distribution becomes sharper in the modulation amplitude a and is unaltered in the Ψ-distribution.

- The symmetric shape in a still results in the unphysical chance to measure a modulation amplitude $a > 1$. The reason for this behavior is the assumption

* The work by Elsner et al. [2012] is based on a combination of Eq. (6.1) with a known background signal which can be polarized or not. It uses the assumption of not too large modulation amplitudes ($a_0^2 \ll 1$) which is no big limitation because the measured degree of polarization is usually low.

† $f(X \mid A)$ describes f as a function of the variable set X given the parameter set A.

‡ The smooth functions allow to use a fast numerical algorithm based on the double exponential transformation by Mori and Sugihara [2001].

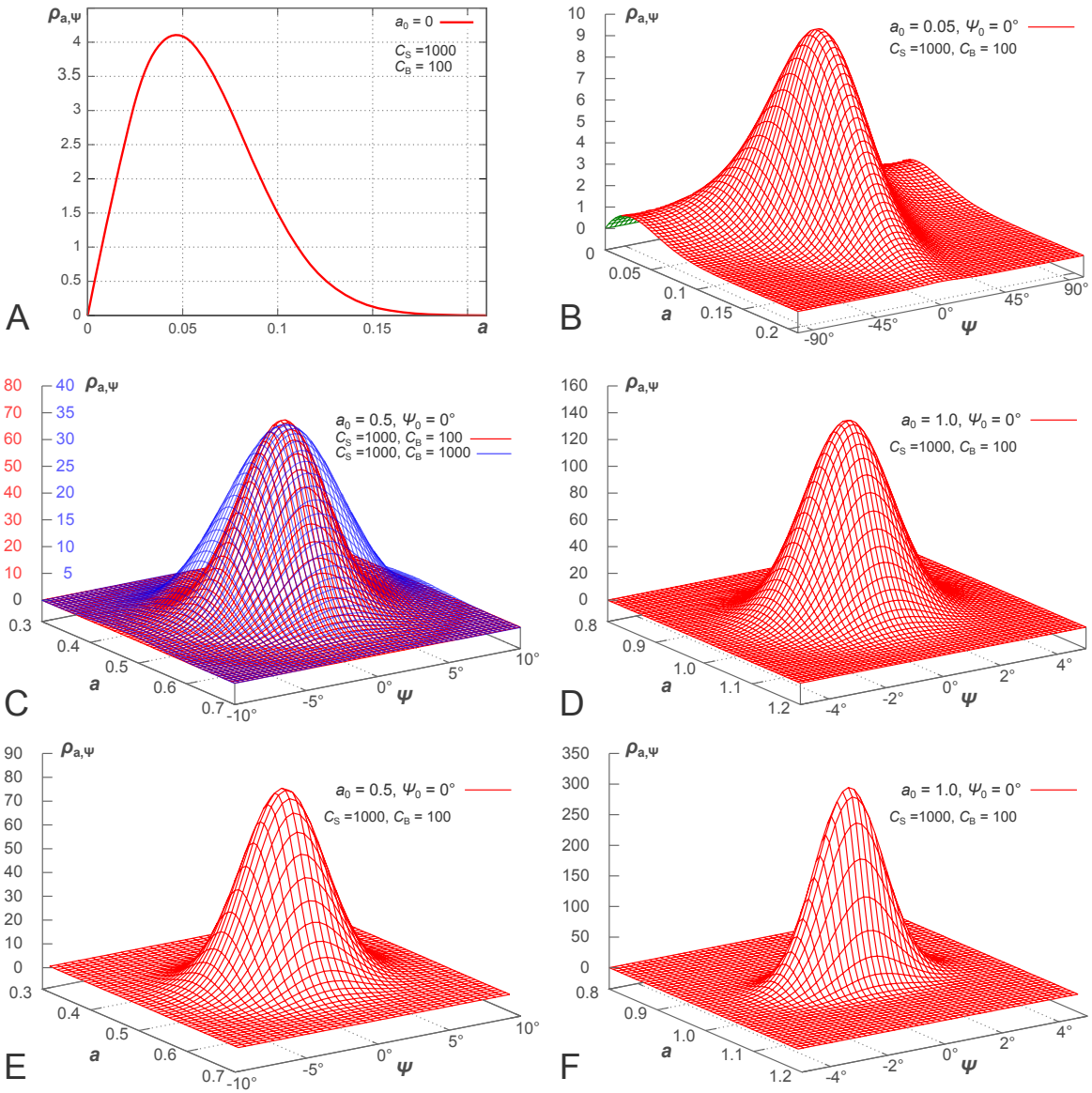

Figure 6.2. The probability density function $\rho_{a,\Psi}(a, \Psi \,|\, a_0, \Psi_0)$ of Eq. (6.8).
A: for unpolarized light $a_0 = 0$, $\rho_{a,\Psi}$ equals the Rayleigh distribution which is a function of the modulation amplitude a but not of Ψ. The expectation value $\langle a \rangle$ is greater than zero ($\langle a \rangle \approx 6\,\%$), so that unpolarized light always appears as partially polarized light.
B: 5 % partially polarized light shows an expected modulation amplitude of $\langle a \rangle \approx 10\,\%$. The distribution of the observed angle of polarization Ψ is centered around Ψ_0.
C: highly polarized light ($a_0 = 50\,\%$) can be approximated with a double Gaussian shape around the center of the true values: $\langle a \rangle \approx a_0$ and $\langle \Psi \rangle = \Psi_0$. The counts C_S and C_B affect a and Ψ in the same way and widen the distribution according to Eq. (6.9). **D:** the approximation $a \ll 1$ does not hold for fully polarized light ($a_0 = 1$). The distribution shows an unphysical chance to to measure a modulation amplitude $a > 1$. **E & F:** the same plots as in C and D but without the approximation $a \ll 1$. For $a_0 = 0.5$, the peak height is increased by only 12 % and the distribution is nearly unaltered in shape. For $a_0 = 1$, the peak height changes by a factor of 2.19 and the distribution becomes much sharper in a and remains nearly unaltered in Ψ.

that the noise can be described with a Gaussian distribution. Figure 6.3 shows that the symmetric shape of a Gaussian distribution results in negative $\mathrm{d}C/\mathrm{d}\phi$-values for low counts per ϕ-interval. This only occurs in the case $\mu \to 1$ and $a_0 \to 1$, which is a very unlikely combination in X-ray polarimetry.

Despite this, Eq. (6.8) with the approximation $a_0 \ll 1$ and a Gaussian noise distribution is the basis for the next sections. This is reasonable, because the limits $\mu \to 1$ and $a_0 \to 1$ do not correspond to the most common polarimeters and sources. In this case the statistics in Sect. 6.2.1 and 6.2.4 should be recalculated numerically.

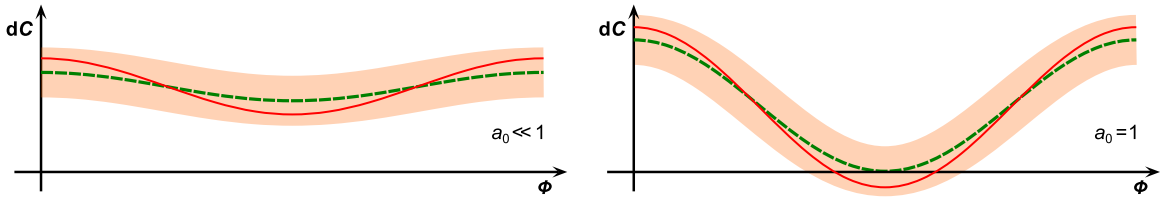

Figure 6.3. A true modulation a_0 (green dashed line) in combination with Gaussian noise (reddish area around a_0) results in a measured modulation a (red solid line)
Left: a true modulation $a_0 \ll 1$ results in lower or higher (shown) measured values of a.
Right: $a_0 \approx 1$ can result in a negative count increment $\mathrm{d}C$ and therefore $a > 1$.

The signal-to-noise ratio p

Equation (6.8) depends on the observed modulation a and the variance σ_c in a way that each* $\frac{a}{\sigma_\mathrm{c}}$ can be substituted with the **signal-to-noise ratio p**†. With Eq. (6.3) follows:

$$p_0 = \frac{a_0}{\sigma_\mathrm{c}} = P_0 \cdot \mu \cdot \frac{1}{\sigma_\mathrm{c}} \tag{6.10}$$

$$p = \frac{a}{\sigma_\mathrm{c}} = P \cdot \mu \cdot \frac{1}{\sigma_\mathrm{c}}. \tag{6.11}$$

Here and in the following the correct term 'signal-to-noise ratio of the modulation amplitude' will be simply called the 'polarization p'. This abbreviation is widely used in literature. The polarization p combines all important variables that are relevant for the following analysis: the source polarization P, the modulation factor of the polarimeter μ and the statistics of the measurement σ_c. The expression $1/\sigma_\mathrm{c}$ is plotted in Fig. 6.4. Substituting Eq. (6.8) by p results in

$$\rho_{\mathrm{p},\Psi}(p, \Psi \,|\, p_0, \Psi_0)\,\mathrm{d}p\,\mathrm{d}\Psi = \frac{p}{\pi} \exp\left(-\frac{1}{2}\left((p-p_0)^2 + pp_0(2\sin(\Psi-\Psi_0))^2\right)\right)\,\mathrm{d}p\,\mathrm{d}\Psi. \tag{6.12}$$

* Note that $\mathrm{d}a$ also has to be substituted.
† In this context, the signal-to-noise ratio is not defined as ratio of signal power to noise power, but as ratio of mean value to standard deviation.

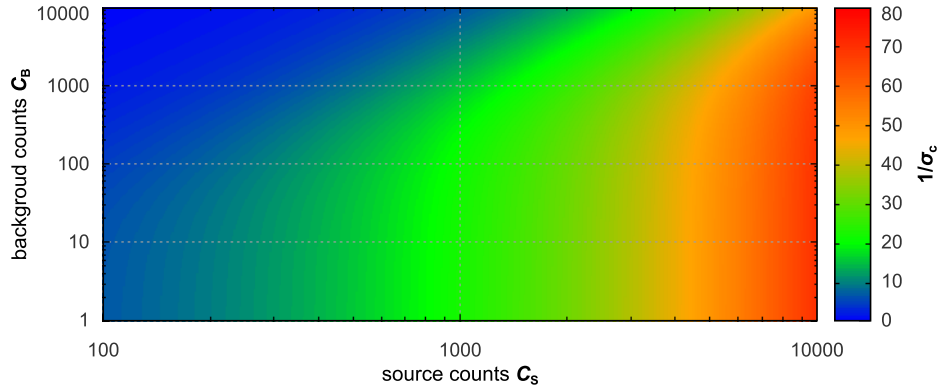

Figure 6.4. Color map of the $1/\sigma$ distribution according to Eq. (6.9). Example: a degree of polarization $P = 20\,\%$ observed with a polarimeter with a modulation factor of $\mu = 50\,\%$ results in $p = 0.1 \cdot 1/\sigma_c$, so that—in this case—the color bar ranges from $p = 0$ (blue) to $p = 8$ (red).

6.2. Frequentist analysis

The basis of frequentist statistics are probabilities of random events. Deductive reasoning leads to systems where unknown consequences can be studied for a known cause. In the example of polarimetric measurements, this means that the true degree and angle of polarization of radiation that enters a polarimeter are known and the different possible manifestations within the observed data are investigated.

6.2.1. The univariate probability distribution ρ_p

Integrating Eq. (6.12) over Ψ results in the well known Rice distribution, [Rice, 1945, (3.10-11)], see Fig. 6.5:

$$\rho_\mathrm{p}(p\,|\,p_0) = \int_{-\pi/2}^{\pi/2} \rho_{\mathrm{p},\Psi}(p,\Psi\,|\,p_0,\Psi_0)\,\mathrm{d}\Psi \tag{6.13}$$

$$\rho_\mathrm{p}(p\,|\,p_0) = p \cdot \exp\left(-\frac{p^2+p_0^2}{2}\right) \cdot I_{1,0}(pp_0) \tag{6.14}$$

with the modified Bessel function of first kind and order zero $I_{1,0}$*. For unpolarized light, the Rice distribution transforms into the Rayleigh distribution, see also Fig. 6.5:

$$\rho_p(p\,|\,0) = p \cdot \exp\left(-\frac{p^2}{2}\right) \tag{6.15}$$

* The modified Bessel function $I_{1,0}$ is the solution of the differential equation $x^2y'' + xy' + x^2y = 0$ for purely imaginary arguments $x = \mathrm{i} \cdot arg$. Note that $arg = (pp_0)$ is the argument of the modified Bessel function $I_{1,0}$.

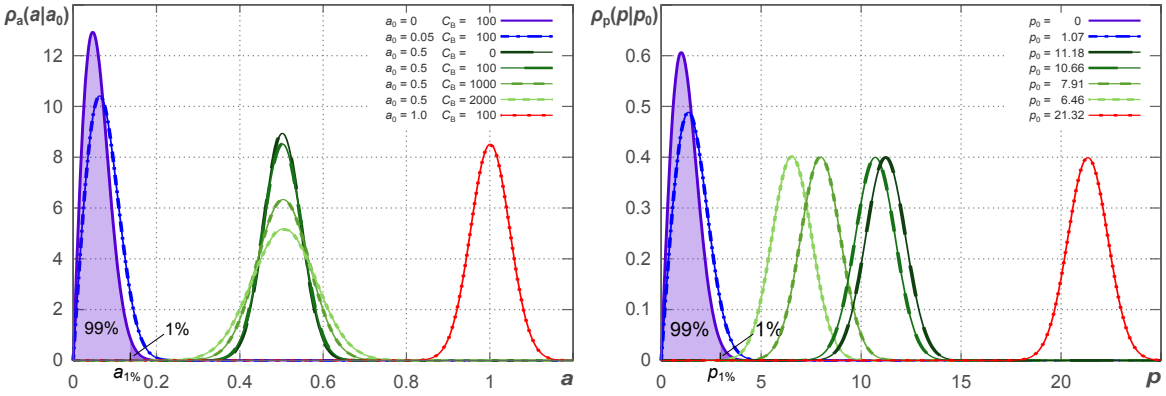

Figure 6.5. Left: The Rice distribution Eq. (6.14) for different modulation amplitudes a_0 and background counts C_B. The source counts are set to $C_\mathrm{S} = 1000$ in all cases. **Right:** The same plots as on the left, but now as a function of p. For $a_0 = 0$ or $p_0 = 0$ respectively, the distribution equals the Rayleigh distribution. For large polarizations, the Rice distribution is not a good approximation for ρ_a or ρ_p. This is directly obvious for ρ_a because the modulation amplitude must always be less than one.

Again, the Rayleigh distribution shows that unpolarized light has an expectation value $\langle p \rangle > 0$:

$$\langle p \rangle = \int_0^\infty p \cdot \rho_\mathrm{p}(p \,|\, 0)\, \mathrm{d}p \approx 1.25 \tag{6.16}$$

Weisskopf et al. [2010] defined a parameter to determine the sensitivity of a polarimetric measurement, the **minimum detectable polarization P_md**. In a measurement with unpolarized light $p_{1\,\%}$ defines a polarization limit so that the chance to measure any polarization $p \geq p_{1\,\%}$ is 1 %, see Fig. 6.5. This signal-to-noise ratio converted to a degree of polarization by Eq. (6.3) equals P_md:

$$\int_0^{p_{1\%}} \rho_\mathrm{p}(p \,|\, 0)\, \mathrm{d}p \stackrel{!}{=} 0.99 \tag{6.17}$$

$$p_{1\,\%} = \sqrt{2 \ln (100)} \approx 3.03 \tag{6.18}$$

$$P_\mathrm{md} := \frac{p_{1\,\%}\, \sigma_\mathrm{c}}{\mu} \approx \frac{4.29 \sqrt{(C_\mathrm{S} + C_\mathrm{B})}}{\mu C_\mathrm{S}} \tag{6.19}$$

Even if P_md is a degree of polarization, it can reach values greater than 100 % according to Eq. (6.19). For example, $\mu = 0.1$, $C_\mathrm{B} = 0$, and $C_\mathrm{S} = 100$ gives $P_\mathrm{md} \approx 4.29$. In such a case the meaning of P_md is the following: an impossible polarization of 429 % would be needed to fulfill the requirements defined by Eq. (6.17). In other words, independent of the degree of polarization, a 3-sigma measurement is impossible under such conditions.

6.2.2. Point estimations of the degree of polarization p

The easiest way to estimate the degree of polarization is to take the observed value as estimation for the true polarization:

$$\hat{p}_{0,\,\mathrm{triv}} = p \tag{6.20}$$

The last section already showed that the Rice distribution is asymmetric, especially for low polarizations. This asymmetry makes it more probable to measure a polarization that exceeds the true polarization. This effect of biasing was first presented by Serkowski [1958]. So, in analyzing a polarimetric measurement, a correction of the polarization bias must be performed. Simmons and Stewart [1985] presented four different methods to estimate the degree of polarization $\hat{p}$ for a given observed polarization p. In Maier et al. [2014,a], we suggested additionally $\hat{p}_{0,\,\mathrm{ebal}}$:

- **Maximum estimator $\hat{p}_{0,\,\mathrm{max}}$:** the estimated polarization equals that true polarization p_0 whose distribution has a maximum at the observed polarization p, see also Wardle and Kronberg [1974]:

$$\hat{p}_{0,\,\mathrm{max}}(p) = p_0 \;\Bigg|\; \frac{\mathrm{d}\rho_\mathrm{p}(p\,|\,p_0)}{\mathrm{d}p} \stackrel{!}{=} 0 \tag{6.21}$$

- **Median estimator $\hat{p}_{0,\,\mathrm{med}}$:** the estimated polarization equals that true polarization p_0 whose distribution's median* equals the observed polarization:

$$\hat{p}_{0,\,\mathrm{med}}(p) = p_0 \;\Bigg|\; \int_0^p \rho_\mathrm{p}(p'\,|\,p_0)\,\mathrm{d}p' \stackrel{!}{=} 0.5 \tag{6.22}$$

- **Mean estimator $\hat{p}_{0,\,\mathrm{mean}}$:** the estimated polarization equals that true polarization p_0 whose distribution has a mean value equal to the observed polarization, see also Serkowski [1958]:

$$\hat{p}_{0,\,\mathrm{mean}}(p) = p_0 \;\Bigg|\; \int_0^\infty p' \cdot \rho_\mathrm{p}(p'\,|\,p_0)\,\mathrm{d}p' \stackrel{!}{=} p \tag{6.23}$$

- **Maximum likelihood estimator $\hat{p}_{0,\,\mathrm{ml}}$:** the estimated polarization is the one that maximizes $\rho_\mathrm{p}(p_0\,|\,p)$, see also Fig. 6.14 and the explanation there:

$$\hat{p}_{0,\,\mathrm{ml}}(p) = p_0 \;\Bigg|\; \frac{\mathrm{d}\rho_\mathrm{p}(p_0\,|\,p)}{\mathrm{d}p_0} \stackrel{!}{=} 0 \tag{6.24}$$

- **ebal estimator† $\hat{p}_{0,\,\mathrm{ebal}}$:** approximate behavior of $\hat{p}_{0,\,\mathrm{ml}}$ for large values of p [Vaillancourt, 2006] in combination with a cut-off at $p \leq 1$ [Maier et al., 2014,a]:

$$\hat{p}_{0,\,\mathrm{ebal}}(p) = 0 \qquad p \leq 1 \tag{6.25}$$

$$= \sqrt{p^2 - 1} \qquad p > 1 \tag{6.26}$$

* The median of a continuous function is calculated as 2-quantile.
† **e**stimator **b**ased on **a**pproximated max. **l**ikelihood.

All these estimation algorithms have different critical polarizations p_{crit}: for all $p < p_{\mathrm{crit}}$ the estimated polarization becomes zero. The functional dependency between observed polarization and estimated polarization is printed in Fig. 6.6. From this figure it is not obvious which estimator works best. The bias, defined as difference of the mean estimated polarization $\langle \hat{p}_0 \rangle$ to the true polarization p_0, is a sensible quantity to evaluate the quality of the different estimators.

$$\mathrm{bias}(p_0) = \int_0^\infty \hat{p}_0(p) \cdot \rho_{\mathrm{p}}(p \,|\, p_0)\, \mathrm{d}p \; - \; p_0 \tag{6.27}$$

Figure 6.7 shows that the maximum likelihood estimator is the best estimator for small polarizations and the maximum estimator is best for large polarizations. The mean- and median estimators show only in a very small region of $0.83 \lesssim p_0 \lesssim 1.33$ their best performance. While the bias determines how close the estimated value and the true value are on average, the variance defines how strong the estimator spreads around the true value. The variance can be computed with the help of the mean squared error (MSE). For an estimator $\hat{e}$ it is:

$$\mathrm{Var}(\hat{e}) = \mathrm{MSE}(\hat{e}) - \mathrm{bias}^2(\hat{e}) \tag{6.28}$$

Considering the small bias values, the MSE and variance are very similar in this case.

$$\mathrm{MSE}(p_0) = \int_0^\infty \left(\hat{p}_0(p) - p_0\right)^2 \cdot \rho_{\mathrm{p}}(p \,|\, p_0)\, \mathrm{d}p \tag{6.29}$$

Figure 6.7 shows that bias and MSE have a similar behavior for all estimators, except for the trivial one. For low polarizations p_0, the maximum likelihood estimator works best. For high polarizations p_0 the maximum estimator is the best. The trivial

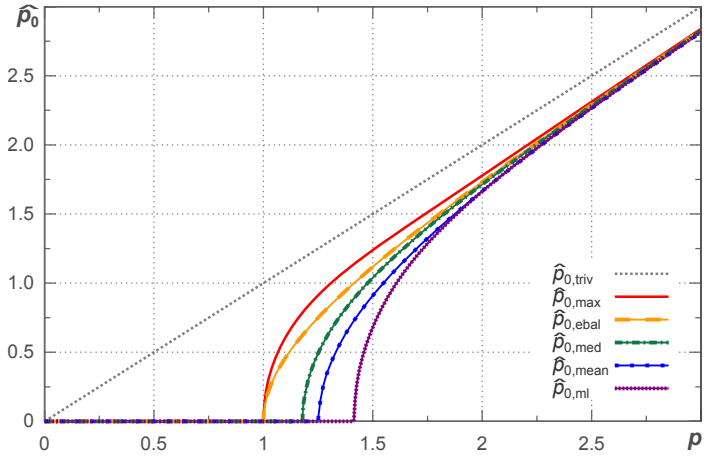

Figure 6.6. Estimated polarizations $\hat{p}_0$ as function of the observed polarization p. These plots were generated by numerically solving the Eqs. (6.21) - (6.24). Least square fits for the different estimators are listed in C.1.

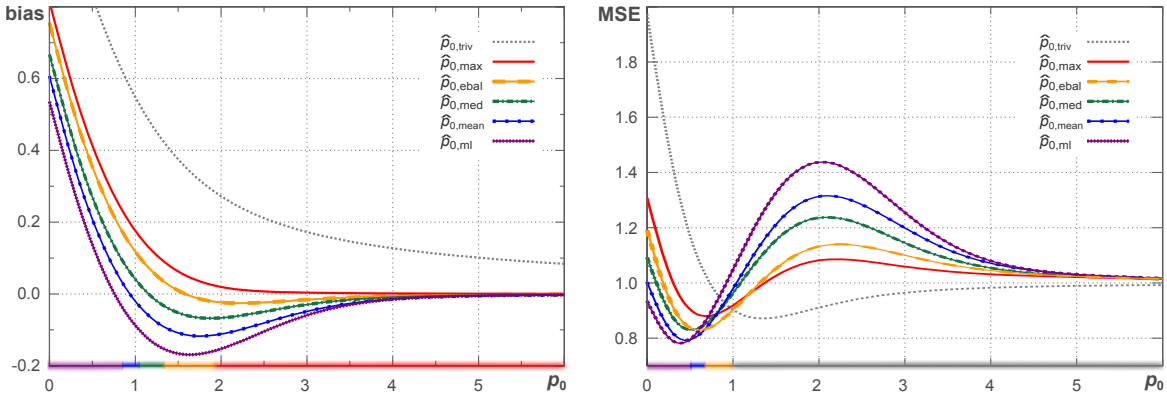

Figure 6.7. Bias and mean squared error (MSE) for the aforementioned estimators. The regions of best performance are indicated as color bars on the p_0-axis. See App. C.2 for listed values.

estimator shows the smallest MSE for polarizations $p_0 > 1$. This effect is related to the fact that the trivial estimator has no critical polarization p_{crit}. Factoring the large bias of $\hat{p}_{0,\,\mathrm{triv}}$ into the selection of an appropriate estimator and the fact that in all practical work p_0 is unknown, leads to the simple rule to take $\hat{p}_{0,\,\mathrm{ml}}$ for small polarizations and $\hat{p}_{0,\,\mathrm{max}}$ for large polarizations. This approach is kind of circular reasoning because one has to know the region of the polarization to get a good estimator for the polarization. See Sect. 6.3.2 for an alternative way to choose the best estimator on the basis of the observed polarizations p.

6.2.3. Interval estimations on p_0

An estimated value is a point estimation. It is the most appropriate value someone can give on the basis of the observation. An interval estimation tries to quantify the reliability of an estimated value. The definition of a confidence interval is the following [Dorey, 2010]:

> "The confidence interval gives us an interval that we believe, with a given level of confidence, contains the true value of the parameter being estimated in the target population."*

In the case of the probability density function ρ_{p}, the confidence interval $\Delta p = [\underline{p},\, \overline{p}]$ corresponding to the confidence level C can be defined as

$$\int_{\underline{p}}^{\overline{p}} \rho_{\mathrm{p}}(p \,|\, p_0)\, \mathrm{d}p = C. \tag{6.30}$$

* This is often misunderstood in the way that the confidence interval contains the true value with a probability equal to the confidence level. This is not the case; the true value is in the confidence interval (interval match), or it is not (interval mismatch). The confidence level is the chance for a interval match.

The interval limits $\underline{p}$ and $\overline{p}$ are not determined unambiguously by this definition. There is an infinite amount of values for $\underline{p}$ and $\overline{p}$ that fulfill Eq. (6.30). Mood and Graybill [1974] modeled this effect with an additional parameter $\lambda \in [0, \alpha)$, see Fig. 6.8:

$$\int_0^{\underline{p}} \rho_\mathrm{p}(p \,|\, p_0)\,\mathrm{d}p = \lambda \qquad \int_{\overline{p}}^{\infty} \rho_\mathrm{p}(p \,|\, p_0)\,\mathrm{d}p = \alpha - \lambda \tag{6.31}$$

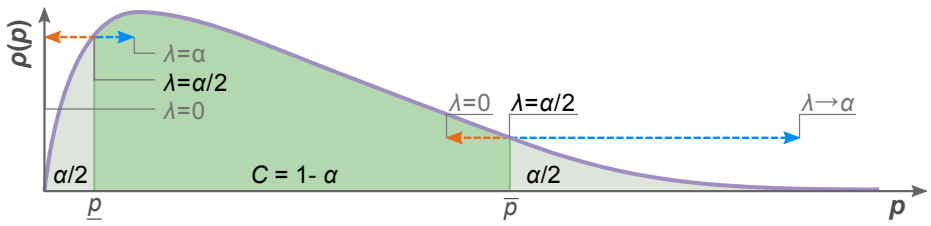

Figure 6.8. Schematic illustration of different confidence intervals with the same confidence level C. The greenish area is defined by the confidence limits $\underline{p}$ and $\overline{p}$ and is equal to C. All intervals that fulfill Eq. (6.30) can be labeled with the parameter λ. The grayish areas to the left of $\underline{p}$ and to the right of $\overline{p}$ are defined by Eq. (6.31) and are shown for the case $\lambda = \alpha/2$. The position of the confidence interval is shifted to the left (right) for $\lambda \to 0$ ($\lambda \to \alpha$). The smallest interval $[\underline{p}, \overline{p}]$ can be found for $\lambda < \alpha/2$.

α is defined by $\alpha = 1 - C$ and determines the region, where the true value is expected to be excluded. In the case of a symmetric distribution $\rho(p)$, $\lambda = \alpha/2$ would result in a symmetric confidence interval around the expectation value. Smaller values of λ shift the confidence interval to the left, whereas larger values shift it to the right. With the additional requirement that the confidence interval shall be as narrow as possible the definition of confidence intervals is unambiguous. For symmetric distributions this is always the case for $\lambda = \alpha/2$. For asymmetric distributions, like the Rice distribution, the smallest confidence interval is the one with $\rho(\underline{p}) = \rho(\overline{p})$.

As the Rice distribution ρ_p is non-Gaussian, confidence intervals in terms of σ are not defined. In analogy to the properties of the Gaussian σ_G, we define:

A σ_n confidence interval has the confidence level corresponding to $n \cdot \sigma_\mathrm{G}$.

For $n = \{1, 2, 3\}$, the confidence levels are $C_1 \approx 68.3\,\%$, $C_2 \approx 95.5\,\%$, and $C_3 \approx 99.7\,\%$. Attention should be paid, that now, $\sigma_n \neq n \cdot \sigma_1$ as in the Gaussian case. There is no meaning of one-, two- and three-σ values. Instead the terms σ_1, σ_2 and σ_3 are used.

Simmons and Stewart [1985] computed confidence intervals for $C = 0.67$, $C = 0.95$ and $C = 0.99$. Before going into details, their idea shall be explained in a nutshell. Their method assumes that the true degree of polarization p_0 is known and calculates for all values of p_0 the corresponding lower and upper limits $\underline{p}$ and $\overline{p}$. Finally, a $p - p_0$ projection is used to get confidence limits $\underline{p_0}$ and $\overline{p_0}$ as a function of p.

Finding optimal λ

The λ value that results in the smallest confidence interval, λ_{opt}, depends on the confidence level C and the degree of polarization p_0. The calculation of λ_{opt} is based on the idea that $\rho_{\text{p}}(\underline{p}_{\text{opt}}) = \rho_{\text{p}}(\overline{p}_{\text{opt}})$. The calculated values of λ_{opt} were fitted by an appropriate function $\lambda_{\text{fit}}(p_0)$ for subsequent calculations. A sigmoid function was chosen because of the S-shape of the calculated λ_{opt}

$$\lambda_{\text{fit}}(p_0) = \frac{1}{4} \cdot \left((2-a) + a \tanh\left(\frac{b\,(p_0 - c)}{2} \right) \right). \tag{6.32}$$

The parameters a, b and c were computed with the method of least square fit. All results are shown in Fig. 6.9 and in App. C.3.

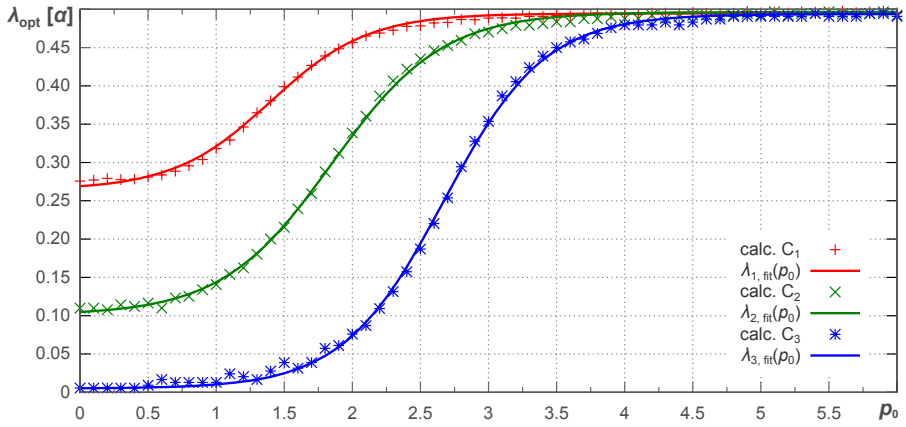

Figure 6.9. Numerically computed values for λ_{opt} for three different confidence levels $C_1 = 68.3\,\%$ ($\alpha_1 = 0.3173$), $C_2 = 95.5\,\%$ ($\alpha_2 = 0.0455$) and $C_3 = 99.7\,\%$ ($\alpha_3 = 0.0027$) in multiples of their α values. The corresponding least square fits are listed in App. C.3.

p - p_0 projection

Equation (6.30) in combination with the additional requirement of smallest possible confidence intervals results in lower and upper limits in p for a given p_0 value. Now,

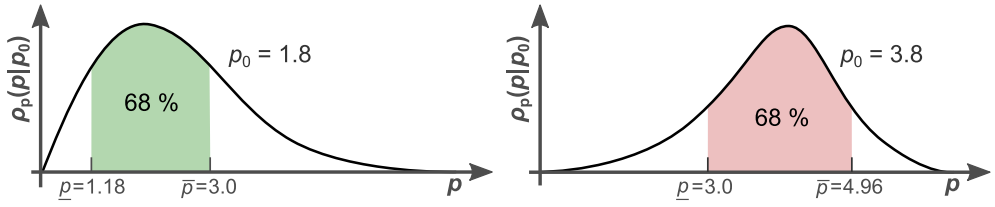

Figure 6.10. Illustration of the p - p_0 projection for $p = 3$ with $C = 0.68$.
Left: for $p_0 = 1.8$ the calculated lower and upper limits are $\underline{p} = 1.18$ and $\overline{p} = 3$.
Right: for $p_0 = 3.8$ the calculated lower and upper limits are $\underline{p} = 3$ and $\overline{p} = 4.96$.
Following the p - p_0 projection, the σ_1 confidence interval for $p = 3$ is $[1.8, 3.8]$.

instead of an interval Δp obtained for a given p_0, an interval $\Delta p_0 = [\underline{p_0}, \overline{p_0}]$ for a given p is needed. This projection is done in two steps:

1. For all p_0 values corresponding $\underline{p}$ and $\overline{p}$ can be calculated with Eq. (6.30).

2. For a specific p value, only two p_0-$\underline{p}$-$\overline{p}$ triplets are of interest: the one triplet with its upper limit $\overline{p}$ equal to p defines the lower limit of p_0 (i.e. $\underline{p_0}$); and the other triplet with its lower limit $\underline{p}$ equal to p defines the upper limit of p_0 (i.e. $\overline{p_0}$). See Fig. 6.10 for the example $p = 3$.

The following example may illustrate the situation for σ_1 confidence intervals (see Fig. 6.11 in pale colors): for $p = 3$, $\Delta p_0 \approx [1.8, 3.8]$ is well defined. For $p = 1.25$, the p_0-projection results only in an upper limit $\overline{p_0} \approx 1.9$. Nevertheless, the interval $\Delta p_0 \approx [0, 1.9]$ is a correct confidence interval for this measurement.

For $p \lesssim 0.4$ (the intersection point of the upper limit curve with the p-axis) there is no way to construct a non-vanishing σ_1 confidence interval in p_0. To avoid the case of non-existing confidence limits, Simmons and Stewart [1985] departed from the term of narrowest confidence intervals in p for small values of p_0. They proposed a tangential progression of the upper limit $\overline{p_0}$ to zero for $p \to 0$ and calculated corresponding new values of $\underline{p_0}$, so that the definition of Eq. (6.30) still holds. This way, confidence intervals can be set for all $p > 0$. Figure 6.11 shows σ_1, σ_2, and σ_3 confidence intervals with and without the tangential progression.

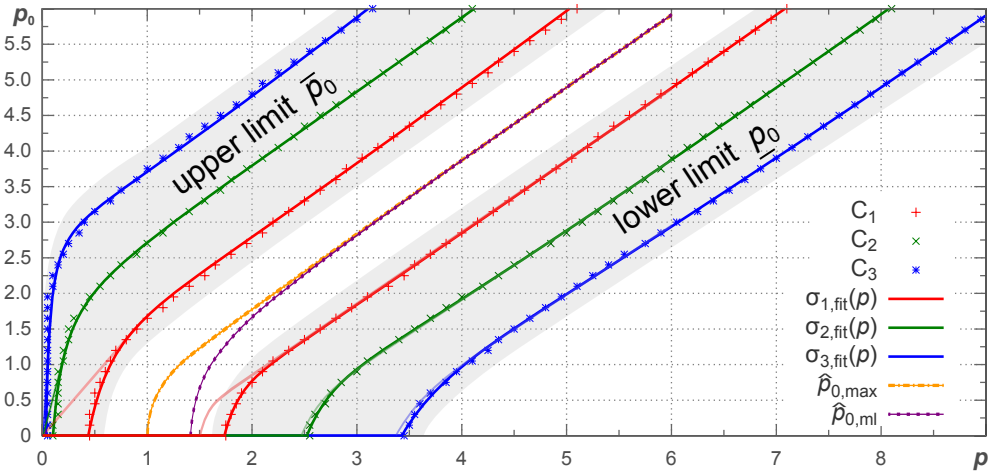

Figure 6.11. Confidence intervals for σ_1, σ_2 and σ_3 as a function of the observed polarization p. The tangent constructions of Simmons and Stewart [1985] are indicated in pale colors. Example: for $p = 3.0$ the corresponding σ_1-confidence limit is approximately [1.8, 3.8]. The best estimate can be found with the estimators introduced in Sect. 6.2.2: $\hat{p}_0(3) \approx 2.84$. The corresponding least square fits are listed in App. C.4.

6.2.4. The univariate probability distribution ρ_Ψ

By integrating Eq. (6.8) Naghizadeh-Khouei and Clarke [1993] calculated the probability density function of Ψ:

$$\rho_\Psi(\Psi \,|\, p_0,\, \Psi_0) = \int_0^\infty \rho_{\mathrm{p},\Psi}(p, \Psi \,|\, p_0, \Psi_0)\, \mathrm{d}p \tag{6.33}$$

$$\rho_\Psi(\Psi \,|\, p_0,\, \Psi_0) = \frac{1}{\sqrt{\pi}} \left(\frac{1}{\sqrt{\pi}} + \eta \mathrm{e}^{\eta^2} \big(1 + \mathrm{erf}(\eta)\big) \right) \mathrm{e}^{-\frac{p_0^2}{2}} \tag{6.34}$$

with $\eta = \frac{p_0}{\sqrt{2}} \cos\big(2(\Psi - \Psi_0)\big)$ and the Gaussian error function erf*. See Fig. 6.12 for a graphical representation of Eq. (6.34). In contrast to ρ_p, the ρ_Ψ-distribution is unbiased and symmetric around the true value Ψ_0. Furthermore, ρ_Ψ does not only depend on the parameter Ψ_0, but also on the polarization p_0.

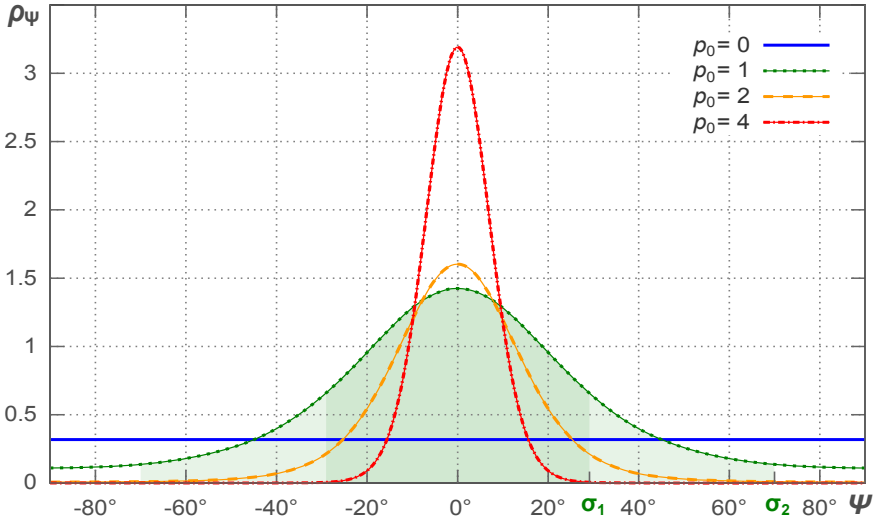

Figure 6.12. The probability density function ρ_Ψ (Eq. (6.34)) for different signal-to-noise ratios p_0. The true direction of polarization is set to $\Psi_0 = 0°$. It can be clearly seen that the distribution is symmetric around Ψ_0. For high values of p_0—which is equal to a high degree of polarization—the distribution becomes Gaussian shaped. For unpolarized light ($p_0 = 0$) each angle of polarization Ψ is equally probable. For $p_0 = 1$ the confidence intervals for $C_1 = 68.3\,\%$ and $C_2 = 95.5\,\%$ are indicated with $\sigma_1 \approx 29°$ and $\sigma_2 \approx 71°$.

6.2.5. Point estimations on Ψ_0

The unbiased ρ_Ψ distribution gives directly:

$$\hat{\Psi}_0(\Psi) = \Psi \tag{6.35}$$

* $\mathrm{erf}(x) = \frac{2}{\sqrt{\pi}} \int_0^x \mathrm{e}^{-t^2}\, \mathrm{d}t$.

6.2.6. Interval estimations on Ψ

With the help of Eq. (6.34) the half width $\Delta\Psi/2$ at any confidence level C can be computed via:

$$\int_{\Psi_0-\Delta\Psi/2}^{\Psi_0+\Delta\Psi/2} \rho_\Psi(\Psi \,|\, p_0, \Psi_0)\, \mathrm{d}\Psi = C \tag{6.36}$$

The σ_1 confidence interval $[\Psi_0 - \sigma_1, \Psi_0 + \sigma_1]$ is then defined as:

$$\int_{\Psi_0-\sigma_1}^{\Psi_0+\sigma_1} \rho_\Psi(\Psi \,|\, p_0, \Psi_0)\, \mathrm{d}\Psi \overset{!}{\approx} 0.683 \tag{6.37}$$

In the same way, the σ_2 and σ_3 values can be calculated for a confidence level of approximately 95.5 % and 99.7 %. Naghizadeh-Khouei and Clarke [1993] calculated σ_1, σ_2 and σ_3 values for low polarizations p_0, see Fig. 6.13.

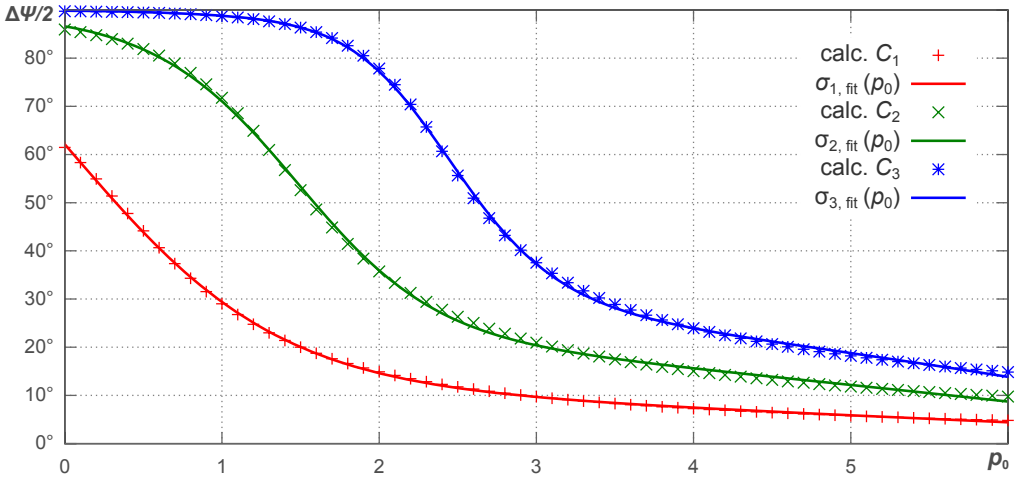

Figure 6.13. σ_1, σ_2 and σ_3 confidence intervals for the polarization angle. The points are results from numerical integration of Eq. (6.36). The corresponding least square fits are listed in App. C.7.

6.3. Bayesian analysis

In contrast to the frequentist approach, Bayesian statistics extends the concept of probabilities to statements that become not only true and false, but more or less plausible. This reasoning allows one to deduce the plausibility of the cause on the basis of observed consequences. This is the usual case for all physical measurements: true values are estimated on the basis of observed data. In the case of polarimetric measurements, the true degree and angle of polarization are unknown parameters that shall be determined with the help of observed data.

6.3.1. The univariate probability distribution ρ_{p_0}

The probability distribution for the true polarization p_0 can be computed directly with Bayes' theorem. Before doing that, an intuitive way of deriving $\rho_{p_0}(p_0 \,|\, p)$ shows the way this theorem works. The properties of a probability density function ρ are:

1. By definition, the probability Q to find an observable x within the interval $[x_1,\, x_2]$ is:

$$Q = \int_{x_1}^{x_2} \rho(x)\,\mathrm{d}x \tag{6.38}$$

   This means that $\rho(x_0)\,\mathrm{d}x$ equals the probability of observing a value within $[x_0,\, x_0 + \mathrm{d}x]$. Because $\rho(x_0)$ is not changing in the infinitesimally small interval $\mathrm{d}x$, it follows that the values of $\rho(x)$ are proportional to the probability of finding a value x.

2. The probability to observe any value must be 100 %:

$$\int_{-\infty}^{\infty} \rho(x)\,\mathrm{d}x = 1 \tag{6.39}$$

Taking the known function $\rho_\mathrm{p}(p \,|\, p_0)$ in Eq. (6.14) and changing variable and parameter yields the function $\rho^*_{\mathrm{p}_0}(p_0 \,|\, p)$ that is formally the same as Eq. (6.14). This expression already fulfills the property that its values are in relation to the probability of finding a true polarization p_0 for an observation within $[p, p + \mathrm{d}p]$.

$$\rho^*_{\mathrm{p}_0}(p_0 \,|\, p) = p \cdot \exp\left(-\frac{p^2 + p_0^2}{2}\right) \cdot I_{1,\,0}(pp_0) \tag{6.40}$$

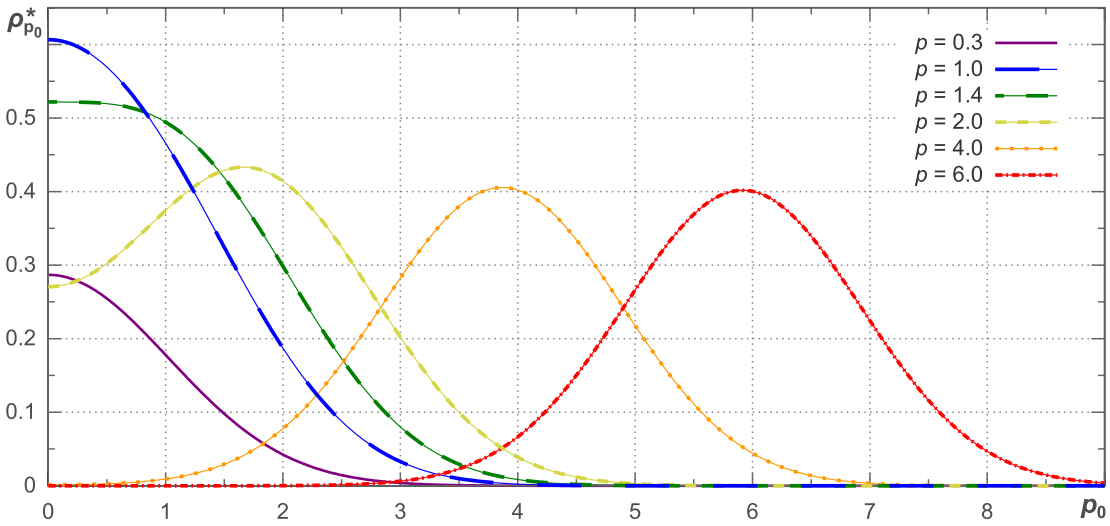

Figure 6.14. The distribution of Eq. (6.40) for different observed polarizations p. The maximum likelihood estimator $\hat{p}_{0,\mathrm{ml}}$ of Sect. 6.2.2 links the p_0-peak position to the corresponding p values. For all $p \leq 1.4$—the critical polarization for $\hat{p}_{0,\mathrm{ml}}$—the most likely true polarization is $p_0 = 0$.

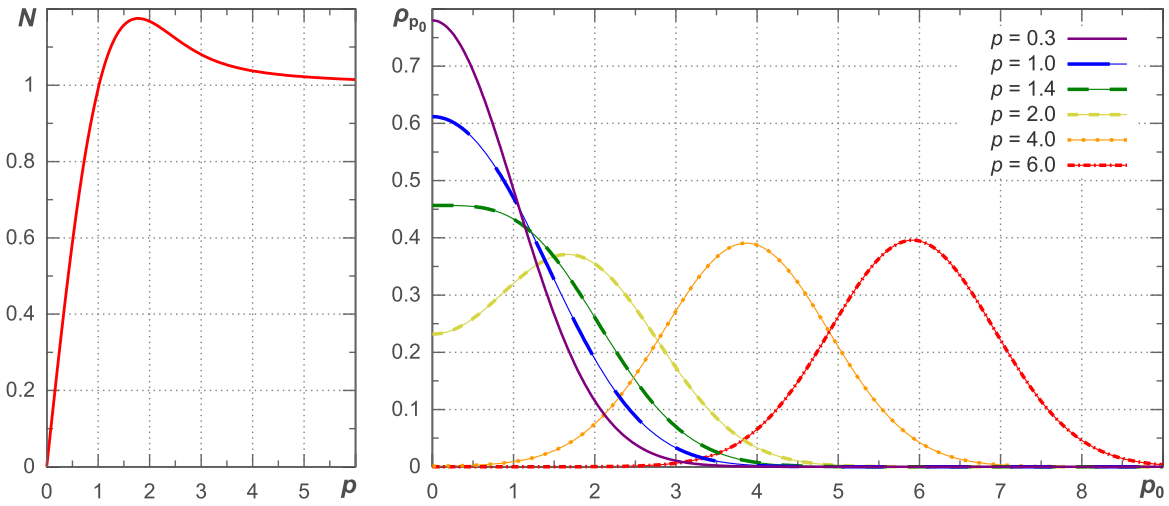

Figure 6.15. Graph of the normalization factor N according to Eq. (6.41) and normalized $\rho_{\mathrm{p}_0}(p_0 \,|\, p)$ distribution according to Eq. (6.42).

Figure 6.14 shows the corresponding plots for different observed polarizations. The probability density function $\rho_{\mathrm{p}_0}(p_0 \,|\, p)$ can now be constructed by normalizing $\rho^*_{\mathrm{p}_0}(p_0 \,|\, p)$ with respect to p_0, see Fig. 6.15:

$$N = \int_0^\infty \rho^*_{\mathrm{p}}(p_0 \,|\, p)\, \mathrm{d}p_0 \tag{6.41}$$

$$\rho_{\mathrm{p}_0}(p_0 \,|\, p) = \frac{1}{N}\, \rho^*_{\mathrm{p}_0}(p_0 \,|\, p) \tag{6.42}$$

Bayes' theorem

Bayes' theorem is working on conditional probabilities. $P(B \,|\, A)$ is the probability that case B happens, given that case A has already happened. If $P(A)$ is the probability that A happens, regardless of the manifestation of B, and $P(B)$ is the probability that B happens, regardless of A, Bayes' theorem states:

$$P(A \,|\, B) = \frac{P(A) \cdot P(B \,|\, A)}{P(B)} \tag{6.43}$$

For continuous variables, the probability changes to the probability density. Applying Eq. (6.43) to polarization measurements results in:

$$\rho_{\mathrm{p}_0}(p_0 \,|\, p) = \frac{\rho(p_0) \cdot \rho_{\mathrm{p}}(p \,|\, p_0)}{\rho(p)} \tag{6.44}$$

$$\rho_{\mathrm{p}_0}(p_0 \,|\, p) = \frac{\rho(p_0) \cdot \rho_{\mathrm{p}}(p \,|\, p_0)}{\int_0^\infty \rho(p_0) \cdot \rho_{\mathrm{p}}(p \,|\, p_0)\, \mathrm{d}p_0} \tag{6.45}$$

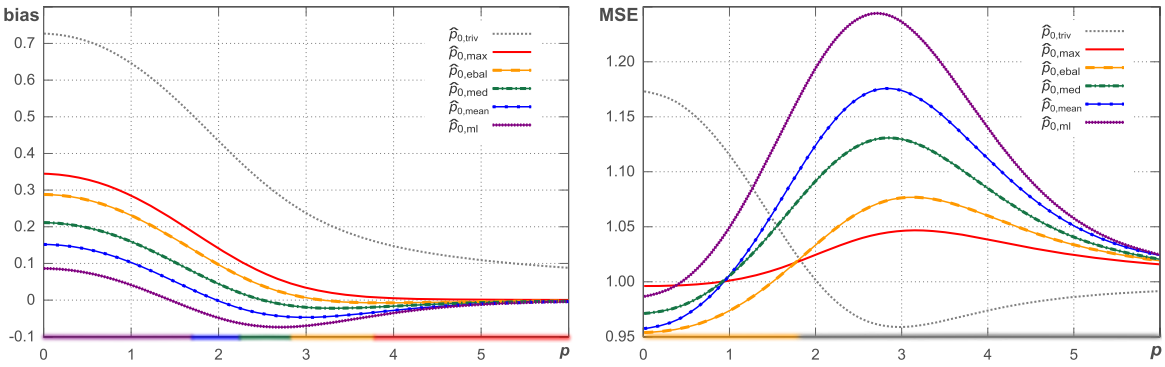

Figure 6.16. Bayesian bias and MSE as function of p. The maximum, median, mean, and maximum likelihood estimator are constructed as in Simmons and Stewart [1985] and recalculated as function of p according to Eq. (6.47) and Eq. (6.48). The ebal-estimator is defined in Eq. (6.26). The regions of best performance are indicated as color bars on the p-axis. See App. C.8 for listed values.

The last equation expresses the probability density $\rho(p)$ as $\rho(p_0) \cdot \rho(p \,|\, p_0)$ integrated over all possible values of p_0. Assuming a non-informative polar prior density* $\rho(p_0) =$ const. gives directly Eq. (6.42). Quinn [2012] studied the impact of non-informative prior densities in general, and the difference of Jeffrey's prior, which is uniform in the Stokes parameters q_0 and u_0 to the uniform polar prior, which is uniform in p_0. With reference to this work, it shall only be mentioned that Jeffrey's prior overstates large values of p_0, so that the polar prior seems to be the best choice if no information of the source polarization is known.

6.3.2. Point estimations on p_0

The probability density $\rho_{\mathrm{p_0}}$ can be used to transform any quantity that is a function of p_0 to an estimation value as a function of p. To get $f(p)$, the function $f(p_0)$ must be weighted for each p_0 with the probability that this p_0 results in the observed p. In general this is:

$$f(p) = \int_0^\infty f(p_0) \cdot \rho_{p_0}(p_0 \,|\, p)\, \mathrm{d}p_0 \tag{6.46}$$

Using the already calculated $\mathrm{bias}(p_0)$ (Eq. (6.27)) and $\mathrm{MSE}(p_0)$ (Eq. (6.29)) leads to

$$\mathrm{bias}(p) = \int_0^\infty \mathrm{bias}(p_0) \cdot \rho_{\mathrm{p_0}}(p_0 \,|\, p)\, \mathrm{d}p_0 \tag{6.47}$$

$$\mathrm{MSE}(p) = \int_0^\infty \mathrm{MSE}(p_0) \cdot \rho_{\mathrm{p_0}}(p_0 \,|\, p)\, \mathrm{d}p_0 \tag{6.48}$$

* Technically speaking, this statement is not fully correct because there is no uniform distribution living on the non-negative half-line R_+ that can be normalized. This mathematical problem can be overcome by considering a maximal possible true degree of polarization $p_{0,\mathrm{max}}$, so that $\rho = p_{0,\mathrm{max}}^{-1}$. Finally: $p_{0,\mathrm{max}} \to \infty$.

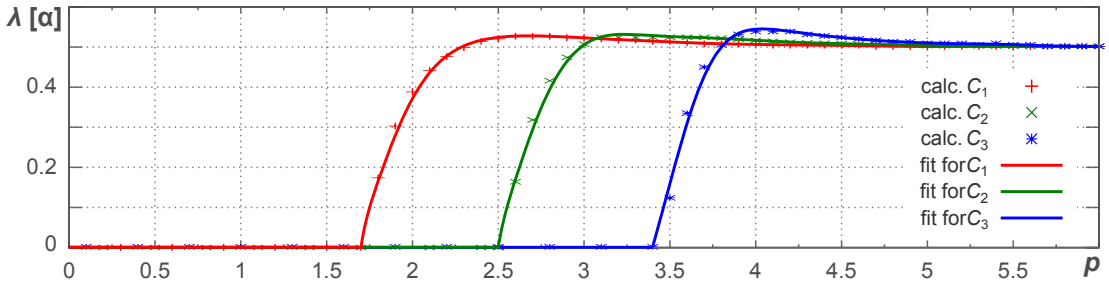

Figure 6.17. Optimal λ values for σ_1, σ_2 and σ_3 confidence levels. The critical polarizations are $p_{1\,\mathrm{crit}} \approx 1.7$, $p_{2\,\mathrm{crit}} \approx 2.5$ and $p_{3\,\mathrm{crit}} \approx 3.4$. The corresponding least square fits are listed in App. C.5.

Figure 6.16 shows bias and MSE as a function of p. This result matches observational needs; the estimator for the true degree of polarization can be estimated on the basis of the observed value p.

6.3.3. Interval estimations on p_0

While the frequentist approach integrates the probability density function $\rho_\mathrm{p}(p\,|\,p_0)$ in p and projects the results to p_0 the Bayesian approach can evaluate the probability density function directly in p_0. Analogous to confidence intervals in frequentist statistics, credibility intervals in Bayesian statistics make a statement on the reliability of an estimated value. Different from confidence intervals, credibility intervals give the probability that the true value is within a specific interval. For all possible values of p_0 that can cause ($\twoheadrightarrow$) the observed p, the credibility interval includes those p_0 that cause p in a fraction C of all cases:

$$\forall\, p_0 : \mathrm{Prob}\left(p_0 \in \left[\underline{p_0},\, \overline{p_0}\right] \twoheadrightarrow p\right) = C \quad \text{, fixed } p. \tag{6.49}$$

Integrating the density distribution ρ_{p_0} over p_0 leads directly to credibility intervals Vaillancourt [2006]:

$$\int_{\underline{p_0}}^{\overline{p_0}} \rho_{\mathrm{p}_0}(p_0\,|\,p)\,\mathrm{d}p_0 = C \quad \Big| \quad \left[\underline{p_0},\, \overline{p_0}\right] \text{ minimal.} \tag{6.50}$$

Again, the asymmetric shape of $\rho_{\mathrm{p}_0}(p_0\,|\,p)$ leads to a nontrivial choice of the interval limits $\overline{p_0}$ and $\underline{p_0}$, see Sect. 6.2.3. With the same argumentation as there, λ values corresponding to a preferably narrow confidence interval were calculated, see Fig. 6.17. The resulting credibility limits are shown in Fig. 6.18 for σ_1, σ_2, and σ_3 credibility intervals. Parametric fitting results can be found in App. C.6.

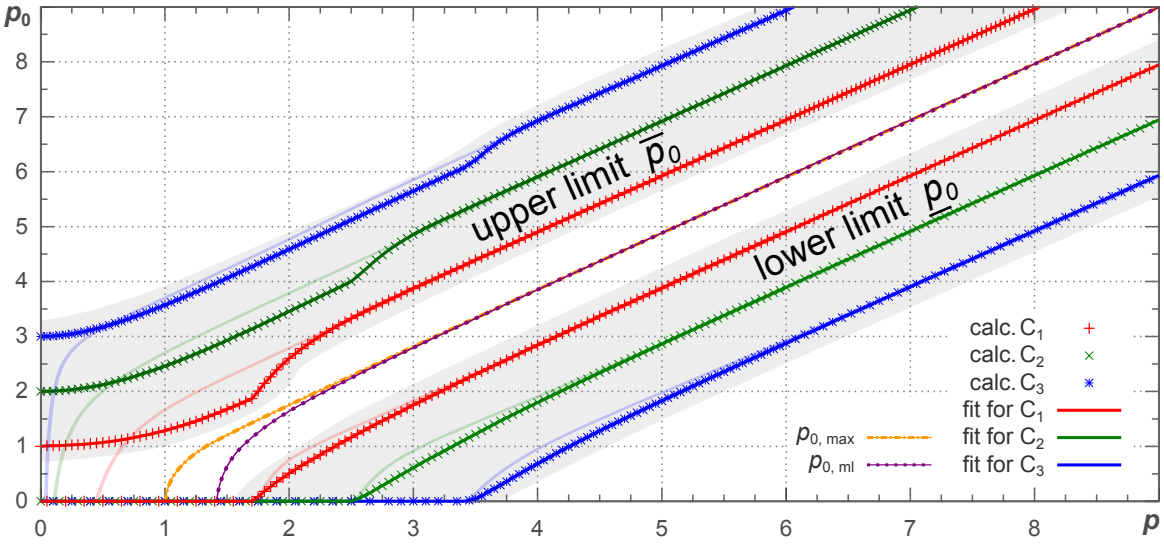

Figure 6.18. Credibility intervals as a function of the observed polarization and the applied credibility level. The estimation values for the maximum and the maximum likelihood method are plotted additionally. The results from Simmons and Stewart [1985] are plotted in pale colors. Example: for $p = 3.0$ the corresponding σ_2-credibility interval is approximately [0.61, 4.86]. The best estimate can be found with the estimators introduced in Sect. 6.2.2: $\hat{p}_0 \approx 2.84$. The corresponding least square fits are listed in C.6.

6.3.4. Point estimations on Ψ_0

Since there is no biasing effect in the angle of polarization, it is sufficient to use the trivial estimator

$$\hat{\Psi}_0(\Psi) = \Psi. \tag{6.51}$$

6.3.5. Interval estimations on Ψ_0

In Maier et al. [2014,a] we proposed a new method to calculate interval estimations on Ψ_0. Before presenting this method, a short overview shall list the difficulties we recognized in constructing interval estimations $\Delta\Psi$ as a function of p and clarify why it is incorrect to proceed in the following way:

- Using the best estimator $\hat{p}_0$ as a parameter for Eq. (6.36) leads to incorrect results because the uncertainty of p_0 does not propagate into the uncertainty of Ψ.

- Calculating $\Delta\Psi$ with the lower limit $\underline{p_0}$ that was computed in Sect. 6.3.3 overestimates the uncertainty in Ψ because the interval Δp_0 is constructed to be minimal in p_0 but not in Ψ (the upper limit $\overline{p_0}$ underestimates $\Delta\Psi$, cf. Fig. 6.13).

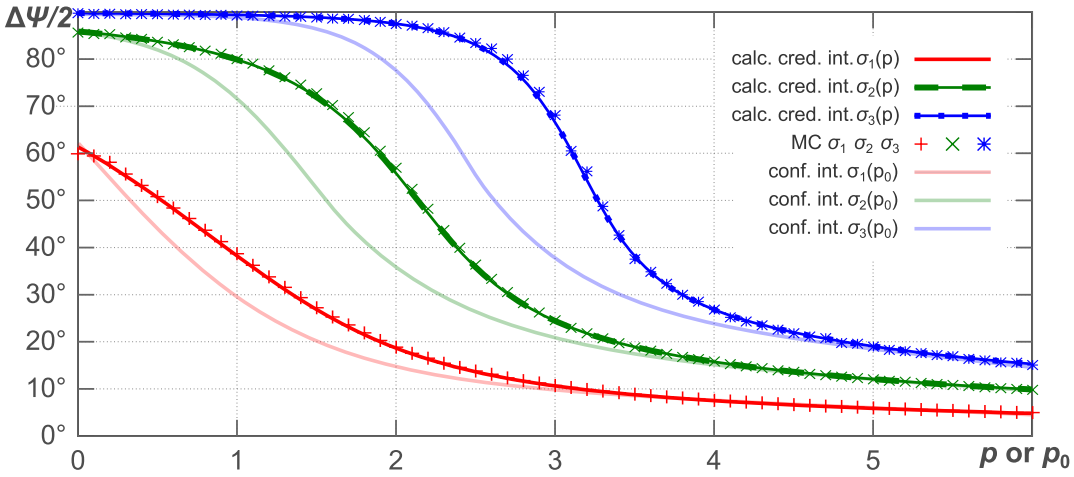

Figure 6.19. Numerically calculated credibility intervals (bold lines) with Monte Carlo (MC) simulated results (crosses) in comparison to the confidence intervals calculated in Sect. 6.2.6 (pale colors). Be aware that the confidence intervals are a function of p_0. The difference is not only a bias, which should be maximal at low degrees of polarization, but originates also from the different statements that confidence and credibility intervals make. Least square fitting results are listed in App. C.9

- Transforming p_0 to p according to Eq. (6.46)

$$\Delta\Psi(p) = \int_0^\infty \Delta\Psi(p_0) \cdot \rho_{p_0}(p_0 \,|\, p)\, \mathrm{d}p_0 \tag{6.52}$$

  averages $\Delta\Psi$. The result is reasonable, but does not match the definition of credibility intervals in Eq. (6.49).

The correct idea is to recalculate Δp_0 credibility intervals with the bivariate probability distribution $\rho(p, \Psi \,|\, p_0, \Psi_0)$ of Eq. (6.12). After integrating over p_0 and normalizing the bivariate distribution for fixed p's with respect to Ψ, the credibility interval $\Delta\Psi$ can be computed ($\Leftarrow$) directly (without loss of generality $\Psi_0 = 0$):

$$\rho^*(p, \Psi) = \int_0^\infty \rho(p, \Psi \,|\, p_0, 0)\, \mathrm{d}p_0, \tag{6.53}$$

$$\rho(p, \Psi) = \frac{\rho^*(p, \Psi)}{N(p)}\ ,\ N(p) = \int_{-\pi/2}^{\pi/2} \rho^*(p, \Psi)\, \mathrm{d}\Psi, \tag{6.54}$$

$$\Delta\Psi(p) \Leftarrow \int_{-\Delta\Psi/2}^{\Delta\Psi/2} \rho(p, \Psi)\, \mathrm{d}\Psi = C \tag{6.55}$$

The numerically computed results are shown in Fig. 6.19.

6.4. Monte Carlo simulation

A Monte Carlo simulation works on repeated random sampling. The presented credibility intervals for the degree and angle of polarization shall be verified and explained more intuitively in the following with a Monte Carlo simulation.

6.4.1. Simulating credibility intervals $\Delta p_0(p)$

The simulation can be broken up into three steps:

1. **Consider a true polarization p_0.** The p_0-value must be limited so that the simulation is terminated. The choice of the limit $p_{0,\max}$ influences the maximal observed polarization $p_{\max}$ that can be simulated. The difference between $p_{\max}$ and $p_{0,\max}$ must be large enough so that all neglected $p_0 > p_{0,\max}$ only have a negligible contribution to all $p < p_{\max}$. With the chosen values $p_{0,\max} = 12$ and $p_{\max} = 6$, the error due to the limitation of p_0 is less than $7 \cdot 10^{-10}$:

$$\int_0^6 \rho_\mathrm{p}(p \,|\, 12)\, \mathrm{d}p \approx 6.9 \cdot 10^{-10} \tag{6.56}$$

   All p_0-values are distributed equally over the interval $[0,\, p_{0,\max}]$ with a constant step size of $\Delta p_0 = 0.01$.

2. **Simulate a measured p.** Based on the probability density function $\rho_\mathrm{p}(p \,|\, p_0)$ (Eq. (6.14)) p values corresponding to a specific p_0 can be simulated. This is done in two steps. The random generator by Park and Miller generates a uniform distribution $u(x) = 1$ with $0 < x < 1$ [Press et al., 1992, § 7.1]. The *inversion method*, see for example Devroye [1986, § 2.1], is used to generate a random variable which has a Rice distribution:

$$p = CDF_{\rho_\mathrm{p}}^{-1}(x) \tag{6.57}$$

   Equation (6.57) has a nice graphical interpretation. It is the projection from the ordinate to the abscissa of the Rice cumulative distribution function* CDF_{ρ_p}, see Fig. 6.20. The p-values are binned into appropriate blocks $[p - \Delta p,\, p + \Delta p]$ because of their continuous distribution. The simulation uses $\Delta p = 0.02$.

3. **Finding the credibility interval.** Repeating steps 1 and 2 numerous times yields a large set of $(p_0 \,/\, p)$ pairs. Now, for a specific value of p, the distribution of p_0 values that correspond to this p can be used to construct a credibility interval, at confidence level C, in p_0: after counting the number of all pairs which have a polarization within $[p - \Delta p,\, p + \Delta p]$, the credibility interval is chosen as the smallest possible interval that contains $C \cdot N$ pairs.

Fig. 6.21 explains the described method graphically in the example $p \approx 2$.

* The $CDF(x)$ is defined as the probability of measuring a value $v \leq x$.

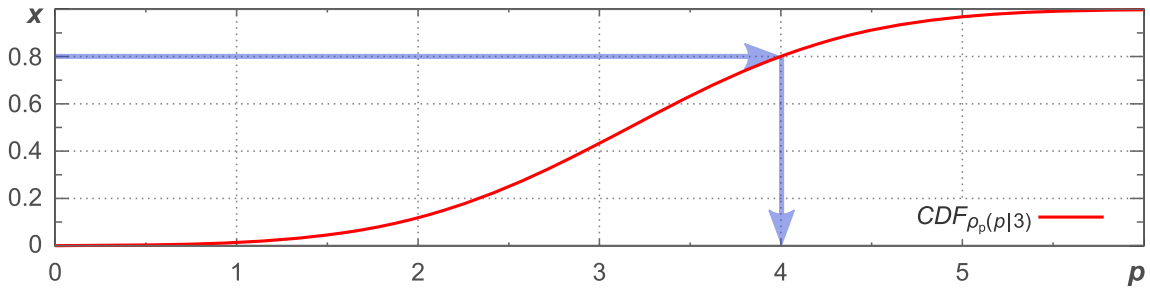

Figure 6.20. Inversion method applied to a Rice CDF with $p_0 = 3$. After choosing a uniformly distributed value $0 < x < 1$, the corresponding polarization follows as $p = CDF^{-1}(x)$. In the example, the random number $x = 0.8$ yields $p = 4$.

6.4.2. Simulating credibility intervals $\Delta\Psi_0(p)$

The considerations on p_0 and the usage of the inversion method to generate non-uniform distributions are identical to the previous section. Beside this, simulating interval estimations on the polarization angle ($\Psi_0 = 0$ is assumed) is done in two steps. First, appropriate random data must be simulated:

1. Choose a true signal-to-noise ratio $p_0 \in [0, 10]$.
2. Simulate a value p following $\rho_\mathrm{p}(p\,|\,p_0)$, cf. Eq. (6.14).
3. Simulate a value Ψ following $\rho(p,\Psi\,|\,p_0, 0)$, Eq. (6.8).

Repeating these steps numerous times yields a large number of $(p_0/p/\Psi)$-triplets. In the second step, analyzing these triplets will result in the desired credibility intervals:

1. Select all triplets with a p-value within a specific p-bin $[p, p+0.01]$, independent of their p_0 and Ψ-values.
2. Count the selected triplets $\rightarrow N_{\mathrm{p}_0,\Psi}$.
3. Sort the triplet list with respect to Ψ.
4. Starting counting at $\Psi = 0$, the credibility interval* $\Delta\Psi/2$ can be obtained as the Ψ value of the data triplet at list number $C/2 \cdot N_{\mathrm{p}_0,\Psi}$.

In this way, the uncertainty in Ψ can be estimated on the basis of the observed signal to noise ratio p. Repeating these steps for a set of different p-values and confidence levels C results in the graphs of Fig. 6.19. Again, the method used is explained graphically in Fig. 6.21.

* The Ψ-symmetry in Eq. (6.8) allows to restrict all calculations on the half credibility interval.

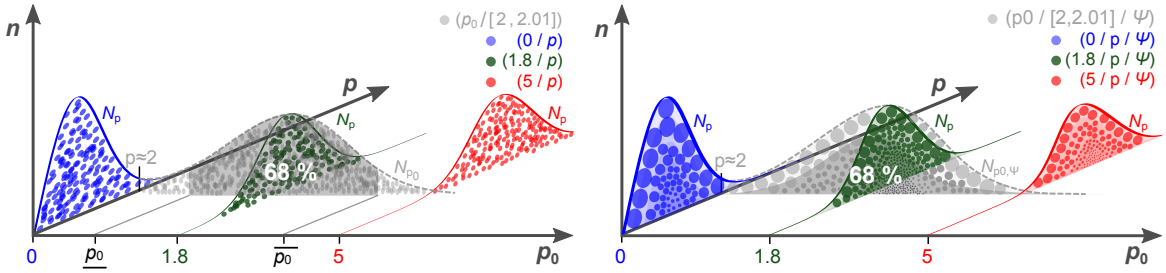

Figure 6.21. Schematic to explain the simulation of credibility intervals. For reasons of clarity only the pairs with $p_0 \in \{0, 1.8, 5\}$ and those with $p = 2$ are shown.
Left: credibility interval simulations for the degree of polarization are based on (p_0/p)-pairs. The third dimension (n) equals the (p_0/p)-pair density. For $p = 2$, the corresponding σ_1 credibility interval (gray shaded area) consists of 68 % of all pairs $(p_0/2)$.
Right: credibility interval simulations for the angle of polarization are based on $(p_0/p/\Psi)$-triplets. As $\Psi_0 = 0$, it follows $\Delta\Psi = \Psi$. The values of Ψ are indicated by the dot size. For $p = 2$, the corresponding σ_1 credibility interval (gray shaded area) consists of 68 % of all triplets $(p_0/2/\Psi)$ with arbitrary p_0 but smallest possible Ψ.

6.5. Analysis in the limit of high polarizations

In the case of high polarizations—which means $p > 6$—the probability density function of Eq. (6.12) can be assumed to be Gaussian shaped in the variable Ψ and a. Point and interval estimations on both variables can be calculated in the following way: the trivial estimator $\hat{\Psi}_0 = \Psi$ is sufficient for the angle of polarization. The biasing effect for the degree of polarization shifts the value for the best estimated polarization approximately to

$$\hat{p}_0 = \sqrt{p^2 - 1}. \tag{6.58}$$

For high polarizations, the univariate uncertainties for p or a [Elsner et al., 2012] and Ψ [Serkowski, 1962] become:

$$\sigma_\mathrm{a} = \sigma_\mathrm{c} = \frac{\sqrt{2(C_\mathrm{S} + C_\mathrm{B})}}{C_\mathrm{S}} \qquad \sigma_\mathrm{p} = \frac{\sigma_\mathrm{a}}{\sigma_\mathrm{c}} = 1 \tag{6.59}$$

$$\sigma_\Psi = \frac{\sigma_\mathrm{c}}{2\,a_0} = \frac{\sqrt{2(C_\mathrm{S} + C_\mathrm{B})}}{2a_0\,C_\mathrm{S}} \qquad \sigma_\Psi = \frac{1}{2p_0} \approx \frac{28.65°}{p_0} \tag{6.60}$$

With Eqs. (6.59) and (6.60) confidence intervals can be computed in the standard way: confidence intervals of $\pm\sigma$, $\pm 2\sigma$ and $\pm 3\sigma$ around the estimated value represent confidence levels of 68.3 %, 95.5 % and 99.7 %. Unfortunately, in many realistic cases the polarization will be of such low degree that the deviations from the Gaussian shape have to be taken into account.

6.6. Binning the ϕ-distribution

The statistical properties of a sinusoidal modulated event distribution (see Sects. 6.2.1 - 6.2.4) serve as theoretical basis that defines the limits in accuracy that can be expected considering the continuous ϕ-distribution of Eq. (6.1). However, real life experiments are not based on such a continuous event distribution, but on a data based histogram that only resembles Eq. (6.1). Besides the different methods how to bin data into a histogram, the chosen number of bins M have a noticeable effect in the point and interval estimations of the degree and angle of polarization. This effect can become prominent for small numbers N of detected events.

X-ray polarimetry of astronomical sources is currently characterized by small numbers of events in combination with a typically small degree of polarization. Therefore, a detailed study of the effects of data binning is essential. This section describes different methods for data binning. Based on a Monte-Carlo simulation, the performance of equal width and equal frequency binning are tested for polarimetric analysis. For both methods, a rule how to choose the optimal number of bins and a comparison to the predictions of the continuous distribution (Eq. (6.1)) are given.

6.6.1. Data binning

The idea of data binning is to quantize data in a way that the major effects that are imprinted in the data distribution are still observable, but the small statistical fluctuations will be canceled out. In the case of analyzing polarimetric measurements, i.e. ϕ-distributed events, the two major errors resulting from event binning are:

- **Uncertainty in the number of counts:** a counting based statistic of N counts is Poisson distributed with a standard deviation of $\sigma = \sqrt{N}$ and a signal-to-noise relation of $SNR = N/\sqrt{N} = \sqrt{N}$. The relative uncertainty in the number of counts increases with a fine binning as the counts decrease. This effect influences mainly the estimated modulation amplitude a, i.e. the degree of polarization.

- **Uncertainty in ϕ:** collecting ϕ-distributed events into bins of width $\Delta\phi$ results in an inaccuracy of ϕ that is—in a first assumption—in the order of $\Delta\phi$. The uncertainty in ϕ influences mainly the phase of the modulation curve, i.e. the angle of polarization Ψ. This effect decreases with a fine binning as $\Delta\phi$ gets smaller.

Looking at these two error sources gives reasons for the two major methods for binning, each concentrating on one of the error sources:

- **equal width binning (EWB):** The most intuitive method of data binning is to divide the interval of interest I (in our case $I = 2\pi$) into a number M of bins of equal width $i = I/M$. The histogram is constructed by the number of events n_k within each bin k. This technique minimizes the uncertainty in ϕ at the expense that some bins possibly have a very low counting statistic.

- **equal frequency binning (EFB):** Here, the width of each binning interval i_k is chosen in a way that each bin k contains the same amount of events $n = N/M$. The density of events $\tilde{n}_k = n/i_k$ is then calculated for each bin and forms the histogram. This technique has a good counting statistic, but some bins can become very large.

In general, it is not possible to state that the one binning method is better than the other. The performance of both methods depends on the underlying probability density distribution, the number of measured events N, and the chosen number of bins M.

General statements for optimal binning are rules of thumb like that "5-20 bins are usually adequate" [Knuth, 2006] or $M \sim \sqrt[3]{N}$ [Scott, 1979]. More elaborate statements for an optimal binning are often restricted to Gaussian distributions and a clear rule for polarimetric analysis is missing.

6.6.2. Monte Carlo Simulation

The aim of the following simulation is to test which of the binning methods (constant width or frequency) works best for polarimetric analysis and what is the optimal number M of binning intervals. In principle, both answers can depend on the underlying data structure, i.e. the number of events N and the modulation amplitude a. The idea of the simulation can be summarized in three steps:

1. **Simulate** an event distribution based on Eq. (6.1) for given N, a, and Ψ. Acting as if the true values a_0 and Ψ_0 are unknown the guessed event distribution is then processed like usual observed data.

2. **Bin** the distribution with EWB or EFB for a fixed number of bins M.

3. **Fit** the resulting histogram with Eq. (6.1). This leads to the estimated values $\hat{a}$ and $\hat{\Psi}$.

Repeating these steps several times results in a distribution of $\hat{a}$ and $\hat{\Psi}$ which can be expressed with the mean expected values $\langle\hat{a}\rangle$ and $\langle\hat{\Psi}\rangle$ with variances $\Delta\hat{a}$ and $\Delta\hat{\Psi}$. Comparing these values with the true values a_0 and Ψ_0 and the theoretical expected variations Δa_0 and $\Delta\Psi_0$ gives a criterion for the goodness of the binning-fitting combination*. Finally all steps can be repeated for different† N, M, a_0, and for both binning methods.

* The goodness of fit was not considered with a "classical" reduced χ^2 approach because the aim of the polarimetric analysis is not to get a well fitting modulation curve, but a good estimation of the modulation amplitude a (or the degree of polarization p) and the angle of polarization Ψ.

† A variation in Ψ_0 was not considered because it only shifts the phase of the modulation curve.

Guessing a sinusoidal modulated event distribution

Like in Sect. 6.4, the sinusoidal event distribution is made with the cumulative distribution function:

$$CDF(\phi) = \int_0^{\phi} PDF(\phi')\,\mathrm{d}\phi' \tag{6.61}$$

$$= \int_0^{\phi} \frac{1}{2\pi}\Big(1 + a\cos\left(2\left(\phi' - \Psi\right)\right)\Big)\,\mathrm{d}\phi' \tag{6.62}$$

$$= \frac{1}{2\pi}\Big(\phi + a\Big[{}^1\!/_2\,\sin\left(2\left(\phi' - \Psi\right)\right)\Big]_0^{\phi}\Big) \tag{6.63}$$

$$= \frac{1}{2\pi}\Big(\phi + \frac{a}{2}\Big(\sin(2(\phi - \Psi)) + \sin(2\Psi)\Big)\Big) \tag{6.64}$$

With the random number generator *ran2* [Press et al., 1992] a uniform distribution $0 \leq x \leq 1$ is generated and the corresponding ϕ-value calculated with $\phi = CDF^{-1}(x)$. For $\Psi = 0$, the CDF for a Compton polarimeter ($\Psi \to \Psi + {}^{\pi}\!/_2$) is reduced to:

$$CDF(\phi) = \frac{1}{2\pi}\Big(\phi - \frac{a}{2}\Big(\sin(2\phi)\Big)\Big) \tag{6.65}$$

Figure 6.22 shows different CDF's with a sample of corresponding event distributions for $N = 200$ events.

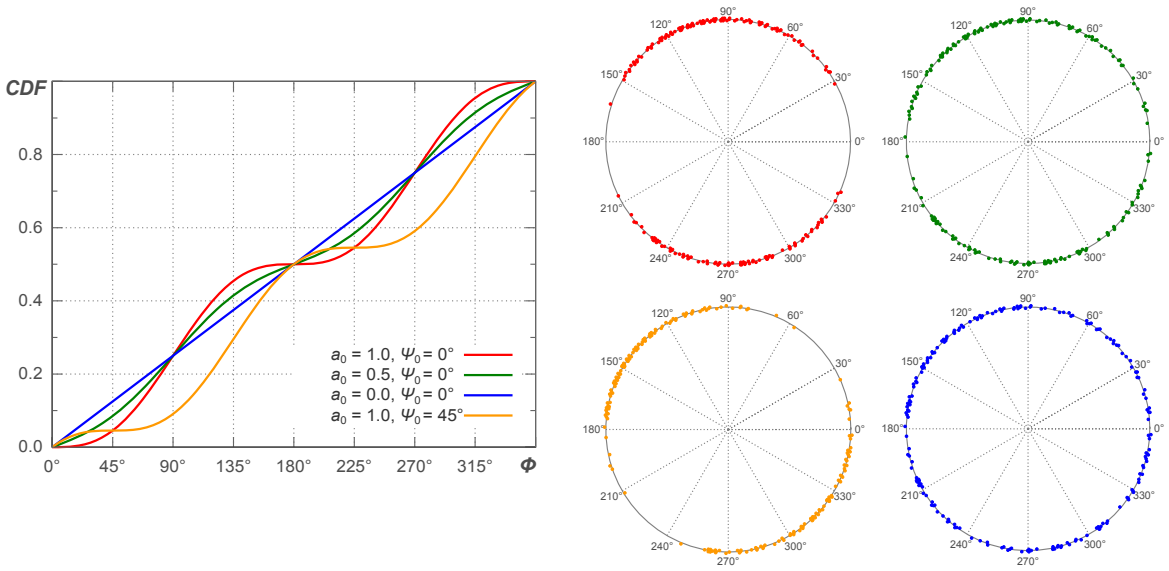

Figure 6.22. Left: cumulative distribution function of the event distribution of a Compton polarimeter for different modulation amplitudes a_0 and polarization angles Ψ_0. **Right:** Monte Carlo simulated event distribution for $N = 200$ events based on the equally colored distribution functions on the left.

Binning and fitting the event distribution

While the implementation for equal width binning is unambiguous in its working mechanism, the implementation of equal frequency binning is not obvious:

- The selection of the start- and endpoint of the binning intervals was considered in two ways. In a first implementation, the position of the counts defined the interval edges. Another idea is to take the center between two events as possible ends. The latter approach shows clearly better results for small event numbers N. Figure 6.23 explains why this makes a difference for locally enhanced event densities which are generated by chance: large gaps are split up to neighboring bins instead of contributing to only one bin.

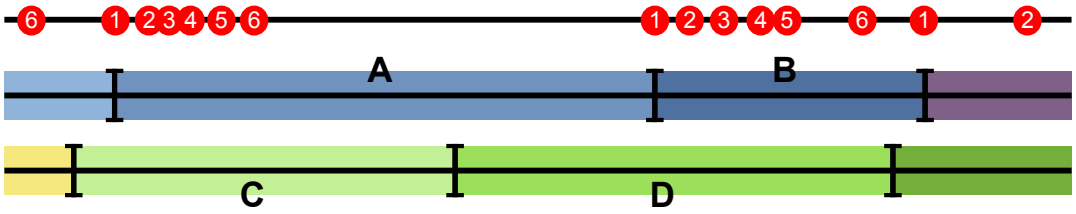

Figure 6.23. Overestimation of enhanced event densities: a random distribution of events (red dots) is binned with an equal number of $M = 6$ counts per bin. Taking the event positions as possible interval limits (bluish intervals, especially A and B) can result in more extreme bin densities (underestimation in A and overestimation in B) than choosing the center between two events as possible interval limits (greenish intervals, especially C and D).

- Because of the large intervals that can result with EFB it was considered not to take the center of an interval, but the event barycenter as position value of the corresponding bin. But, it turned out, that this degrades the efficiency of binning, so that the bin center was chosen as position value for EWB and EFB. The reason for this is possibly the same as before; an overestimation of enhanced event densities.

Equal width and equal frequency binning turns the observed events into a histogram that can be fitted to an appropriate modulation function f with a least-squares fitting routine [Markwardt, 2009]. The shape of f is related to Eq. (6.1):

$$f(\phi) = k\left(1 + c(M) \cdot a\, \cos(2(\phi - \Psi))\right) \tag{6.66}$$

Only the modulation amplitude a and the polarization angle Ψ are free fitting parameters. The constant of proportionality k, i.e. the mean of the distribution, is considered fixed. It is $k = N/M$ for EWB and $k = N/(2\pi)$ for EFB. The factor $c(M)$ corrects for the underestimation of the modulation amplitude a due to the roughness of binning. In this section, the emphasis is to explain the cause that enforces this correction while the calculation of $c(M)$ can be found in App. D.1.

The idea is to correct the binning related blurring of the amplitude. Figure 6.24 shows an example how binning of a peak-like distribution will reduce the observed amplitude. Surprisingly, the correction factor does not depend on the phase between bin and distribution; it is the same, even for non-central peak binning. For EWB, $c(M)$ can be expressed as:

$$c(M) = \frac{M}{2\pi} \sin\left(2\pi/M\right) \tag{6.67}$$

In the case of EFB, the variable bin width necessitates to calculate $c(M)$ individually for each bin.

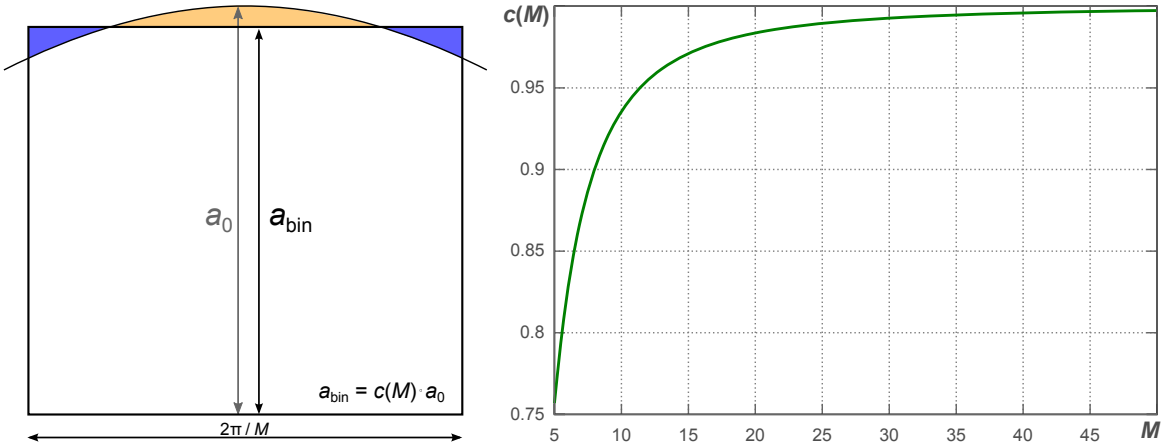

Figure 6.24. Binning reduced amplitude reduction. A sinusoidal distribution with true amplitude a_0 is reduced in amplitude due to binning so that the bluish and orange areas are equal. The right graph shows the reduction for equal width binning with $5 \leq M \leq 50$. See App. D.1 for more details.

The theoretical limits $0 \leq a \leq 1$ and $-\pi/2 < \Psi \leq \pi/2$ are not a good choice as parameter limits for the fitting routine. Because of the identity

$$a\cos(2(\phi - \Psi)) = -a\cos(2(\phi - \Psi \pm \pi/2)) \tag{6.68}$$

the fitting routine tries to choose in some cases negative a-values as best fitting parameters. The limitation $0 \leq a \leq 1$ does only result in the locally best estimator $a = 0$. Therefore, the parameter limitations were extended to negative a-values and enlarged in Ψ by $\pm\pi/2$:

$$-1 \leq a \leq 1 \quad \text{and} \quad -\pi < \Psi \leq \pi \tag{6.69}$$

After fitting, negative a-values are mirrored to positive ones and Ψ is shifted according to Eq. (6.68) so that finally $0 \leq a \leq 1$ and $-\pi/2 < \Psi \leq \pi/2$ holds. Figure 6.25 (EWB) and Fig. 6.26 (EFB) show binning and fitting results for the same samples that are shown in Fig. 6.22.

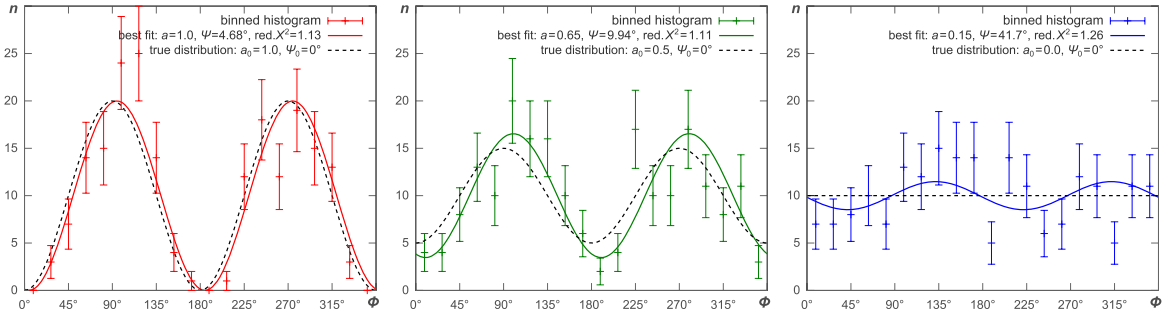

Figure 6.25. Equal width binning with 20 bins for different samples with $N = 200$ events. The color code is identical to the one in Fig. 6.22. The fitting results a and Ψ and the true values a_0 and Ψ_0 are shown in the corresponding legend. The restriction $a \leq 1$ explains the direct match for $a_0 = 1.0$ (left).

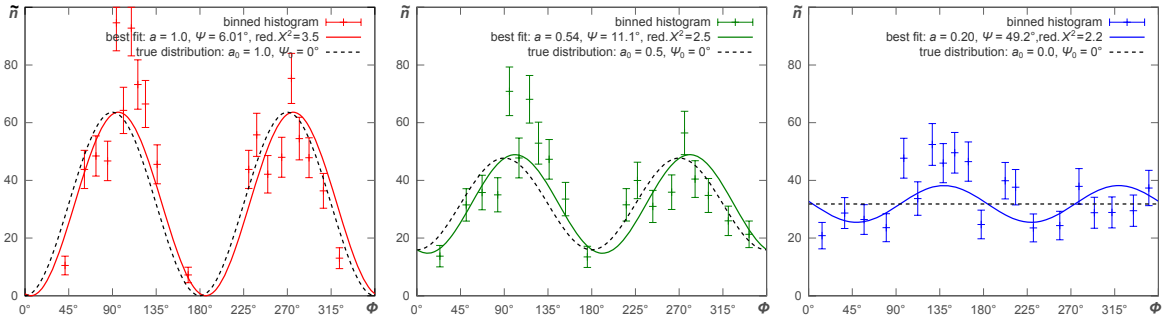

Figure 6.26. Equal frequency binning with 20 bins for different samples with $N = 200$ events. The color code is identical to the one in Fig. 6.22. The fitting results a and Ψ and the true values a_0 and Ψ_0 are shown in the corresponding legend. The restriction $a \leq 1$ explains the direct match for $a_0 = 1.0$ (left).

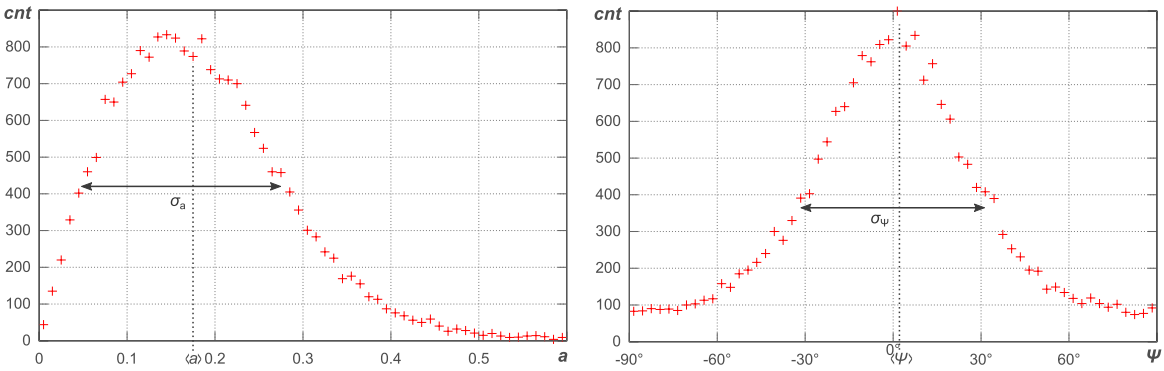

Figure 6.27. Distribution of observed a and Ψ for 20 000 samples with $a_0 = 0.1$, $\Psi_0 = 0°$, $N = 200$, and $M = 20$ for EWB. Both histograms are generated with a final binning of 60 bins in a or Ψ, respectively. The bias in the modulation amplitude (left) and the unbiased, symmetrical but non-Gaussian distribution of the polarization angle (right) are noticeable. The mean values $\langle a \rangle$ and $\langle \Psi \rangle$ and the corresponding standard deviations σ_a and σ_Ψ are the important values for the following steps of the simulation.

Finding the optimal number of bins M

The presented procedure of simulating, binning, and fitting results in observed parameters a and Ψ. Repeating this procedure several times gives a distribution of the observables, see Fig. 6.27 for 20 000 repetitions. To decide on the efficiency of the number of chosen bins M, the mean values $\langle a \rangle$ and $\langle \Psi \rangle$ and the corresponding standard deviations σ_a and σ_Ψ have to be calculated for each value of M. See Fig. 6.28 and 6.30 for $a_0 = 0.05$ and $N = 1000$ in the case of EWB or EFB, respectively. The optimal number of bins M_opt is the one that minimizes σ_a and σ_Ψ and that results in a bias of the modulation amplitude which is comparable with the one expected by the proposed estimators of Sect. 6.2.2.

Results

The simulation procedure of the last section is repeated for different sample sizes N and initial modulations a_0. Figures 6.29 and 6.31 show the estimated polarization and the number of bins M_opt for best binning performance. In the case of polarimetric analysis, equal frequency binning outperforms equal width binning in the following ways:

- The choice of M_opt is for EFB in general not so critical. The binning performance becomes only slightly worse for $M > M_\mathrm{opt}$.
- The distribution widths σ_a and σ_Ψ are slightly better for EFB than for EWB.
- For EFB, the bias in estimating p is distributed in a sharp way resembling the behavior of the mean-estimator (see Fig. 6.31). In contrast, the bias for EWB is distributed over a broad range and it is on average stronger than expected by all theoretical estimators (see Fig. 6.29).

Least square fits for M_opt are obtained for EWB and EFB in the range of the simulation parameters: $0 \leq a_0 \leq 0.5$ and $50 \leq N \leq 2000$. In the case of EWB, the square root like dependence $M_\mathrm{opt} \sim N^{0.5}$ for small values of a_0 and the more constant behavior at larger values of a_0 leads to:

$$\text{EWB:} \quad M_\mathrm{opt}(a_0, N) = 0.43 \cdot N^{0.5 - 0.41 a_0} + 4.78(1 - a_0) \tag{6.70}$$

In the case of EFB, a linear dependency $M_\mathrm{opt} \sim N$ is sufficient for $a_0 < 0.3$. For larger values of a_0 this linear approximation overestimates M_opt, which is fine as EFB has still very good performance if M is slightly larger than M_opt, see Fig. 6.30. A linear least square fit leads to:

$$\text{EFB:} \qquad M_\mathrm{opt}(N) = 0.0153 \cdot N + 24 \tag{6.71}$$

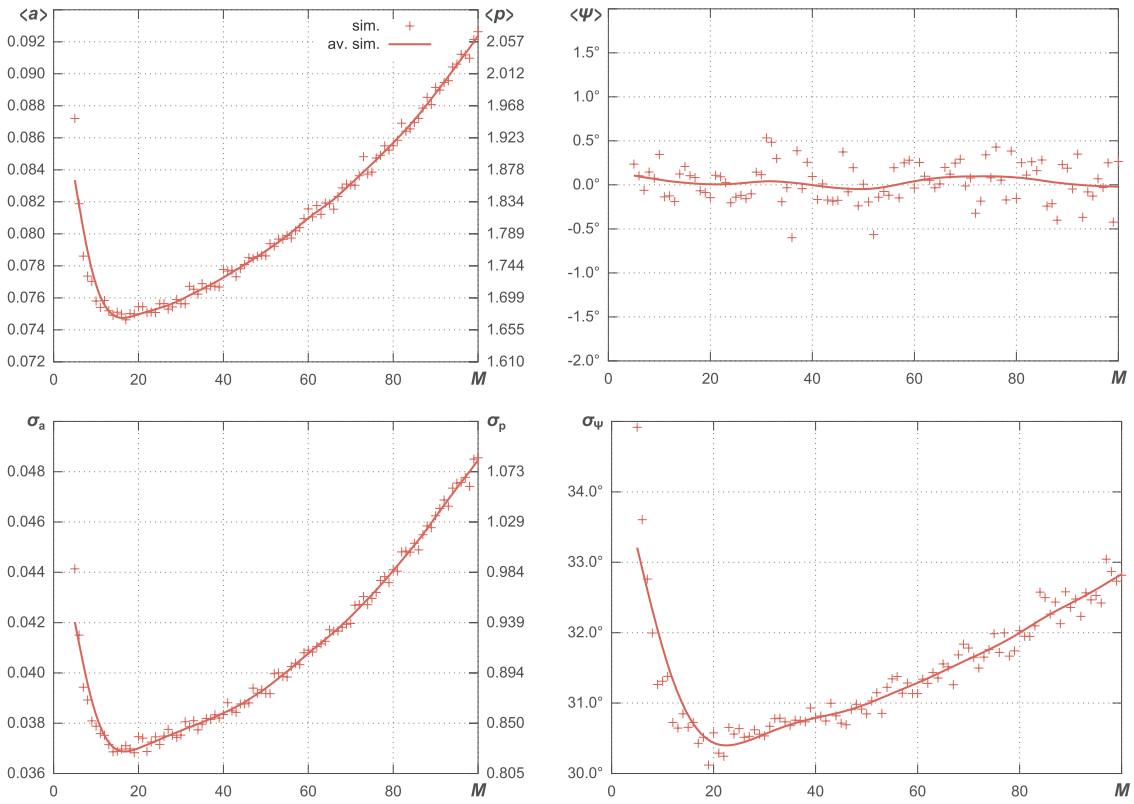

Figure 6.28. Simulated results for the modulation amplitude a and the polarization angle Ψ as function of the number of bins M in the case of equal width binning. The simulation parameters are: $N = 1000$ events, $a_0 = 0.05$ ($p_0 \approx 1.12$), and $\Psi_0 = 0°$. The simulated results are shown as crosses, which are averaged with a smoothing routine (solid line) for illustrative reasons. The optimal number of bins is $M_{\text{opt}} = 18$.

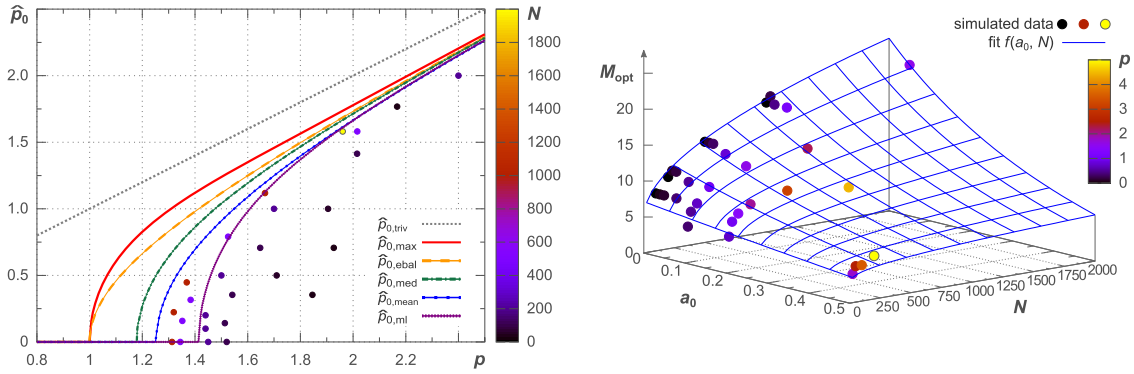

Figure 6.29. Performance of equal width binning.
Left: comparing the true and observed polarization shows, that the bias is, for a small number of events ($N \leq 200$), more prominent than expected by the estimators, which are presented in Sect. 6.2.2. For $p > 3$ the simulation results and the estimators approach each other with a difference of less than $\Delta p_0 = 0.15$ (not shown in this graph).
Right: the optimal number of bins M_{opt} depends on a_0 and N but not on p. A least square fit results in $M_{\text{opt}}(a_0, N) \approx 0.43N^{0.5-0.41a_0} + 4.78(1 - a_0)$.

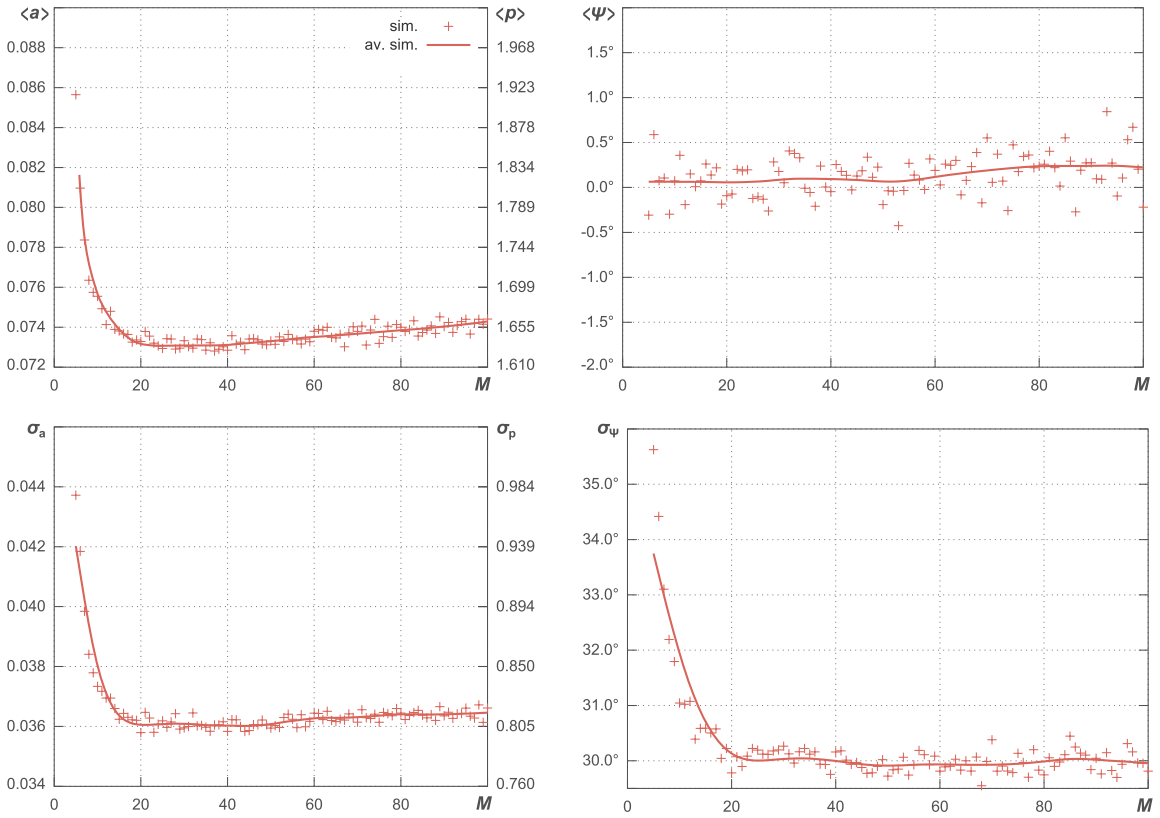

Figure 6.30. Simulated results for the modulation amplitude a and the polarization angle Ψ as function of the number of bins M in the case of equal frequency binning. The simulation parameters are: $N = 1000$ events, $a_0 = 0.05$ ($p_0 \approx 1.12$), and $\Psi_0 = 0°$. For more information, see Fig. 6.28. The optimal number of bins is $M_{\text{opt}} \approx 38$.

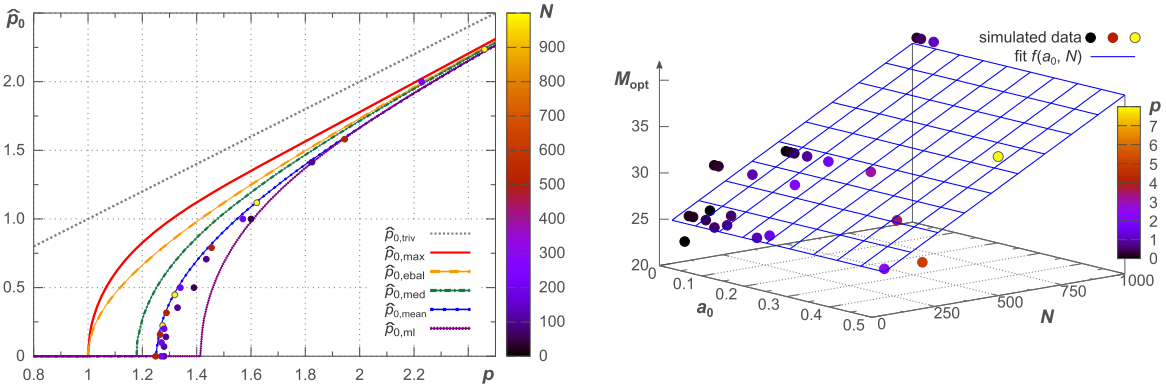

Figure 6.31. Performance of equal frequency binning
Left: the simulation results are in good agreement with the mean estimator. All simulations are color coded with the number of events N. The signal-to-noise ratio $p = a\sqrt{N/2}$ determines the bias independent of its constitution of a or N.
Right: as seen in Fig. 6.30 the performance of EFB is nearly constant over a wide range of M. M_{opt} is nearly independent of a_0 and a linear function of N. A least square fit results in: $M_{\text{opt}} \approx 0.0153N + 24$.

6.7. Summary

The working principle of a photoelectric or a Compton polarimeter is based on an azimuthal dependent cross section which results in an azimuthal dependent event density. The aim of the analysis of this event density is to estimate the true degree of polarization P_0 and the true angle of polarization Ψ_0. The biased and unsymmetrical distribution of P_0 and the unbiased, symmetrical, but non-Gaussian distribution of Ψ_0 requires a careful statistical treatment.

Frequentist and Bayesian statistics address two different points of view. A direct comparison of both methods is not reasonable because both methods result in different statements. To find the appropriate method for a given problem, one has to answer the question of whether the true values or the observables are known or unknown.

Because of the symmetric distribution of the observed angles of polarization Ψ around the true value Ψ_0, point estimations on Ψ_0 are trivial ($\hat{\Psi}_0 = \Psi$) for both approaches. With a frequentist approach, point and interval estimations on the true (signal-to-noise ratio of the) degree of polarization p_0 can be made on the basis of the observed degree of polarization p. But, for the angle of polarization, the frequentist approach allows only to conclude on interval estimations on Ψ_0 as a function of the true degree of polarization p_0, but not as function of the observed value p.

Bayesian statistics matches observational needs best. For observed signal-to-noise ratios p the estimator of best performance can be chosen directly. Point and interval estimations on p_0 and Ψ_0 as a function of p can be obtained with the tabulated values in App. C.2 - App. C.9 for $p < 6$. For large polarizations ($p > 6$), confidence and credibility intervals approach each other. Point and interval estimations on p_0 and Ψ_0 can be calculated by the approximations of Sect. 6.5.

Simulating the binning and fitting behavior shows that they can have a severe impact on the results of the analysis. Only equal frequency binning in combination with the event centered interval selection and the correction of the binning reduced amplitude, shows good agreement with the theoretical considerations of continuously distributed event densities. Applying other binning or fitting routines than the demonstrated, requires a thorough reconsideration of the statistical impacts.

7. Summary and outlook

The presented work shows the construction, the operation and the performance of a stacked detector system consisting of a silicon based active pixel matrix which serves as a low energy detector (LED) in combination with a cadmium telluride based Schottky diode detector which serves as a high energy detector (HED). Both detectors are pixelated semiconductor detectors with a pixel specific preamplification. The construction of the LED subsystem is to a large fraction an in-house development of the IAAT (Institute for Astronomy and Astrophysics Tübingen). Besides the detector control electronics, the signal digitization, the signal preprocessing, and the data transfer are newly developed and tested, which is done to a large fraction in the framework of this thesis.

The necessity of a pixel specific, non-linear energy calibration is observed for both detectors using the emission spectra of Fe-55 and Am-241. Besides an energy calibration that is based on cubic spline interpolation of the pulse-height-to-energy relation, an energy calibration via correlation was studied. Both methods show similar results applied to a calibration measurement with a high counting statistics but the correlation method is promising if the calibration spectrum has a low counting statistics. Because the calibration method uses not just the line position but the whole line shape, it is based on more information and can therefore handle lower counting statistics. Furthermore, it can be applied to the calibration of continuous emissions. Besides the similar pixel specific energy calibration needed for both detector systems, each detector has some characteristics that must be considered for its operation.

The LED uses a continuous readout of the detector matrix each 2.44 ms in combination with an event preprocessing electronics that reduces the high data rate that results because of the fast readout. The continuous operation allows to apply periodic signal discharges (signal clearing) resulting in a (relatively) constant offset level for each pixel. The pixel specific variation of the offset, the pixel noise is used to calculate pixel specific thresholds for the event recognition. This approach allows to optimize the tradeoff between rejecting noise and detecting all events or splits of events.

An exceptionally large amount of bad pixels makes it necessary to study the effects of bad pixels and possible analysis methods that reduce these effects. The detector settings (the offset map, the energy threshold map, and the bad pixel map) must be obtained via dark and flat-field measurements and must be uploaded to the preprocessing electronics for each operation of the LED. The spectral resolution of the LED is studied for different gains g_{CMX} of the signal amplifier and measured to $\Delta E = 168\,\mathrm{eV}$ (FWHM, at 5.9 keV; $g_{\mathrm{CMX}} = 100\,\%$) and $\Delta E = 342\,\mathrm{eV}$ (FWHM, at 59.5 keV; $g_{\mathrm{CMX}} = 21\,\%$). A systematic error in the energy calibration that could not be cancelled because of the limited number of emission lines of the calibration spectra is observed to be less than 100 eV for energies $E < 28.5\,\mathrm{keV}$.

In contrast to the LED, the HED is working with an event triggered pixel readout and can be operated directly after its power-on. The large amount of deep acceptor levels in CdTe result in a polarization effect of the CdTe crystal which redistributes the applied electric field inside the crystal and makes the signal generation near the cathode of the detector inefficient or even impossible. This crystal polarization is studied theoretically and experimentally and the time duration for stable detector operation as well as the spectroscopic effects of the crystal polarization are both well known. The critical factors for the stability of the HED operation are the crystal temperature and the applied electric field. The spectroscopic performance of the HED is measured with $\Delta E = 1023\,\mathrm{eV}$ (FWHM, at 59.5 keV); the systematic error in the energy calibration is less than 60 eV in the whole observed energy range $3\,\mathrm{keV} < E < 60\,\mathrm{keV}$.

The combined operation of the stacked detector system, i.e. the positioning of the LED in front of the HED, allows to study mutual influences between both subsystems which are mainly:

- an absorption effect in the HED spectrum at low energies
- the observation of Cd and Te fluorescence lines in the LED
- a small heating effect of both detectors that is observed with an increased offset and noise distribution in the LED

The Compton reprocessing is not observed, neither in the LED spectrum, nor in the HED spectrum. In the LED spectrum, the low energy detector noise blurs the prominent Compton edge and in the HED spectrum, the statistics of Compton scattered events, compared to all other events, is too low to be observed.

A detailed analytical and numerical calculation results in an expected efficiency to detect Compton forward scattered events, which peaks at roughly 60 keV with a value of 6.1 ‰: roughly 6 of 1000 photons that hit the LED are Compton scattered in the LED, not absorbed in the LED, directed into the HED, and detected by the HED. Fortunately, the other 994 events can be effectively filtered with an analysis that is restricted to time coincident events. The limiting factor for this reduction is the timing inaccuracy of the LED which is theoretically 2.44 ms and measured with 3 ms in the current configuration of the CANDELA setup.

Outlook

The identification of time coincident events between the LED and the HED defines the current status of the CANDELA setup. An extended statistics is necessary to observe and study the proposed analysis methods of the stacked setup experimentally. The possible applications are:

- the suppression of fluorescence lines in the LED and of escape lines in the HED
- the application as a Compton camera
- the application as a Compton polarimeter

An operation of the CANDELA setup as a Compton camera is possible in the current configuration. Compton scattered, time coincident events can be analyzed to conclude on their origin. To measure the LED and the HED spectrum of Compton scattered events and to compare it with the expected spectral distributions can serve as a first test of this analysis mode. Furthermore, the spatial resolution of the Compton camera can be studied in all three dimensions. Because of the combined analysis of two detector events, the uncertainty of such a position reconstruction is non-trivial and depends on the spectral and the spatial resolution of both detectors. The theoretical derivation of point and interval estimations for the position reconstruction of a Compton camera and the comparison to experimental observations are challenging goals for further investigations.

In order to test the application of the CANDELA setup as a Compton polarimeter, polarized radiation—with a variable degree and angle of polarization—could be produced via scattering of Am-241 (59.5 keV) or Co-57 (122 keV) emission lines. The detection efficiency and the modulation factor can be measured for different distances between both detectors while observing the mutual influences between the LED and the HED carefully. The modulation factor is expected to $\mu_{\max} = 73\,\%$ for an intended detector distance of 2 mm. The analysis of the measurements will be straightforward because the binning and fitting routines are tested via simulations, and the calculated point and interval estimations can be applied directly via their parametric descriptions.

Acknowledgements

"Knowledge is in the end based
on acknowledgement."

(Ludwig Wittgenstein)

I always felt comfortable at the IAAT and want to thank all my colleagues for the warm working atmosphere during the last years. Special thanks goes to all people that helped me to build the CANDELA setup, especially

Prof. Dott. Andrea Santangelo, for the opportunity to do this thesis and his trust in my work. It was his sparkling way of teaching astrophysics that wakens my interest to this field.

Dr. Chris Tenzer, for the stimulating discussions about all the different physical topics that came up during this work; especially for his disagreements, that made me often to reconsider.

Thomas Schanz, for his inspiring work ethic which is based on three things: quality, quality, quality. Thanks also for the many interesting discussions during lunch.

Jürgen Dick, for the fruitful discussions on electronics.

Jurek Loebell, for his nice work on the ADC of the LED.

Henning Wende, for his collaborative work for the Sensapolis, the nice vacations in Poland, and for all his useful PC tricks that mostly started with "In der c't war neulich ein Artikel über...".

Sabina Pürckhauer, for her work on Geant4 simulations of the CANDELA setup. The comparisons of our results showed me the usefulness of Geant4.

The groups at the MPI HLL and at the CEA² that produced the LED and the HED, respectively.

Der Werkstattgruppe, insbesondere Herrn Renner und Herrn Gäbele für die Vielzahl an angefertigten Bauelementen, aus denen CANDELA letztendlich besteht und für ihre Geduld, wenn im Nachhinein doch nochmals alles anders sein sollte.

Meinen Eltern, für ihre bedingungslose Unterstützung während der ganzen Zeit.

Meinen Freunden, für eine abwechslungsreiche Freizeit, in der ich genügend Kraft für diese Arbeit sammeln konnte.

A. Klein-Nishina formula in polar coordinates

The differential cross-section $\frac{\mathrm{d}\sigma}{\mathrm{d}\Omega}$ for Compton scattering is originally described by Klein and Nishina [1929]:

$$\frac{\mathrm{d}\sigma}{\mathrm{d}\Omega} = \frac{1}{4}\mathrm{r_e^2}\left(\frac{k(\theta)}{k_0}\right)^2\left(\frac{k(\theta)}{k_0} + \frac{k_0}{k(\theta)} - 2 + 4\cos^2(\Theta)\right) \tag{A.1}$$

All variables with the index 0 refer to the incident photon and all variables without an index refer to the scattered photon. $\mathrm{r_e}$ represents the classical electron radius, k the energy and $\vec{k}$ the direction of the photons. θ is the scattering angle between $\vec{k}_0$ and $\vec{k}$. ϕ is the azimuthal scattering angle between the electric field of the incident photon and the direction of the scattered photon.
The polarization of the photon is described by $\vec{e}_0$ and $\vec{e}$. Θ is the angle between the two photon polarizations $\vec{e}_0$ and $\vec{e}$. It is convenient to split the scattered photon into a perpendicular part with $\vec{e} \perp \vec{e}_0$ so that $\Theta = 90°$ and a parallel part with ($\vec{k}_0$, $\vec{e}_0$, $\vec{k}$, $\vec{e}$) lying in the same plane, see [Heitler, 1954, § 22.4]. The cross-section is split in the same way, so that $\sigma = \sigma_\perp + \sigma_\parallel$.

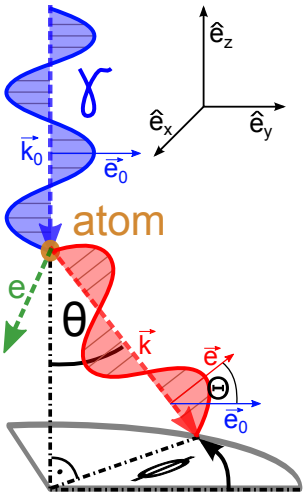

Assertion: in the parallel part (if $\vec{e}$ is in the ($\vec{k}$, $\vec{e}_0$) plane) it is:

$$\cos^2(\Theta) = 1 - \sin^2(\theta)\cos^2(\phi) \tag{A.2}$$

Proof: without loss of generality we assume the origin of the coordinate system at the place of interaction and orientate it so that: $\vec{e}_0 = \hat{e}_y$
With $\vec{k} = \begin{pmatrix}\sin(\theta)\sin(\phi)\\ \sin(\theta)\cos(\phi)\\ -\cos(\theta)\end{pmatrix}$ the ($\vec{k}$, $\vec{e}_0$) plane E can be described as

$$\mathrm{E}: \begin{pmatrix}x\\ y\\ z\end{pmatrix} \cdot \begin{pmatrix}\cos(\theta)\\ 0\\ \sin(\theta)\sin(\phi)\end{pmatrix} = 0 \tag{A.3}$$

Because $\vec{e} \in \mathrm{E}$ and $\vec{e} \perp \vec{k}$

$$\begin{pmatrix} e_x \\ e_y \\ e_z \end{pmatrix} \cdot \begin{pmatrix} \cos(\theta) \\ 0 \\ \sin(\theta)\sin(\phi) \end{pmatrix} = 0 \tag{A.4}$$

$$\begin{pmatrix} e_x \\ e_y \\ e_z \end{pmatrix} \cdot \begin{pmatrix} \sin(\theta)\sin(\phi) \\ \sin(\theta)\cos(\phi) \\ -\cos(\theta) \end{pmatrix} = 0 \tag{A.5}$$

This can be solved to

$$\vec{e} = \begin{pmatrix} \sin^2(\theta)\ \sin(\phi)\ \cos(\phi) \\ -\sin^2(\theta)\ \sin^2(\phi) - \cos^2(\theta) \\ -\sin(\theta)\ \cos(\theta)\ \cos(\phi) \end{pmatrix} \tag{A.6}$$

Using the identity $\sin^2(x) + \cos^2(x) = 1$ multiple times, we get the norm of $\vec{e}$

$$|\vec{e}| = \sqrt{e_x^2 + e_y^2 + e_z^2} \tag{A.7}$$

$$= ... \tag{A.8}$$

$$= \sqrt{\sin^4(\theta)\sin^2(\phi) + \cos^2(\theta) + \sin^2(\theta)\cos^2(\theta)\sin^2(\phi)} \tag{A.9}$$

$$= \sqrt{\sin^2(\theta)\ \sin^2(\phi) + \cos^2(\theta)} \tag{A.10}$$

Finally, with the definition of the scalar product

$$\cos(\Theta) = \frac{|\vec{e} \cdot \vec{e}_0|}{|e| \cdot |e_0|} \tag{A.11}$$

$$= \frac{\sin^2(\theta)\ \sin^2(\phi) + \cos^2(\theta)}{\sqrt{\sin^2(\theta)\ \sin^2(\phi) + \cos^2(\theta)}} \tag{A.12}$$

$$\cos^2(\Theta) = \sin^2(\theta)\ \sin^2(\phi) + \cos^2(\theta) \tag{A.13}$$

$$= \sin^2(\theta)\ \sin^2(\phi) + 1 - \sin^2(\theta) \tag{A.14}$$

$$= 1 - \sin^2(\theta)\left(1 - \sin^2(\phi)\right) \tag{A.15}$$

$$= 1 - \sin^2(\theta)\cos^2(\phi) \qquad \text{q.e.d.} \tag{A.16}$$

The Klein-Nishina formula is then

$$\frac{\mathrm{d}\sigma}{\mathrm{d}\Omega} = \frac{\mathrm{d}\sigma_\parallel}{\mathrm{d}\Omega} + \frac{\mathrm{d}\sigma_\perp}{\mathrm{d}\Omega} \tag{A.17}$$

$$= \frac{1}{4}\mathrm{r_e^2}\left(\frac{k(\theta)}{k_0}\right)^2 \left(\frac{k(\theta)}{k_0} + \frac{k_0}{k(\theta)} + 2 - 4\sin^2(\theta)\cos^2(\phi) + \frac{k(\theta)}{k_0} + \frac{k_0}{k(\theta)} - 2\right) \tag{A.18}$$

$$= \frac{1}{2}\mathrm{r_e^2}\left(\frac{k(\theta)}{k_0}\right)^2 \left(\frac{k(\theta)}{k_0} + \frac{k_0}{k(\theta)} - 2\sin^2(\theta)\cos^2(\phi)\right) \tag{A.19}$$

B. LED start routine

1. Start piston pump
2. If $P \leq 6\,\text{mbar}$ start turbo molecular pump
3. If $P \leq 10^{-5}\,\text{mbar}$ start cooling
4. If $T_{\text{cooling mask}} \leq -50°\text{C}$ start LED:
   a) Turn on all power supplies
   b) Start PC
   c) Turn on V_SEQ, V_bst, V_AIT_PP, VDD(D,T), VSS(D,T), VSS(ADC), Vref
   d) Start Idef-X batch 1
   e) Send w_cmx_status
   f) Send w_cmx_memo
   g) Send w_cmx_upload
   h) Turn on VDDF, Vext, SW GATE, SW CLEAR, Vdrain, Vback
   i) Send w_sw_status
   j) Send w_sw_hreset
   k) Send w_sw_upload
   l) Turn on SW GATE high, SW CLEAR high
   m) Send w_sw_reset
   n) Send w_epp_byp
   o) Send w_epp_run
   p) Send w_seq_run
   q) Turn on VGon, VGoff, VCGon, VCGoff, VCon, VCoff
   r) Wait approximately 3 hours for temperature stability
   s) Send w_ifc_re_ns → dark frames
   t) Send ONE-maps
   u) Send w_epp_not_bypass
   v) Send w_epp_run
   w) Send w_ifc_re_ns → flat-field data or scientific data

C. Least square fits

C.1. Estimated polarization $\hat{p}_0(p)$ (Fig. 6.6)

Table C.1. The listed estimators are fitted to Eq. (C.1). $|\Delta_{\max}|$ is the maximal difference between the calculated values and the corresponding fitting function for $0 \leq p \leq 6$.

estimator	p_{crit}	a	b	c	d	$\lvert\Delta_{\max}\rvert$
$\hat{p}_{0,\,\text{max}}$	1.000	0.80	0.300	1.180	-1.196	0.0730
$\hat{p}_{0,\,\text{med}}$	1.180	0.70	0.365	1.170	-1.070	0.0224
$\hat{p}_{0,\,\text{mean}}$	1.250	0.526	0.521	1.178	-1.025	0.0300
$\hat{p}_{0,\,\text{ml}}$	1.414	0.58	0.300	1.147	-0.836	0.0832

$$\begin{aligned} \hat{p}_0(p) &= 0 && p \leq p_{\text{crit.}} \\ \hat{p}_0(p) &\approx (p - p_{\text{crit}})^a + (p - p_{\text{crit}})^b + (p - p_{\text{crit}})^c - d(p - p_{\text{crit}}) && p > p_{\text{crit}} \end{aligned} \tag{C.1}$$

C.2. Regions of best estimator performance as function of p_0 (Fig. 6.7)

Table C.2. Best estimated bias calculated with the frequentist approach.

estimator	p_{start}	p_{stop}
$\hat{p}_{0,\,\text{ml}}$	0.000	0.849
$\hat{p}_{0,\,\text{mean}}$	0.849	1.039
$\hat{p}_{0,\,\text{med}}$	1.039	1.332
$\hat{p}_{0,\,\text{ebal}}$	1.332	1.918
$\hat{p}_{0,\,\text{max}}$	1.918	∞

Table C.3. Best estimated MSE calculated with the frequentist approach.

estimator	p_{start}	p_{stop}
$\hat{p}_{0,\,\text{ml}}$	0.000	0.505
$\hat{p}_{0,\,\text{mean}}$	0.505	0.685
$\hat{p}_{0,\,\text{ebal}}$	0.685	1.000
$\hat{p}_{0,\,\text{triv}}$	1.000	∞

C.3. Optimal $\lambda(p_0)$ (Fig. 6.9)

$$\begin{aligned} \lambda_{1,\text{fit}}(p_0) &= 0.115\,(3.30 + \tanh\,(1.40(p_0 - 1.40))) && p \leq 1 && \chi^2_{\text{red}} = 1.2 \cdot 10^{-6} \\ \lambda_{2,\text{fit}}(p_0) &= 0.198\,(1.51 + \tanh\,(1.24(p_0 - 1.85))) && p > 1 && \chi^2_{\text{red}} = 3.8 \cdot 10^{-8} \\ \lambda_{3,\text{fit}}(p_0) &= 0.244\,(1.02 + \tanh\,(1.35(p_0 - 2.67))) && p \leq 1.41 && \chi^2_{\text{red}} = 1.7 \cdot 10^{-10} \end{aligned}$$

C.4. Confidence intervals $\Delta p_0(p)$ (Fig. 6.11)

Lower and upper limits for σ_1, σ_2, and σ_3 confidence intervals are presented in Fig. 6.11. A functional description for the tangential construction method is obtained by fitting the function

$$f(p) = Ap^B - Cp^{-D} + Ep \tag{C.2}$$

to the computed data points with the least square method. The results are listed in Tab. C.4.

Table C.4. Fitting results of Eq. (C.2) for the lower and upper confidence interval limits for the degree of polarization. See also Fig. 6.11. The deviation between the numerically calculated data points and f is maximal ± 0.05. $f = 0$ for all undefined regions with $p < 6$.

f	A	B	C	D	E	validity
$\underline{p_1}(p)$	-1.17	0.027	5413	23.63	1.018	$1.51 \leq p \leq 6$
$\underline{p_2}(p)$	-1.86	0.192	1.0e5	13.58	1.083	$2.50 \leq p \leq 6$
$\underline{p_3}(p)$	-2.72	0.085	1.0e7	13.94	1.018	$3.41 \leq p \leq 6$
$\overline{p_1}(p)$	1.691	1.000	0.000	0.000	0.000	$0 \leq p \leq 0.77$
	0.715	0.328	0.021	4.766	0.936	$0.77 < p \leq 6$
$\overline{p_2}(p)$	5.441	1.000	0.000	0.000	0.000	$0 \leq p \leq 0.22$
	1.741	0.083	0.027	1.913	0.980	$0.22 < p \leq 6$
$\overline{p_3}(p)$	22.86	1.000	0.000	0.000	0.000	$0 \leq p \leq 0.065$
	4.621	-0.19	1.937	0.435	1.091	$0.065 < p \leq 6$

C.5. Optimal $\lambda(p)$ (Fig. 6.17)

$$\begin{aligned}
\lambda_{1,\mathrm{fit}}(p_0) &= 0 && p \leq 1.7 \\
&= 1.67x^{-0.9675} - 11.83x^{-4.655} && 1.7 < p \leq 2.6 \quad \chi^2_{\mathrm{red}} = 1.1 \cdot 10^{-5} \\
&= 92.9x^{-6.536} - 387x^{-8.182} + 0.5 && p > 2.6 \quad \chi^2_{\mathrm{red}} = 8.0 \cdot 10^{-7} \\
\lambda_{2,\mathrm{fit}}(p_0) &= 0 && p \leq 2.5 \\
&= 83.8x^{-3.277} - 297x^{-4.655} && 2.5 < p < 3.1 \quad \chi^2_{\mathrm{red}} = 1.6 \cdot 10^{-4} \\
&= 307x^{-6.856} - 20903x^{-10.72} + 0.5 && 2.5p > 1 \quad \chi^2_{\mathrm{red}} = 3.7 \cdot 10^{-6} \\
\lambda_{3,\mathrm{fit}}(p_0) &= 0 && p \leq 3.4 \\
&= 25073x^{-6.562} - 148981x^{-8.001} && 3.4 < p < 4 \quad \chi^2_{\mathrm{red}} = 6.9 \cdot 10^{-5} \\
&= 2.37{\cdot}10^7 x^{-12.817} - 1.78{\cdot}10^8 x^{-14.332} + 0.5 && p > 3.4 \quad \chi^2_{\mathrm{red}} = 2.7 \cdot 10^{-6}
\end{aligned}$$

C.6. Credibility intervals $\Delta p_0(p)$ (Fig. 6.18)

Calculated lower and upper limits for of σ_1, σ_2, and σ_3 credibility intervals are presented in Fig. 6.18. A functional description is obtained by fitting the function

$$f(p) = Ap^B - Cp^{-D} + Ep \tag{C.3}$$

to the computed data points with the least square method. The results are listed in Tab. C.5.

Table C.5. Fitting results of Eq. (C.3) for the lower and upper credibility interval limits for the degree of polarization. See also Fig. 6.18. The deviation between the numerically calculated data points and the fit f is maximal ± 0.025. $p < 6$ for all cases and $f = 0$ for all remaining undefined regions.

f	A	B	C	D	E	validity
$\underline{p_1}(p)$	4.241	1.021	2.286	1.134	-3.535	$p \geq 1.72$
$\underline{p_2}(p)$	0.468	1.177	3.974	0.874	0.145	$p \geq 2.54$
$\underline{p_3}(p)$	1.327	1.121	7.599	1.131	-1.00	$p \geq 3.45$
$\overline{p_1}(p)$	0.292	2.063	-1.00	0.000	0.000	$p \leq 1.72$
	0.855	0.020	17.87	6.012	1.009	$p > 1.72$
$\overline{p_2}(p)$	1.819	1.185	-2.00	0.000	-1.345	$p \leq 2.54$
	1.910	-0.028	13794	11.21	1.018	$p > 2.54$
$\overline{p_3}(p)$	0.564	1.632	-3.00	0.000	0.000	$p \leq 1.40$
	1.058	1.000	-2.47	0.000	0.00	$1.4 < p \leq 3.5$
	4.130	-0.38	2.0e5	10.65	1.140	$p > 3.50$

C.7. Confidence intervals for $\Delta\Psi_0(p_0)$ (Fig. 6.13)

$$\sigma_{1,\text{fit}}(p_0) = 47.38(1.27 + \tanh(-0.77(p_0 - 0.05))) - 1.42\,p_0 \qquad \chi^2_{\text{red}} = 0.062$$

$$\sigma_{2,\text{fit}}(p_0) = 31.21\,(1.84 + \tanh\,(-1.15(p_0 - 1.48))) - 2\,p_0^{1.2} \qquad \chi^2_{\text{red}} = 0.346$$

$$\sigma_{3,\text{fit}}(p_0) = 28.97\,(2.10 + \tanh\,(-6.56(p_0^{0.4} - 1.44))) - 0.86\,p_0^{1.7} \qquad \chi^2_{\text{red}} = 0.227$$

C.8. Regions of best estimator performance as function of p (Fig. 6.16)

Table C.6. Best estimated bias calculated with the Bayesian approach.

estimator	p_{start}	p_{stop}
$\hat{p}_{0,\,\text{ml}}$	0.000	1.706
$\hat{p}_{0,\,\text{mean}}$	1.706	2.260
$\hat{p}_{0,\,\text{med}}$	2.260	2.832
$\hat{p}_{0,\,\text{ebal}}$	2.832	3.779
$\hat{p}_{0,\,\text{max}}$	3.779	∞

Table C.7. Best estimated MSE calculated with the Bayesian approach.

estimator	p_{start}	p_{stop}
$\hat{p}_{0,\,\text{ebal}}$	0.000	1.807
$\hat{p}_{0,\,\text{triv}}$	1.807	∞

C.9. Credibility intervals for $\Delta\Psi_0(p)$ (Fig. 6.19)

Calculated lower and upper limits for σ_1, σ_2, and σ_3 credibility intervals are presented in Fig. 6.19. A functional description is obtained by fitting the function

$$g(p) = A\left(B + \tanh\Big(C\,(D-p)\Big)\right) - Ep \quad \Big[\text{in deg.}\Big] \tag{C.4}$$

to the computed data points with the least square method.

Table C.8. Fitting results of Eq. (C.4) for the lower and upper credibility interval limits for the angle of polarization. See also Fig. 6.19. The deviation between the numerically calculated data points and g is maximal $\pm 1.7°$.

g	A	B	C	D	E	validity
$\sigma_1(p)$	32.50	1.350	0.739	0.801	1.154	$0.0 < p \leq 6.0$
$\sigma_2(p)$	65.65	0.323	0.858	2.688	0.000	$0.0 < p \leq 2.2$
	517	1.044	0.806	0.015	2.186	$2.2 < p \leq 6.0$
$\sigma_3(p)$	62.88	0.423	1.385	3.546	0.000	$0.0 < p \leq 3.2$
	102	1.380	1.327	2.506	3.958	$3.2 < p \leq 6.0$

D. Calculations

D.1. Correcting the binning reduced amplitude (Sect. 6.6.2)

Without loss of generality, $\Psi = 0$ is assumed. The azimuthal event density of Eq. (6.1), adjusted to equal width or equal frequency binning by $k = N/M$ or $k = N/(2\pi)$, respectively, becomes then

$$f(\phi) = k(1 + a \cdot \cos(2\phi)). \tag{D.1}$$

The idea of averaging is to set the integral of the function f equal to a rectangle of constant height $\overline{f}$. This way, averaging f at the location ϕ_0 over an interval $\Delta\phi$ becomes

$$\begin{aligned}
\overline{f} \cdot \Delta\phi &= \int_{\phi_0 - \Delta\phi/2}^{\phi_0 + \Delta\phi/2} f(\phi)\,\mathrm{d}\phi && \text{(D.2)}\\
&= k\left(\Delta\phi + a\Big[0.5\sin(2\phi)\Big]_{\phi_0 - \Delta\phi/2}^{\phi_0 + \Delta\phi/2}\right) && \text{(D.3)}\\
&= k\left(\Delta\phi + a/2\Big\{\sin(\Delta\phi + 2\phi_0) - \sin(-\Delta\phi + 2\phi_0)\Big\}\right) && \text{(D.4)}\\
&= k\left(\Delta\phi + a/2\Big\{\sin(\Delta\phi + 2\phi_0) + \sin(\Delta\phi - 2\phi_0)\Big\}\right) && \text{(D.5)}\\
&= k\Big(\Delta\phi + a/2\Big\{\sin(\Delta\phi)\cos(2\phi_0) + \cos(\Delta\phi)\sin(2\phi_0) + \\
&\qquad\qquad \sin(\Delta\phi)\cos(2\phi_0) - \cos(\Delta\phi)\sin(2\phi_0)\Big\}\Big) && \text{(D.6)}\\
&= k\Big(\Delta\phi + a \cdot \sin(\Delta\phi)\cos(2\phi_0)\Big) && \text{(D.7)}\\
\overline{f} &= k\Big(1 + a\frac{\sin(\Delta\phi)}{\Delta\phi}\cos(2\phi_0)\Big) && \text{(D.8)}
\end{aligned}$$

Comparing Eq. (D.8) with Eq. (D.1) shows, that the averaged (binned) amplitude of the event density function is reduced compared to the continuous density function. This binning reduced amplitude can be modeled with an additional factor $c(\Delta\phi)$:

$$f(\phi) = k(1 + c(\Delta\phi) \cdot a \cdot \cos(2\phi)) \tag{D.9}$$

$$c(\Delta\phi) = \frac{\sin(\Delta\phi)}{\Delta\phi}. \tag{D.10}$$

For equal width binning $\Delta\phi = \frac{2\pi}{M}$. For equal frequency binning $\Delta\phi$ is not constant and must be calculated for each bin individually.

D.2. Trammell-Walter equation 1 (Eq. 1.26)

The relation between the charge collection efficiency CCE and the absorption depth z can be calculated on the basis of the Hecht equation (Eq. (1.20)). Because of $L_\mathrm{e} \to \infty$ it is sufficient to develop $\exp\left(-\frac{(d-z_0)}{L_\mathrm{e}}\right)$ to the first order. $\exp\left(-\frac{z_0}{L_\mathrm{h}}\right)$ is expanded to the second order.

$$\begin{aligned} CCE(z_0) &= \frac{L_\mathrm{e}}{d}\left(1-\mathrm{e}^{-\frac{(d-z_0)}{L_\mathrm{e}}}\right)+\frac{L_\mathrm{h}}{d}\left(1-\mathrm{e}^{-\frac{z_0}{L_\mathrm{h}}}\right) \\ &\Rightarrow \frac{L_\mathrm{e}}{d}\left(1-\left[1-\frac{d-z_0}{L_\mathrm{e}}\right]\right)+\frac{L_\mathrm{h}}{d}\left(1-\left[1-\frac{z_0}{L_\mathrm{h}}+\frac{1}{2}\left(\frac{z_0}{L_\mathrm{h}}\right)^2\right]\right) \\ &= \frac{L_\mathrm{e}}{d}\left(\frac{d-z_0}{L_\mathrm{e}}\right)+\frac{L_\mathrm{h}}{d}\left(\frac{z_0}{L_\mathrm{h}}-\frac{1}{2}\left(\frac{z_0}{L_\mathrm{h}}\right)^2\right) \\ &= 1-\frac{z_0^2}{2\,d\,L_\mathrm{h}} \end{aligned} \tag{D.11}$$

The relative pulse height equals the charge collection efficiency $h \equiv CCE$ if noise is neglected. The inverse of Eq. (D.11) becomes

$$z_0(h) = \sqrt{2\,d\,L_\mathrm{h}\,(1-h)} \tag{D.12}$$

D.3. Trammell-Walter equation 2 (Eq. 1.27)

Beer's law expressed as probability distribution

$$\rho_\mathrm{abs}(z) = \mu\,\mathrm{e}^{-\mu\,z} \tag{D.13}$$

is normalized for all absorption depths $0 \le z < \infty$:

$$\int_0^\infty \mu \mathrm{e}^{-\mu\,z}\,\mathrm{d}z = 1 \tag{D.14}$$

Equation (D.14) states that a photon must be absorbed anywhere in a (infinitely thick) medium. If Beer's law is expressed as a function of the relative pulse height h

$$\rho_\mathrm{abs}(h) = \mu\,\mathrm{e}^{-\mu\,\sqrt{2\,d\,L_\mathrm{h}\,(1-h)}} \tag{D.15}$$

it must be renormalized.

$$\int_{h_\mathrm{min}}^{h_\mathrm{max}} \mu\,\mathrm{e}^{-\mu\,\sqrt{2\,d\,L_\mathrm{h}\,(1-h)}}\,\mathrm{d}h = \tilde{n} \neq 1 \tag{D.16}$$

The highest possible relative pulse height is $h_\mathrm{max} = 1$ (absorption close to the cathode). The lowest possible relative pulse height h_min (absorption close to the anode) is defined

by the detector thickness $z_0 = d$. With Eq. (D.12) it is

$$z_0(h_{\min}) = \sqrt{2\,d\,L_\mathrm{h}\,(1-h_{\min})} \stackrel{!}{=} d \tag{D.17}$$

$$h_{\min} = 1 - \frac{d}{2\,L_\mathrm{h}} \tag{D.18}$$

With $a = \mu\sqrt{2\,d\,L_\mathrm{h}}$ the normalization factor $1/\tilde{n}$ is:

$$\tilde{n} = \int_{h_{\min}}^{1} \mu \exp\Big(-\mu\sqrt{2\,d\,L_\mathrm{h}(1-h)}\Big)\,\mathrm{d}h \tag{D.19}$$

$$\tilde{n} = \int_{h_{\min}}^{1} \mu \exp\big(-a\sqrt{1-h}\big)\,\mathrm{d}h \tag{D.20}$$

Substitute: $H = -a\sqrt{1-h} \Rightarrow \frac{\mathrm{d}H}{\mathrm{d}h} = \frac{a}{2\sqrt{1-h}} \Rightarrow \mathrm{d}h = -\frac{2H}{a^2}\,\mathrm{d}H$
The integration limits become: $h_{\min} \to -a\sqrt{\frac{d}{2\,L_\mathrm{h}}} = -\mu\,d$ and $1 \to 0$

$$\tilde{n} = -\frac{2\mu}{a^2}\int_{-b}^{0} H\exp(H)\,\mathrm{d}H \tag{D.21}$$

$$= -\frac{2\mu}{a^2}\left\{\Big[H\mathrm{e}^H\Big]_{-b}^{0} - \int_{-\mu\,d}^{0}\mathrm{e}^H\,\mathrm{d}H\right\} \tag{D.22}$$

$$= -\frac{2\mu}{a^2}\Big\{\left(\mu\,d\,\mathrm{e}^{-\mu\,d}\right) - \left(1-\mathrm{e}^{-\mu\,d}\right)\Big\} \tag{D.23}$$

$$= \frac{2\mu}{a^2}\Big\{1 - \mathrm{e}^{-\mu\,d} - \mu\,d\,\mathrm{e}^{-\mu\,d}\Big\} \tag{D.24}$$

D.4. The input-output ratio λ for TRM (Eq. 1.41)

$$\begin{aligned}
F_0 &= F_1 + 2\,F_2 + 3\,F_3 + 4\,F_4 + \ldots \\
&= \left(\mathrm{e}^{-\lambda} + 2\,\lambda\mathrm{e}^{-\lambda} + 3\,\frac{\lambda^2}{2}\mathrm{e}^{-\lambda} + 4\,\frac{\lambda^3}{6}\mathrm{e}^{-\lambda} + \ldots\right)\cdot R_\mathrm{trig} \\
&= \mathrm{e}^{-\lambda}\left(1 + 2\,\lambda + \frac{3\lambda^2}{2} + \frac{4\lambda^3}{6} + \ldots\right)\cdot R_\mathrm{trig} \\
&= \mathrm{e}^{-\lambda}\Bigg(\underbrace{1 + \lambda + \frac{\lambda^2}{2} + \frac{\lambda^3}{6}}_{\mathrm{e}^{\lambda}} + \ldots + \underbrace{\lambda + \frac{2\lambda^2}{2} + \frac{3\lambda^3}{6}\ldots}_{\lambda\cdot\mathrm{e}^{\lambda}}\Bigg)\cdot R_\mathrm{trig} \\
&= (1+\lambda)\cdot R_\mathrm{trig}
\end{aligned} \tag{D.25}$$

D.5. Estimating the maximal split ratio for quadruple events (Sect. 2.8.7)

In case of a quadruple split event four pixels share the signal charge of one photon. The transition from a triple to a quadruple event occurs if the charge split q_4 exceeds the detection threshold q_{th}. By reason of symmetry the maximal split ratio $\eta_{1\,\max}$ is obtained at $q_4 = q_{\text{th}}$ and $q_2 = q_3$

$$\eta_1 = \frac{q_1}{q_1 + q_2 + q_3 + q_4} \tag{D.26}$$

$$\eta_{1\,\max} = \frac{q_1}{q_1 + (2m(x) + 1)q_{\text{th}}} \tag{D.27}$$

$$\eta_{1\,\max} = \frac{q_0 - (2m(x) + 1)q_{\text{th}}}{q_0} \tag{D.28}$$

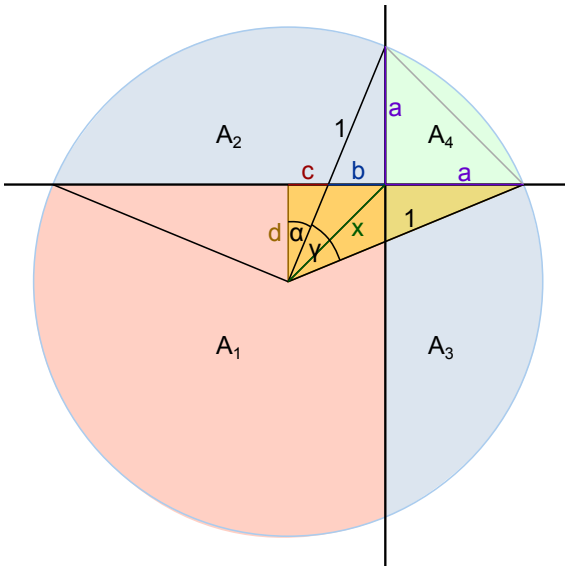

Figure D.1. Geometry of quadruple splits. The areas A_n represent the split charges q_n.

Assuming a spherical symmetric charge distribution q_2 can be expressed as multiple $m(x)$ of q_4. The following calculation is based on a geometrical consideration: the split charges are equal to the green, blue, and red areas of Fig. D.1. The radius of the charge cloud is assumed to be $r = 1$. All areas can be expressed as a function of the diagonal distance x between the center of the charge cloud and the edge of the pixel:

$$d = b + c = \frac{x}{\sqrt{2}} \tag{D.29}$$

$$a + b + c = \sqrt{1 - d^2} \tag{D.30}$$

$$a = \sqrt{1 - d^2} - d \tag{D.31}$$

$$\gamma = \arccos\left(1 - \left(\sqrt{1 - d^2} - \frac{x}{\sqrt{2}}\right)^2\right) \tag{D.32}$$

$$\alpha = \frac{\pi}{4} - \frac{\gamma}{2} \tag{D.33}$$

$$c = d\tan(\alpha) \tag{D.34}$$

$$b = d(1 - \tan(\alpha)) \tag{D.35}$$

$$A_4 = \pi \cdot \frac{\gamma}{2\pi} - ab - (d^2 - cd) \tag{D.36}$$

$$A_2 = \pi \cdot \frac{\pi - 2\alpha}{2\pi} - d(a + b + c) - A_4 \tag{D.37}$$

The transformations from areas to charges is done with the relation $q_0 = \pi$: $q_2 = A_2/\pi$ and $q_4 = A_4/\pi$. The multiplication factor $m(x) = q_4/q_2$ and $\eta_{1\,\max}$ are shown in Fig. 2.42.

D.6. Calculating variation of the signal duration due to variations of the absorption depth (Sect. 3.5.4)

The probability $\mathrm{d}P$ that a photon which travels in the z-direction through a medium is absorbed within an element of width $\mathrm{d}z$ can be calculated with Beer's law:

$$\frac{\mathrm{d}P}{\mathrm{d}z} = \frac{\eta}{L}\mathrm{e}^{-z/L}, \tag{D.38}$$

with the absorption length L. The normalization factor η allows to normalize Eq. (D.38) to only those events that are absorbed within the medium of width d:

$$P = \int_0^d \frac{\mathrm{d}P}{\mathrm{d}z}\,\mathrm{d}z \stackrel{!}{=} 1 \tag{D.39}$$

results in

$$\eta = \left(1 - \mathrm{e}^{-\frac{d}{L}}\right)^{-1}. \tag{D.40}$$

The mean absorption depth $\bar{z}$ can be calculated via

$$\bar{z} = \int_0^d z \cdot \frac{\mathrm{d}P}{\mathrm{d}z}\,\mathrm{d}z \tag{D.41}$$

with the solution

$$\bar{z} = \eta\left(L - \left(\mathrm{e}^{-\frac{d}{L}}(L+d)\right)\right). \tag{D.42}$$

The one sigma variation Δz of the absorption depth can be roughly estimated via

$$\int_{\bar{z}-2\Delta z}^{\bar{z}} \frac{\mathrm{d}P}{\mathrm{d}z}\,\mathrm{d}z \stackrel{!}{=} 0.683 \tag{D.43}$$

which results in

$$\Delta z = 0.5 \cdot \left(\ln\left(\frac{0.683}{\eta} + \mathrm{e}^{-\frac{\bar{z}}{L}}\right) \cdot L + \bar{z}\right). \tag{D.44}$$

See Fig. 3.16 for the graphs of $\bar{z}$ and Δz as a function of the photon energy E.
The signal pulse results by the drift of signal charges and has an averaged duration that can be estimated for electron and hole drifts via

$$\bar{t}_\mathrm{e} = \bar{s}_\mathrm{e}/(\mu_\mathrm{e} \cdot |\vec{E}|) \quad \text{and} \quad \bar{t}_\mathrm{h} = \bar{s}_\mathrm{h}/(\mu_\mathrm{h} \cdot |\vec{E}|). \tag{D.45}$$

The ratio of the mean drift distance for electrons $\bar{s}_\mathrm{e} = d - \bar{z}$ and for holes $\bar{s}_\mathrm{h} = \bar{z}$ is equal to the ratio of the electron signal to the hole signal (assuming a constant electric field $|\vec{E}|$). The signal duration $\bar{t}_\mathrm{drift}$ is estimated by weighting the mean drift time of the electrons $\bar{t}_\mathrm{e}$ and holes $\bar{t}_\mathrm{h}$ with their mean, relative drifts $\bar{s}_\mathrm{e}/d$ and $\bar{s}_\mathrm{h}/d$

$$\bar{t}_\mathrm{drift} = \frac{\bar{s}_\mathrm{e}}{d} \cdot \bar{t}_\mathrm{e} + \frac{\bar{s}_\mathrm{h}}{d} \cdot \bar{t}_\mathrm{h}. \tag{D.46}$$

The variation of the signal duration t_drift is estimated via

$$\Delta t_\mathrm{drift} = \frac{\bar{s}_\mathrm{e}}{d} \cdot \Delta t_\mathrm{e} + \frac{\bar{s}_\mathrm{h}}{d} \cdot \Delta t_\mathrm{h} \tag{D.47}$$

with

$$\Delta t_\mathrm{e} = \Delta z/(\mu_\mathrm{e} \cdot |\vec{E}|) \quad \text{and} \quad \Delta t_\mathrm{h} = \Delta z/(\mu_\mathrm{h} \cdot |\vec{E}|). \tag{D.48}$$

See Fig. 3.16 for the graphs of $\bar{t}_\mathrm{drift}$ and Δt_drift as a function of the photon energy E.

Curriculum vitae

16.02.1983	Born in Ulm
1989 - 1993	Elementary school *Carl-Joseph-Leiprecht*, Rottenburg
1993 - 2002	Secondary school *Eugen-Bolz-Gymnasium*, Rottenburg
2002 - 2003	Basic military service, *III. Gebirgsartilleriebataillon 225*, Füssen
2003 - 2009	Study of physics, *Eberhard Karls University*, Tübingen
2008 - 2009	Diploma student, Institute for Astronomy and Astrophysics Tübingen(IAAT), Tübingen. Thesis: assembly of the Simbol-X science verification model.
since 2009	PhD student, *IAAT*, Tübingen. Thesis: development of a stacked detector system and its application as an X-ray polarimeter.

Bibliography

S. Agostinelli and GEANT4 Collaboration. GEANT4 - a simulation toolkit. *Nuclear Instruments and Methods in Physics Research A*, 506:250–303, 2003. doi: 10.1016/S0168-9002(03)01368-8.

J. Als-Nielsen and D. McMorrow. *Elements of Modern X-ray Physics*. Wiley, 2011. ISBN 9781119970156.

C. Amsler. *Kern- und Teilchenphysik*. Uni-Taschenbücher M. UTB GmbH, 2007. ISBN 9783825228859.

J. R. Angel, R. Novick, P. vanden Bout, and R. Wolff. Search for X-Ray Polarization in Sco X-1. *Physical Review Letters*, 22:861–865, Apr. 1969. doi: 10.1103/PhysRevLett.22.861.

R. Antonucci. Unified models for active galactic nuclei and quasars. *Annual Review of Astron and Astrophys*, 31:473–521, 1993. doi: 10.1146/annurev.aa.31.090193.002353.

R. R. J. Antonucci and J. S. Miller. Spectropolarimetry and the nature of NGC 1068. *Astrophysical Journal*, 297:621–632, Oct. 1985. doi: 10.1086/163559.

J. Ballet. Pile-up on X-ray CCD instruments. *Astronomy and Astrophysics, Supplement*, 135:371–381, Mar. 1999. doi: 10.1051/aas:1999179.

R. Bell. Time-dependent polarization of CdTe gamma-ray detectors. *Nuclear Instruments and Methods*, 117:267–271, May 1974. doi: 10.1016/0029-554X(74)90408-X.

M. Berger, J. Hubbel, S. Seltzer, J. Chang, J. Coursey, R. Sukumar, D. Zucker, and K. Olsen. Xcom: Photon cross sections database (version 1.5), 2010. URL `http://www.nist.gov/pml/data/xcom/index.cfm`.

S. Bianchi, R. Maiolino, and G. Risaliti. AGN Obscuration and the Unified Model. *Advances in Astronomy*, 2012:782030, 2012. doi: 10.1155/2012/782030.

G. S. Bisnovatyi-Kogan and S. I. Blinnikov. A hot corona around a black-hole accretion disk as a model for Cygnus X-1. *Soviet Astronomy Letters*, 2:191–193, Oct. 1976.

K. Biswas and M.-H. Du. What causes high resistivity in CdTe. *New Journal of Physics*, 14(6):063020, June 2012. doi: 10.1088/1367-2630/14/6/063020.

A. L. Buck. New Equations for Computing Vapor Pressure and Enhancement Factor. *Journal of Applied Meteorology*, 20:1527–1532, Dec. 1981. doi: 10.1175/1520-0450(1981)020<1527:NEFCVP>2.0.CO;2.

S. Chandrasekhar. *Radiative transfer*. Oxford, Clarendon Press, 1950.

T. Chattopadhyay, S. V. Vadawale, A. R. Rao, S. Sreekumar, and D. Bhattacharya. Prospects of hard X-ray polarimetry with Astrosat-CZTI. *Experimental Astronomy*, 37:555–577, Nov. 2014. doi: 10.1007/s10686-014-9386-1.

D. Clarke, B. G. Stewart, H. E. Schwarz, and A. Brooks. The statistical behaviour of normalized Stokes parameters. *A&A*, 126:260–264, Oct. 1983.

A. Comastri. Compton-Thick AGN: The Dark Side of the X-Ray Background. In A. J. Barger, editor, *Supermassive Black Holes in the Distant Universe*, volume 308 of *Astrophysics and Space Science Library*, page 245, Aug. 2004.

P. A. J. de Korte. High-throughput replica optics. *Applied Optics*, 27:1440–1446, Apr. 1988. doi: 10.1364/AO.27.001440.

L. Devroye. *Non-uniform random variate generation*. Springer-Verlag, 1986. ISBN 9783540963059.

F. Dorey. Statistics in brief: Confidence intervals: What is the real result in the target population? *Clin Orthop Relat Res.*, 468:3137–3138, Nov. 2010. doi: 10.1007/s11999-010-1407-4.

H. Elhadidy, J. Franc, P. Moravec, P. Höschl, and M. Fiederle. Deep level defects in CdTe materials studied by thermoelectric effect spectroscopy and photo-induced current transient spectroscopy. *Semiconductor Science Technology*, 22:537–542, May 2007. doi: 10.1088/0268-1242/22/5/014.

R. F. Elsner, S. L. O'Dell, and M. C. Weisskopf. Measuring x-ray polarization in the presence of systematic effects: known background. volume 8443 of *SPIE*, Sept. 2012. doi: 10.1117/12.924889.

I. N. Evans, H. C. Ford, A. L. Kinney, R. R. J. Antonucci, L. Armus, and S. Caganoff. HST imaging of the inner 3 arcseconds of NGC 1068 in the light of forbidden O III 5007 A. *Astrophysical Journal, Letters*, 369:L27–L30, Mar. 1991. doi: 10.1086/185951.

A. C. Fabian, I. M. George, S. Miyoshi, and M. J. Rees. Reflection-dominated hard X-ray sources and the X-ray background. *Monthly Notices of the RAS*, 242:14P–16P, Jan. 1990.

U. Fano. Ionization Yield of Radiations. II. The Fluctuations of the Number of Ions. *Physical Review*, 72:26–29, July 1947. doi: 10.1103/PhysRev.72.26.

L. Feretti, G. Giovannini, F. Govoni, and M. Murgia. Clusters of galaxies: observational properties of the diffuse radio emission. *Astronomy and Astrophysics Reviews*, 20:54, May 2012. doi: 10.1007/s00159-012-0054-z.

P. Ferrando, M. Arnaud, U. Briel, E. Cavazutti, R. Clédassou, J. L. Counil, F. Fiore, P. Giommi, A. Goldwurm, O. Lamarle, P. Laurent, F. Lebrun, G. Malaguti, S. Mereghetti, G. Micela, G. Pareschi, M. Piermaria, J. P. Roques, and G. Tagliaferri. The simbol-x mission. *Mem. Soc. Astron. Italiana*, 79:19, 2008.

L. Ferrarese and D. Merritt. A Fundamental Relation between Supermassive Black Holes and Their Host Galaxies. *Astrophysical Journal, Letters*, 539:L9–L12, Aug. 2000. doi: 10.1086/312838.

F. Fiore, G. C. Perola, G. Pareschi, O. Citterio, A. Anselmi, and A. Comastri. HEXIT-SAT: a mission concept for x-ray grazing incidence telescopes from 0.5 to 70 keV. In G. Hasinger and M. J. L. Turner, editors, *UV and Gamma-Ray Space Telescope Systems*, volume 5488 of *Society of Photo-Optical Instrumentation Engineers (SPIE) Conference Series*, pages 933–943, Oct. 2004. doi: 10.1117/12.551373.

R. B. Firestone, C. M. Baglin, and S. Chu. *Table of isotopes*. Number 4. Wiley, 1999. ISBN 9780471356332.

M. Funaki, T. Ozaki, K. Satoh, and R. Ohno. Growth and characterization of CdTe single crystals for radiation detectors. *Nuclear Instruments and Methods in Physics Research A*, 436:120–126, Oct. 1999. doi: 10.1016/S0168-9002(99)00607-5.

B. M. Gaensler and P. O. Slane. The Evolution and Structure of Pulsar Wind Nebulae. *Annual Review of Astron and Astrophys*, 44:17–47, Sept. 2006. doi: 10.1146/annurev.astro.44.051905.092528.

E. Gatti. Semiconductor drift chamber. An application of a novel charge transport scheme. *Nuclear Instruments and Methods in Physics Research*, 225:608–614, Sept. 1984. doi: 10.1016/0167-5087(84)90113-3.

K. Gebhardt, R. Bender, G. Bower, A. Dressler, S. M. Faber, A. V. Filippenko, R. Green, C. Grillmair, L. C. Ho, J. Kormendy, T. R. Lauer, J. Magorrian, J. Pinkney, D. Richstone, and S. Tremaine. A Relationship between Nuclear Black Hole Mass and Galaxy Velocity Dispersion. *Astrophysical Journal, Letters*, 539: L13–L16, Aug. 2000. doi: 10.1086/312840.

I. M. George and A. C. Fabian. X-ray reflection from cold matter in active galactic nuclei and X-ray binaries. *Monthly Notices of the RAS*, 249:352–367, Mar. 1991.

L. Gerward, N. Guilbert, K. Bjørn Jensen, and H. Levring. X-ray absorption in matter. Reengineering XCOM. *Radiation Physics and Chemistry*, 60:23–24, Jan. 2001. doi: 10.1016/S0969-806X(00)00324-8.

R. Giacconi, H. Gursky, F. R. Paolini, and B. B. Rossi. Evidence for x Rays From Sources Outside the Solar System. *Physical Review Letters*, 9:439–443, Dec. 1962. doi: 10.1103/PhysRevLett.9.439.

R. Gilli, A. Comastri, and G. Hasinger. The synthesis of the cosmic X-ray background in the Chandra and XMM-Newton era. *Astronomy and Astrophysics*, 463:79–96, Feb. 2007. doi: 10.1051/0004-6361:20066334.

M. Guainazzi, T. Mihara, C. Otani, and M. Matsuoka. Spectral Variability and Iron Line Emission in the ASCA Observations of the Seyfert 1 Galaxy NGC 4051. *Publications of the ASJ*, 48:781–799, Dec. 1996. doi: 10.1093/pasj/48.6.781.

M. Guainazzi, F. Nicastro, F. Fiore, G. Matt, I. McHardy, A. Orr, P. Barr, A. Fruscione, I. Papadakis, A. N. Parmar, P. Uttley, G. C. Perola, and L. Piro. A swan song: the disappearance of the nucleus of NGC 4051 and the echo of its past glory. *Monthly Notices of the RAS*, 301:L1–L4, Nov. 1998. doi: 10.1046/j.1365-8711.1998.02089.x.

F. A. Harrison and the NuSTAR collaboration. The Nuclear Spectroscopic Telescope Array (NuSTAR) High-energy X-Ray Mission. *Astrophysical Journal*, 770:103, June 2013. doi: 10.1088/0004-637X/770/2/103.

Z. He. Review of the Shockley-Ramo theorem and its application in semiconductor gamma-ray detectors. *Nuclear Instruments and Methods in Physics Research A*, 463:250–267, May 2001. doi: 10.1016/S0168-9002(01)00223-6.

K. Hecht. Zum Mechanismus des lichtelektrischen Primärstromes in isolierenden Kristallen. *Zeitschrift für Physik*, 77:235–245, Mar. 1932. doi: 10.1007/BF01338917.

W. Heitler. *The Quantum Theory of Radiation*. Dover Books on Physics Series. Dover Publ., 1954. ISBN 9780486645582.

P. Holl, P. Fischer, R. Hartmann, G. Hasinger, J. Kollmer, N. Krause, P. Lechner, G. Lutz, N. Meidinger, I. Peric, R. H. Richter, H. Soltau, L. Strueder, J. Treis, J. E. Truemper, and N. Wermes. Active pixel sensors for imaging X-ray spectrometers. In J. E. Truemper and H. D. Tananbaum, editors, *X-Ray and Gamma-Ray Telescopes and Instruments for Astronomy.*, volume 4851 of *Society of Photo-Optical Instrumentation Engineers (SPIE) Conference Series*, pages 770–778, Mar. 2003. doi: 10.1117/12.461356.

J. H. Hubbell and S. Seltzer. Tables of X-Ray Mass Attenuation Coefficients and Mass Energy-Absorption Coefficients. *National Institute of Standards and Technology (NIST)*, Sept. 2007.

J. H. Hubbell, W. J. Veigele, E. A. Briggs, R. T. Brown, D. T. Cromer, and R. J. Howerton. Atomic form factors, incoherent scattering functions, and photon scattering cross sections. *Journal of Physical and Chemical Reference Data*, 4:471–538, July 1975. doi: 10.1063/1.555523.

W. Jaffe, K. Meisenheimer, H. J. A. Röttgering, et al. The central dusty torus in the active nucleus of NGC 1068. *Nature*, 429:47–49, May 2004. doi: 10.1038/nature02531.

Y.-F. Jiang, J. M. Stone, and S. W. Davis. Radiation Magnetohydrodynamic Simulations of the Formation of Hot Accretion Disk Coronae. *Astrophysical Journal*, 784:169, Apr. 2014. doi: 10.1088/0004-637X/784/2/169.

J. Kemmer and G. Lutz. New detector concepts. *Nuclear Instruments and Methods in Physics Research A*, 253:365–377, Jan. 1987. doi: 10.1016/0168-9002(87)90518-3.

G. Khlyap and P. Sydorchuk. Growth and Electrical Properties of New Semiconductor Compound ZnCdHgTe. *Cryst. Res. Technol.*, 36:1027–1034, Oct. 2001. doi: 10.1002/1521-4079(200110)36:8/10<1027::AID-CRAT1027>3.0.CO;2-C.

N. Kimmel, R. Andritschke, R. Hartmann, P. Holl, N. Meidinger, R. Richter, and L. Strüder. Experimental and theoretical study of the signal electron motion in fully depleted silicon. *Nuclear Instruments and Methods in Physics Research A*, 624:334–339, Dec. 2010. doi: 10.1016/j.nima.2010.05.005.

O. Klein and T. Nishina. Über die Streuung von Strahlung durch freie Elektronen nach der neuen relativistischen Quantendynamik von Dirac. *Zeitschrift für Physik*, 52:853–868, Nov. 1929. doi: 10.1007/BF01366453.

G. Knoll. *Radiation Detection and Measurement*. Wiley, 2000. ISBN 9780471073383.

K. H. Knuth. Optimal Data-Based Binning for Histograms. *ArXiv Physics e-prints*, May 2006.

J. Kormendy and D. Richstone. Inward Bound—The Search For Supermassive Black Holes In Galactic Nuclei. *Annual Review of Astron and Astrophys*, 33:581, 1995. doi: 10.1146/annurev.aa.33.090195.003053.

M. O. Krause. Atomic radiative and radiationless yields for K and L shells. *Journal of Physical and Chemical Reference Data*, 8:307–327, Apr. 1979.

H. Krawczynski. The Polarization Properties of Inverse Compton Emission and Implications for Blazar Observations with the GEMS X-Ray Polarimeter. *Astrophysical Journal*, 744:30, Jan. 2012. doi: 10.1088/0004-637X/744/1/30.

H. Krawczynski, A. Garson, Q. Guo, M. G. Baring, P. Ghosh, M. Beilicke, and K. Lee. Scientific prospects for hard X-ray polarimetry. *Astroparticle Physics*, 34:550–567, Feb. 2011. doi: 10.1016/j.astropartphys.2010.12.001.

J. H. Krolik. *Active Galactic Nuclei: From the Central Black Hole to the Galactic Environment*. Princeton series in astrophysics. Princeton University Press, 1999. ISBN 9780691011516.

T. Kubicki, K. Lübelsmeyer, J. Ortmanns, D. Pandoulas, O. Syben, M. Toporowsky, and W. J. Xiao. Calculation of the electric field in GaAs particle detectors. *Nuclear Instruments and Methods in Physics Research A*, 345:468–473, July 1994. doi: 10.1016/0168-9002(94)90501-0.

A. Laor. Line profiles from a disk around a rotating black hole. *Astrophysical Journal*, 376:90–94, July 1991. doi: 10.1086/170257.

S. Lotti, L. Natalucci, P. Giommi, B. Grefenstette, F. A. Harrison, K. K. Madsen, M. Perri, S. Puccetti, and A. Zoglauer. Polarization studies with NuSTAR. In *Society of Photo-Optical Instrumentation Engineers (SPIE) Conference Series*, volume 8443 of *Society of Photo-Optical Instrumentation Engineers (SPIE) Conference Series*, page 4, Sept. 2012. doi: 10.1117/12.925989.

B. Lowe and R. Sareen. *Semiconductor X-Ray Detectors*. Series in Sensors. Taylor & Francis, 2013. ISBN 9781466554009.

G. Lutz. *Semiconductor Radiation Detectors: Device Physics*. Accelerator Physics Series. U.S. Government Printing Office, 1999. ISBN 9783540648598.

O. Madelung, editor. *Landolt-Börnstein: Numerical Data and Functional Relationships in Science and Technology - New Series "Group 3 Crystal and Solid State Physics" Volume 17b*, 1982.

D. Maier. *Aufbau eines Science Verification Models für die Simbol-X Mission*. Diploma thesis, Eberhard Karls University Tübingen, Institut for Astronomy and Astrophysics, Apr. 2009.

D. Maier, F. Aschauer, J. Dick, G. Distratis, H. Gebhardt, S. Herrmann, E. Kendziorra, T. Lauf, P. Lechner, A. Santangelo, T. Schanz, L. Strüder, C. Tenzer, and J. Treis. Development of the Simbol-X science verification model and its contribution for the IXO Mission. In *Society of Photo-Optical Instrumentation Engineers (SPIE) Conference Series*, volume 7742 of *Society of Photo-Optical Instrumentation Engineers (SPIE) Conference Series*, July 2010. doi: 10.1117/12.857110.

D. Maier, J. Dick, G. Distratis, E. Kendziorra, A. Santangelo, T. Schanz, C. Tenzer, and G. Warth. Development of fast data processing electronics for a stacked x-ray detector system with application as a polarimeter. In *Society of Photo-Optical Instrumentation Engineers (SPIE) Conference Series*, volume 8443 of *Society of Photo-Optical Instrumentation Engineers (SPIE) Conference Series*, Sept. 2012. doi: 10.1117/12.926819.

D. Maier, C. Tenzer, and A. Santangelo. Point and Interval Estimation on the Degree and the Angle of Polarization: A Bayesian Approach. *Publications of the Astronomical Society of the Pacific*, 126:459–468, May 2014,a. doi: 10.1086/676820.

D. Maier, O. Limousin, A. Meuris, S. Pürckhauer, A. Santangelo, T. Schanz, and C. Tenzer. Development of a stacked detector system for the x-ray range and its possible applications. In *Society of Photo-Optical Instrumentation Engineers (SPIE) Conference Series*, volume 9154 of *Society of Photo-Optical Instrumentation Engineers (SPIE) Conference Series*, page 22, July 2014,b. doi: 10.1117/12.2055881.

R. Maiolino, M. Salvati, L. Bassani, M. Dadina, R. della Ceca, G. Matt, G. Risaliti, and G. Zamorani. Heavy obscuration in X-ray weak AGNs. *Astronomy and Astrophysics*, 338:781–794, Oct. 1998.

H. L. Malm and M. Martini. Polarization Phenomena in CdTe Nuclear Radiation Detectors. *IEEE Transactions on Nuclear Science*, 21:322–330, Dec. 1974. doi: 10.1109/TNS.1974.4327478.

P. H. Mao, F. A. Harrison, Y. Y. Platonov, D. Broadway, B. Degroot, F. E. Christensen, W. W. Craig, and C. J. Hailey. Development of grazing incidence multilayer mirrors for hard x-ray focusing telescopes. In O. H. Siegmund and M. A. Gummin, editors, *EUV, X-Ray, and Gamma-Ray Instrumentation for Astronomy VIII*, volume 3114 of *SPIE Conference Series*, pages 526–534, Oct. 1997.

C. B. Markwardt. Non-linear Least-squares Fitting in IDL with MPFIT. In D. A. Bohlender, D. Durand, and P. Dowler, editors, *Astronomical Data Analysis Software and Systems XVIII*, volume 411 of *Astronomical Society of the Pacific Conference Series*, page 251, Sept. 2009.

K. Mathieson, M. S. Passmore, P. Seller, M. L. Prydderch, V. O'Shea, R. L. Bates, K. M. Smith, and M. Rahman. Charge sharing in silicon pixel detectors. *Nuclear Instruments and Methods in Physics Research A*, 487:113–122, July 2002. doi: 10.1016/S0168-9002(02)00954-3.

G. Matt. Dust lanes, thick absorbers, and the unification model for Seyfert galaxies. *Astronomy and Astrophysics*, 355:L31–L33, Mar. 2000.

G. Matt, W. N. Brandt, and A. C. Fabian. The iron Kalpha line complex in Compton-thick Seyfert 2 galaxies. *Monthly Notices of the RAS*, 280:823–834, June 1996.

R. Matz and M. Weidner. Charge collection efficiency and space charge formation in CdTe gamma and X-ray detectors. *Nuclear Instruments and Methods in Physics Research A*, 406:287–298, Apr. 1998.

P. Meszaros, R. Novick, A. Szentgyorgyi, G. A. Chanan, and M. C. Weisskopf. Astrophysical implications and observational prospects of X-ray polarimetry. *Astrophysical Journal*, 324:1056–1067, Jan. 1988. doi: 10.1086/165962.

A. Meuris, O. Limousin, F. Lugiez, O. Gevin, F. Pinsard, I. Le Mer, E. Delagnes, M. C. Vassal, F. Soufflet, and R. Bocage. Caliste 64, an Innovative CdTe Hard X-Ray Micro-Camera. *IEEE Transactions on Nuclear Science*, 55:778–784, Apr. 2008. doi: 10.1109/TNS.2008.918742.

A. Meuris, O. Limousin, F. Lugiez, O. Gevin, C. Blondel, F. Pinsard, M. C. Vassal, F. Soufflet, and I. Le Mer. Caliste 64, a new CdTe micro-camera for hard X-ray spectro-imaging. *Nuclear Instruments and Methods in Physics Research A*, 610: 154–157, Oct. 2009. doi: 10.1016/j.nima.2009.05.071.

A. Meuris, O. Limousin, and C. Blondel. Characterization of polarization phenomenon in Al-Schottky CdTe detectors using a spectroscopic analysis method. *Nuclear Instruments and Methods in Physics Research A*, 654:293–299, Oct. 2011. doi: 10.1016/j.nima.2011.05.084.

H. B. Michaelson. The work function of the elements and its periodicity. *Journal of Applied Physics*, 48:4729–4733, Nov. 1977. doi: 10.1063/1.323539.

T. Mizuno. Polarimetry with the Soft Gamma-ray Detector onboard ASTRO-H. In *39th COSPAR Scientific Assembly*, volume 39 of *COSPAR Meeting*, page 1259, July 2012.

A. Mood and F. Graybill. *Introduction to the theory of statistics 3rd ed.* McGraw-Hill series in probability and statistics. McGraw-Hill, 1974.

P. Moran, A. Shearer, C. Gouiffes, and P. Laurent. INTEGRAL/IBIS and optical observations of the Crab nebula/pulsar polarisation. *ArXiv e-prints*, Feb. 2013.

C. W. Morgan, C. S. Kochanek, N. D. Morgan, and E. E. Falco. The Quasar Accretion Disk Size-Black Hole Mass Relation. *Astrophysical Journal*, 712:1129–1136, Apr. 2010. doi: 10.1088/0004-637X/712/2/1129.

M. Mori and M. Sugihara. The double-exponential transformation in numerical analysis. *Journal of Computational and Applied Mathematics*, 127:287–296, Jan. 2001. doi: 10.1016/S0377-0427(00)00501-X.

B. Mück. *Low-Mass X-Ray Binary Studies with XMM-Newton*. PhD thesis, Eberhard Karls University Tübingen, Institut for Astronomy and Astrophysics, July 2014.

F. Muleri and R. Campana. Sensitivity of Stacked Imaging Detectors to Hard X-Ray Polarization. *The Astrophysical Journal*, 751:88, June 2012. doi: 10.1088/0004-637X/751/2/88.

M. Murgia, D. Eckert, F. Govoni, C. Ferrari, M. Pandey-Pommier, J. Nevalainen, and S. Paltani. GMRT observations of the Ophiuchus galaxy cluster. *Astronomy and Astrophysics*, 514:A76, May 2010. doi: 10.1051/0004-6361/201014126.

J. Naghizadeh-Khouei and D. Clarke. On the statistical behaviour of the position angle of linear polarization. *Astronomy and Astrophysics*, 274:968, July 1993.

R. Novick, M. C. Weisskopf, R. Berthelsdorf, R. Linke, and R. S. Wolff. Detection of X-Ray Polarization of the Crab Nebula. *Astrophysical Journal, Letters*, 174:L1, May 1972. doi: 10.1086/180938.

M. Nynka, C. J. Hailey, S. P. Reynolds, H. An, F. K. Baganoff, S. E. Boggs, F. E. Christensen, W. W. Craig, E. V. Gotthelf, B. W. Grefenstette, F. A. Harrison, R. Krivonos, K. K. Madsen, K. Mori, K. Perez, D. Stern, D. R. Wik, W. W. Zhang, and A. Zoglauer. NuSTAR Study of Hard X-Ray Morphology and Spectroscopy of PWN G21.5-0.9. *Astrophysical Journal*, 789:72, July 2014. doi: 10.1088/0004-637X/789/1/72.

A. Owens and A. Peacock. Compound semiconductor radiation detectors. *Nuclear Instruments and Methods in Physics Research A*, 531:18–37, Sept. 2004. doi: 10.1016/j.nima.2004.05.071.

G. Pareschi, G. Tagliaferri, P. Attinà, S. Basso, G. Borghi, O. Citterio, M. Civitani, V. Cotroneo, B. Negri, G. Sironi, D. Spiga, D. Vernani, and G. Valsecchi. Design and development of the optics system for the NHXM Hard X-ray and Polarimetric Mission. In *Society of Photo-Optical Instrumentation Engineers (SPIE) Conference Series*, volume 7437 of *SPIE Conference Series*, Aug. 2009. doi: 10.1117/12.828142.

F. Pinsard and C. Cara. High Resolution Time Synchronization over SpaceWire Links. *Aerospace Conference, IEEE*, 1:4729–4733, Mar. 2008. doi: 10.1109/AERO.2008.4526462.

C. J. Powell and A. Jablonski. Evaluation of calculated and measured electron inelastic mean free paths near solid surfaces. *Journal of Physical and Chemical Reference Data*, 28(1), 1999.

W. H. Press, S. A. Teukolsky, W. T. Vetterling, and B. P. Flannery. *Numerical recipes in C (2nd ed.): the art of scientific computing*. Cambridge University Press, New York, NY, USA, 1992. ISBN 0-521-43108-5.

S. Pürckhauer. *Simulation studies of the expected background for X-ray missions*. Diploma thesis, Eberhard Karls University Tübingen, Institut for Astronomy and Astrophysics, Dec. 2015.

J. L. Quinn. Bayesian analysis of polarization measurements. *Astronomy and Astrophysics*, 538:A65, Feb. 2012. doi: 10.1051/0004-6361/201015785.

S. Ramo. Currents induced by electron motion. *Proceedings of the IRE*, 27(9):584–585, Sept. 1939. ISSN 0096-8390. doi: 10.1109/jrproc.1939.228757.

S. O. Rice. Mathematical Analysis of Random Noise. *Bell Systems Tech. J., Volume 24, p. 46-156*, 24:46–156, 1945.

G. Risaliti, R. Maiolino, and M. Salvati. The Distribution of Absorbing Column Densities among Seyfert 2 Galaxies. *Astrophysical Journal*, 522:157–164, Sept. 1999. doi: 10.1086/307623.

D. M. Russell and T. Shahbaz. The multiwavelength polarization of Cygnus X-1. *Monthly Notices of the RAS*, 438:2083–2096, Mar. 2014. doi: 10.1093/mnras/stt2330.

C. L. Sarazin. The Energy Spectrum of Primary Cosmic-Ray Electrons in Clusters of Galaxies and Inverse Compton Emission. *Astrophysical Journal*, 520:529–547, Aug. 1999. doi: 10.1086/307501.

T. Schanz, C. Tenzer, D. Maier, E. Kendziorra, and A. Santangelo. A Fast Event Preprocessor and Sequencer for the Simbol-X Low Energy Detector. In J. Rodriguez and P. Ferrando, editors, *American Institute of Physics Conference Series*, volume 1126 of *American Institute of Physics Conference Series*, pages 31–34, May 2009. doi: 10.1063/1.3149443.

V. Schöenfelder, H. Aarts, K. Bennett, H. de Boer, J. Clear, W. Collmar, A. Connors, A. Deerenberg, R. Diehl, A. von Dordrecht, J. W. den Herder, W. Hermsen, M. Kippen, L. Kuiper, G. Lichti, J. Lockwood, J. Macri, M. McConnell, D. Morris, R. Much, J. Ryan, G. Simpson, M. Snelling, G. Stacy, H. Steinle, A. Strong, B. N. Swanenburg, B. Taylor, C. de Vries, and C. Winkler. Instrument description and performance of the Imaging Gamma-Ray Telescope COMPTEL aboard the Compton Gamma-Ray Observatory. *Astrophysical Journal, Supplement*, 86:657–692, June 1993. doi: 10.1086/191794.

V. Schönfelder, A. Hirner, and K. Schneider. A telescope for soft gamma ray astronomy. *Nuclear Instruments and Methods*, 107:385–394, 1973. doi: 10.1016/0029-554X(73)90257-7.

D. W. Scott. On optimal and data-based histograms. *Biometrika*, 66(3):605–610, 1979. doi: 10.1093/biomet/66.3.605.

P. J. Sellin, A. W. Davies, A. Lohstroh, M. E. Ozsan, and J. Parkin. Drift Mobility and Mobility-Lifetime Products in CdTe:Cl Grown by the Travelling Heater Method. *IEEE Transactions on Nuclear Science*, 52:3074–3078, Dec. 2005. doi: 10.1109/TNS.2005.855641.

K. Serkowski. Statistical Analysis of the Polarization and Reddening of the Double Cluster in Perseus. *Acta Astronomica*, 8:135, 1958.

K. Serkowski. Polarization of starlight. volume 1 of *Advances in Astronomy and Astrophysics*, pages 289 – 352. Elsevier, 1962. doi: http://dx.doi.org/10.1016/B978-1-4831-9919-1.50009-1.

G. Setti and L. Woltjer. Active Galactic Nuclei and the spectrum of the X-ray background. *Astronomy and Astrophysics*, 224:L21–L23, Oct. 1989.

W. Shockley. Currents to conductors induced by a moving point charge. *Journal of Applied Physics*, 9(10):635–636, 1938. doi: 10.1063/1.1710367.

E. H. Silver, M. C. Weisskopf, H. L. Kestenbaum, K. S. Long, R. Novick, and R. S. Wolff. The first search for X-ray polarization in the Centaurus X-3 and Hercules X-1 pulsars. *Astrophysical Journal*, 232:248–254, Aug. 1979. doi: 10.1086/157283.

J. F. L. Simmons and B. G. Stewart. Point and interval estimation of the true unbiased degree of linear polarization in the presence of low signal-to-noise ratios. *Astronomy and Astrophysics*, 142:100–106, Jan. 1985.

H. Spieler. *Semiconductor Detector Systems*. Series on Semiconductor Science and Technology. OUP Oxford, 2005. ISBN 9780191523656.

P. Stallinga. *Electrical Characterization of Organic Electronic Materials and Devices*. Wiley, 2009. ISBN 9780470750179.

M. Stobbe. Zur Quantenmechanik photoelektrischer Prozesse. *Annalen der Physik*, 399:661–715, 1930. doi: 10.1002/andp.19303990604.

L. Strüder. High-resolution imaging X-ray spectrometers. *Nuclear Instruments and Methods in Physics Research A*, 454:73–113, Nov. 2000. doi: 10.1016/S0168-9002(00)00811-1.

S. M. Sze. *Physics of semiconductor devices*. 1981.

T. Tabata, P. Andreo, and K. Shinoda. An analytic formula for the extrapolated range of electrons in condensed materials. *Nuclear Instruments and Methods in Physics Research B*, 119:463–470, Dec. 1996. doi: 10.1016/S0168-583X(96)00687-8.

S. Tashenov, T. Bäck, R. Barday, B. Cederwall, J. Enders, A. Khaplanov, Y. Fritzsche, K.-U. Schässburger, A. Surzhykov, V. A. Yerokhin, and D. Jakubassa-Amundsen. Bremsstrahlung polarization correlations and their application for polarimetry of electron beams. *Physical Review A: General Physics*, 87(2):022707, Feb. 2013. doi: 10.1103/PhysRevA.87.022707.

A. Thompson. *X-ray data booklet*. University of Berkeley, 2009.

H. Toyama, A. Higa, M. Yamazato, T. Maehama, R. Ohno, and M. Toguchi. Quantitative Analysis of Polarization Phenomena in CdTe Radiation Detectors. *Japanese Journal of Applied Physics*, 45:8842, Nov. 2006. doi: 10.1143/JJAP.45.8842.

R. Trammell and F. J. Walter. The effects of carrier trapping in semiconductor gamma-ray spectrometers. *Nuclear Instruments and Methods*, 76:317–321, 1969. doi: 10.1016/0029-554X(69)90034-2.

J. Treis, P. Fischer, O. Hälker, M. Harter, S. Herrmann, R. Kohrs, H. Krüger, P. Lechner, G. Lutz, I. Peric, M. Porro, R. H. Richter, L. Strüder, M. Trimpl, and N. Wermes. Study of noise and spectroscopic performance of DEPMOSFET matrix prototypes for XEUS. *Nuclear Instruments and Methods in Physics Research A*, 568:191–200, Nov. 2006. doi: 10.1016/j.nima.2006.05.237.

C. M. Urry and P. Padovani. Unified Schemes for Radio-Loud Active Galactic Nuclei. *Publication of the Astronomical Society of the Pacific*, 107:803, Sept. 1995. doi: 10.1086/133630.

J. E. Vaillancourt. Placing Confidence Limits on Polarization Measurements. *Publications of the Astronomical Society of the Pacific*, 118:1340–1343, Sept. 2006. doi: 10.1086/507472.

J. F. C. Wardle and P. P. Kronberg. The linear polarization of quasi-stellar radio sources at 3.71 and 11.1 centimeters. *The Astrophysical Journal*, 194:249–255, Dec. 1974. doi: 10.1086/153240.

M. C. Weisskopf, R. Berthelsdorf, G. Epstein, R. Linke, D. Mitchell, R. Novick, and R. S. Wolff. A graphite crystal polarimeter for stellar X-ray astronomy. *Review of Scientific Instruments*, 43:967–976, 1972. doi: 10.1063/1.1685840.

M. C. Weisskopf, G. G. Cohen, H. L. Kestenbaum, K. S. Long, R. Novick, and R. S. Wolff. Measurement of the X-ray polarization of the Crab Nebula. *Astrophysical Journal, Letters*, 208:L125–L128, Sept. 1976. doi: 10.1086/182247.

M. C. Weisskopf, R. F. Elsner, and S. L. O'Dell. On understanding the figures of merit for detection and measurement of x-ray polarization. volume 7732 of *SPIE*, July 2010. doi: 10.1117/12.857357.

K. C. Westfold. The Polarization of Synchrotron Radiation. *Astrophysical Journal*, 130:241, July 1959. doi: 10.1086/146713.

J. Wilms. Relativistic Fe Kalpha lines with SIMBOL-X. *Mem. Societa Astronomica Italiana*, 79:128, 2008a.

J. Wilms. Unity among Black Holes: Observational Similarities between Galactic Black Holes and Active Galactic Nuclei. *Chinese Journal of Astronomy and Astrophysics Supplement*, 8:281–290, Oct. 2008b.

S. Wölfel. *Neuartige DEPFET-RNDR-Detektoren im experimentellen Betrieb*. PhD thesis, Universität Siegen, 2007.

H. Wolter. Spiegelsysteme streifenden Einfalls als abbildende Optiken für Röntgenstrahlen. *Annalen der Physik*, 445:94–114, 1952. doi: 10.1002/andp.19524450108.

R. Yamazaki, Y. Ohira, M. Sawada, and A. Bamba. Synchrotron X-ray diagnostics of cutoff shape of nonthermal electron spectrum at young supernova remnants. *Research in Astronomy and Astrophysics*, 14:165, Feb. 2014. doi: 10.1088/1674-4527/14/2/005.

C. Zhang, P. Lechner, G. Lutz, M. Porro, R. Richter, J. Treis, L. Strüder, and S. Nan Zhang. Development of DEPFET Macropixel detectors. *Nuclear Instruments and Methods in Physics Research A*, 568:207–216, Nov. 2006. doi: 10.1016/j.nima.2006.05.239.

List of Figures

1.1. Wolter 1 telescope . . . 18
1.2. Centaurus A, observed by Chandra . . . 21
1.3. Urry and Padovani model for radio-loud AGN . . . 22
1.4. The cosmic X-ray background spectrum . . . 23
1.5. CXB and CIB . . . 24
1.6. NGC 4051, observed by the Hubble space telescope . . . 25
1.7. Scheme for the time delay between primary and secondary radiation . . 26
1.8. X-ray spectrum of NGC 4051 . . . 27
1.9. Binding energy E_b as function of the atomic number Z . . . 28
1.10. Electron range r_max . . . 29
1.11. Fluorescence and Auger yield for K and L-vacancies . . . 29
1.12. Absorption of a 6 keV X-ray photon in silicon . . . 30
1.13. Fano limited energy resolution for Si and CdTe . . . 31
1.14. Silicon escape peak . . . 31
1.15. Calculation of the intensity of an escape peak . . . 32
1.16. Shockley-Ramo Theorem . . . 34
1.17. Charge collection efficiency . . . 36
1.18. Visualization of the Trammell-Walter equation . . . 37
1.19. Signal formation in Si and CdTe . . . 38
1.20. Types of split events . . . 39
1.21. Simulated split distribution . . . 41
1.22. Pile-up in continuous and triggered readout mode . . . 42
1.23. Pile-up probability $P_k(R_\mathrm{in}/R_\mathrm{out})$ . . . 43
1.24. Spectrum of a monoenergetic source with pile-up . . . 44
1.25. Spectral impact of pile-up . . . 45
1.26. A typical detector front-end circuit . . . 47
1.27. Equivalent noise charge $ENC(t_\mathrm{shape})$ . . . 48
1.28. Photo of the CANDELA setup . . . 49
1.29. Photo and schematic drawing of the test setup . . . 50
1.30. Dew point temperature as function of pressure . . . 50
1.31. The CANDELA cooling structure . . . 51
1.32. Spectrum of used radiation sources . . . 53
1.33. Grounding scheme for CANDELA . . . 53
1.34. graphical user interface of Idef-X . . . 54

2.1. The low energy DEPFET detector . . . 55
2.2. Sideward depletion principle . . . 56

2.3. Scheme of a LED macro pixel . . . 57
2.4. Schematic view of a DePFET pixel . . . 57
2.5. Scheme of a DEPFET matrix . . . 59
2.6. Elementary switcher unit . . . 60
2.7. The SWITCHER chip . . . 61
2.8. Block diagram of the CAMEX . . . 62
2.9. Scheme of the signal digitization . . . 63
2.10. Interaction between CAMEX, adjustment stage, and ACD . . . 64
2.11. SEQ-signals for the LED operation of two rows . . . 65
2.13. EPP pipeline structure . . . 68
2.14. Common-mode correction . . . 68
2.15. The IFC and its modules . . . 69
2.16. Schematic overview of the LED system . . . 70
2.17. LED operation . . . 71
2.18. Analyzing LED dark-frame measurements . . . 72
2.19. LED offset and noise distributions . . . 74
2.20. Analyzing LED flat-field measurements . . . 75
2.21. Bad-map example . . . 75
2.22. Generating the bad2 map . . . 76
2.23. Analyzing LED scientific measurements . . . 77
2.24. Split types . . . 77
2.25. Regions surrounding a bad pixel . . . 78
2.26. Pattern types near bad pixels and their classification . . . 78
2.27. Pixel individual pulse height spectra and their distribution . . . 80
2.28. Differences in analyzing neighbors of bad pixels . . . 82
2.29. Split ratio distribution . . . 83
2.30. Detailed split ratio distribution . . . 84
2.31. Distributions of triple and quadruple splits . . . 84
2.32. Graph of the pulse-height-to-energy relation . . . 85
2.33. Spectral consequences of the energy offset . . . 86
2.35. LED spectra observed with different gain modes . . . 88
2.36. The Am-59 peak at 59.54 keV . . . 89
2.37. Low energetic LED fluorescence spectrum . . . 89
2.38. LED Am-241 spectra in comparison with a Geant4 simulation . . . 92
2.39. Averaged offset and noise drift . . . 93
2.40. Splits and their fractional charges . . . 93
2.41. Model of an elliptical charge cloud . . . 94
2.42. Calculating the maximal split ratio assuming a spherical charge cloud . . . 94

3.1. HED images . . . 97
3.2. Band diagram of p-doped CdTe . . . 98
3.3. Illustration of band bending in a Schottky p-semiconductor contact . . . 99
3.4. Diagram of different electric field distribution in solids . . . 101
3.5. The electric field for a uniform space charge distribution . . . 102

3.6. Representation of the modified Hecht equation . . . 103
3.7. Charge collection efficiency in CdTe in general . . . 104
3.8. Charge collection efficiency in CdTe for different U and n_{ion} . . . 105
3.9. Polarization time as a function of the temperature . . . 107
3.10. Scheme of Caliste-64 . . . 108
3.11. Schematic diagram of a Caliste-64 readout channel . . . 109
3.12. HED readout scheme . . . 110
3.13. Temporal sequence of a HED readout . . . 111
3.14. Caliste-64 with cooling plate and cooling funnel . . . 111
3.15. Caliste-64 with external high voltage pin connection . . . 112
3.16. Absorption depth and drift duration . . . 113
3.17. Signal processing and time-walk . . . 113
3.18. HED data analysis chain . . . 115
3.19. Creation of synthetic pulse height spectra . . . 116
3.20. Correlation map for a linear ECC . . . 118
3.21. Linear ECC . . . 119
3.22. Mismatch with a linear and a non-linear ECC . . . 119
3.23. Non-linear ECC . . . 120
3.24. Event rate, hit map, and pulse height spectrum of a HED measurement 121
3.25. HED Am-241 spectra obtained with energy calibration techniques. . . . 123
3.26. Pixel individual spectral resolution of the HED . . . 124
3.27. HED pixel specific spectra . . . 125
3.28. Crystal polarization in CdTe . . . 126
3.29. A quantitative measurement of crystal polarization . . . 126
3.30. Polarization time and peak drift as a function of the temperature . . . 127

4.1. Front view on the setup with installed HED and LED . . . 129
4.2. LED offset and noise evolution after HED power up . . . 130
4.3. LED hit map for CdTe fluorescence . . . 131
4.4. HED spectrum observed with and without LED . . . 132
4.5. Structure diagram of the combined LED and HED data analysis . . . 133
4.6. Coordinate systems of LED and HED . . . 133
4.7. The IAAT logo as image on the LED and the HED . . . 134
4.8. LED and HED timing synchronization via flux modulation . . . 135
4.9. Timing calibration with coincident fluorescence events . . . 136
4.10. Compton forward and backward scattering . . . 138

5.1. Polarimetry analysis of NGC 1068 . . . 145
5.2. Attenuation coefficients for photon energies $1\,\mathrm{keV} \leq E \leq 100\,\mathrm{MeV}$ . . . 148
5.3. Photoelectric effect . . . 148
5.4. Correction factor for photoelectric effect in Si . . . 149
5.5. Differential cross section for photoelectric effect and Compton scattering 150
5.6. Energy of the Compton electron as a function of the scattering angle . 151
5.7. Terminology of Compton scattering . . . 151

5.8. θ-differential and total cross section for Compton scattering 152
5.9. Incoherent scattering factor $S(\theta)$ 153
5.10. Differential cross section for incoherent scattering 153
5.11. Graphs of the analytic expressions for σ_{PE} and σ_{CS} 154
5.12. Ter-minology for pair production 154
5.13. The spectrum of Compton electrons in the LED 156
5.14. Probability of a CFS event detected with the CANDELA setup 158
5.15. Illustration of the Compton camera principle 159
5.16. Compton ellipses for different distances of the source plane 160
5.17. The ϕ modulation of the differential cross section for inc. scattering . . 161
5.18. Optimizing the sensitivity for the polarization measurement 162

6.1. The $\frac{\Delta C(\phi)}{\Delta \phi}$-plot 166
6.2. The probability density function $\rho_{\mathrm{a},\Psi}(a, \Psi \,|\, a_0, \Psi_0)$ 169
6.3. Sinusoidal signals and noise 170
6.4. Color map of the $1/\sigma$ distribution 171
6.5. Rice distribution 172
6.6. Correction of polarization biasing with different estimators 174
6.7. Bias and MSE for polarization estimators 175
6.8. Schematic illustration of the λ parameter 176
6.9. Graph of $\lambda_{\mathrm{opt}}(p_0)$ 177
6.10. Schematic p-p_0 projection 177
6.11. Confidence intervals for σ_1, σ_2 and σ_3 178
6.12. The probability density function ρ_Ψ 179
6.13. σ_1, σ_2 and σ_3 confidence intervals for Ψ 180
6.14. Unnormalized Bayesian Rice distribution 181
6.15. Normalization of $\rho_{\mathrm{p}}(p_0 \,|\, p)$ 182
6.16. Bayesian bias(p) and MSE(p) 183
6.17. Optimal λ values for σ_1, σ_2 and σ_3 confidence levels 184
6.18. Credibility intervals for σ_1, σ_2 and σ_3 credibility levels 185
6.19. Credibility intervals for the angle of polarization 186
6.20. Inversion method 188
6.21. Schematic to explain the simulation of credibility intervals 189
6.22. CDF and event distributions for a Compton polarimeter 192
6.23. Overestimation of enhanced event densities 193
6.24. Binning reduced amplitude reduction 194
6.25. Equal width binning and fitting 195
6.26. Equal frequency binning and fitting 195
6.27. Simulated Distribution of a and Ψ 195
6.28. Optimal number of equal width bins 197
6.29. Point estimation and optimal number of bins for EWB 197
6.30. Optimal number of equal frequency bins 198
6.31. Point estimation and optimal number of bins for EFB 198

List of Tables

1.1. Properties of Si and CdTe . . . 33
1.2. Poisson distribution for continuous and triggered readout . . . 43
1.3. Noise sources and their classifications . . . 47
1.4. Radioactive sources . . . 52

2.1. Applied potentials to operate a DEPFET cell . . . 58
2.2. LED operation commands . . . 70
2.3. Detection efficiency of different bad pixel analysis modes . . . 81
2.4. Summary of the spectroscopic properties of the LED . . . 87
2.5. Low energetic LED fluorescence lines . . . 90
2.6. High energetic LED fluorescence lines . . . 90

3.1. Summary of the spectroscopic properties of the HED . . . 122

5.1. Expected performance of CANDELA as a Compton polarimeter . . . 163

6.1. Terminology in polarization analysis . . . 165

C.1. Parametrized estimators for the degree of polarization . . . 211
C.2. Best estimated bias calculated with the frequentist approach . . . 211
C.3. Best estimated MSE calculated with the frequentist approach . . . 211
C.4. Parametrized confidence intervals for p_0 . . . 212
C.5. Parametrized credibility intervals for p_0 . . . 213
C.6. Best estimated bias calculated with the Bayesian approach . . . 214
C.7. Best estimated MSE calculated with the Bayesian approach . . . 214
C.8. Parametrized credibility intervals for Ψ_0 . . . 214